Analysis and Development of a Decanter Centrifuge

Power consumption analysis, development of a composite bowl, and feed accelerator analysis

George Ross Arana Bell

A thesis submitted in fulfilment of the requirements for the

Degree of Doctor of Philosophy

in Mechanical Engineering

at the University of Canterbury

2013

Table of Contents

List of Figures

List of Tables

Acknowledgements

Firstly I would like to thank Bellmor Engineering Ltd. for giving me the opportunity to undertake this project. It has been greatly beneficial to my engineering skills and expertise.

To John Pearse I extend thanks for being a dedicated supervisor throughout the course of my project. I have acquired new skills and experiences working alongside Doctor Pearse. To Brian Donohue, I owe thanks for his unquestionable advice and guidance, without his experience and knowledge this project would have been impossible to undertake. Thank you to Digby Symons of the University of Cambridge, it was greatly beneficial to work alongside you and publish a paper.

Groups that I would like to thank for their assistance during the course of this project are the team at ASP Ltd., workshop staff in the Department of Mechanical Engineering, McClay Tooling, and SAI Global.

I would like to express my deepest gratitude to my parents, Dianna and Stephen Bell. You have always supported me in any endeavour I have chosen to undertake and have always been proud of anything I have achieved.

To Rachael Palmer, thank you very much for your support throughout the course of my PhD. Thank you for waiting up on the late nights, cooking dinner, and being wonderfully supportive.

Throughout the course of my undergraduate and postgraduate studies I have become friends with some great people, who I will not name individually. You have all played a role in the completion of my PhD, and to that I am truly grateful.

Abstract

This project was concerned with the analysis and development of a decanter centrifuge. The aim of the project was to increase the understanding of the operation of the machine, and identify and implement methods of improving the performance.

A comprehensive breakdown of the power consumption of a GTech-Bellmor 1456 Centrifuge Decanter was completed. There are four components of the power consumption in a decanter centrifuge: friction during product transport, viscous and kinetic losses during feed acceleration, inefficiencies in power transmission components, and aerodynamic losses, known as windage. A mathematical model was developed to predict the power, torque, and axial force required by product transport. A relationship for the power consumed during feed acceleration was derived from first principles. The power transmission losses are comprised of inefficiencies in the motors, belt drives, gearbox, bearings, and seals; each of these was quantified. The windage has two components: the surface drag on the bowl as it rotates in an annular space and the pressure drag on external protrusions. The windage was predicted empirically and computationally. Methods that were identified for improving the decanter centrifuge were: reduce the mass of bowl and scroll, improve wear resistance, reduce the coefficient of friction of the bowl wall and scroll faces, optimise scroll geometry, redesign the feed accelerator to increase acceleration efficiency, implement control of the bowl speed, differential speed, and pool depth, and recess the bolt heads on the bowl and cover the third phase ports.

An analysis of several worn centrifuges revealed that the majority of the wear occurs on the scroll, bowl wall, accelerator, and solids discharge ports. An experiment was developed to recreate the wear conditions inside a centrifuge. A high pressure abrasive film was forced between materials moving relative to each other. Similar results were observed for acetel, UHMWPE, and 316 stainless steel when using a pin-on-disk wear test rig. A new composite bowl was developed for two main reasons, weight reduction, and improved wear and friction characteristics. The full design process was applied to the bowl and several concepts were generated for a new scroll. The design of the bowl included conceptual design, material selection, material testing, constructing scale models, and the manufacture of a full-size bowl for a GTech-Bellmor 1456 Centrifuge Decanter. The potential for using composite materials in decanter centrifuges was

demonstrated. The manufacturing method developed during this project was novel and produced parts suitable for use in high-speed rotating machinery.

The feed accelerator analysis consisted of three components: theoretical, experimental, and computational analysis. Three feed acceleration mechanisms were identified: viscous dissipation, impulse force, and mass flow induced velocity. An experimental method was developed to examine decanter centrifuge feed accelerator designs. The method allowed for the measurement of efficiency and high-speed photography of the flow between the accelerator and the rotating pool. The order of best to worst performing of the six tested designs was Modified Disk, Disk, Plate, Conical, Drum, and Esbjerg. The feed accelerator was modelled using ANSYS-CFX 14.5 and compared to the experimental results. There was excellent agreement between the flow in the annular space observed using high-speed photography and the paths predicted using the computational model. A parametric study of the Drum and Disk feed accelerator designs was undertaken using the computational model. It was found that increasing the surface area of the port faces of the Drum accelerator and increasing the discharge angle and discharge radius for the Disk accelerator improved the performance.

Publications

Title: Mathematical Model for Solids Transport Power in a Decanter Centrifuge

Status: In review Submitted: 9th July 2013

Authors: George R.A. Bell, Digby D. Symons, and John R. Pearse

Journal: Chemical Engineering Science

Abstract: A mathematical model of the transport of sedimented solids within a decanter centrifuge has been developed. The primary purpose of the model is to calculate the power, torque and axial force required for the scroll to transport the solids along the bowl. The model is presented in a non-dimensional form and the procedure for implementing the model is included. The model is compared to test data from an existing publication; there was good agreement between the model and data. Example results are presented in the form of graphs to illustrate the influence of key parameters.

Title: Experimental and Computational Analysis of the Feed Accelerator for a Decanter Centrifuge

Status: In review Submitted: 25th July 2013

Authors: George R.A. Bell, and John R. Pearse

Journal: Separation and Purification Technology

A well designed decanter centrifuge feed accelerator can increase product throughput, solids recovery, and liquid clarity, while a poorly designed accelerator can increase wear and reduce the overall efficiency of the machine. An experimental method was developed that allowed for the measurement of acceleration efficiency and high-speed photography of the flow in the annular space between the accelerator and the rotating pool. The order of best to worst performing of the six tested designs was: Modified Disk, Disk, Plate, Conical, Drum, and Esbjerg, having acceleration efficiencies of 91.7%, 85.5%, 77.2%, 77%, 75.8%, and 74.6%, respectively. The high efficiency of the Modified Disk accelerator was attributed to the over-speeding effect of the forward curving vanes and the larger discharge radius. The feed accelerators were modelled using ANSYS-CFX. There was excellent agreement between the flow in the annular space observed using high-speed photography and predicted using the computational model. The predicted torque acting

on the accelerator walls was found to have good correlation with the experimentally measured increase in pool speed. A parametric study of the Disk and Drum feed accelerator designs was undertaken using the computational model. It was found that increasing the discharge angle and discharge radius for the Disk accelerator and increasing the surface area of the port faces of the Drum accelerator improved the performance.

Chapter 1

Background and Introduction

1.1 Introduction

Increasing energy demand and limited energy resources, reflected in higher energy cost, has instigated a strong drive over the past decade to design and use energy efficient machinery. As the momentum behind the efficiency movement builds, fewer industries are excluded. Consequently, a high efficiency product has the ability to stand out from competing products. A contributing factor to the continued use of inefficient technology is that the current design is known to work, regardless of whether or not there is room for improvement. To remedy this situation, older technology needs to be revisited using modern engineering methods - this approach was used on the project at hand. A decanter centrifuge was analysed and modified with the aim of reducing power consumption and improving performance.

A centrifuge is a device that uses centripetal force to separate mixtures of solids and liquids. Centrifuges can be used to separate almost any mixture, ranging from drilling mud to fish oil. A decanter centrifuge is a particular type of centrifuge that uses a scroll conveyor to allow for continuous separation of mixtures with up to three different phases. For a more detailed description of centrifuges and separation refer to Appendix A. The performance of a decanter can be quantified in several ways, including: throughput, centrate clarity, solids dryness, or solids recovery fraction. While the decanter centrifuge utilises modern manufacturing technology to improve balance and increase operating speed, the materials and design have remained relatively unchanged since the modern decanter was developed in the 1970s [1]. While work has been completed to develop variations of decanter centrifuges, there has been little research on improving the current design by applying new materials and scientific analysis methods. There is a clear opportunity to develop the existing design of a decanter centrifuge to reduce power consumption and improve performance.

This project considered the GTech-Bellmor 1456 Centrifuge Decanter. The power consumption of this decanter was theoretically predicted and used machines were examined to determine areas of potential improvements. The analysis revealed that the best course for improving the centrifuge was developing a new rotating assembly and an

in-depth analysis of the feed accelerator. A new bowl was designed and manufactured using modern composite materials for a variety of potential improvements. The feed accelerator was extensively investigated using theoretical, experimental, and computational methods to determine the effectiveness of multiple designs currently used by industry. The different parts of the project combined to give a better understanding of decanter centrifuges and improve the design by the application of modern engineering practices. The knowledge acquired during the project has a wide variety of applications that extend beyond decanter centrifuges.

1.2 Research Questions

Several questions were developed and addressed during the course of this project, these were:

- How is power consumed within a decanter centrifuge? How does each design and operating parameter influence the power consumption? What areas of the design can be modified to improve the overall performance and reduce power consumption? How can the design be modified to improve separation quality?
- What material combinations can be used for the bowl of a decanter centrifuge that would improve performance, reduce power consumption, extend component life, and reduce the cost of manufacturing? Can composite materials be used in a high-speed rotating assembly? How can a component be manufactured to ensure accurate dimensions and balance for use in a high-speed rotating assembly?
- How is feed rotationally accelerated in a decanter centrifuge? Of the current feed accelerator designs used by industry, which is the best for accelerating the incoming feed? What design features of a feed accelerator provide a significant improvement in performance? How can the current designs be improved or optimised?

1.3 Objectives

The central objective of this project was to reduce the power consumption and improve the performance of a decanter centrifuge. The performance of the centrifuge refers to quality of the outputs of the machine, the rate at which separation is achieved, and the general operation, such as vibration, sound power, etc. The project was broken down into three interrelated areas: power consumption analysis, composite bowl development, and feed accelerator analysis.

The first objective was to produce a comprehensive breakdown of the power consumption of a GTech-Bellmor 1456 Centrifuge Decanter. This included power consumed by: frictional losses during product transport, accelerating the product and rotating assembly, power transmission losses, and windage losses. Once this was achieved, the results were used to identify methods of reducing the power consumption.

The second objective arose from the discovery that friction within the centrifuge was one of the largest consumers of power. It was also discovered that excessive wear in areas of the bowl and scroll lead to premature component failure. The engineering design process was to be implemented to develop a new bowl that was superior to the current design.

The third objective was to thoroughly analyse the feed accelerator design of a decanter centrifuge. The feed accelerator strongly influences the performance of the machine. There are many designs in use today but little research has been conducted to differentiate between the performance of each. This analysis included theoretical, experimental, and computational evaluation of existing designs and a parametric study of the two of the designs.

To summarise the three main objectives:

- Produce a comprehensive breakdown of the power consumption within a decanter centrifuge and identify methods of reducing it.
- Develop a new bowl using modern materials to supersede the existing design.
- Analyse the feed accelerator to determine which of the commonly used designs performs the best.

These three objectives combine under the banner of using modern science and engineering methods to improve the performance and understanding of existing technology.

1.4 GTech-Bellmor 1456 Centrifuge Decanter

The GTech-Bellmor 1456 Centrifuge Decanter (see Figure 1.1 and Figure 1.2) is manufactured by Bellmor Engineering Ltd. in Christchurch, New Zealand. The key specifications for the GTech-Bellmor 1456 Centrifuge Decanter are given in Table 1.1. The design of the decanter was completed by Bellmor Engineering Ltd. and was based on other commercially available solid bowl decanters. Almost all components for the

decanter are manufactured by Bellmor Engineering Ltd., they also make replacement parts for competitor machines.

Figure 1.1 GTech-Bellmor 1456 Centrifuge Decanter

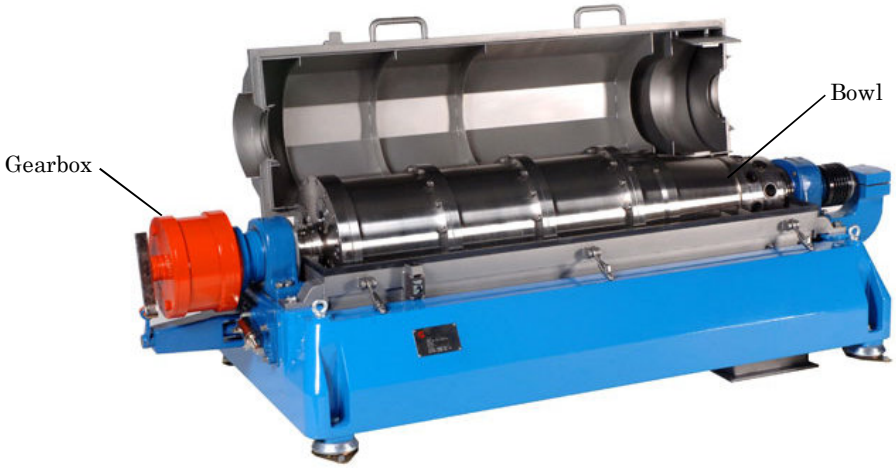

Figure 1.2 GTech-Bellmor 1456 Centrifuge Decanter with the lid open

Table 1.1 Specifications of the GTech-Bellmor 1456 Centrifuge Decanter

Main drive motor	30 kW
Back-drive motor	15 kW
Motor controllers	VSD
Internal bowl diameter	355 mm (14")
Normal bowl speed	3250 rpm
Maximum bowl speed	4000 rpm
Maximum G-force	3200g
Differential speed	2 – 45 rpm
Maximum throughput	~12 t/hr
Bowl material	316 stainless steel
Auger material	304 stainless steel

1.5 Commercially Available Decanter Centrifuges

At present, the two leading decanter manufacturers are Alfa Laval and GEA Westfalia Separator Group [1]. Another prominent manufacturer is ANDRITZ. The latest decanters that each of these manufacturers currently offer are described below.

Alfa Laval's latest range of decanters is the ALDEC G3 [2] (see Figure 1.3 (a)). All components that are in contact with the process material are made from either 316 or duplex stainless steel. The main and back-drive motors are controlled by variable speed drives (VSD) to allow for independent tuning of the bowl and differential speed. There is a strong emphasis on efficiency and power consumption. Alfa Laval claims that the power consumption is reduced by up to 40% by new 'power plate' technology. These plates are fitted to the liquid weirs and supposedly reduce power consumption by recapturing the energy of the discharging liquid phase. There is an inbuilt torque transducer on the conveyor shaft. The bowl is fitted with a baffle to restrict cake flow and aid with product transport. There is also a claim that there is improved wear resistance, but no details are given on the material selection other than stainless steel.

GEA Westfalia Separator Group's range of decanters is available at [3]. The CFE 500-01-772 is shown in Figure 1.3 (b). The technology presented by Westsfalia is very similar to that offered by Alfa Laval.

The ANDRITZ line of decanter centrifuges is detailed at their website [4]. These decanters are separated into two classes, A and D, the A class is designed for chemical and industrial separation applications, and the D class has been adapted for the

treatment of wastewater. The D class decanter is shown in Figure 1.3 (c). One of the main points of difference of these machines is the drive system. The drive for the D class is coaxial and it is claimed to have energy re-circulation. They also claim to have a novel synchronous motor and coupling type. ANDRITZ also offer the patented XL-Plus feed accelerator [5]. The bowls can be delivered in stainless steel, hastelloy, titanium, or nickel. The bowl, scroll, and ports can be fitted with wear resistant ceramic tiles for harsh applications. Of the three manufacturers discussed in this section, it appears that the ANDRITZ decanters have undergone the most development.

(a) (b) (c)

Figure 1.3 (a) Alfa Laval ALDEC G3 Decanter Centrifuge (b) GEA Westfalia Separator Group CSE 500-01-772 (c) ANDRITZ Solid Bowl Decanter Centrifuge D

The main themes from each of these leading manufacturers were energy efficiency, product quality, and throughput. All of the manufacturers claimed that their machine was developed to offer optimal efficiency and product throughput, but none produced sound reasoning as to how it was achieved. While some of the features offered are new, they are mostly subtle changes and there is clear potential to further develop the decanter centrifuge.

1.6 Developments in Decanter Centrifuge Technology

This section introduces some of the developments that have been made to decanter centrifuges since their conception. This is not an exhaustive survey and areas that have been further explored in this project are discussed in more detail in their respective sections. This review is limited to work that was conducted specifically on centrifuges and does not extend to literature on similar technology. While the initial decanter centrifuge utilised the same concepts as a modern day one, there have been advances in technology that have allowed for improvements in manufacturing and operation. These advances include drive systems, control and monitoring, materials, manufacturing accuracy, improved off-the-shelf componentry, and adaptions of decanters. Developments in each of these fields are discussed below.

The speed of a centrifuge was originally mechanically fixed by belt and gear ratios, if the speed needed to be changed it would involve stopping the machine and changing the pulleys. With the invention of the VSD for electric motors and high-torque hydraulic motors, it is now possible to tune the speed of the machine during operation.

The Octopus control system [2] was developed by Alfa Laval. It is a control system for a dewatering centrifuge that monitors outputs and adjusts the centrifuge to optimise operation. A control system was developed that provided constant adjustment of the pool level [6], this allowed fine tuning and optimisation of the specific process. Sensor development for moisture content of solids allows operators to constantly monitor the outputs of the machine and adjust the inputs accordingly.

The materials used in decanters have not changed significantly over the past several decades. The most commonly used material is stainless steel, grade 304, 316, and duplex. Some manufacturers offer other materials such as titanium. Machines in high wear applications can be fitted with hard wearing ceramic tiles, made from materials such as tungsten carbide.

Precision manufacturing machinery has improved decanters due to their ability to repeatedly achieve finer tolerances. The cost of this equipment has decreased and now many larger workshops possess full CNC capability. Bigger machines can now be made and in greater quantities than previously achievable with the same manufacturing resources.

There has been a significant amount of investment in the development of technology such as bearings, seals, and belt drives, all of which are utilised in decanter centrifuges. Bearings have seen improvements in service life, lubrication, tolerances, and friction. Seals are now offered in a large range of configurations for a number of applications. Belt drives have evolved to be a highly efficient method of transmitting power. The efficiency of these components will continue to increase as research and development progresses.

There have been several adaptions of decanter centrifuges for varying reasons. A concept of a decanter with a compound beach and cake flow control is presented in [7], which reported an increase in solids dryness and throughput. Minaker [8] provided a critical discussion of the developments in decanters over the 50 years preceding 1995. In this work Minaker stated that the fundamental achievement of decanters is a bowl

speed of 70-100 m/s and a maximum bowl length to diameter ratio of 4. It was suggested that these fundamental limitations are imposed by fixed rolling element bearings, the first harmonic of the bowl and scroll, and material limitations. These factors must be overcome if decanters are to hold their place as the first choice of separator in many applications. Sutherland [1] published a review of separator technology and concluded that there has been only a few areas of progress in decanters since the 1970s.

1.7 Project Scope

This project was separated into three distinct, yet interrelated parts. Each part is introduced and briefly discussed below.

1.7.1 Power consumption of a decanter centrifuge

An investigation of the power consumption and potential reductions was undertaken. The outcome of this part was a comprehensive understanding and breakdown of the power use within the GTech-Bellmor 1456 Centrifuge Decanter. The power consumption within the centrifuge was broken down into the following areas: product transport, acceleration of the product, power transmission losses, windage losses, and accelerating the rotating assembly. The power consumed by each of these components was analysed and quantified.

Product transport

Once the solids have settled against the bowl wall they are transported to the solids discharge ports by the scroll conveyor. A large normal force acts on the bowl wall due to the high centripetal acceleration. This high normal force, combined with the constant relative motion gives rise to friction, it is this friction that consumes a large amount of power. The power consumed by friction is a function of the coefficient of friction between the settled solids and the machine components. The coefficient of friction is a function of material, surface finish, product, and product wetness [9].

A mathematical model of the product transport was developed that can be used to predict the power, torque, and axial force. At present, there are no mathematical models available that can be used to predict this. Alternative models for product transport are presented in [10, 11], neither of these models provides enough information to be able to apply them to a different decanter.

Feed acceleration

The incoming product is accelerated within the hub of the scroll prior to entering the bowl. During this acceleration process there are large viscous losses that are equal to the gain in kinetic energy [12]. The gain in kinetic energy is fundamental to the operation of most types of centrifuges. Accelerating the product is typically the largest consumer of power in a decanter centrifuge [10]. If the feed is not fully accelerated before entering the bowl it can disturb the rotating pool, re-suspend settled solids, decrease centrate clarity, and increase component wear. Poor acceleration leads to poor product quality and a decrease in the overall performance of the centrifuge. The design of the accelerator is one of most important aspects of a decanter centrifuge. A relationship for the power consumed by feed acceleration was derived.

Power transmission losses

The components that transmit power in a decanter centrifuge are: drive motors, belt drives, gearbox, bearings, and seals. The losses in each of these systems were quantified and discussed. A test rig was designed to measure the gearbox efficiency under full load.

Windage losses

The rotating components of the centrifuge are exposed to both the working fluid and air within the cover. There is a significant amount of drag due to the surrounding air, this is known as windage. Not only does windage result in energy losses, it also adds to the acoustic emissions of the decanter. Windage losses were predicted using an empirical model and ANSYS CFX.

Accelerating the rotating assembly

The rotating components of the decanter require accelerating during start-up. The power required to accelerate the rotating assembly was calculated for the current design and a new design using various materials. The power requirement for accelerating the rotating assembly is not part of the continuous running power and was considered to establish its relative magnitude.

1.7.2 Wear analysis of a decanter centrifuge and development of a composite bowl

A new bowl was developed for the decanter for a variety of reasons. The wear on the bowl and scroll was analysed as part of the bowl development.

Wear

The wear within several used decanters was analysed. The analysis highlighted that there was significant wear occurring in parts of the machines. Two test rigs were developed to simulate the environment within the centrifuge. A variety of materials were evaluated to attempt to find a suitable replacement for stainless steel. The replacement material would ideally be more wear resistant and have a lower coefficient of friction than 316 stainless steel. If the coefficient of friction between the bowl and product was reduced it would result in a decrease in power consumption.

Composite bowl development

The original design of a decanter centrifuge used either steel or stainless steel for the majority of the components. Few developments have occurred over the past 40 years with regards to the use of different materials. Some of the other materials used in decanters include: titanium, Hastelloy, nickel, alloyed aluminium, and others [13]. From the power consumption and wear analysis it was evident that there were several potential benefits to redesigning the bowl using different materials, these benefits included:

- Increased lifespan of components due to higher wear resistance.
- Reduced power consumption and product destruction due to a lower coefficient of friction between the settled solids and the bowl wall.
- Lower bearing loads, leading to extended life and lower power consumption.
- Improved ease of handling during manufacturing and assembly of a lighter bowl.
- Lower manufacturing costs.
- Reduced freight cost due to lower weight.
- Reduced noise emissions due to the removal of protrusions [14].

The full engineering design process was applied to the bowl. This included specifications, material selection, material testing, sourcing suppliers and manufacturers, small scale testing, and full size component manufacturing. The

material combination and manufacturing method that was developed during this part was novel. At the conclusion of this part of the project a full size bowl was manufactured.

1.7.3 Feed accelerator analysis

Feed acceleration is the most important aspect of any continuous separator. Many different designs are being used by centrifuge manufacturers. Little published research exists of the difference between common designs and specific features are often added with only a small amount of understanding of what the effect of it will be. The technology of accelerators has been investigated by Leung [5, 13, 15-19]. There are patents by others on the design of feed accelerator systems [20], but there has been no published research to provide validation. A numerical model of a Disk accelerator for a two-stage pusher centrifuge was created by Tan et al [21]. Once a satisfactory design was achieved it was tested in an industrial experiment. It was predicted that the mass flow rate would improve, which was demonstrated in the experiment. A CFD analysis of the multiphase flow in a solid bowl centrifuge was conducted by Fernandez [22]. The model did not include the specific accelerator geometry or the weir geometry. A well designed feed accelerator can increase product throughput, solids recovery, and liquid clarity, while a poorly designed accelerator can increase wear and reduce the overall efficiency of the machine.

This part of the project considered the effect of different designs and development of a new accelerator. Six accelerator designs were identified from literature and manufacturers' catalogues. An apparatus was developed to evaluate the performance of each of these designs. A computational model was created using ANSYS CFX that accurately predicted the performance of the accelerator designs in the test apparatus. The experimental and computational analysis gave a clear insight into the feed stream between the accelerator and the rotating pool. The results showed the difference in performance between each of the designs. The computational model was used to conduct a parametric study of two of the accelerator designs.

1.8 Resources and Facilities

This project was conducted at the University of Canterbury and Bellmor Engineering Ltd. The University provided modern mechanical testing facilities, and academic and technical support. The University also provided access to software such as ANSYS™,

MATLAB™, and SolidWorks™. A wide range of literature was available through the library at the University of Canterbury. Bellmor Engineering Ltd. offered access to state-of-the-art manufacturing facilities and the experience of their staff in the field of manufacturing and centrifuges. Several suppliers and external manufacturers were used during the course of this project, including: ASP Ltd., SAI Global, and McClay Tooling.

1.9 Contributions

The components of this research that were novel and contributed to the understanding and development of this field were:

- A comprehensive breakdown of the power consumed within a decanter centrifuge with a list of potential modifications to reduce the power consumption and improve the performance.
- A mathematical model of the product transport that can predict power, torque, and axial force for a given geometry and throughput.
- A relationship for the power consumed by feed acceleration.
- Development of a method of manufacturing a composite cylinder lined with an abrasion resistant coating.
- Using a monolithic silicon carbide liner inside a composite shell.
- Design and manufacture of a composite bowl for a decanter centrifuge to improve performance, reduce wear, reduce cost, and simplify manufacturing.
- Experimental and computational evaluation of multiple feed accelerator designs to determine which performed the best. The findings were used to design a new feed accelerator that performed better than any other design tested. This work provides centrifuge designers with a reliable comparison between feed accelerator designs.
- A parametric study of the Drum and Disk feed accelerators to determine which parameters have the greatest influence on performance.

These novel components are not only relevant for decanter centrifuges, but can be applied to other rotating equipment.

Part I

Power Consumption of a Decanter Centrifuge

Part I contains a comprehensive analysis of the power consumed by a decanter centrifuge. The analysis includes the evaluations of the power consumed by the frictional losses during product transport, acceleration of the incoming feed, power transmission losses, windage losses, and acceleration of the rotating assembly. Part I concludes with a chapter containing a summary of the power consumption and recommendations for reducing it.

Chapter 2

Product Transport

2.1 Introduction

This chapter covers one of the most fundamental processes occurring within a decanter centrifuge, the product transport. Product transport is the process of the scroll conveyor moving the solids that have settled against the bowl wall to the solids discharge ports. Understanding the product transport is important in the design and operation of any centrifuge as it strongly influences product quality and consumes a substantial portion of the total power required by the centrifuge.

The product transport is influenced by many design features and operating parameters. The operating parameters include those controllable during operation, such as flow rate, bowl and differential speed, pool depth, and feed temperature. Other operating parameters that were explored include flow paths, cake dryness, hydrostatic pressure, and lifting of the solids. Design features that are discussed include the bowl geometry, scroll geometry, and coefficient of friction. These design features are fixed during design and manufacturing and cannot usually be varied during operation.

The primary resistance to product transport is Coulomb friction between the settled solids, also known as the cake, and the bowl wall and scroll blade faces. The second component of product transport is the force required to lift the solids against the centripetal force from the larger radius of the cylindrical section to the smaller radius of the exit ports [11].

A model of the product transport within a decanter centrifuge was developed. The model predicts the power and torque required to transport the solids along the bowl; it can also be used to calculate the axial bearing loads, axial bowl stress, effect of design parameters, and the effect of operating variables. The model was compared against experimental data obtained from an existing publication [23]; there was reasonable agreement between the model and data. A detailed procedure for implementing the model is described.

In the GTech-Bellmor 1456 Centrifuge Decanter the scroll is driven by a 15 kW electric motor via a belt drive and a high reduction (57:1), two stage, epicyclic gearbox. The

back-drive torque is limited to 3.6 kNm to prevent destruction of machine components if the centrifuge were to become blocked.

This chapter contains a discussion of the relevant operating and design parameters, the derivation of the forces acting on a cylindrical element of solid, the presentation of the equations for power, torque, and axial force, a description of the four discrete regions in the bowl of a decanter centrifuge, instructions of how to implement the model, validation of the model, results for the GTech-Bellmor 1456 Centrifuge Decanter, and a discussion of the findings.

2.2 Operating and Design Parameters

This section contains a discussion of relevant operating and design parameters and how each influences the operation, power consumption, and product transport. There is also some discussion of work completed by others on specific aspects of decanter centrifuges.

2.2.1 Flow paths

While product transport is concerned with the movement of the solids, it is important to understand how the liquid phase flows through the centrifuge. A schematic of the feed flow path and liquid and solids discharge ports is shown in Appendix A.

The liquid enters the rotating bowl as part of the slurry through the feed accelerator discharge ports. Once the liquid has entered the pool it follows the helical path made by the scroll towards the liquid discharge ports; this is shown by the line in Figure 2.1. If the incoming slurry has not reached the solid body rotational speed of the bowl it is accelerated in the liquid pool. If the pool is rotating at a lower speed than the bowl the centripetal force acting on the solids will be reduced and therefore the effective settling area of the cylindrical section would be smaller.

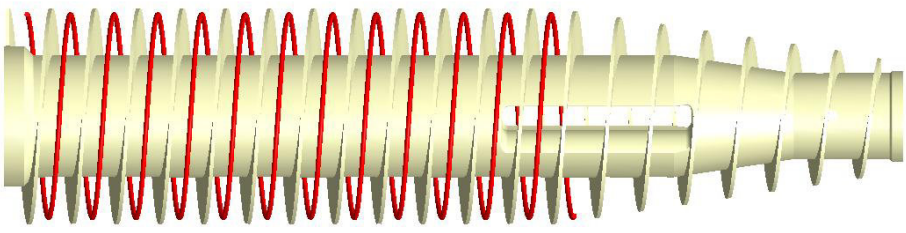

Figure 2.1 Liquid phase following the helical path formed by the scroll (the liquid flows to the left)

The helical scroll stops the liquid phase from simply flowing straight to the discharge ports, this significantly increases the distance the liquid must travel, resulting in a higher average velocity. As the liquid follows the helical path of the scroll it flows in a thin layer on the inner surface of the pool [13, 22], it is important that this layer does not entrain the settled solids as this can reduce solids recovery and centrate clarity. The pool surface should be kept well above the settled solids to reduce entrainment. Openings are added to the scroll in some decanters that allow for axial flow; this reduces the distance the liquid must travel. An example of a scroll with axial openings is shown in Figure 2.2. The shape and size of the openings must be carefully designed to ensure the desired results are achieved.

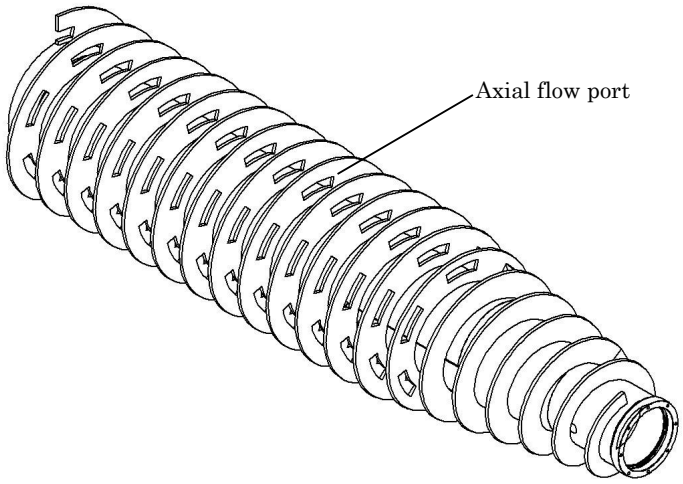

Figure 2.2 Scroll with axial openings

The solids enter the bowl through the feed accelerator discharge ports as part of the slurry. The centripetal force causes the solids to move outwards and settle against the bowl wall. The rate that the solids settle is determined by Stokes' Law, which relies on the solids having a higher density than the suspending liquid phase. As the solids are settling on the wall, or on top of previously settled solids, the scroll transports them along the bowl. The solids move along the bowl somewhere between two extremes, axially or circumferentially. If the solids are only moving circumferentially there is no product transport; as the solids are rotating with the scroll. Axial motion of the solids can be encouraged by the addition of axial ribs on the bowl wall. In a decanter that is operating correctly the product transport can be treated as being predominantly axial. As the solids move up the conical beach they lift out of the liquid pool, this is where they

are dewatered. When the solids reach the discharge ports they are ejected into the surrounding casing.

2.2.2 Bowl speed

The bowl speed ω is one of the most important operating parameters of a centrifuge as it is related to the centripetal acceleration a in the cylindrical section by the expression

$$a = \omega^2 r_o \qquad 2.1$$

where

r_o inner radius of the bowl in the cylindrical section (m).

Higher bowl speeds result in higher centripetal acceleration, which results in faster separation and higher clarity of the centrate. The bowl speed has varying effects on different types of solids; for crystalline solids the dryness increases with speed, while for other solids, finer particles are captured resulting in wetter solids. The wetter solids result, in part, from the increased surface area of the solids that have been separated carrying a film of liquid. While increasing the speed leads to higher throughput it also increases the transport torque and power consumption due to the increased normal force on the bowl wall.

2.2.3 Differential speed

The differential speed Δ is the difference in rotational speed between the scroll and bowl. The differential speed can be adjusted during operation for centrifuges fitted with a variable speed drive (VSD); this allows for constant optimisation of the process to achieve better separation. At low differential speed the layer of settled solids is thicker. If the surface of the cake is too close to the surface of the pool this can increase the entrainment of the solids into the flow, decreasing the centrate clarity and solids recovery. If the differential speed is too high this can cause disturbance to the pool and re-suspension of solids. The optimal differential speed depends on the requirements of the centrifuge; such as cake dryness and centrate clarity. The axial transport velocity v is related to the differential speed by

$$v = \frac{G\Delta}{2\pi} \qquad 2.2$$

where

G scroll pitch (m).

The scroll pitch G of the GTech-Bellmor 1456 Centrifuge Decanter is 70 mm for meat and fish products and 110 mm for drilling mud processing. The specified differential speed range is 2 to 45 rpm (0.21 to 4.71 rad/s), corresponding to axial conveyor velocities of 2.3 to 52.5 mm/s with a 70 mm scroll pitch.

2.2.4 Flow rate

The power consumption for feed acceleration is linearly proportional to the volumetric flow rate of the feed. Increasing the flow rate results in higher flow velocities within the centrifuge, leading to turbulence and potentially re-suspension of settled solids. The flow rate must be kept below a critical value to ensure that the phases leaving the centrifuge meet the required specifications; this critical value will be different for each application [13]. The flow rate can be significantly limited by the design of the feed accelerator [13, 17], this is investigated in detail in Part III. One of the constraints of the flow rate of a decanter centrifuge is the settling area, which is discussed further in Section 2.2.11.

2.2.5 Pool depth

The pool depth h_p is the inner radius of the cylindrical section of the bowl minus the inner radius of the rotating liquid pool. Increasing the pool depth reduces the transport torque due to the additional buoyancy of the cake and the reduction of the length of the conical beach. The power required for acceleration is also decreased as the tangential velocity of the inner surface of the pool is lower. Leung [11] states that the power for transport and acceleration consume 60-80% of the total power and increasing the pool depth can significantly reduce power consumption. When the pool is deeper, the length of the dry beach is shortened, reducing the time available for dewatering the solids, which ultimately leads to wetter solids. A compromise must be made between power consumption, cake dryness, and centrate clarity. For some applications there is an optimal pool level to give the greatest product recovery [24].

Pasol *et al* [6] developed a pool level control system and monitored its effect on the centrifuge performance. They reasoned that the pool depth is a key operating variable, therefore it would be advantageous to control it during operation. They used an *Easy pond* ™ system to control the depth; this consisted of a controllable choke plate that can add resistance to the liquid discharge ports while the machine is operating, which changes the pool depth. When used in conjunction with control of the bowl speed, differential speed, and polymer dosing, the centrifuge was able to be continuously optimised for different types of incoming feeds.

2.2.6 Feed temperature

In applications where the feed temperature is higher, the film of liquid on the solids will be thinner due to the liquid having a lower viscosity [25]. A higher feed temperature results in a lower viscosity, leading to thinner boundary layers on the inner surfaces of the centrifuge, which can result in fewer disturbances to the pool and settled solids. The feed temperature is determined by processing requirements such as cooking or heating before the feed enters the centrifuge.

2.2.7 Cake dryness

It is well understood that cake dryness is strongly proportional to transport torque and power consumption [13]. This is due to the increased coefficient of friction between the drier solids and the surfaces within the bowl. Cake dryness is normally a specified requirement of the centrifuge, therefore it cannot be changed to relieve the power consumption.

2.2.8 Control system

As the environment within the centrifuge is continuously changing, due to feed and ambient conditions, one set of optimal operating variables does not exist. Continuous control can be used to achieve constant optimal running conditions. The variables that are practical to control are the bowl speed, differential speed, and, if practical, the pool depth.

To enhance the solids transport, a VSD can be used to control the differential speed. Using a VSD allows for continuous optimisation of the differential speed or torque. The bowl speed can also be controlled by a VSD, allowing for a variable g-force. Varying the pool depth is more difficult but can be controlled as discussed in Section 2.2.5.

Leung [11] suggested using one of three types of control for the scroll:

- Torque control
- Speed control
- Hybrid of both speed and torque control

Hybrid control has proven to be the most effective [11]. The controller would need to be designed specifically for each application.

King [26] introduces the use of dual-drive motors, where the back-drive motor acts as a brake/generator. The power from the back-drive motor was recycled via a DC bus to the main drive motor. When using this system it was found to be easier to optimise the centrifuge for peak efficiency. This system would offer no reduction in the power required for product transport.

2.2.9 Hydrostatic pressure

The g-forces necessary for high separation rates result in a large pressure acting on the inner surface of the bowl, therefore the bowl acts as a pressure vessel. It is necessary to know the maximum hydrostatic pressure acting on the bowl so the stresses can be determined. The hydrostatic pressure at radius r for a hollow cylinder with inner radius r_{dL} of fluid rotating at ω, having density ρ is

$$P_r = \frac{\rho\omega^2}{2}(r^2 - r_{dL}^2) \qquad 2.3$$

The inner radius of the pool r_{dL} is also the liquid discharge radius.

2.2.10 Lifting the solids

As the solids are transported up the conical section they must be lifted against the centripetal force. In the GTech-Bellmor 1456 Centrifuge Decanter the radius of the cylindrical section r_o is equal to 176.6 mm, and the solids discharge radius r_{dS} is equal to 126 mm.

Consider the element of mass m shown in Figure 2.3 rotating at ω moving from radius r_o to r_{dS}. There are two components of force acting on the block: the centripetal force F_r acting in the radial direction, and the Coriolis force acting in the tangential direction. The Coriolis force is a result of the decreasing tangential velocity. These are evaluated separately and combined to give the total change in energy. Constant angular and radial velocities are assumed.

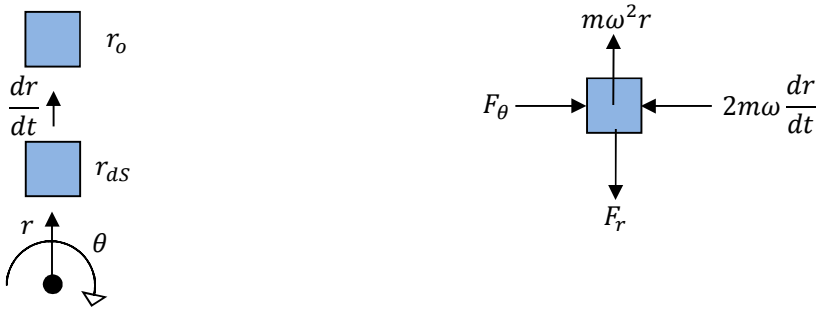

(a) (b)

Figure 2.3 (a) Element of mass $\boldsymbol{m}$ rotating at $\boldsymbol{\omega}$ moving from radius $\boldsymbol{r_o}$ to $\boldsymbol{r_{dS}}$ and (b) free body diagram of mass at radius $\boldsymbol{r}$

The energy required to overcome the centripetal force is

$$E_{Lr} = \int_{r_o}^{r_{dS}} F_r \, dr \tag{2.4}$$

where

$$F_r = -m\omega^2 r \tag{2.5}$$

therefore

$$E_{Lr} = \frac{1}{2} m\omega^2 (r_o^2 - r_{dS}^2). \tag{2.6}$$

The work done by F_θ is equal to

$$E_{L\theta} = \int_{r_o}^{r_{dS}} F_\theta \, r d\theta \tag{2.7}$$

where

$$F_\theta = -2m\omega \frac{dr}{dt}. \tag{2.8}$$

Substituting 2.8 into 2.7 gives

$$E_{L\theta} = \int_{r_o}^{r_{dS}} -2m\omega^2 r \, dr. \tag{2.9}$$

Integration yields

$$E_{L\theta} = -m\omega^2(r_o^2 - r_{dS}^2), \tag{2.10}$$

which is negative, meaning energy has been recovered.

The sum of the two work components equates to

$$E_L = E_{Lr} + E_{L\theta} = -\frac{1}{2}m\omega^2(r_o^2 - r_{dS}^2). \tag{2.11}$$

The change of kinetic energy can be used to verify Equation 2.11. The difference in rotational kinetic energy ΔE_K is

$$\Delta E_K = E_{K1} - E_{K2} = \frac{1}{2}I_1\omega^2 - \frac{1}{2}I_2\omega^2 \tag{2.12}$$

$$\Delta E_K = E_{K1} - E_{K2} = -\frac{1}{2}m(r_o^2 - r_{dS}^2)\omega^2 \tag{2.13}$$

The kinetic energy has reduced as the mass has moved to a smaller radius while maintaining constant angular velocity.

Equations 2.6 and 2.10 can be used to calculate the power consumption by substituting the mass for the solids mass flow rate $\dot{m}_S$, which gives

$$\dot{E}_{Lr} = \frac{1}{2}\dot{m}_S\omega^2(r_o^2 - r_{dS}^2) \tag{2.14}$$

and

$$\dot{E}_{L\theta} = -\dot{m}_S\omega^2(r_o^2 - r_{dS}^2). \tag{2.15}$$

When the solids are transported up the conical beach there is a net gain of power for the centrifuge equal to

$$\Delta\dot{E}_K = -\frac{1}{2}\dot{m}_S(r_o^2 - r_{dS}^2)\omega^2 \tag{2.16}$$

The power required to lift the solids up the conical beach $\dot{E}_{Lr}$ is provided by the scroll conveyor. The power that is recovered $\dot{E}_{L\theta}$ is alleviated from the main drive motor. Note that this calculation does not include the effect of buoyancy, which would reduce the power required to lift the solids.

2.2.11 Bowl geometry

The bowl is comprised of two sections, the cylindrical and the conical sections. Settling of the solids occurs in the cylindrical section. The surface area of the cylindrical section is equal to

$$A_{Cyl} = 2\pi r_o L_{Cyl} \tag{2.17}$$

where

L_{Cyl} length of cylindrical section (m).

A number of different expressions have been proposed for the equivalent clarification area Σ, see [27-29]. For a given solids volumetric feed rate Q_f the "sigma" theory can be used to calculate the required size of the bowl. This is based on the equivalent clarification area Σ compared to that required under gravity and the Stokes' sedimentation velocity v_s under 1g.

$$Q_f = \Sigma v_s = \frac{\pi L_{cyl}\omega^2(r_o^2 - r_{dL}^2)}{g \ln r_o/r_{dL}} \frac{d_p^2(\rho_S - \rho_L)g}{18\eta_L} \tag{2.18}$$

where

g acceleration due to gravity (9.81 m/s)

d_p average particle diameter (m)

ρ_S solids density (kg/m^3)

ρ_L liquid density (kg/m^3)

η_L dynamic viscosity of the liquid (kg/m.s).

Sigma theory assumes that the liquid pool is rotating at the solid body rotational speed of the bowl. If this is not satisfied the effective settling area will be reduced, proportional to the speed squared.

The solids are lifted out of the rotating liquid pool and dewatered in the conical section. The cone angle β is the angle between the axis of rotation and the cone. The cone angle was shown to be proportional to the back-drive torque and hence power by Reif et al [29]. It was also shown that the dryness of the discharging solids is proportional to the cone angle [29]. Intuitively, giving the solids a longer residence time on the dry conical beach will result in drier solids.

2.2.12 Scroll geometry

Pitch

The scroll pitch G is the axial distance between scroll flights, this is fixed and cannot be changed without replacing the scroll. The greater the scroll pitch the higher the axial speed for a given differential speed, this is shown in Equation 2.2. A higher axial speed leads to a reduced thickness of the settled solids. Extending the pitch also has the effect of increasing the pitch angle α and therefore increasing the circumferential force applied to the solids by the scroll. The pitch angle is expressed as

$$\alpha = \tan^{-1}\left(\frac{G}{2\pi r_o}\right). \qquad 2.19$$

The pitch varies along the length of the bowl in some decanters. For example, having a longer pitch in the cylindrical section and a shorter pitch in the conical section results in increased residence time of the solids in the conical section. The scroll pitch in the GTech-Bellmor 1456 Centrifuge Decanter is constant along the length of the bowl and is either 70 or 110 mm depending on the application.

Blade angle

The scroll blade angle γ is typically perpendicular to the bowl wall along the length of the cylindrical and conical section [10, 11, 13, 25, 30]. This ensures that the scroll does not apply a normal force to the bowl wall. The effect of this would be limited as the settled solids cannot typically support shear loading. At present, the scroll blades in the GTech-Bellmor 1456 Centrifuge Decanter are perpendicular to the axis of rotation for the length of the bowl. Adjusting the blades to be perpendicular to the bowl wall in the conical section would partially alleviate the normal force on the wall.

Addition of a dip weir

A dip weir, or baffle plate, can be installed at the bottom of the beach to alleviate the additional power requirements to lift the solids up the beach. Using a baffle capitalises on the hydraulic pressure difference and aids in lifting the solids [13, 27]. The liquid level is higher on the cylindrical side, causing a pressure differential at the gap at the bottom of the baffle. An incorrectly designed dip weir will severely hinder the performance of the centrifuge. A dip weir also allows for a greater pool depth within the cylindrical section without reducing the length of the conical beach.

2.2.13 Coefficient of friction

To predict the power consumed by product transport the coefficient of friction μ between the solids and the bowl and scroll must be known. The coefficient of friction is dependent on the cake properties; these can vary significantly for each process fluid. To achieve ideal axial motion of the solids the coefficient of friction between the solids and the scroll must be small relative to the that between the solids and the bowl [24].

Reif and Stahl [9] conducted experiments to determine the coefficient of friction of glass and PVC in a test apparatus designed to recreate the conditions in a decanter. The experimental procedure and results are presented here.

2.2.13.1 **Testing**

A test apparatus was developed to replicate the conditions within the bowl of a centrifuge to determine the coefficient of friction. The device consisted of a variable number of knives/blades turning inside a rotating drum. The knives were rotated at a slightly higher speed than the drum to induce motion of the solids against the drum; causing the product to form triangular wedges in front of each knife blade. The product is only rotating circumferentially in the test rig. The layout of the rig is shown in Figure 2.4. The torque on the central shaft was measured by strain gauges. The speed of the knives was measured by inductive transducers. The knives and drum were made from stainless steel. The surface roughness was not a variable in this experiment.

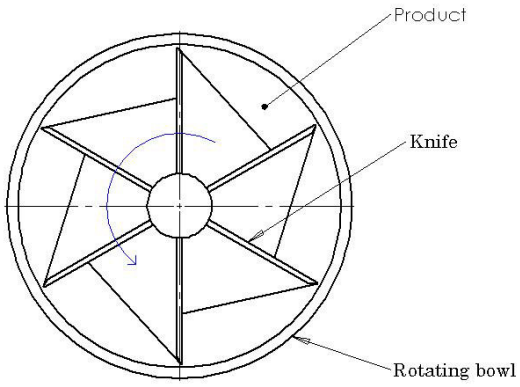

Figure 2.4 Test rig used by Reif and Stahl to determine coefficient of friction [9]

The rig was designed to allow for variation of several variables. The variables that were changed and their respective ranges are shown in Table 2.1.

Table 2.1 Experimental settings used by Reif and Stahl when measuring the coefficient of friction

Rotation speed	635-1600 rpm
Scraper velocity	0.12-0.52 m/s
Saturation	0-100%
Blade angle	78°-90°
Clearance	1-3 mm
Number of knives	1-6

PVC and glass were used as the test materials with water as the suspension medium. Both materials are commonly processed using decanting centrifuges. The two materials have significantly different properties; glass has smooth spherical particles while PVC has smaller rougher particles.

2.2.13.2 **Results**

Rotation speed - The centripetal force is proportional to the rotational speed squared. The experiment showed that the coefficient of friction decreases with increasing centripetal force. This is due to the relative size of the fluid forces decreasing compared to the centripetal force.

Scraper velocity - There was no appreciable difference in the coefficient of friction for the range of differential speeds used.

Blade angle - It was observed that the measured coefficient of friction reduced with decreasing blade angle. When this was further investigated it became apparent that the coefficient of friction is unchanged as the blades begin to support the cake, therefore reducing the normal force on the drum.

Clearance - The clearance was set to three levels: 1, 2, and 3 mm. There were subtle differences between each; the 2 mm clearance had the overall lowest coefficient of friction. There was no conclusive trend but as the intermediate value was the lowest it does elude to a potential optimal value.

Saturation - The coefficient of friction as a function of saturation S followed the same trend for both PVC and glass. The coefficient of friction initially increased with moisture content before reaching a maximum. Once this maximum is reached, the coefficient of

friction decreased steadily until the solids were fully saturated. A graphical depiction of this trend is shown in Figure 2.5; this is not to scale.

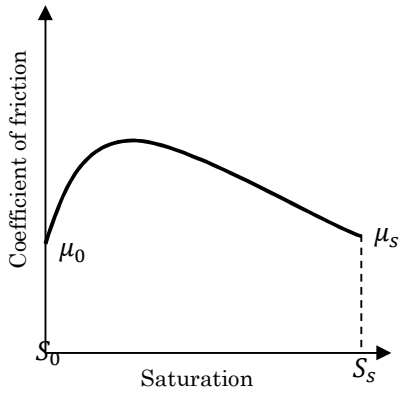

Figure 2.5 Trend of coefficient of friction as function of liquid saturation

The coefficients of friction for glass and PVC are given in Table 2.2. The coefficients of friction of glass are consistent with the values produced by Abel [31]. The results for PVC were scattered between 0.2 and 0.3, although it was stated as being 0.2.

Table 2.2 Coefficient of friction for glass and PVC

Material	μ_0	μ_s
PVC	0.2-0.3	0.2-0.3
Glass	0.2	0.2

2.3 Product Transport Model

A mathematical model of the product transport within a decanter centrifuge was developed. The model can predict the power, torque, and axial force required for product transport. This information can be used in the design of a decanter centrifuge. Indicative values were calculated for the case study given in Table 2.3. The case study is for a GTech-Bellmor 1456 Centrifuge Decanter processing a mixture of PVC and water.

Table 2.3 Case study variables for GTech-Bellmor 1456 Centrifuge Decanter separating PVC and water

Solid density (ρ_S)	1400 kg/m^3
Liquid density (ρ_L)	1000 kg/m^3
Rotation speed (ω)	3250 rpm
Solid mass flow rate ($\dot{m}_S$)	1.2 t/h
Liquid mass flow rate ($\dot{m}_L$)	10.8 t/h
Total mass flow rate ($\dot{m}_T$)	12 t/h
Bowl radius (r_o)	177.6 m
Length of conical section (L_{Con})	560 mm
Length of cylindrical section (L_{Cyl})	900 mm
Coefficient of friction (μ_1, μ_2, μ_3)	0.2
Differential speed (Δ)	23.5 rpm
Cone half angle (β)	8.5°
Liquid discharge radius (r_{dL})	136.6 mm
Solids discharge radius (r_{dS})	126 mm

2.3.1 Current models

Several models for the product transport exist. Reif and Stahl produced an analytical model, while Leung, Corner-Walker and Records, and Minaker created empirical models.

To date, the most thorough work regarding product transport was carried out by Reif and Stahl [9, 23, 29]. They developed an analytical model for the solids transport that can estimate the solids transport angle, solids forces, and of most interest to the present study, the transport torque and power. They also discussed the influence that each design parameter has on product transport torque and power. There is no known method available to apply their model to a different decanter as they did not present exact equations or provide a calculation procedure. Reif and Stahl [9] conducted experiments to determine the coefficient of friction of glass and PVC in a test apparatus designed to recreate the conditions in a decanter**.** They concluded that the coefficient of friction is a function of material, surface finish, product, and product wetness.

Leung [11] derived an empirical relationship for the transport power of a decanter operating in high solids mode – where the solids thickness can be greater than the pool depth. Leung defined an effective coefficient of friction *I,* which takes account of buoyancy, as

$$I = \frac{\rho_S - \rho_L}{\rho_S}\mu = \frac{\dot{E}_T}{\dot{m}_S r_o \omega^2 L_{eff}} \qquad 2.20$$

Where

ρ_S density of solids (kg/m^3)

ρ_L densite of liquid (kg/m^3)

L_{eff} 2/3 of the total length of the bowl (m)

$\dot{E}_T$ solids transport power (W)

$\dot{m}_S$ solids mass flow rate (kg/s)

r_o inner bowl radius (m).

Experimental results for I were presented for dewatering of sewage and industrial sludge at five different plants with the measured value of I in the range of 0.5 to 1.5. The presented results show I as a function of solids mass fraction. A large amount of scatter is seen in the experimental results. I was apparently insensitive to variation of solids mass fraction for two of the plants that were investigated. For the other three sets of results there was a critical value of the solids mass fraction, above which I increased. Leung defined the term $\dot{E}_T/\dot{m}_S$ as the specific power consumption, where $\dot{E}_T$ is the product transport power, and $\dot{m}_S$ is the mass flow rate of solids. Leung observed that this varied between 5 and 20 kW/t/h for high-solids decanters.

An empirical relationship for the scaling of the transport torque requirement between dry solids decanters was presented by Corner-Walker and Records [30]. Four components of torque are introduced: friction, lifting the solids against the centripetal force, feed acceleration, and the differential pressures present on the scroll faces that arise from product transport. They concluded that the cake dryness is proportional to the scrolling torque divided by the bowl volume. Good correlation was observed when compared to multiple data sets, but it is only useful when an existing decanter is available for comparison.

Minaker [8] discusses how the settled solid phase is handled. Options include: a friable solid, or a plastic, liquid solid. The Bingham body can be used, or, as a more generalised approach, a Newtonian fluid. Minaker presented a relationship for the scroll induced flow of the solids. There are two components, forced flow and back flow. He suggests there are only a limited number of methods for increasing the throughput of a decanter, these are: improved scroll geometry, increased rotor length to diameter ratio, and the addition of flexible bearings to enable higher speeds.

2.3.2 Description of the model and assumption

The product transport model considers friction, lifting the solids, Coriolis forces, buoyancy, and the pressure acting on the scroll. The model does not include the effects of solids back-flow, and drag induced by the liquid flow. The model is presented as a partial model, where the power and torque is calculated for a finite slice of solids in the bowl. The procedure for calculating the total torque and power is included in this section.

The system that was considered is shown in Figure 2.6. The feed enters as a mixture of solids and liquid at the intersection of cylindrical and conical sections. The mixture follows the helical path made by the scroll to the liquid discharge ports. The solids settle against the bowl wall where they are transported axially along the bowl by the scroll conveyor to the solids discharge ports.

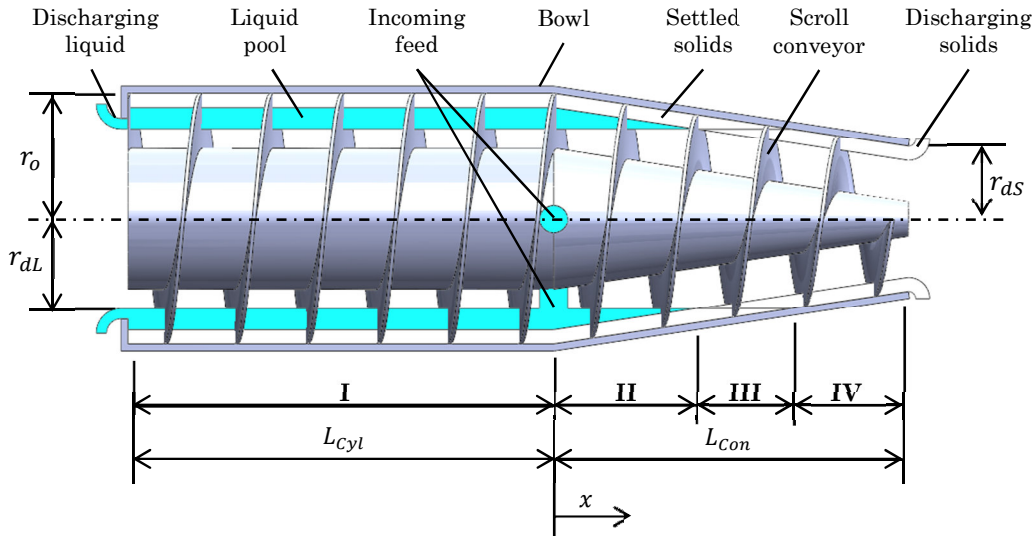

Figure 2.6 Schematic of decanter centrifuge showing the four bowl regions and key dimensions

The assumptions that were used in this model were:

1. The solids are constrained to move axially along the bowl. This is valid when the circumferential coefficient of friction is significantly larger than the coefficient of friction between the scroll faces and the solids. This can be achieved by adding an axial profile to the bowl surface, such as ribs or grooves. The solids were

considered to move in a channel to enforce the constraint of axial motion in the model.

2. A constant coefficient of friction is assumed between the solids and bowl and scroll, with no dependency on relative velocity or g-force.
3. The internal coefficient of friction of the settled solids is higher than that between the solids and bowl and scroll, therefore the solids will tend to move as a solid body.
4. The solids settle as a uniformly thick layer against the bowl wall. Therefore the inner radius and radius of the centre of force are able to be calculated as a function of mass flow rate, scroll pitch, and differential speed.
5. The solids have settled uniformly over the cylindrical section, thus all solids travel to the liquid discharge ports before settling. This is the most conservative assumption, compared to assuming the solids settle as they enter the bowl and there are no solids in the cylindrical section.
6. The liquid level remains constant and the solids are instantly dried when they leave the liquid pool.
7. The force applied to solids by the scroll is parallel to the axis of rotation, regardless of the scroll blade angle. Decreasing this angle means the scroll alleviates the normal force on the bowl wall; this assumption is only true if the settled solids can support a shear load, which is not the case for most solids.

2.3.3 Derivation of the product transport model

A diagram of the solids being transported along the conical section is shown in Figure 2.7. Two-dimensional free-body diagrams for the $x-\theta$ and $x-r$ planes are presented. The model considers steady state motion of an axial slice of settled solids, having axial thickness δx, rotating at an angular velocity ω, being transported by a scroll conveyor rotating at $\omega + \Delta$ with pitch G. The highlighted element in Figure 2.7 is being transported to the right. Cylindrical coordinates are used with the x direction along the axis of rotation, θ in the circumferential direction, positive in the same direction as the scroll, and r radially from the axis of rotation. Three coefficients of friction are used in the free body diagrams, μ_1, μ_2, and μ_3, which correspond to the coefficient of friction between the settled solids and the scroll face, bowl wall, and guide vanes, respectively.

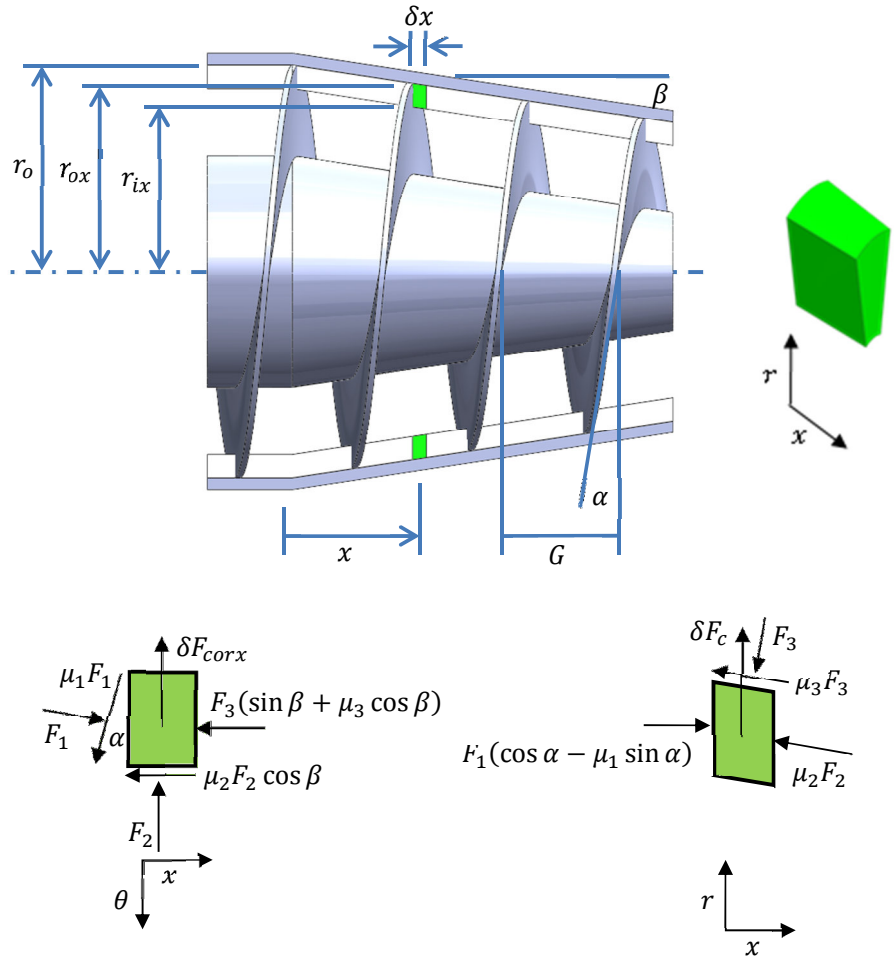

Figure 2.7 Free body diagrams of an axial element of solids that has settled against the bowl wall that is being transported to the right by the scroll conveyor

The expressions for the outer radius r_{ox}, inner radius r_{ix}, and radius of the centre of force r_{avx} of the element at a distance x from the start of the conical section are

$$r_{ox} = r_o - x\tan\beta, \tag{2.21}$$

$$r_{ix} = \sqrt{(r_o - x\tan\beta)^2 - \frac{2\dot{m}_S}{(1-\eta)\rho_S \mathrm{G}\Delta'}}, \tag{2.22}$$

and

$$r_{avx} = \frac{2}{3}r_{ox} + \frac{1}{3}r_{ix} \tag{2.23}$$

respectively, where

η void fraction of settled solids.

The inner radius is calculated by conservation of mass of the solids as they are transported along the bowl. The centre of force is at two-thirds of the depth of the solids.

The effective density ρ_E is used to account for buoyancy forces within regions I and II. If the solids phase is partially or fully submerged the effective density should be used for that component. If the solid phase is not submerged the effective density is equal to the solids density. The effective density is

$$\rho_E = \rho_S - S\rho_L \tag{2.24}$$

where S is the portion of the submerged solids, or saturation. When the solids are completely submerged $S = 1$ and when the solids are lifted completely out of the pool $S = 0$. When the solids are being lifted out of the pool the saturation is

$$S = \frac{r_{ox}^2 - r_{dL}^2}{r_{ox}^2 - r_{ix}^2} \tag{2.25}$$

The mass of a slice δm_x of the solids at a given axial position can be expressed as

$$\delta m_x = \frac{2\pi\dot{m}_S}{\mathrm{G}\Delta}\delta x. \tag{2.26}$$

The radial velocity of the solids moving up the conical section is

$$\frac{\delta r}{\delta t} = -\frac{G\Delta}{2\pi}\tan\beta. \tag{2.27}$$

The centripetal body force of an element of the solids is

$$\delta F_{cx} = \frac{\rho_E}{\rho_S}\omega^2 r_{avx}\frac{2\pi\dot{m}_S}{\mathrm{G}\Delta}\delta x. \tag{2.28}$$

The Coriolis body force of an element of solids moving along the conical section is

$$\delta F_{corx} = 2m_x\omega\frac{\delta r}{\delta t} = 2\dot{m}_S\omega\tan\beta\,\delta x. \tag{2.29}$$

The equilibrium equations for the two free body diagrams in Figure 2.7 are

$$F_1(\cos\alpha - \mu_1\sin\alpha) = F_2\mu_2\cos\beta + F_3(\sin\beta + \mu_3\cos\beta) \tag{2.30}$$

$$F_1(\sin\alpha + \mu_1\cos\alpha) = F_2 + \delta F_{corx} \tag{2.31}$$

$$F_3 = \delta F_{cx}\cos\beta + F_1\sin\beta\,(\cos\alpha - \mu_1\sin\alpha) \tag{2.32}$$

The power required to overcome friction and lift the solids for the partial section of thickness δx is

$$\delta\dot{E}_P = F_1(\sin\alpha + \mu_1\cos\alpha)\Delta r_{avx} \tag{2.33}$$

Solving Equations 2.30, 2.31, and 2.32 for F_1 gives

$$F_1 = \frac{(\sin\beta + \mu_3\cos\beta)\delta F_{cx} - \mu_2\delta F_{corx}}{C} \tag{2.34}$$

where

$$C = \begin{pmatrix} \sec\beta\,(\cos\alpha - \mu_1\sin\alpha) \\ -(\sin\beta + \mu_3\cos\beta)(\cos\alpha - \mu_1\sin\alpha)\tan\beta \\ -\mu_2(\sin\alpha + \mu_1\cos\alpha) \end{pmatrix}. \tag{2.35}$$

Substituting Equation 2.34 into Equation 2.33 for the power consumption gives

$$\delta\dot{E}_P = \frac{\Delta r_{avx}(\sin\alpha + \mu_1\cos\alpha)\big((\sin\beta + \mu_3\cos\beta)\delta F_{cx} - \mu_2\delta F_{corx}\big)}{C}. \tag{2.36}$$

The drive torque required for partial product transport is

$$\delta T_P = \frac{\delta\dot{E}_P}{\Delta}. \tag{2.37}$$

The axial force required to overcome the partial product transport is

$$\delta F_{Ax} = \frac{(\cos\alpha - \mu_1\sin\alpha)\big((\sin\beta + \mu_3\cos\beta)\delta F_{cx} - \mu_2\delta F_{corx}\big)}{C}. \tag{2.38}$$

2.3.4 Bowl regions

The bowl can be considered as having four distinct regions; shown in Figure 2.6. A description of each region is given below.

The solids in region I are fully submerged. The two bounding cases for the mass flow in region I are constant mass flow and no mass flow. Constant mass flow means that the solids travel in the suspension along the full length of the cylindrical section and settle

at $x = -L_{Cyl}$, this is the worst-case assumption. No mass flow means the solids settle at the intersection of the conical and cylindrical sections as they enter the bowl. Regions II, III, and IV are all within the conical section of the bowl. In region II the solids are being transported up the conical sections but are fully submerged in the liquid pool. In region III the solids are partially submerged in the liquid pool and therefore buoyancy forces are only acting on part of the solids. In region IV the solids are completely out of the liquid pool. The values for x, β, and ρ_E for each region are given in Table 2.4.

Table 2.4 Variables in each region of the bowl

I - Cylindrical	$-L_{Cyl} < x < 0$ $\beta = 0°$ $\rho_E = \rho_S - \rho_L$
II - Fully submerged conical	$0 < x < \frac{1}{\tan\beta}\left(r_o - \sqrt{\left(r_o - h_p\right)^2 + \frac{2\dot{m}_S}{\eta\rho_S \mathrm{G}\Delta}}\right)$ β = Cone angle $\rho_E = \rho_S - \rho_L$
III - Partially submerged conical	$\frac{1}{\tan\beta}\left(r_o - \sqrt{\left(r_o - h_p\right)^2 + \frac{2\dot{m}_S}{\eta\rho_S \mathrm{G}\Delta}}\right) < x < \frac{h_p}{\tan\beta}$ β = Cone angle $\rho_E = \rho_S - \left(\frac{r_{ox}^2 - r_{dL}^2}{r_{ox}^2 - r_{ix}^2}\right)\rho_L$
IV - Dry conical	$\frac{h_p}{\tan\beta} < x < L_{Con}$ β = Cone angle $\rho_E = \rho_S$

2.3.5 Implementing the model

The procedure for calculating the product transport power and torque is:

1. Break the bowl down into the four distinct regions shown in Figure 2.6.
2. Divide each region into discrete slices that will be solved for individually, it is sufficiently accurate to use one slice per region. Calculate the values of x, β, and ρ_E using the equations in Table 2.4. Use the average value of x in each region.
3. Solve Equations 2.36, 2.37, and 2.38 for each region for the partial power, torque, and axial force, respectively
4. Sum all of the partial power, torque, and axial force for all four regions to give the total power, torque, and axial force.

2.3.6 Validation

The results were compared to data published by Reif and Stahl [23] to validate the proposed model. The torque measured by Reif and Stahl included the torque required to accelerate the incoming feed, although acceleration torque is small relative to the transport torque. The design parameters and operating variables are given in Table 2.5. Constant mass flow was assumed in region I. There is a reasonable correlation between the predicted and measured specific torque versus solids mass flow, as shown in Figure 2.8. The specific torque is the total torque divided by the mass flow rate of solids.

Table 2.5 Parameters used by Reif and Stahl [23] for a decanter centrifuge separating PVC and water

Solid density (ρ_S)	1400 kg/m^3
Liquid density (ρ_L)	1000 kg/m^3
Solids void fraction (η)	0.38
Rotation speed (ω)	2000 rpm
Solid mass flow rate ($\dot{m}_S$)	1 – 5 t/h
Solids weight percentage	20%
Pool depth (h_p)	90 mm
Bowl radius (r_o)	375 mm
Liquid discharge radius ((r_{dL}))	285 mm
Solids discharge radius ((r_{ds})	209 mm
Scroll pitch (G)	110 mm
Length of conical section (L_{Con})	550 mm
Length of cylindrical section (L_{Cyl})	650 mm
Coefficient of friction (μ_1, μ_2, μ_3)	0.2 – 0.3
Differential speed (Δ)	57.1 rpm
Cone half angle (β)	16.7°

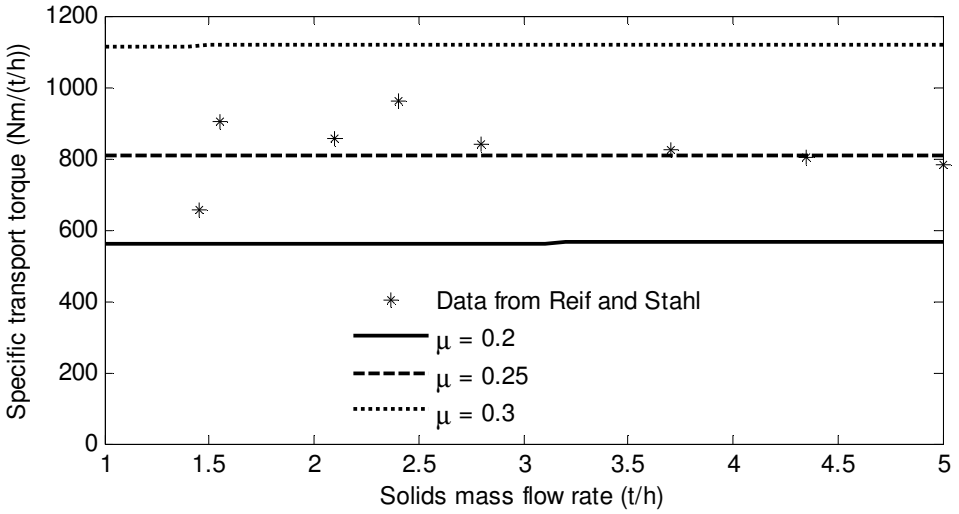

Figure 2.8 Measured and predicted specific torque for varying coefficients of friction

2.3.7 Results for GTech-Bellmor 1456 Centrifuge Decanter

The total power required to transport 1.2 t/h of PVC suspended in water using a GTech-Bellmor 1456 Centrifuge Decanter was predicted to be 3.56 kW. The required back-drive torque is 1.44 kNm at 23.5 rpm. The axial force is 37.0 kN. For regions I, II, III, and IV the power consumption contributions are 41.7%, 11.8%, 12.5%, and 33.9%, respectively. The power consumed by lifting the solids is 0.19 kW. This is aided by buoyancy, if there were no liquid in the bowl this would increase to 0.30 kW. The power consumption due to product transport along the bowl is shown in Figure 2.9, the units on the vertical axis are in kilowatts per metre. Each region was broken down into 1,000 slices for this plot.

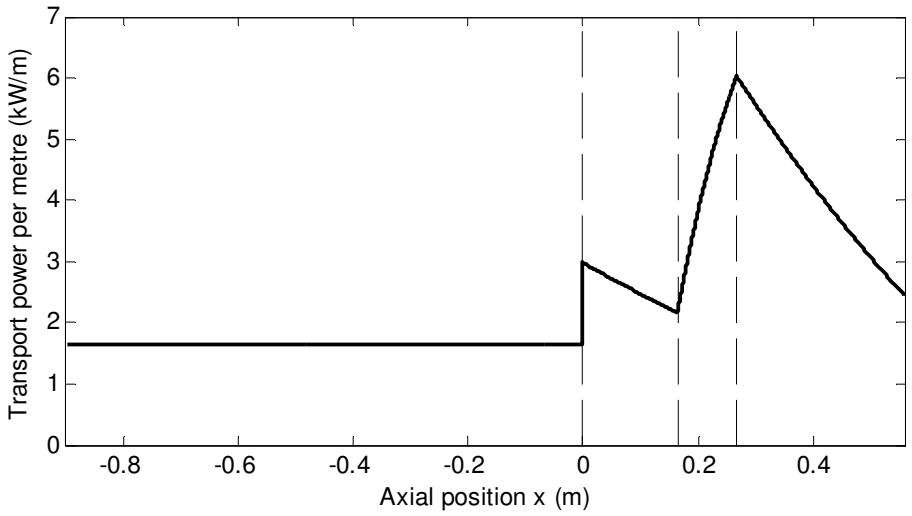

Figure 2.9 Specific power consumption due to product transport throughout the bowl for a GTech-Bellmor 1456 Centrifuge Decanter

Figure 2.10 shows the total power consumption as a function of the number of slices in each region. The figure reveals that convergence is achieved with approximately 10 slices. It is satisfactory to only use one slice per region as there is negligible difference between using one slice and the converged solution. It can also be seen from the linearity of the power distribution in Figure 2.9 that it is appropriate to use the average value in each region to calculate the power, torque, and axial force.

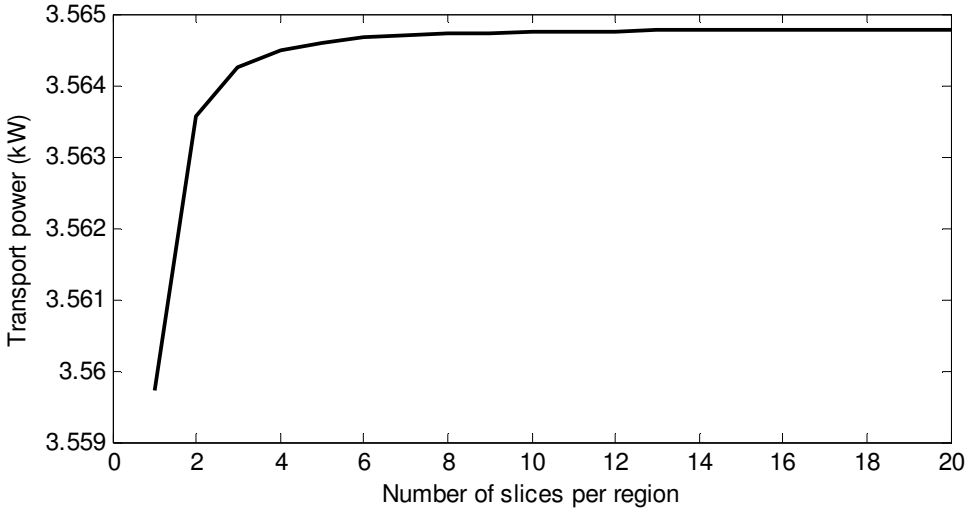

Figure 2.10 Power consumption as a function of the number of slices taken in each of the four regions

The following plots show the specific power consumption as a function of selected parameters. The plots were created by varying one or two parameters and holding the others constant at the values given in Table 2.3. Figure 2.11 shows the specific power consumption as a function of scroll pitch angle for various coefficients of friction. Figure 2.12 shows the specific power consumption as a function of differential speed for various scroll pitch angles. Figure 2.13 shows the specific power consumption as a function of the solids and liquid discharge radii ratio for different density ratios. The radius ratio was varied by holding the solids discharge radius constant and changing the pool depth. Figure 2.14 shows specific transport power as a function of differential speed and for a reduced pool depth. Overfilling occurs when the solids thickness becomes greater than the pool depth and is occurring below the discontinuity in the specific transport power.

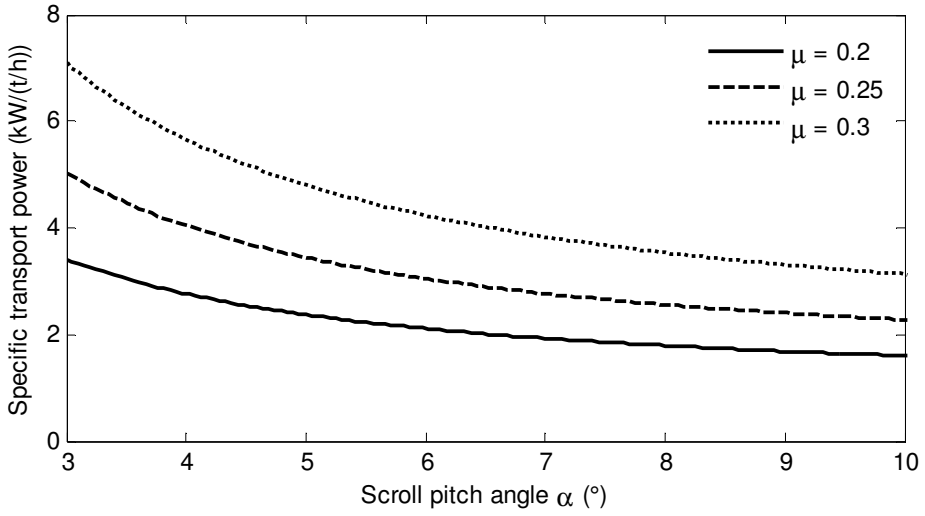

Figure 2.11 Specific power consumption as a function of scroll pitch angle for various coefficients of friction

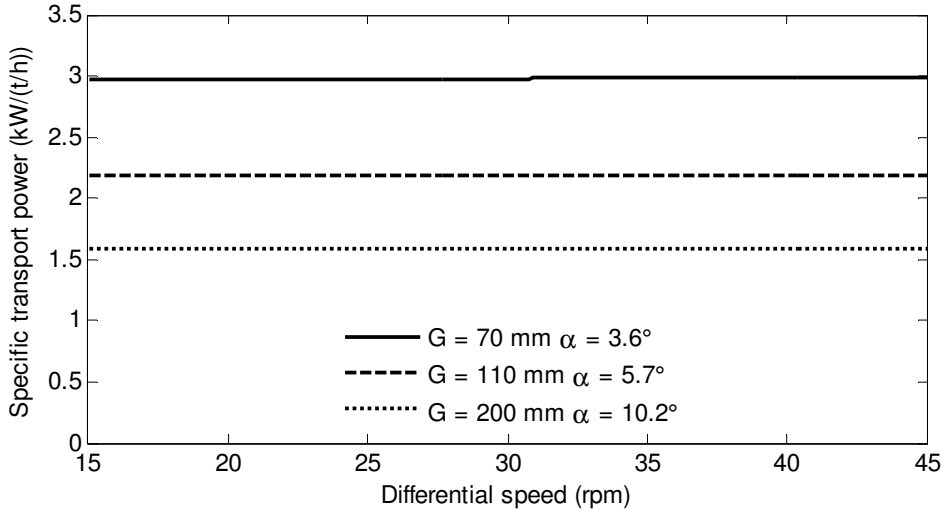

Figure 2.12 Specific power consumption as a function of differential speed for various scroll pitch lengths

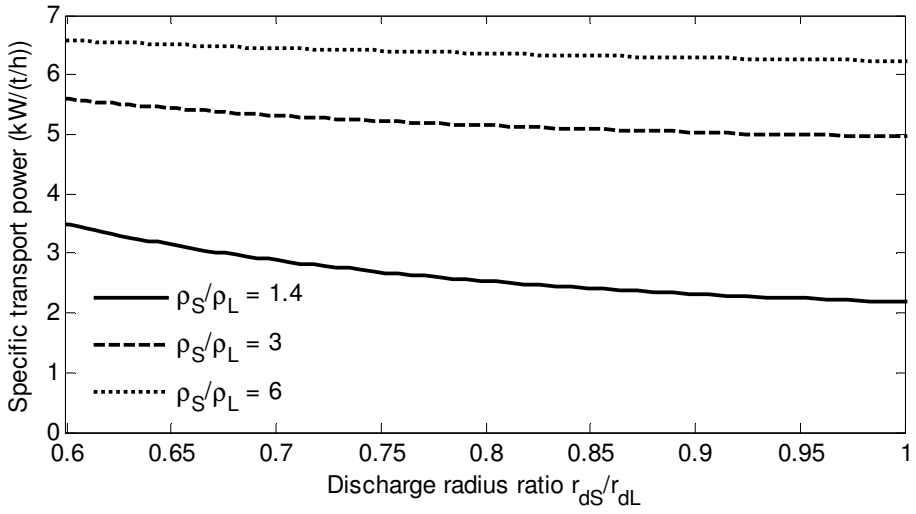

Figure 2.13 Specific power consumption as a function of the ratio of solids and liquid discharge radii for various solids and liquid density ratios (fixed bowl length)

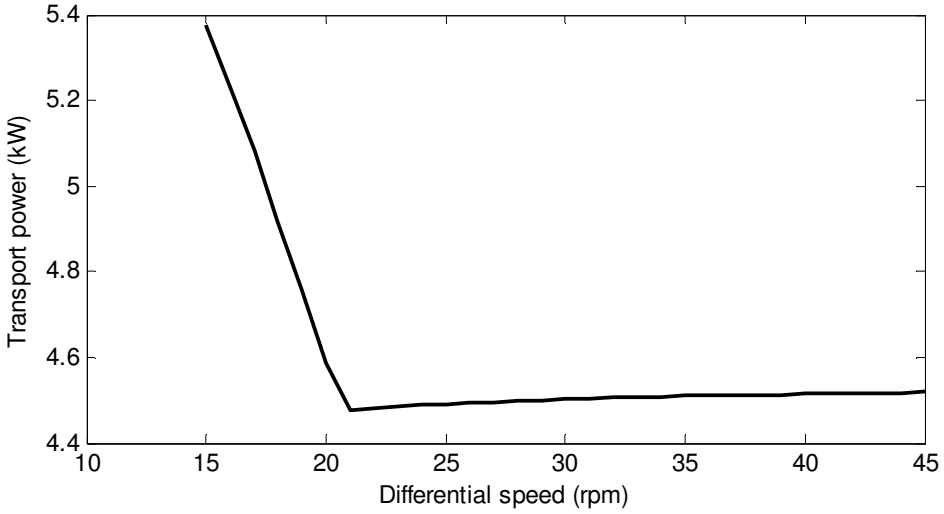

Figure 2.14 Transport power as a function of the differential speed with the pool depth reduced to 15 mm to show the effect of the solids thickness being greater than the pool depth

2.4 Discussion

There is reasonable correlation between the predicted and measured transport power shown in Figure 2.8. Reif and Stahl did not include a description of the experimental procedure; it is unclear whether their data includes other forms of power consumption such as power transmission losses and windage. If the power transmission and windage were not included this could explain the slight under-prediction of the power for a coefficient of friction of 0.2. The result shows the sensitivity to the coefficient of friction. The power consumption and torque are linearly related to the coefficient of friction. Reducing the coefficient of friction on the scroll faces and along the axial direction on the bowl wall would reduce the power consumption. The power consumed per unit mass of solids is insensitive to the mass flow rate of solids, except when the solids thickness is greater than the pool depth.

In region I the friction is relatively low due to buoyancy. In region II the solids must be lifted up the conical section, and therefore there is an increase in the partial power consumption at the intersection of the cylindrical and conical sections. The specific power begins to decrease with decreasing radius until region III is reached and the solids begin to leave the liquid pool, reducing the buoyancy effects and therefore increasing the centripetal force. The largest specific power consumption occurs in region IV, the dry conical beach, due to there being no buoyancy to alleviate the normal force on the bowl wall.

Figure 2.11 and Figure 2.12 show the effect of varying the scroll pitch for a fixed differential speed and varying the coefficient of friction. When there is no friction, the transport power reduces to the level required to lift the solids up the conical beach against the centripetal force. Transport power decreases with increasing scroll pitch. When the pitch is increased the scrolling velocity increases, resulting in a lower cake height and hence normal force. The scroll pitch angle also increases with increasing pitch, this results in a greater circumferential force, raising the potential for the solids to rotate with the scroll. The differential speed has almost no effect on the power consumed by product transport.

Figure 2.13 shows the decreasing effect of buoyancy as the ratio of the solids and liquid density increases. The effect of decreasing the liquid discharge radius for a fixed bowl radius and solids discharge radius is also shown. For less dense solids the power consumption decreases with increasing pool depth as the length of regions II and III are increased. Buoyancy alleviates the friction force in region I, II, and III. Increasing the pool depth also has the effect of decreasing the length of region IV. This should be carried out tentatively, as the shortened beach would potentially lead to wetter solids.

Figure 2.14 shows the differential speed versus the transport power for a reduced pool depth. This shows the effect of overfilling the machine, where the thickness of the solids is greater than the pool depth and therefore buoyancy effects are less. There is a clear discontinuity where the solids layer becomes thicker than the liquid pool and an increase in predicted power consumption was observed.

The Coriolis force can either reduce or increase the force required depending on whether the scroll is rotating co- or counter-currently. However, the Coriolis term is small relative to the centripetal force.

2.5 Conclusions

Frictional losses and lifting of the solids during product transport consumes one of the largest portions of power in a decanter centrifuge, along with acceleration power (discussed in the following chapter). Small reductions in the frictional losses translate to a large savings in operating costs. Friction in the conical section dominates the frictional losses. The mathematical model derived in this chapter allows for the calculation of the power, torque, and axial force required by product transport. This model will be of use in the design of decanter centrifuges.

The power consumed by product transport can be reduced by minimising the coefficient of friction between the solids and scroll faces, and the solids and the bowl wall along the axial direction. The geometry of the decanter and the operating variables can also be optimised to reduce power consumption. Given fixed bowl dimensions, the bowl speed, differential speed, and pool depth can be controlled to ensure that each centrifuge is operating optimally for different products and output requirements. Optimisation cannot be conducted without considering the particular product and the required output specifications.

Chapter 3

Feed Acceleration Power

3.1 Introduction

Accelerating the feed to the high rotational speeds required for separation consumes the largest portion of the total power consumed by a decanter centrifuge. The feed enters the centrifuge through an axial feed tube, where it has no rotation; it must then be accelerated to the angular velocity of the bowl. If the feed is not fully accelerated when it enters the liquid pool it is detrimental to the operation of the centrifuge; detrimental effects include re-suspension of settled solids, disturbance to the surface of the pool, poor product output quality, and high wear on the bowl and scroll adjacent to the accelerator.

The feed is either gravity fed or pumped into the centrifuge. The feed enters as a mixture through the feed tube and travels to the accelerator. The accelerator is located over the intersection of the cylindrical and conical sections. The feed is partially accelerated by the accelerator before entering the bowl, if the feed has not reached the solid body rotation speed it is further accelerated within the liquid pool. The power required to accelerate the feed is predominantly supplied by the main drive motor. The acceleration occurs for both the solid and liquid phases. The power consumption consists of two components, loss of rotational kinetic energy of the solids and liquids as they leave their respective discharge ports, and viscous losses during acceleration. The accelerator efficiency ε_a was defined by Leung [13] as

$$\varepsilon_a = \frac{u}{\omega r_h} \qquad 3.1$$

where

u tangential velocity of the feed stream as it leaves the accelerator (m/s)

ω angular velocity of the bowl (rad/s)

r_h discharge radius of the accelerator (m).

This chapter contains a description of the accelerator design that is currently being used in the GTech-Bellmor 1456 Centrifuge Decanter and an alternative design that has shown improvements over the standard accelerator. The chapter concludes with the derivation of the power consumed during feed acceleration.

3.2 Feed Accelerator Design

The ideal feed accelerator would pre-accelerate the feed to the tangential speed of the rotating pool while minimising the radial velocity. If the feed is not accelerated to the same tangential speed as the bowl shearing forces are created with the liquid pool. These shearing forces can result in the re-suspension of solids, excessive vibrations, and reduced product quality. A high radial velocity component would result in the feed plunging into the rotating pool, disturbing settled solids and reducing the clarity of the centrate.

The feed leaving the accelerator must be evenly distributed both circumferentially and axially. If there is uneven distribution or localised jets, excessive wear can occur on both the scroll and bowl adjacent to the accelerator. The majority of the feed acceleration power is consumed by viscous losses. Viscous forces and diffusion of momentum are poor methods of inducing rotation.

3.2.1 Current feed accelerator

The current feed accelerator is shown in Figure 3.1 and Figure 3.2. This accelerator is slightly different from conventional accelerators as it does not have localised ports; rather it has two relatively long axial vents with curved paths leading to the bowl. This design is commonly referred to as the Esbjerg accelerator.

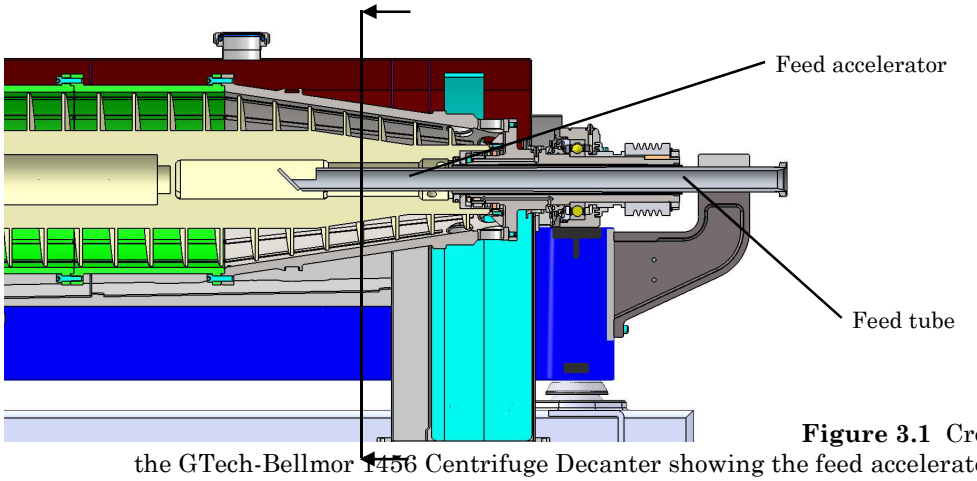

Figure 3.1 Cross-section of the GTech-Bellmor 1456 Centrifuge Decanter showing the feed accelerator

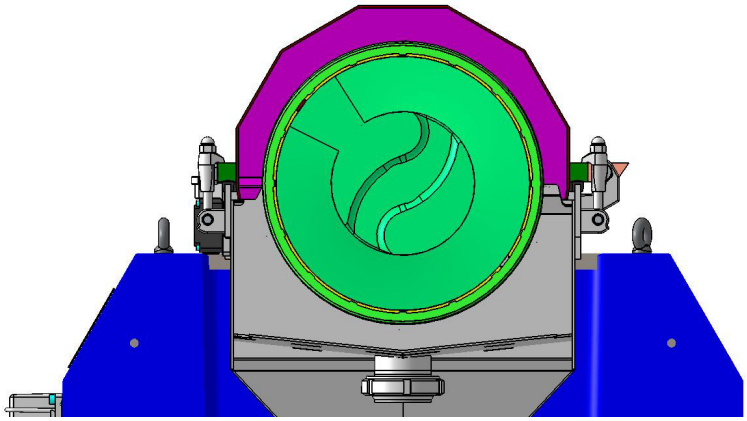

Figure 3.2 Cross-section of the Esbjerg feed accelerator rotating clockwise

The faces of the accelerator provide an impulse force to the feed as it passes through the accelerator. The long vents increase the axial distribution of the feed into the bowl. The current design still allows the feed to plunge into the rotating pool as there is a radial jump between the exit of the accelerator and the pool. As the exit area of the accelerator is relatively large the mass flow induced velocity would be low. This implies a low acceleration efficiency resulting in the feed requiring acceleration within the pool.

3.2.2 Alternative accelerator design

Leung and Shapiro produced a concept for an alternative accelerator design [5, 16, 17]. They realised that viscosity was a poor method of accelerating the incoming feed and added vanes to a standard cone accelerator to assist with acceleration. The concept they developed is shown in Figure 3.3.

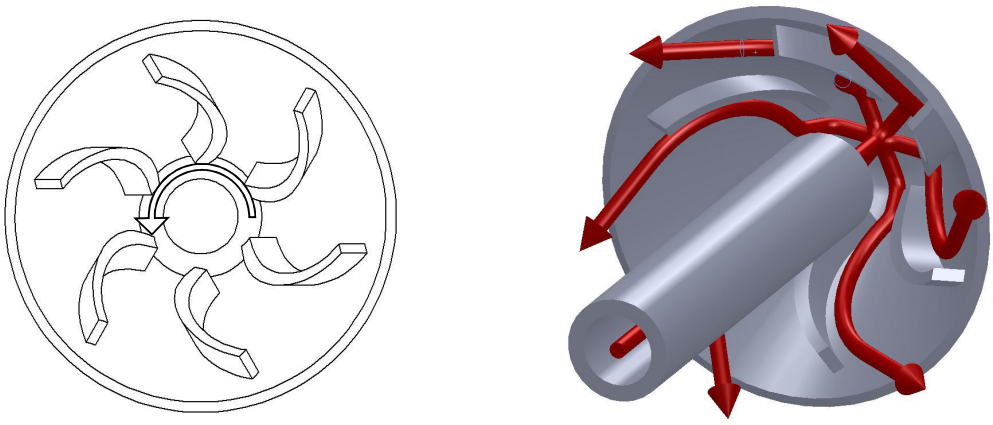

(a) (b)

Figure 3.3 Conical accelerator concept (a) view along axis (b) flow paths

Using forward curving vanes significantly aids in the acceleration of the feed. Curving the vanes can have an over-speeding effect due to the mass flow induced velocity; this is beneficial as the tangential speed of the feed is increased. The vanes are withdrawn from the outer radius of the cone to stop each of the vanes producing a concentrated jet, allowing for the flow to smooth out before entering the pool. It is important that the feed stream first contacts the cone approximately at its centre when using a cone accelerator. This ensures even distribution and reduces splashing, which can reduce acceleration and increase wear. The droop of the feed between the pipe exit and contacting the cone should be less than 3 mm [13]. Leung gave several examples of installations of the XL●PLUS® conical accelerator [13]. The improvements identified were: increased throughput, reduced polymer consumption for flocculation, higher solids recovery, and increased centrate clarity. The use of an accelerator fitted with forward curving guide vanes is investigated further in Part III.

3.3 Power Consumed by Feed Acceleration

This analysis only covers steady state feed acceleration; which assumes that the bowl is full and there is a constant mass flow rate. The dynamic period during start up lasts a very short time and has no effect on the continuous operation of the centrifuge.

An analysis of the feed acceleration was completed by Fainerman and Paramonov [12] based on the work of Gosele [32]. Both demonstrated from first principles that the viscous losses during acceleration are equal to the gain in kinetic energy. Fainerman and Paramonov likened feed acceleration in a centrifuge to dropping a mass onto a flat conveyor traveling at constant speed; slip will occur between the mass and conveyor until the mass has reached the same speed as the conveyor. There is no dependence on the coefficient of friction as the lower the coefficient of friction the further the block slides with less force as opposed to sliding less with a higher force. The analysis method presented by Fainerman and Paramonov is repeated below. The power required to accelerate a block of mass m that has been dropped onto a belt conveyor moving at constant speed v is calculated. Once accelerated the block has kinetic energy $E_k = 0.5mv^2$. Like the feed in the centrifuge, the block does not instantly reach the speed v, it must be accelerated to this speed by a friction force F_{fr}. The friction force is equal to

$$F_{fr} = ma \qquad 3.2$$

where

a constant acceleration (m/s²).

Assuming that the acceleration occurred over the time Δt, the distance travelled by the block is

$$s_b = 0.5v\Delta t \tag{3.3}$$

where the velocity is

$$v = a\Delta t. \tag{3.4}$$

The distance travelled by the block can be expressed as

$$s_b = 0.5a\Delta t^2. \tag{3.5}$$

Substituting Δt into Equation 3.2 gives

$$F_{fr} = \frac{mv}{\Delta t} = \frac{mv^2}{2s_b}. \tag{3.6}$$

While the block was being accelerated the conveyor travelled s_c, which is equal to $v\Delta t$. The energy provided by the conveyor E_C is equal to the friction force F_{fr} multiplied by the distance travelled by the conveyor s_c. The total energy input by the conveyor is equal to

$$E_C = F_{fr}s_c = \frac{mv}{\Delta t}v\Delta t = mv^2. \tag{3.7}$$

Equation 3.7 shows that the energy required to accelerate the block is twice the gain in kinetic energy. Half the energy required to accelerate the block is converted to heat by friction between the block and conveyor.

When considering the initial problem of accelerating the feed in a decanter centrifuge, two areas were considered: 1) initial acceleration of the feed and 2) ejection of the different phases from the bowl. If viscous losses had been ignored the energy consumed would be equal to the kinetic energy of the feed as it left the bowl. It is known from the above analysis that the viscous losses are irreversible and equal to the gain in kinetic energy.

3.3.1 Viscous losses

The feed, comprised of two or three phases, enters the bowl with zero rotational energy and is accelerated to have rotational energy

$$E_{RK} = \frac{1}{2} I\omega^2 \tag{3.8}$$

where

I rotational moment of inertia (kg.m^2).

Assuming that the viscous losses are equal to the kinetic energy gain, the viscous losses are

$$E_V = E_{RK} = \frac{1}{2} I\omega^2. \tag{3.9}$$

The rotational moment of inertia of the body is

$$I = \frac{1}{2} m(r_o^2 + r_{dL}^2) \tag{3.10}$$

where

m mass of element (kg)

r_o outer radius of the body/inner radius of the bowl (m)

r_{dL} inner radius of rotating pool, which is equal to the liquid discharge radius (m).

Substituting Equation 3.10 into Equation 3.9 gives

$$E_V = \frac{1}{4} m(r_o^2 + r_{dL}^2)\omega^2 \tag{3.11}$$

The total mass flow rate into the centrifuge is $\dot{m}_T$. This is made up from the following

$$\dot{m}_T = \dot{m}_S + \dot{m}_L + \dot{m}_{L2} \tag{3.12}$$

where

$\dot{m}_s$ mass flow rate of solids (kg/s)

$\dot{m}_L$ mass flow rate of primary liquid phase (kg/s)

$\dot{m}_{L2}$ mass flow rate of secondary liquid phase (third phase) (kg/s).

The power consumed by viscous losses while accelerating the incoming feed is

$$\dot{E}_V = \frac{1}{4}\dot{m}_T(r_o^2 + r_{dL}^2)\omega^2. \quad 3.13$$

From Equation 3.13 it can be deduced that the power consumed by viscous losses is linearly related to the total mass flow rate and the square of the angular velocity. Decreasing the liquid discharge radius decreases the power consumed by viscous losses. It was assumed that once the feed is accelerated there is no slip between the inner and outer radii. If there was slip, the rotational kinetic energy of the rotating fluid pool would be less than predicted and hence the viscous losses would be overestimated.

3.3.2 Kinetic energy losses

Each of the phases discharges at a different radius and mass flow rate. The analysis for each is the same. The rate of loss of kinetic energy of the discharging flow is

$$\dot{E}_D = \frac{1}{2}\dot{m}u^2 \quad 3.14$$

where

u tangential velocity of phase as it leaves the bowl at discharge radius r (m/s)

$\dot{m}$ mass flow rate of discharging phase (kg/s).

Substituting the expression for the tangential velocity gives

$$\dot{E}_D = \frac{1}{2}\dot{m}r^2\omega^2 \quad 3.15$$

where

r discharge radius (m).

Solid phase losses

The solid phase discharges at the conical end of the bowl and is forced out of ports with an average discharge radius of 126 mm. The power consumed accelerating the solids is equal to the rotational kinetic energy the solids have when they leave the bowl. An example of the solids discharge ports is shown in Figure 3.4.

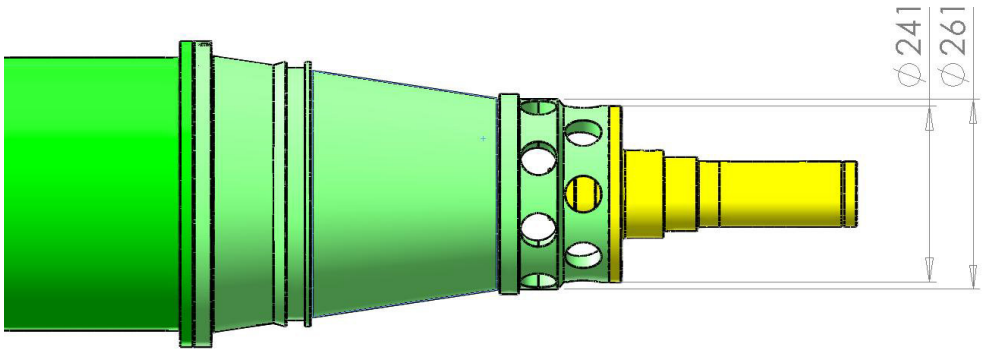

Figure 3.4 Dimensions of the solids discharge ports (mm)

The power lost by the discharging solids is

$$\dot{E}_{DS} = \frac{1}{2}\dot{m}_s r_{ds}^2 \omega^2 \qquad 3.16$$

where

r_{dS} average solids discharge radius (m).

From Equation 3.16 it can be seen that the power consumption is linearly related to the solids mass flow rate and to the square of the rotational speed and solids discharge radius.

Liquid phase losses

The liquid ports control the pool depth by rotating eccentric weir plates. The pool depth is varied to set the cake dryness; in general a shallower pool results in a drier cake due to an increase in the length of the dry conical beach. The geometry of one of the liquid discharge ports is shown in Figure 3.5. The discharge radius range is 131.9 to 155.3 mm, these correspond to pool depths of 44.7 to 21.3 mm. A pool depth of 40 mm was used for this analysis, which is equal to a liquid discharge radius of 136.6 mm. The thickness of the liquid discharging over the weirs was assumed to be negligible.

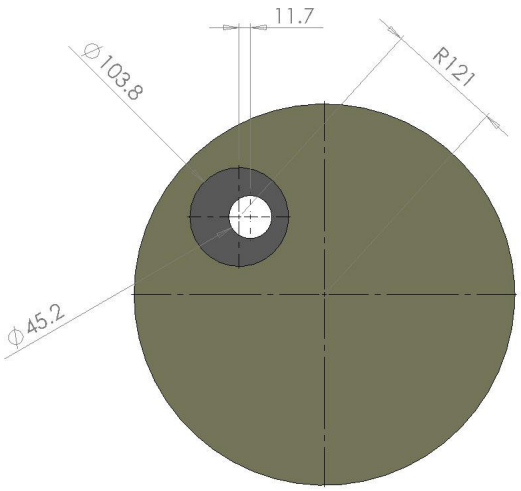

Figure 3.5 Liquid discharge port geometry (mm)

The power lost by the discharging liquid is

$$\dot{E}_{DL} = \frac{1}{2}\dot{m}_L r_{dL}^2 \omega^2 \qquad 3.17$$

where

r_{dL} liquid discharge radius (m).

The kinetic energy lost by the discharging liquid is linearly related to the liquid mass flow rate and to the square of the angular velocity and liquid discharge radius.

Secondary liquid phase losses

The second liquid phase, also known as the third phase, is discharged from ports on the exterior of the bowl. The radius of discharge is 212.5 mm. The third phase ports are not used in all applications. The rate of kinetic energy lost by the secondary liquid phase is

$$\dot{E}_{DL2} = \frac{1}{2}\dot{m}_{L2} r_{dL2}^2 \omega^2 \qquad 3.18$$

where

r_{dL2} discharge radius of third phase (m).

3.3.3 Combined feed acceleration power consumption

The total power required to accelerate the feed is made up of four components: $\dot{E}_V$. $\dot{E}_{DS}$, $\dot{E}_{DL}$, and $\dot{E}_{DL2}$. The total power consumed by accelerating the feed is the sum of these four components

$$\dot{E}_A = \dot{E}_V + \dot{E}_{DS} + \dot{E}_{DL} + \dot{E}_{DL2} \tag{3.19}$$

$$\dot{E}_A = \frac{1}{2}\omega^2\left(\frac{1}{2}\dot{m}_T(r_o^2 + r_{dL}^2) + \dot{m}_S r_{dS}^2 + \dot{m}_L r_{dL}^2 + \dot{m}_{L2} r_{dL2}^2\right). \tag{3.20}$$

A summary of each component for the case study presented in Table 2.3 is given in Table 3.1. Note that only two phases are being processed in this example.

Table 3.1 Components of power consumed by feed acceleration

	Power consumption (kW)	Equation
Viscous losses $\dot{E}_V$	4.81	3.13
Solids discharge $\dot{E}_{DS}$	0.30	3.16
Liquid discharge $\dot{E}_{DL}$	3.24	3.17
Total $\dot{E}_A$	8.35	3.20

The power consumed by accelerating the feed decreases with increasing solid content as solids are discharged at a smaller radius with less rotational kinetic energy. The power consumption is higher for lower pool depths. While a high pool depth reduces the power consumption it is normally constrained by other factors, such as required product dryness. There are no methods available for reducing this power required to accelerate the feed as it is fundamental to the operation of a centrifuge.

3.4 Conclusions

Feed acceleration is important to the operation of any decanter centrifuge. Poor acceleration can have a variety of detrimental effects on the operation of a decanter centrifuge. The power consumed during feed acceleration consists of two components: irreversible viscous losses as the feed is accelerated to the bowl speed, and the loss of kinetic energy as the solids and liquid leave their respective discharge ports. There are many different feed accelerator designs that are used in industrial decanter centrifuges and there is presently an absence of literature that quantifies the difference between them. Further analysis of the feed accelerator is presented in Part III.

Chapter 4

Estimation of the Power Transmission Losses

4.1 Introduction

All power transmission inevitably results in a loss of power across the transmitting system. These systems commonly consist of motors, belts, gearboxes, and bearings. In most cases the power that is absorbed is a fixed percentage of the power being transmitted. The losses are relatively insignificant when the amount of power transmitted is small, but can accumulate to several kilowatts in applications requiring a significant amount of power.

The GTech-Bellmor 1456 Centrifuge Decanter has several components that transmit power. There are two electric motors, two belt drives, a high reduction epicyclic gearbox, and a selection of bearings and seals. A schematic of the GTech-Bellmor 1456 Centrifuge Decanter is shown in Figure 4.1 with the corresponding symbols and notations in Table 4.1. The 30 kW motor drives the bowl and the 15 kW motor drives the scroll via the gearbox. The system for driving the scroll is commonly referred to as the back-drive.

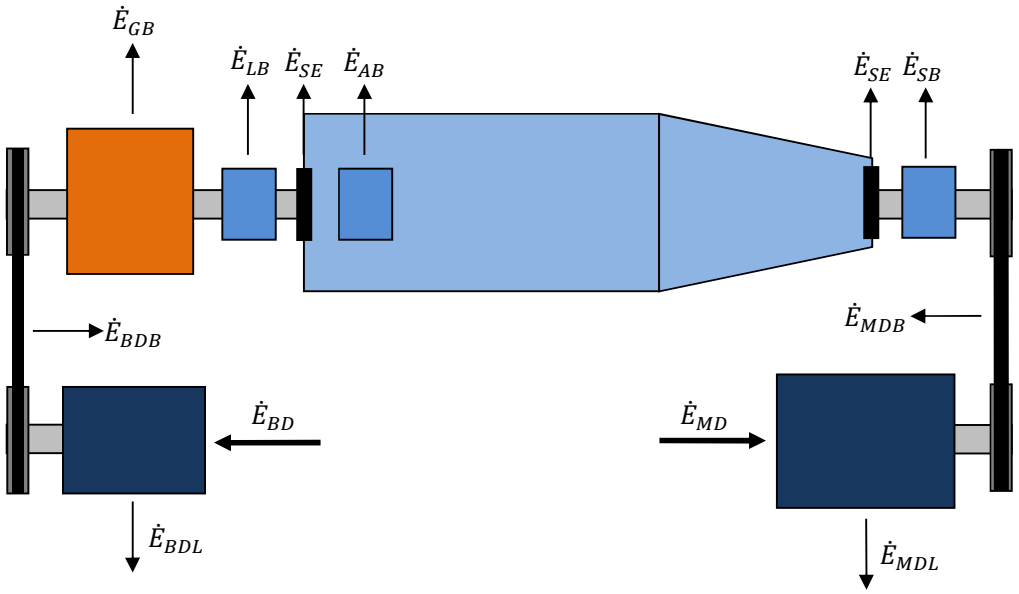

Figure 4.1 Schematic showing the power transmission elements and path

Table 4.1 Symbols and notations for power transmission losses

$\dot{E}_{MD}$	Main drive power input		
$\dot{E}_{BD}$	Back-drive power input		
$\dot{E}_{MDL}$	Main drive motor losses	ε_{MD}	Main drive motor efficiency
$\dot{E}_{BDL}$	Back-drive motor losses	ε_{BD}	Back-drive motor efficiency
$\dot{E}_{MDB}$	Main drive belt losses	ε_{MDB}	Main drive belt efficiency
$\dot{E}_{BDB}$	Back-drive belt losses	ε_{BDB}	Back-drive belt efficiency
$\dot{E}_{GB}$	Gear box losses	ε_{EG}	Gearbox efficiency
$\dot{E}_{SB}$	Solids end bearing losses		
$\dot{E}_{LB}$	Liquid end bearing losses		
$\dot{E}_{AB}$	Axial scroll bearing losses		
$\dot{E}_{SE}$	Combined seal losses		

Figure 4.2 shows a detailed cross-section view of the liquid discharge end of the centrifuge. The scroll is driven by the motor via a three strand v-belt, clutch, and a two stage 57:1 reduction epicyclic gearbox. The bowl is driven by the main drive motor via a five strand v-belt.

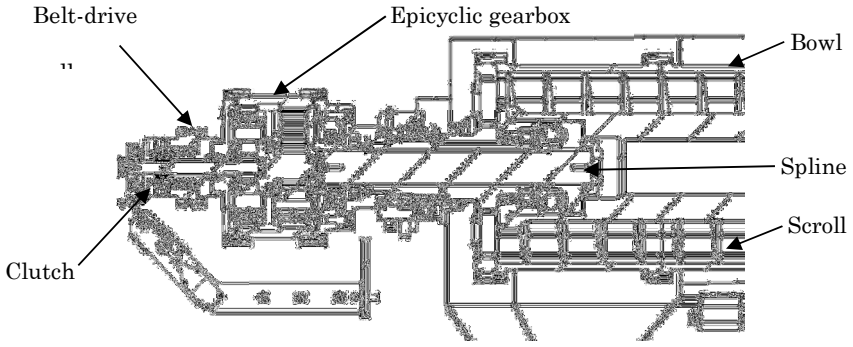

Figure 4.2 Cross-section of liquid discharge end showing gearbox, clutch, and rotating assembly support bearings

The power consumed during power transmission within the GTech-Bellmor 1456 Centrifuge Decanter is evaluated in this chapter. The power losses in the drive motors, belt drives, gearbox, bearings, and seals were determined. A test rig was designed to evaluate the gearboxes under load prior to their installation. As the load on the centrifuge increases due to friction and/or flow rates, the power consumption increases.

For this assessment the power input has been assumed to be between 50% and 100% of maximum possible input.

4.2 Drive Motors

The GTech-Bellmor 1456 Centrifuge Decanter has two motors; the main drive motor and the back-drive motor. The specifications of each are shown in Table 4.2. Both motors are WEG products. All data and curves were taken from the WEG website [33].

Table 4.2 Specifications for the WEG AC motors

	Main drive	Back-drive
Output (kW)	30	15
Voltage (V)	415	415
Poles	4	4
Frequency (Hz)	50	50
Speed (rpm)	1480	1470
Torque (Nm)	194	97.5
Mass (kg)	240	120
Efficiency (100% load) (ε)	0.938	0.918
Efficiency (50% load) (ε)	0.925	0.901
No load current (A)	26.3	13.8

The input power for the main drive motor is

$$\dot{E}_{MD} = \frac{\dot{E}_{MDO}}{\varepsilon_{MD}} \tag{4.1}$$

and the input power for the back-drive motor is

$$\dot{E}_{BD} = \frac{\dot{E}_{BDO}}{\varepsilon_{BD}} \tag{4.2}$$

where $\dot{E}_{MDO}$ and $\dot{E}_{BDO}$ are the shaft output power of the main drive and back-drive motors, respectively. The electric motor efficiency is the ratio between shaft output power and electrical input power. The power lost by the main drive motor is

$$\dot{E}_{MDL} = (1 - \varepsilon_{MD})\dot{E}_{MD}. \tag{4.3}$$

The same relationship exists for the back-drive motor

$$\dot{E}_{BDL} = (1 - \varepsilon_{BD})\dot{E}_{BD}. \quad 4.4$$

At maximum loads the main drive and back-drive motors require 31.98 and 16.34 kW, respectively. Therefore the loss for each motor is 1.98 kW for the main drive and 1.34 kW for the back-drive. The maximum combined loss for the motors is 3.32 kW. The maximum total power input into the centrifuge is 48.3 kW. The power lost in the main drive motor will be 1.22 to 1.98 kW, and 0.82 to 1.34 kW in the back-drive motor when the motors are operating between 50 and 100%, respectively.

4.3 Belt Drives

Two belt drives are used in the GTech-Bellmor 1456 Centrifuge Decanter, one transmits power from the back-drive motor to the gearbox input and the other drives the bowl. Table 4.3 contains the belt and pulley specifications for both belt drives.

Table 4.3 Belts and pulley specifications for the GTech-Bellmor 1456 Centrifuge Decanter

Drive	Drive pulley	Driven pulley	Belt	Ratio
Main	SPZ355/5 Groove	SPZ139.5/5 Groove	SPZ2680	2.55:1
Back	SPZ250/3 Groove	SPZ138.2/3 Groove	SPZ2240	1.81:1

The belts and pulleys must be optimally sized to maximise the efficiency. A belt drive runs at its highest efficiency when it is running at its rated load (i.e. 100% capacity), the efficiency drops when it is over or under loaded. A well designed belt drive will typically have an efficiency of 95 – 98% [34]. The energy consumed by a belt drive has two components, torque losses and speed losses. Torque losses arise from hysteresis caused by bending and the friction between the belt and pulley. The speed losses are due to windage as the belt and pulleys pass through air.

Belt efficiency is dependent on several factors including belt tension, running speed, pulley size, flexural stiffness, and load capacity [34]. Peak efficiency can be obtained if belts and pulleys are correctly selected and installed. Belt drive efficiency can be given as a function of applied load compared to the rated load. Francis [35] displayed the empirically derived plot of efficiency as a function of load, which is shown in Figure 4.3.

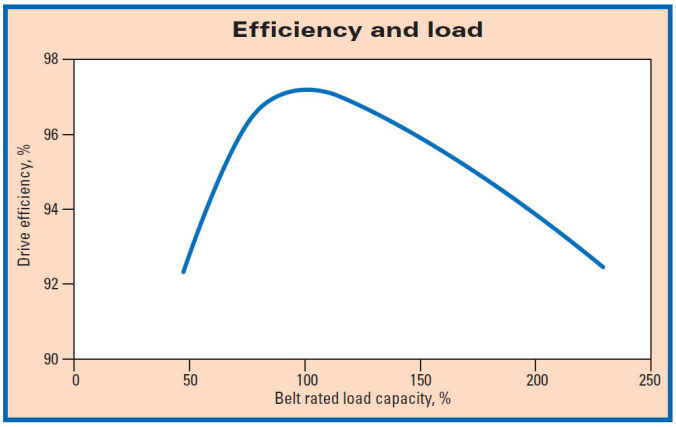

Figure 4.3 Belt drive efficiency, taken from [8]

The power consumed by the main and back-drive belts is

$$\dot{E}_{MDB} = (1 - \varepsilon_{MDB})\varepsilon_{MD}\dot{E}_{MD} \quad 4.5$$

$$\dot{E}_{BDB} = (1 - \varepsilon_{BDB})\varepsilon_{BD}\dot{E}_{BD} \quad 4.6$$

where the efficiencies of the belt drives were determined using Figure 4.3. All the power from the motors is transmitted via the belt drives to the bowl and gearbox. The total maximum power output of the two motors is 45 kW. If the belt drives are both assumed to be 97% efficient, the power lost across the belt drives is 1.35 kW, therefore only 43.7 kW is transmitted to the bowl and gearbox.

The belts will not always be at peak load and hence will not continuously be at peak efficiency. Assuming that the loading range is 50% to 100% the efficiency range will be 0.93 to 0.97. At 50% load the belts consume1.58 kW (1.05 kW main drive, 0.53 kW back-drive). The power consumed as a function of power input is shown in Figure 4.4.

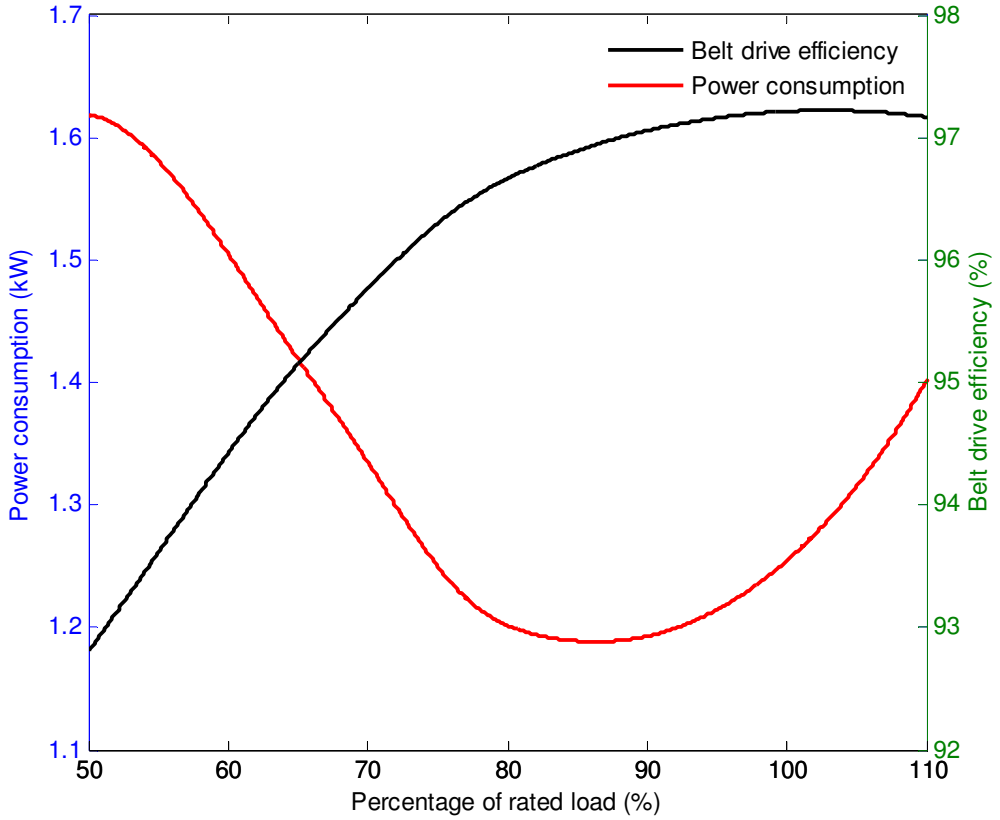

Figure 4.4 Belt drive load versus efficiency and power consumption

The maximum belt speed for an SPZ belt is 40 m/s [36]. The back-drive has a maximum speed of 1,470 rpm and the main drive has a maximum speed of 1,480 rpm. These correspond to belt speeds for the back-drive and main drive of 19.2 m/s and 27.5 m/s, respectively, A single SPZ belt is rated at approximately 6 kW. Therefore the five main drive belts allow sufficiently for the 30 kW transmission and the three back-drive belts allow for the 15 kW transmission. These values indicate that the correct belt and number of belts have been selected.

4.4 Back-Drive Gearbox

The GTech-Bellmor 1456 Centrifuge Decanter employs a GB-57 gearbox as part of the back-drive system. The GB-57 is a two stage epicyclic gearbox. The gearbox reduces the speed and increases the torque from the back-drive motor to rotate the scroll. A very high torque is required to move the solids along the bowl, thus the gearbox must be sufficiently strong to withstand the forces acting on it. The GB-57 gearbox has a maximum output rating of 3.6 kNm. It is important that the correct gearbox is selected

for a centrifuge; Broadbent Engineering Ltd completed a project that involved upgrading undersized gearboxes on decanter centrifuges in a chemical plant [38], the gearbox upgrades and modifications to the scroll led to a significant improvement in throughput.

The reduction ratio, efficiency, and heat loss of the gearbox were evaluated. The reduction ratio was evaluated so that the path of power transmission path was clear. The heat loss was evaluated so the approximate temperature distribution throughout the gearbox and maximum oil temperature could be estimated.

4.4.1 Gearbox ratio

Figure 4.5 shows the power transmission path from the back-drive motor through the gearbox. The back-drive motor is connected to the gearbox by a belt drive; the power is transmitted through a clutch into the gearbox. The outside of the gearbox is fixed to the bowl and rotates at the same speed. The scroll would rotate at the same speed as the bowl if the gearbox pinion was allowed to rotate freely, but there would be no product transport.

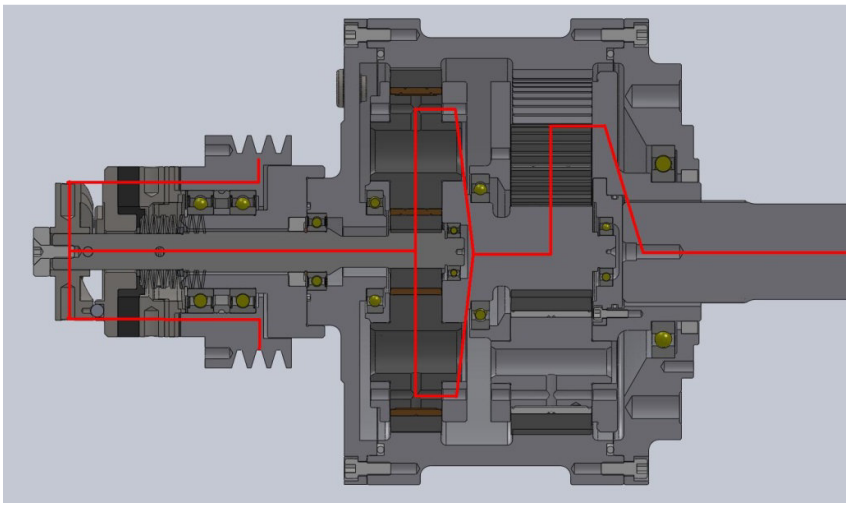

Figure 4.5 GB-57 gearbox cross-section with the path of power transmission

Each gear in the two stages has been labelled in Figure 4.6**.** The pressure angle of all teeth is 20°, which is considered the industry standard [39]. The number of teeth and diametral pitch of each gear is shown in Table 4.4. There are two planet gears in stage one (gear 3), and three in stage two (gear 5). There are more planet gears in the second stage as the torque being transmitted is higher than in the first stage. The power input starts at the first sun gear (gear 1), the output shaft is attached to the second set of planetary gears; these are connected to the scroll via a spline.

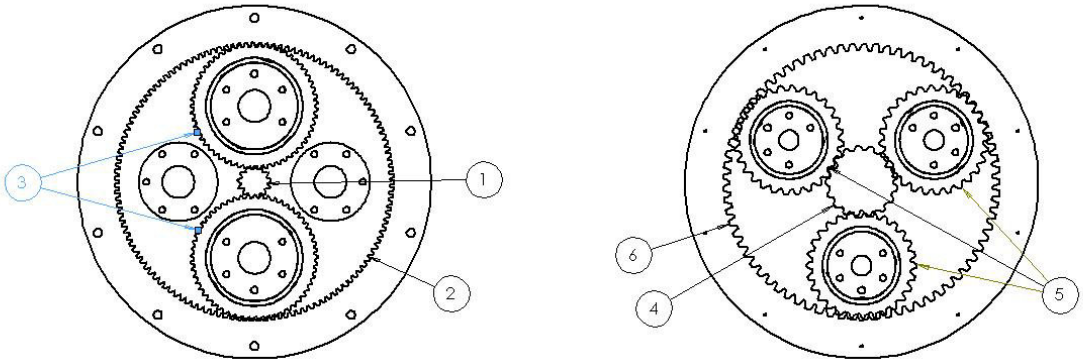

Stage One **Stage Two**

Figure 4.6 GB-57 stage one (left) and two (right)

Table 4.4 Number of teeth on each gear in the GB-57 gearbox

Gear	Number of teeth (N_i)
1	13
2	127
3	57
4	17
5	28
6	73

The first stage provides a reduction of

$$R_1 = \left(1 + \frac{N_2}{N_1}\right) = \left(1 + \frac{127}{13}\right) = 10.77. \tag{4.7}$$

The second stage provides an additional reduction of

$$R_2 = \left(1 + \frac{N_6}{N_4}\right) = \left(1 + \frac{73}{17}\right) = 5.29. \tag{4.8}$$

The total reduction ratio of the gearbox R is 57, which is the product of the two stages ratios. The differential speed Δ is the bowl speed ω_b minus the gearbox input shaft speed ω_{gb} divided by the total gear ratio R, which is

$$\Delta = \frac{\omega_b - \omega_{gb}}{R}. \tag{4.9}$$

4.4.2 Gearbox efficiency

Gears are a very effective means of transmitting power, and in the subject application they are the most efficient way of achieving the high reduction ratio required to drive the scroll. The efficiency of gears is sometimes overlooked; while this is acceptable in some applications, it can have detrimental effects in others. Losses within gearboxes can be broken down into four main areas; gear meshing, oil churning, windage, and bearing losses [40]. Oil churning and windage are generally combined as the dynamic losses. The gear meshing losses are typically dependent on the amount of sliding the gear teeth undergo; worm gears are prone to a high amount of sliding, while spur gears have the least [40]. Gearbox efficiency is best evaluated for a specific design.

Assuming the efficiency per stage is 97% [39], the overall efficiency of the gearbox is 94.1%. The maximum input into the gearbox is 14.55 kW. Therefore the maximum power output is 13.69 kW with a corresponding loss of 860 W. At 50% load the input is 6.98 kW, corresponding to a power loss of 412 W. The power consumed by the gearbox is

$$\dot{E}_{GB} = (1 - \varepsilon_{EG})\varepsilon_{BDB}\varepsilon_{BD}\dot{E}_{BD} \qquad 4.10$$

4.4.3 Gearbox heat transfer

The energy that is lost within a gearbox is converted to heat. This energy must be dissipated to the surroundings directly or via conduction through surrounding components of the centrifuge. The temperature distribution in the gearbox is important as the oil will begin to degrade above its maximum working temperature. The gearbox uses Mobil SHC 630 oil, which has a maximum working temperature of 100°C [41].

For this analysis the output shaft of the gearbox has been set as a boundary temperature depending on the temperature of the process fluid. The process fluid ranges from ambient to 90°C. The temperature of the gearbox was evaluated for a temperature range of 15 to 90°C.

The gearbox was simplified for analysis; a cross-section of the simplified gearbox is shown in Figure 4.7. The gears and bearings were not included in the analysis. The output shaft is on the left end; this face is where the boundary temperature was set. The input shaft is on the right-hand-side.

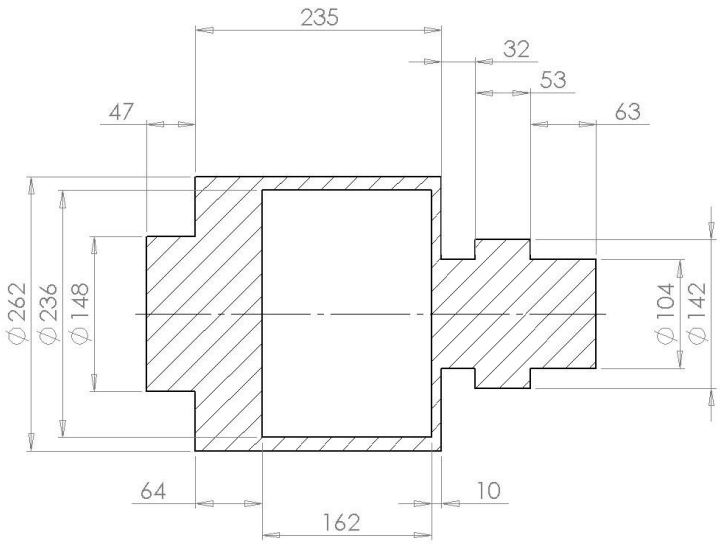

Figure 4.7 Simplified gearbox model cross-section with dimensions (mm)

The steady-state temperature distribution in the gearbox was evaluated using the Steady State Thermal module in ANSYS 13.0. The convection coefficients were calculated using the theory presented in [42]. The convection coefficient is a function of the air properties, rotational speed, diameter, and temperature difference [43]. The convection coefficients were calculated using the assumption that the gearbox was in quiescent air, whereas the gearbox is actually in a vented enclosure, which would somewhat reduce the relative velocity and hence convective heat transfer. The boundary temperatures were set to 15 and 90°C. The emissivity of all surfaces was assumed to be 0.9. The thermal conductivity of steel was used. The relevant heat transfer properties are given in Table 4.5 for the various surfaces identified in Figure 4.8. The heat input was divided between the two internal faces, with the majority being transferred through the cylindrical surface.

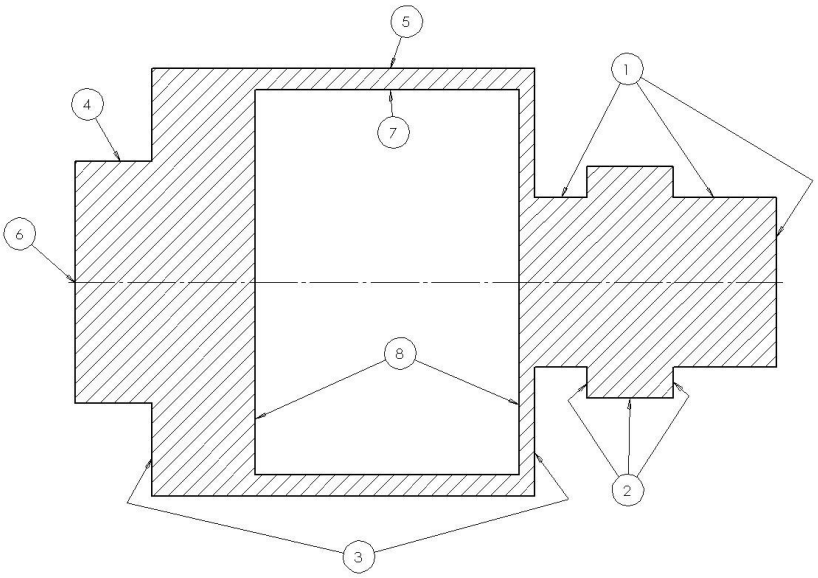

Figure 4.8 Simplified gearbox surface labels

Table 4.5 Heat transfer parameters of the rotating gearbox

Surface	Temperature (°C)	rpm	Convection coefficient (W/m^2K)	Heat flux (W)
1	(-)	2565	49.8	(-)
2	(-)	2565	56.9	(-)
3	(-)	3250	56.5	(-)
4	(-)	3250	67.2	(-)
5	(-)	3250	45.8	(-)
6	15-90	3250	(-)	(-)
7	(-)	3250	(-)	500
8	(-)	3250	(-)	300

For applications where the product arrives at the centrifuge at ambient temperature, such as vegetable processing, the shaft temperature will be approximately ambient. This neglects heat added by losses within the centrifuge. The shaft temperature was consequently set to 15°C. The temperature distribution is shown in Figure 4.9. The maximum temperature in the gearbox is 60°C.

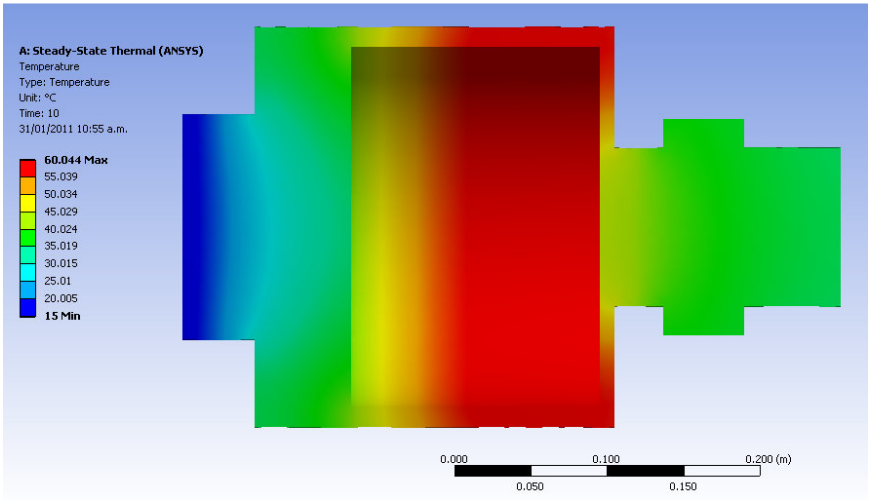

Figure 4.9 Gearbox temperature distribution with 15°C output shaft

For applications where the product is heated before arriving at the centrifuge, such as meat processing, the shaft temperature will be significantly above ambient. The shaft temperature was set to 90°C to simulate these applications. The temperature distribution is shown in Figure 4.10. The maximum temperature in the gearbox is approximately 75°C.

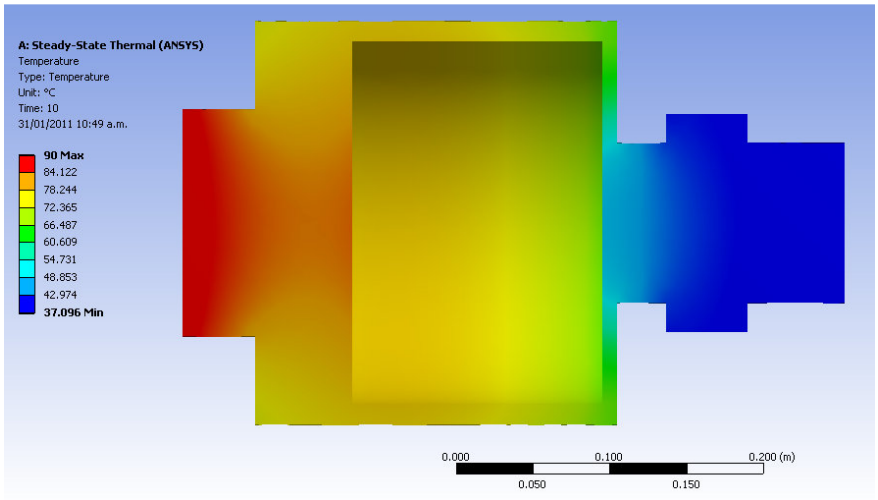

Figure 4.10 Gearbox temperature distribution with 90°C output shaft

If a test rig was constructed the outer casing of the gearbox would be stationary; this would significantly reduce the convection coefficients. The drive coupling would still be rotating at full speed so the convection coefficient would remain the same. The model has been re-evaluated for the parameters shown in Table 4.6. The end temperature of

the gearbox has been set to 20°C, as this is the assumed ambient temperature in the factory during testing.

Table 4.6 Heat transfer parameters for a stationary gearbox

Surface	Temperature (°C)	rpm	Convection coefficient (W/m^2K)	Heat flux (W)
1	(-)	2565	49.8	(-)
2	(-)	2565	56.9	(-)
3	(-)	0	5	(-)
4	(-)	0	5	(-)
5	(-)	0	5	(-)
6	20	0	(-)	(-)
7	(-)	0	(-)	500
8	(-)	0	(-)	300

The temperature distribution for a stationary gearbox is shown in Figure 4.11. The maximum temperature in the gearbox is approximately 100°C. The implications of a high temperature will need to be considered in the design of the test rig.

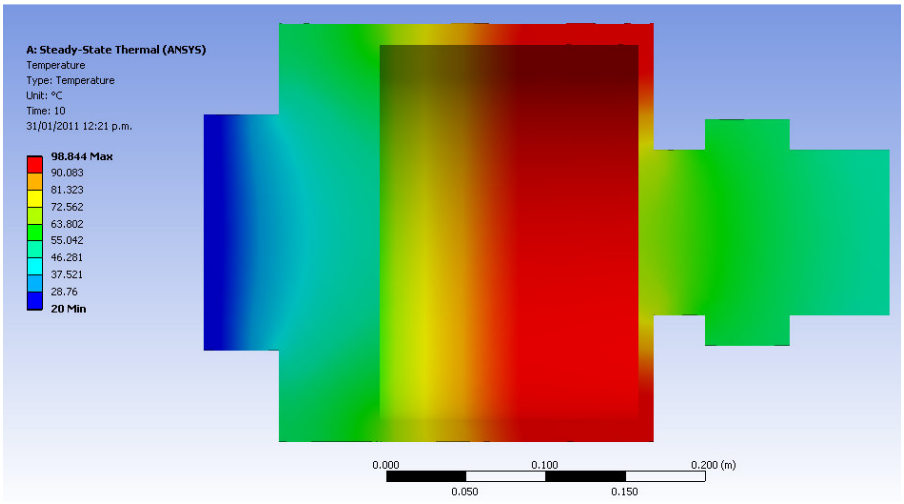

Figure 4.11 Temperature distribution of a gearbox with a stationary outer casing

4.4.4 Gearbox test rig

A test rig was designed to verify the predicted performance of the gearbox. The rig was designed to fulfil two requirements; measure the efficiency of the gearbox, and test the gearbox under full load prior to installation. The design process for the gearbox test rig is presented in Appendix B.

Figure 4.12 is the final conceptual design of the gearbox test rig. This concept reduces the plan area by stacking the motors and gearboxes vertically. This also allows for use of the clutch assemblies. The belt and chain drives will need to be accounted for in the efficiency calculation. An oil pump and heat exchanger were included in the design to remove the heat generated within the gearbox. The lower gearbox is intended to remain as part of the rig and the upper gearbox is the one being tested. The mounting assembly for the gearboxes can be changed to allow different gearboxes to be tested.

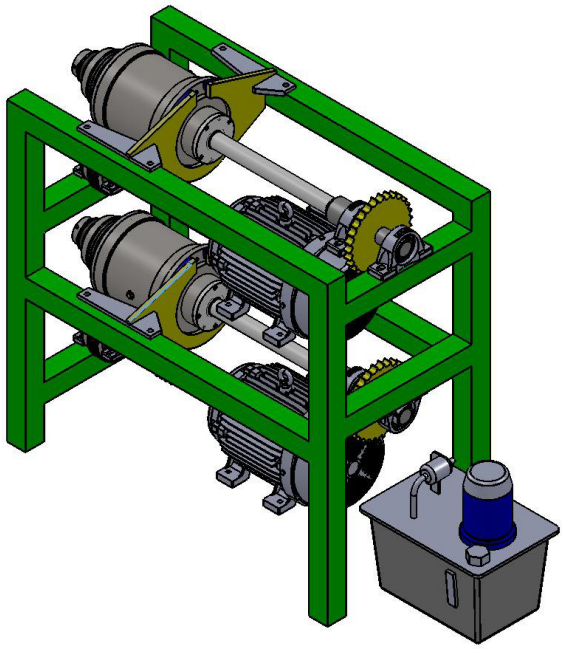

Figure 4.12 Final concept for the gearbox test rig

Detailed manufacturing drawings were prepared for the test rig, but at the time of completion of this thesis it was not yet constructed. Bellmor Engineering Ltd. intend on manufacturing and commissioning the test rig when the resources become available.

4.5 Bearings

The power consumed by bearings arises from the frictional moment. The amount of friction within a bearing determines its operating temperature range. The friction arises from rolling and sliding of the rolling contact points and from viscous forces within the lubricant. SKF provides a method of calculating the friction moment of bearings under normal conditions. The resisting moment induced by a bearing is

$$M = \frac{1}{2}\mu F d \tag{4.11}$$

where

μ constant coefficient of friction (see [44])

F equivalent dynamic bearing load (N)

d bearing bore diameter (m).

The power consumed by the bearing $\dot{E}_B$ is the torque multiplied by the relative speed φ between the inner and outer races of the bearing

$$\dot{E}_B = \frac{1}{2}\mu F d\varphi. \tag{4.12}$$

There are three bearings within the centrifuge that are under a significant load. These bearings are the two bearings that support the rotating assembly, and the axial support bearing for the scroll. The locations are shown in Figure 4.13 and a description of each is given in Table 4.7.

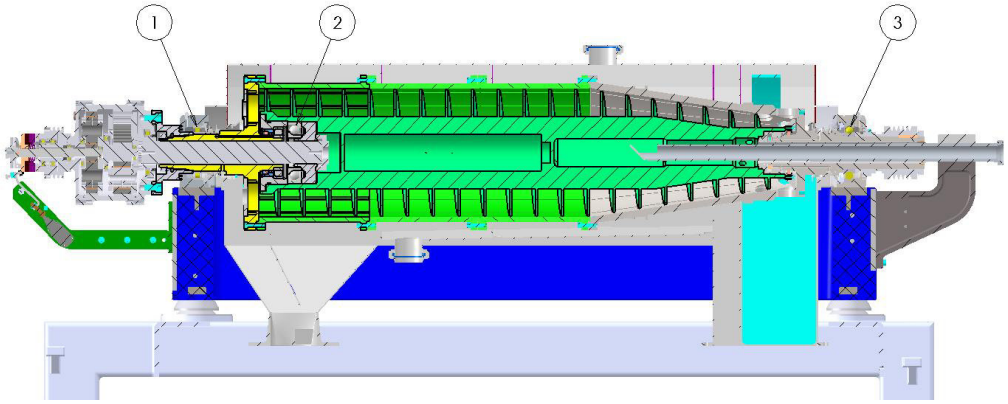

Figure 4.13 Bearing locations for the rotating assembly

Table 4.7 Bearing labels and types

Bearing	Description	Type
1	Liquid end bearing	Cylindrical roller bearing
2	Scroll bearing	Angular contact ball bearing
3	Solids end bearing	Deep groove ball bearing

Two bearings support the rotating assembly. A deep groove ball bearing supports the solids end and a cylindrical roller bearing supports the liquid end. The components supported by the rotating assembly bearings are shown in Table 4.8.

Table 4.8 Rotating assembly weight breakdown

Component	Weight (N)
Bowl weight	2413
Scroll weight	2413
Process fluid weight	491
Belt tension	625
Main drive belt force	6,250
Back-drive belt force	3,750
Gearbox mass (GB-57)	861

The load on the solids end bearing is assumed to be half the weight of the bowl and scroll and the force from the main drive belts; giving a total force of 8,660 N. The deep groove ball bearing has a coefficient of friction of 0.0015. The speed of the bearing is 3250 rpm. The race diameter is 103.86 mm. The power consumed by the bearing is estimated to be 227 W.

Assuming that the liquid end bearing supports the weight of the gearbox, half the scroll and bowl, half the process fluid and the force from the back-drive belts, this corresponds to a force of 7,270 N. A cylindrical roller bearing has a coefficient of friction of 0.002. The speed of the bearing is 3250 rpm. The diameter is 113 mm. The power consumed by the bearing is estimated to be 280 W.

Assuming that all the power transferred to the scroll is used to overcome an axial force, the load is passed back onto the angular contact bearing; this is the worst-case loading. The force created by the scroll F_{Sc} is equal to

$$F_{Sc} = \frac{\dot{E}_{Sc}}{v} \tag{4.13}$$

where

$\dot{E}_{Sc}$ power provided to scroll from gearbox (W)

v axial conveyor speed (m/s).

Substituting Equation 2.2 into Equation 4.3 gives

$$F_{Sc} = \frac{2\pi \dot{E}_{Sc}}{G\Delta}. \quad 4.14$$

Substituting Equation 4.14 into Equation 4.12 gives

$$\dot{E}_{AB} = \frac{\mu\pi \dot{E}_{Sc} d}{G}. \quad 4.15$$

The relative speed φ is equal to the differential speed Δ. The power provided to the scroll is the remaining portion of the back-drive motor power after it has passed through the belt drive and gearbox. The remaining power is theoretically 13.7 kW. The diameter of the bearing is 97.1 mm. The coefficient of friction of an angular contact ball bearing is 0.002. The power consumed by the scroll bearing is estimated to be 119 W. In reality the motor will not be providing full power at all times; assuming that the load ranges from 50-100%, the bearing will consume 59 to 119 W. It should be noted that the power consumed by the bearing does not decrease linearly with load as the efficiencies of the belt drives and motors vary with load.

The product transport model described in Chapter 2 was used to calculate the axial load on the scroll bearing for the operating conditions described in Table 2.3. The axial load was predicted to be 37.0 kN for a differential speed of 23.5 rpm, which results in a bearing loss of less than 10 W. The result is significantly lower than the estimated worst case scenario as the power required for product transport is lower than the full capacity of the back drive. The loss from the axial scroll bearing can be considered negligible compared to the other losses.

The combined power consumed by the two rotating assembly support bearings is 510 W.

4.6 Seals

There are several seals used within the centrifuge. The type and condition of each seal determines its effectiveness and how much power is consumed by it. Friction is created at the interface between the seal and the sealing face and converted to heat. The power consumed by a seal is proportional to the sealing force F, relative speed φ, coefficient of friction μ, fluid medium, and diameter d. A comprehensive investigation would be required to obtain even an approximate estimate of the power consumed by the seals. The power consumed by the friction on a dynamic seal is

$$\dot{E}_{Se} \propto \mu F d\varphi. \quad 4.16$$

Plath *et al* [45] conducted an experiment on the friction torque of rotary shaft lip type seals. They investigated the effect of temperature and rotation speed on the friction torque. The torque was relatively constant with rotation speed. It was found that the torque reduced significantly above approximately 60°C [45]. It was assumed that the seal losses will be of similar magnitude to the bearing losses. The seal losses were estimated to be 500 W in total for all seals. The power consumed by the seals is assumed to be independent of load.

4.7 Total Transmission Losses

The total estimated losses from each element in the transmission path are shown in Table 4.9. The total maximum power input into the centrifuge is 48,770 W. The transmission losses make up 13.8% of the total power consumption at 100% load and 23% at 50% load. The increase in power transmission losses at lower loads is due to the motors and belts being less efficient when operating below their rated loads.

Table 4.9 Summary of power transmission losses

	50% load (W)	100% load (W)	Equation
$\dot{E}_{MD}$	16,220	32,430	4.1
$\dot{E}_{BD}$	8,320	16,340	4.2
Total input	24,520	48,770	-
$\dot{E}_{MDL}$	1,220	1,980	4.3
$\dot{E}_{BDL}$	824	1,340	4.4
$\dot{E}_{MDB}$	1,050	900	4.5
$\dot{E}_{BDB}$	525	450	4.6
$\dot{E}_{GB}$	412	860	4.10
$\dot{E}_{SB}$	227	227	4.12
$\dot{E}_{LB}$	280	280	4.12
$\dot{E}_{SE}$	500	500	4.16
Total losses $\dot{E}_T$	5,040	6,540	-

4.8 Conclusions

The transmission losses are made up of inefficiencies in the motors, belt drives, gearbox, bearings, and seals. The total combined transmission losses when the centrifuge is fully loaded were estimated to be 6.54 kW, which is 14% of the total power input. When the centrifuge is loaded to 50% the transmission losses were estimated to be 5.04 kW, which is 21% of the total power input. There are few methods of reducing the individual losses. Correct component selection ensures that the transmission losses are minimised.

A concept has been developed to test the efficiency of the gearbox. The concept was developed in a way that the transducers can be removed and the rig used to test every gearbox under full load before it is fitted to a centrifuge. This would allow manufacturing and assembly faults to be detected before a gearbox is installed.

Chapter 5

Assessment of Windage Losses

5.1 Introduction

Windage is defined as the force created on a rotating body by viscous effects due to relative movement between the body and a surrounding fluid. Windage can cause a rotating body to slow down or require more torque to overcome the additional force. Windage can potentially consume a considerable amount of power in machinery containing components rotating at high speed. Windage is a function of the fluid properties, geometry, and speed of rotation.

The GTech-Bellmor 1456 Centrifuge Decanter has several components rotating at high speed. The rotational speed of the components (bowl and gearbox casing) exposed to air is 3250 rpm. Both bodies are contained by close fitting housings, which replicate a larger concentric cylinder. The actual spaces have complex geometries, but as the boundary layer immediately above the surface of the rotating component is the only flow of interest, it is not necessary to consider the cavity in detail. The complete bowl assembly is shown in Figure 5.1.

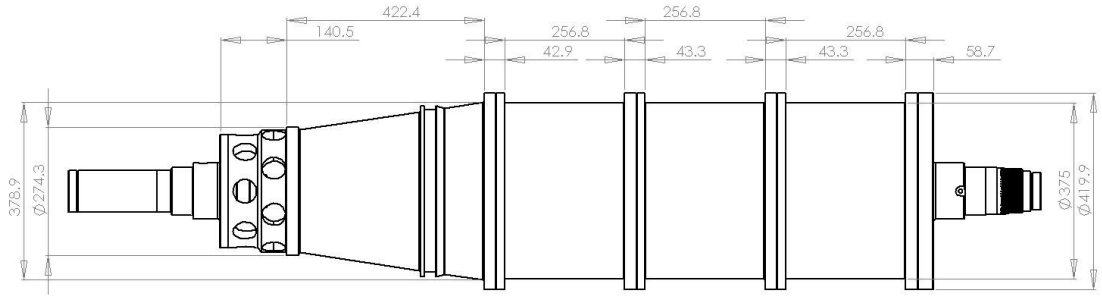

Figure 5.1 GTech-Bellmor 1456 Centrifuge Decanter bowl assembly (mm)

Components that protrude into the air flow can have a significant amount of pressure drag, which can make a considerable contribution to the windage losses. Drag on other bodies, due to the high speed of rotation, has been examined. This includes drag on the bolt heads and third phase ports.

The power consumed by windage was estimated in this chapter. Several techniques were used to calculate the drag due to windage: empirical methods devised by other researchers, and a computational model created in ANSYS CFX. It was not practical to experimentally determine the power consumed by windage on the bowl.

5.2 Empirical Estimation of Windage Power

A relationship between the drive torque and rotation speed of a cylinder rotating in an annular space was developed by Bilgen and Boulos [46]. The relationship does not consider the ends of the cylinders, nor does it include flow parallel to the axis of rotation.

The windage on the bowl was investigated using two geometries. The first geometry was for two concentric cylinders, the radius of both cylinders being constant. This did not account for the conical section of the bowl. The second geometry included the conical section of the bowl. The bowl was broken up into discrete slices that were analysed individually. Both geometries assumed the annular space is always concentric. The actual annular space is shown in Figure 5.2. For this method of calculation it was assumed that the outer wall is approximately a constant distance from the bowl, and that the bowl and cavity wall are concentric.

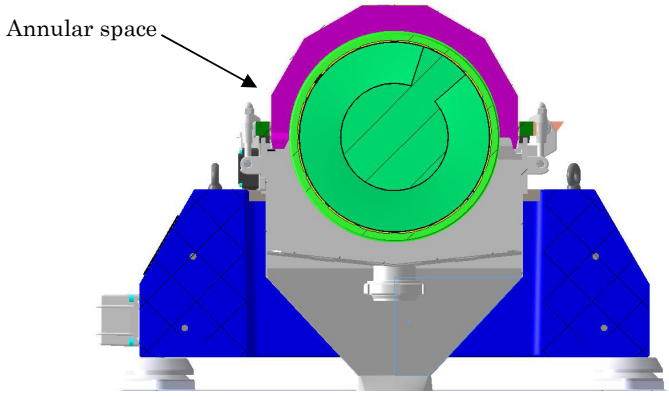

Figure 5.2 Annular space geometry for the GTech-Bellmor 1456 Centrifuge Decanter

The bolts and flanges were excluded from this analysis and are addressed in a later section. There would also be drag on the solid and liquid ports but these components rotate in areas filled with process fluid and have been neglected from this analysis.

5.2.1 Concentric cylinders

The first approximation of the windage on the bowl was made based on two concentric cylinders with a constant annular space. The drag on the ends of the cylinders was neglected. The ends of the bowl have limited exposure to air as this is where the process fluid flows. The bowl was approximated as a 1,522 mm long by 375 mm diameter cylinder and assumed to be contained within a concentric cylinder with an annular gap of 49 mm. An axial view of the bowl rotating in an annular space is shown in Figure 5.3.

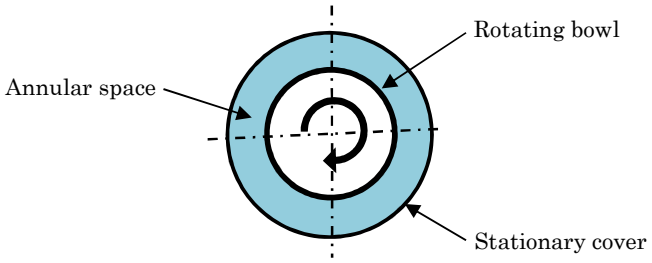

Figure 5.3 Bowl rotating within an annular space

The windage was evaluated at 3250 rpm, the tangential velocity at this angular velocity is 64 m/s. The film temperature was assumed to be 25°C. The process fluid temperatures can vary from 15 to 90°C for different applications. All properties were determined at atmospheric pressure. The properties of air at 25°C are given in Table 5.1.

Table 5.1 Properties of air at 25°C **[47]**

Density (ρ)	1.184 kg/m^3
Dynamic viscosity (μ)	1.849 x 10-5 kg/m.s
Kinematic viscosity (v)	1.562 x 10-5 m^2/s

The Reynolds number can be used to determine the state of the fluid flow, i.e. whether the flow is laminar or turbulent. The rotational Reynolds number for flow in an annular space is given by

$$Re = \frac{\omega R_I g_r}{v} \qquad 5.1$$

where

ω angular velocity (rad/s)

R_I radius of inner cylinder (m)

g_r annular gap (m)

υ kinematic viscosity (m²/s).

To determine the flow regime in the annular space the Taylors number must be evaluated. The Taylors number is

$$Ta = \left(\frac{\rho\omega R_i g_r}{\mu}\right)\sqrt{\frac{g_r}{R_i}}. \quad 5.2$$

When the Taylors number is above 400 the flow becomes turbulent [46]. Wendt [48] derived the empirical formula for the moment coefficient for Reynolds numbers above 10,000 as

$$C_M = 0.146(g_r R_o/R_i^2)^{0.25} Re^{-0.3} \quad 5.3$$

where

R_o outer radius of annular space (m).

The calculated moment coefficients are consistent with the work of Wild *et al* [49], where the moment coefficient is approximately 0.002. Using the calculated moment coefficient, the torque required to maintain constant speed due to windage can be calculated. The moment on the cylinder is

$$M_{Cyl} = 0.5 C_m \pi \rho \omega^2 R_I^4 L. \quad 5.4$$

where

C_m moment coefficient of cylinder

L length of cylinder (m).

The power required is given by the following relationship

$$\dot{E}_W = M_{Cyl}\omega. \quad 5.5$$

Substituting Equations 5.1 and 5.3 into 5.4, and then into 5.5 gives

$$\dot{E}_W = 0.073\pi\rho L \frac{\omega^{2.7}\upsilon^{0.3} R_o^{0.25} R_i^{3.2}}{g_r^{0.05}}. \quad 5.6$$

Equation 5.6 shows that the power consumed due to windage is proportional to the rotation speed to the power of 2.7. The power consumed by the rotating cylinder due to windage and ignoring the ends is shown in Table 5.2.

Table 5.2 Results calculated using empirical method

		Equation
Rotational Reynolds number (Re)	204,300	5.1
Taylors number (Ta)	105,500	5.2
Moment coefficient (C_M)	0.0028	5.3
Torque (M_{Cyl})	1.151	5.4
Power ($\dot{E}_W$)	392	5.5

5.2.2 Inclusion of the conical section

The above analysis did not account for the conical section of the bowl. The conical section was included by splitting the cone into N discrete slices and calculating the windage power for each slice. The conical section of the bowl was broken down into 10,000 sections, each of which was analysed individually. The conical section will cause flow parallel to the axis of rotation due to the pressure gradient created by the wall velocity. This is in accordance with the Bernoulli principle [47]. This flow is difficult to model and even more difficult to measure. Coupling between each of the discretised sections has been neglected as the drag is the only property of interest.

The power consumption reduced to 328 W when the conical section was included, comprising of 247 W and 81 W from the cylindrical and conical sections respectively. This is due to the smaller radius and the increased annular space in the conical section.

The error as a function of the number of slices is shown in Figure 5.4. The error is defined as the percentage difference from the result that used the greatest number of slices. The figure shows that there is <<1% variation when using more than approximately 500 slices.

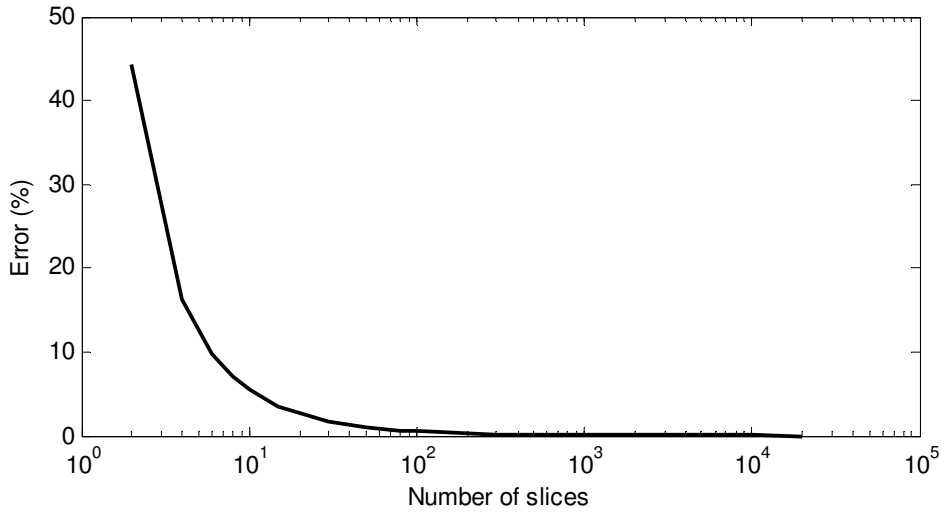

Figure 5.4 Error percentage in power consumed by windage versus number of slices

5.2.3 Drag on flanges

The additional drag caused by the flanges that connect the bowl sections was also considered as their radius is larger than the bowl. The empirical model presented in [46] was used to calculate the drag on the flanges. There are four flanges on the cylindrical section of the bowl. The radius of the flanges is 209.9 mm, with a combined thickness of 188.2 mm. The power consumed by windage on the flanges is an additional 23 W over the bowl diameter. This analysis does not include the drag on the sides of the flanges.

5.2.4 Effect of air properties on windage

The power consumption is proportional to the density of air ρ multiplied by the kinematic viscosity υ of air to the power of 0.3

$$\dot{E}_W \propto \rho \upsilon^{0.3}. \qquad 5.7$$

Figure 5.5 shows the percentage reduction of windage power as a function of the film temperature. The film temperature is the average of the wall and ambient temperature. Overall, there is a 10.7% variation in windage power in a film temperature range of 15 to 90°C.

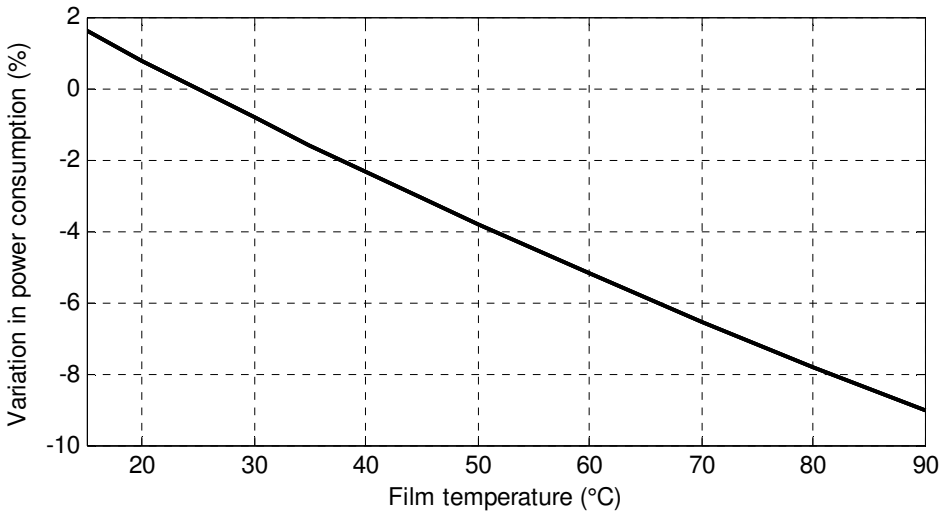

Figure 5.5 Windage power as a function of film temperature

5.2.5 Gearbox windage

The gearbox was approximated as a finite cylinder of radius 131 mm and length 235 mm. The gearbox and belts are enclosed in a vented protective cover, which is approximated as having a 99 mm wide annular gap. The surface of the gearbox will always be above ambient temperature due to inefficiencies within the gearbox. The temperature range of the gearbox surface is approximately 60 to 75°C. The windage power consumed by the gearbox was calculated using Equation 5.6. The windage on the gearbox consumes approximately 20 W at 3250 rpm, which is small relative to the windage associated with the bowl.

5.2.6 External protrusions

The drag on the bolt heads, and third phase ports was estimated. The drag on the bolt heads and ports is primarily pressure drag, which in most instances is higher than surface friction drag. The external protrusions were analysed as if they were in an unimpeded uniform flow at an estimated free-stream velocity. This will not be the exact case in reality, but it provides a magnitude for the power consumed by the drag force acting on the component. The protruding component will be partially within the wall layer and the flow would have been disturbed further upstream by other protruding components. The reduction in drag due to slipstreaming has not been accounted for in this analysis.

The drag is dependent on the properties of air within the region surrounding the bowl. The film temperature was assumed to be 25°C for this analysis. The density and kinematic viscosity of air at 25°C are given in Table 5.1.

5.2.6.1 **Drag on bolts**

The four bowl sections are connected by flanges (see Figure 5.6). The round bolt heads protrude into the moving air stream. There are 16 bolts per flange, giving a total of 48 bolt heads. The heads have a height of 10 mm and an external diameter of 16 mm. They are on a pitch circle diameter (PCD) of 394 mm.

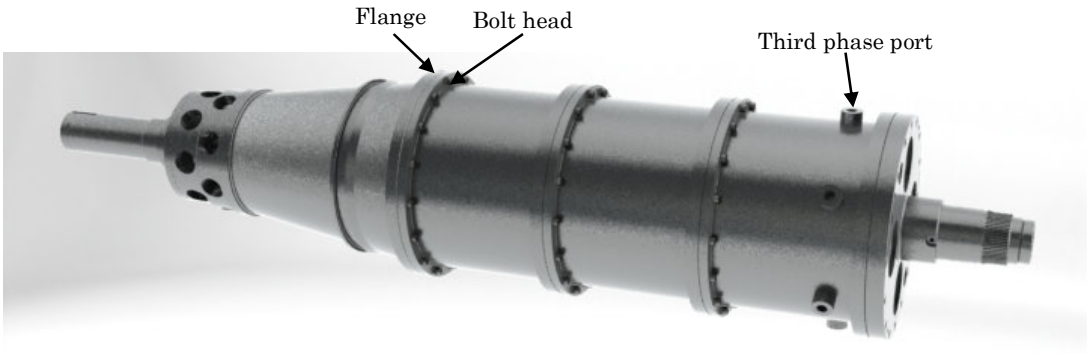

Figure 5.6 Bowl showing flanges, bolts, and third phase discharge ports

The relative velocity V_{rel} between the bolt heads and air in the annular space is

$$V_{rel} = r_{PCD}\omega - u_\theta \qquad 5.8$$

where

r_{PCD} radius of the PCD (m)

u_θ tangential velocity of the air within the annular space (m/s).

The relative velocity of the bolt heads moving through quiescent air (u_θ=0) is 67 m/s. The Reynolds number of the flow passing over the bolt head is

$$Re = \frac{V_{rel}D}{v} \qquad 5.9$$

where

D diameter of protruding body (m).

The Reynolds number is 63,030 for the flow passing over the bolt heads. The drag coefficient C_D for a finite cylinder when the Reynolds number is greater than 10,000 is approximately 0.6 [47]. The drag force on one bolt head is

$$F_D = \frac{1}{2} C_D \rho A V_{rel}^2 \qquad 5.10$$

where

A normal area of protruding body (m²).

The power is the force multiplied by the tangential velocity

$$\dot{E}_D = \frac{1}{2} C_D \rho A V_{rel}^2 V_\theta. \qquad 5.11$$

The drag on an individual bolt head is 0.255 N, which results in a power consumption of 17.1 W. The total power consumed by the 48 bolts is 822 W. In reality the relative speed between the bolt heads and the air will decrease as the air is also rotating with the bowl. This phenomenon implies the power consumed by the bolts will be lower than calculated above. Using the velocity profile in Figure 5.9 the average relative velocity V_{rel} reduces to 39 m/s, lowering the power consumed by the bolt heads to 278 W.

5.2.6.2 **Drag on third phase ports**

There are six ports around the bowl with a height of 25 mm and a diameter of 40 mm. The radius at the centre height of the ports is 200 mm. The six ports are equally spaced at 60° around the perimeter of the bowl. Using Equation 5.8 the tangential velocity of the port stand along the PCD is 68 m/s, which corresponds to a Reynolds number of 160,000. Using Equation 5.10 the drag force on one port is 1.65 N, therefore the power consumed by drag on one port is 112 W. The total power required by the 6 ports is 672 W. As is the case for the bolts, the relative velocity will be lower due to the rotating air in the annular space, implying that the power consumption is likely to be less than calculated. Using the velocity profile in Figure 5.9, the average relative velocity V_{rel} reduces to 42 m/s, lowering the estimated power consumption to 256 W.

5.3 Computational Analysis

The bowl was simplified as shown in Figure 5.7 for CFD analysis. The discharge ports and support shafts were omitted as it was deemed they would have little effect on the windage during operation. The small passages between the bolt heads and the bowl wall

were also removed from the analysis, there will be little airflow through this passage and it was shown that the higher pressure is concentrated on a small area on the leading face of the bolt. Closing off the space between the bolt heads and bowl will result in a small over prediction of the drag force.

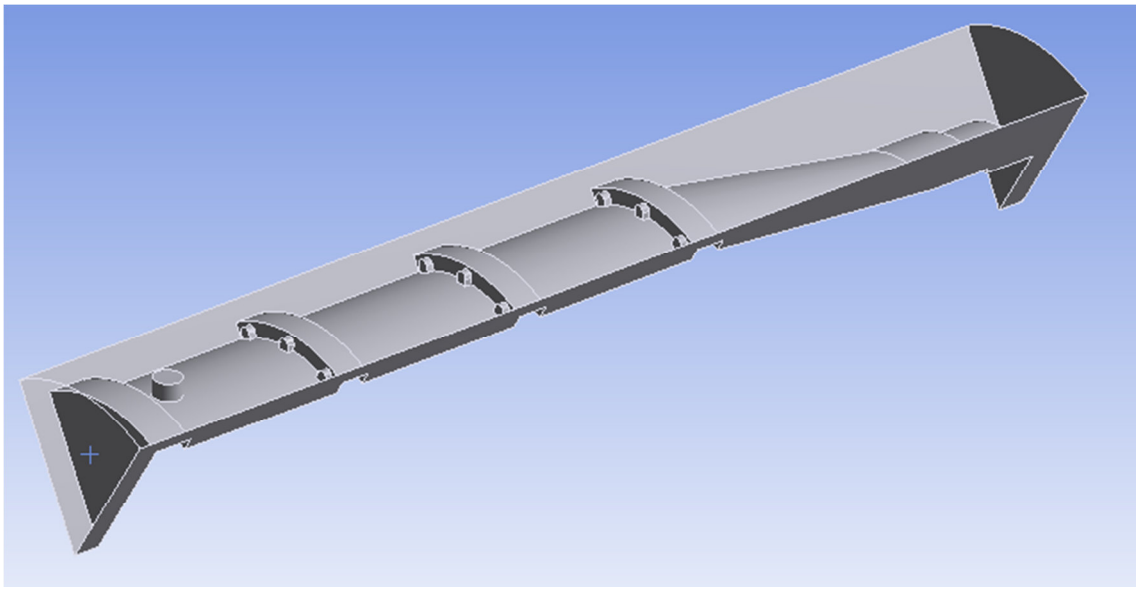

Figure 5.7 Bowl model used for CFD analysis

Only one sixth of the annular space was modelled as the problem was considered as having periodic symmetric. Using the periodic symmetry assumption effectively increased the number of bolt heads to 18, therefore the drag on the bolts was reduced by a factor of 16/18 in the results. The mesh contained 640,509 nodes with 15 inflation layers on the surface of the bowl and cover. There was less than 5% variation in the torque when the mesh was increased to 6.4 million nodes with extra inflation layers. Part of the mesh that was used is shown in Figure 5.8. A rotating domain was used with the SST turbulence model with curvature correction. The bowl wall was set to rotate with the domain at 3250 rpm and the exterior cover was set to be stationary. The convergence criteria was an RMS value of 1e-4.

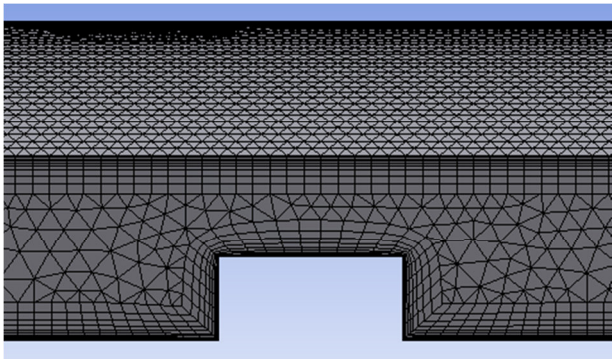

Figure 5.8 Mesh used for the analysis showing inflation layers on the bowl wall, flanges, and cover

The velocity profile across the annular space for 3250 rpm is shown in Figure 5.9. The axial location of the velocity profile is 1 m from the solids discharge end of the bowl. The velocity gradient is very steep near the bowl and cover walls. Qualitative pressure distributions on the third phase ports and bolt heads are shown in Figure 5.10.

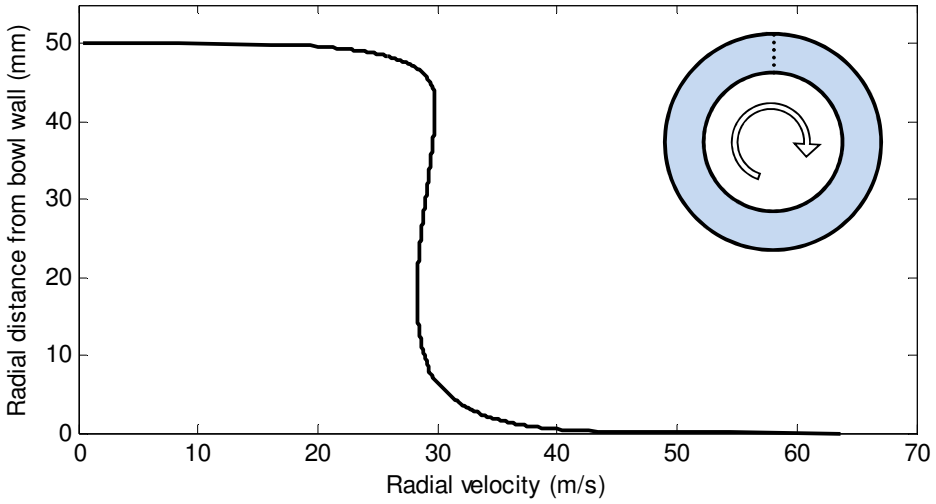

Figure 5.9 Velocity profile across annular space at 3250 rpm

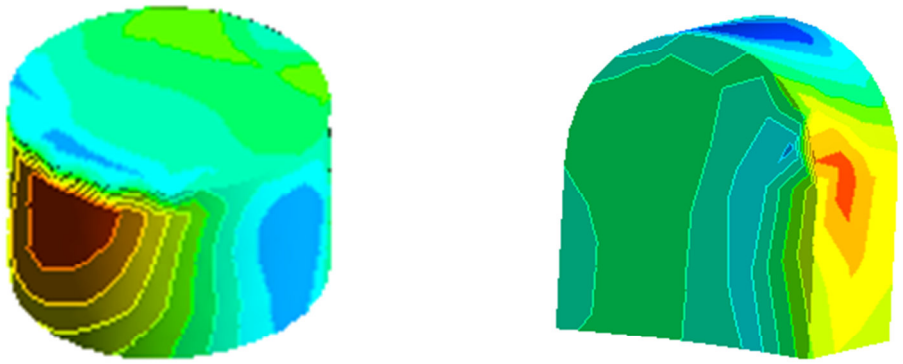

(a) (b)

Figure 5.10 Qualitative pressure distribution on a (a) third-phase port and (b) bolt head

The predicted power consumption due to windage on each component of the GTech-Bellmor 1456 Centrifuge Decanter is given in Table 5.3.

Table 5.3 Power consumed due to windage estimated using ANSYS CFX

	ANSYS CFX	Empirical prediction
Surface drag (W)	477	331
Bolt heads (W)	267	278
Third-phase ports (W)	157	256
Total (W)	934	651

The windage was also simulated for 2000, 4000, and 5000 rpm. The total drag acting on each component is shown in Figure 5.11. The total power consumed by windage predicted using the computational model was proportional to the speed to the exponent of 3.17 ($P \propto \omega^{3.17}$), while the power consumed due to surface drag on the bowl was proportional to the speed to the exponent of 3.05 ($P \propto \omega^{3.05}$). An exponent of 2.7 was observed by Bilgen [46] for the surface drag.

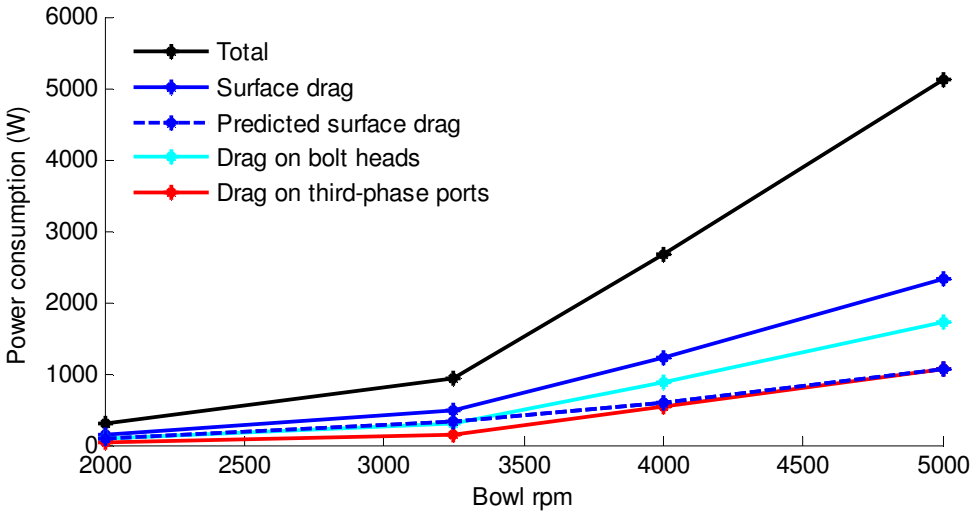

Figure 5.11 Power consumed by windage as a function of bowl speed

5.4 Induced Flow

When the decanter is running dry (there is no process fluid) a flow of air is induced by the rotating components. This flow has been measured at the inlet port, identified in Figure 5.12, using a handheld anemometer.

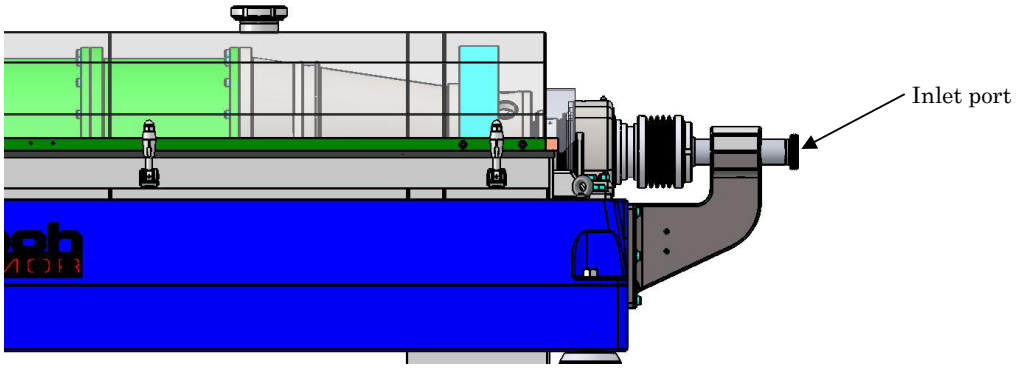

Figure 5.12 Position of air flow measurement at inlet port

The flow speed u was measured to be 40 m/s at 19°C. The air density at this temperature is 1.208 kg/m^3. The cross-sectional area of the device is 564.5 mm^2. The volumetric flow rate and mass flow $\dot{m}$ are 0.226 m^3/s and 0.0273 kg/s, respectively. The flow power is

$$\dot{E}_{Flow} = \frac{1}{2}\dot{m}u^2. \qquad 5.12$$

The measured induced flow power passing through the feed tube was 21.8 W.

Aeroacoustic sound generation is known to be a significant source of noise, particularly at high flow velocities [50]. Consequently, effects such as the induced flow in the decanter and vortex shedding from external protrusions contribute to the overall acoustic emissions [14].

5.5 Conclusions

The power consumed by windage on the bowl was estimated in this chapter by an empirical method and a computational model. The two components of windage are surface drag on the bowl and pressure drag on bodies that protrude into the flow. The total maximum power consumed by the centrifuge under full load is 48.3 kW, therefore the windage losses account for approximately 2% of the total power. The magnitude of the windage losses does not vary with load, only with speed. Two potential benefits of reducing windage are decreased power consumption and sound emissions. Table 5.4 contains a summary of the losses predicted using ANSYS CFX with their contribution to the total windage power at 3250 rpm.

Table 5.4 Summary of windage losses within the centrifuge

Loss	Magnitude (W)	Contribution (%)
Surface drag	477	52
Bolt heads	267	31
Third-phase ports	157	17
Drag on gearbox	20	2
Total $\dot{E}_W$	921	

If the bolt heads were fully countersunk they would be removed from the air stream and their contribution to the drag would be removed. A solid ring could be added around the circumference of the bowl to remove the third phase ports from the air flow. Both of these methods require adding extra material to the bowl, which would increase the surface area and hence increase the surface friction drag by approximately ~10 W. The increase in friction drag would be significantly less than the reduction in pressure drag on the protrusions.

The overall analysis involved simplifying the bowl so it could be easily analysed without the need for a complex computational model. The minor details of the bowl were not

included in this analysis; their contribution has been assumed to be negligible compared to those analysed.

Chapter 6

Accelerating the Rotating Assembly

6.1 Introduction

Power is required to accelerate the rotating assembly to the operating speed during start-up. The main components of the rotating assembly are the bowl, end hubs, and scroll. The approximate times taken to fully accelerate and decelerate the rotating assembly of the GTech-Bellmor 1456 Centrifuge Decanter are 3 and 10 minutes, respectively. Windage and transmission losses draw power while the bowl is being accelerated. The transient phase of accelerating the bowl only lasts a short amount of time relative to continuous operation. The effect the mass of the rotating assembly has on the power consumption is investigated in this chapter.

6.2 Rotational Kinetic Energy

The rotational kinetic energy of an object rotating at constant speed is

$$E_K = \frac{1}{2} I \omega^2 \qquad 6.1$$

where

I moment of inertia (kg.m^2)

ω angular velocity (rad/s).

The complete bowl and cross-section are shown in Figure 6.1 and Figure 6.2 for a GTech-Bellmor 1456 Centrifuge Decanter. The bowl can be separated into two sections; the bowl and the end hubs. The individual sections are shown in Figure 6.3 and Figure 6.4. The scroll, shown in Figure 6.5, also adds a significant mass to the rotating assembly.

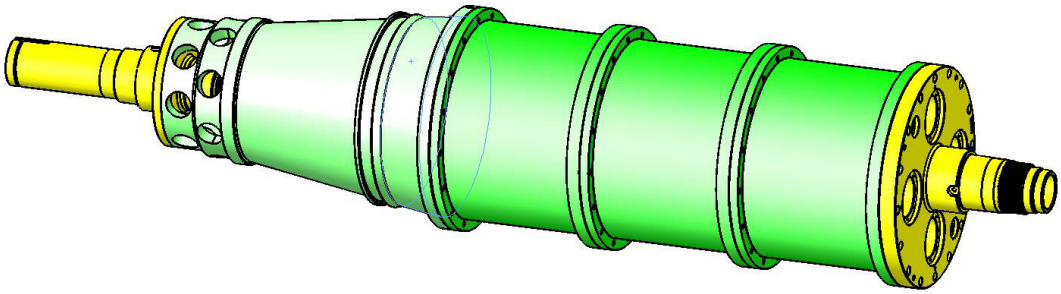

Figure 6.1 Complete bowl assembly

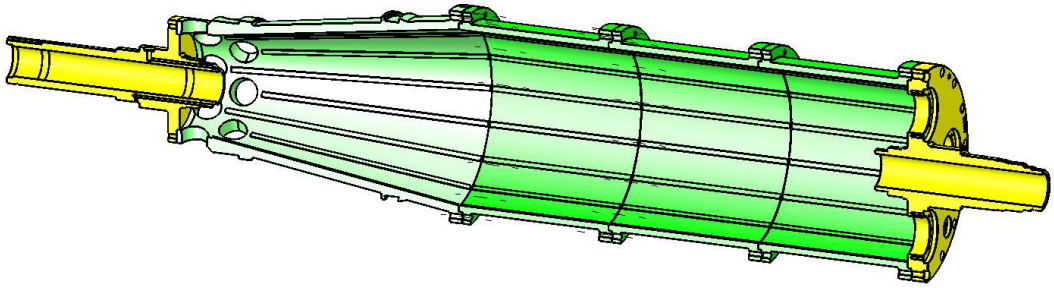

Figure 6.2 Cross-section of bowl assembly

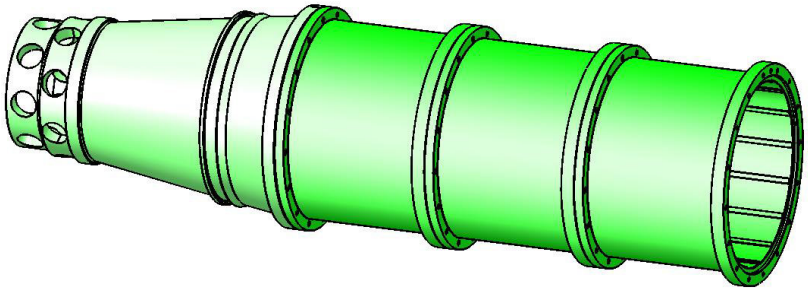

Figure 6.3 Bowl with no end hubs

Figure 6.4 Liquid and solids end hubs

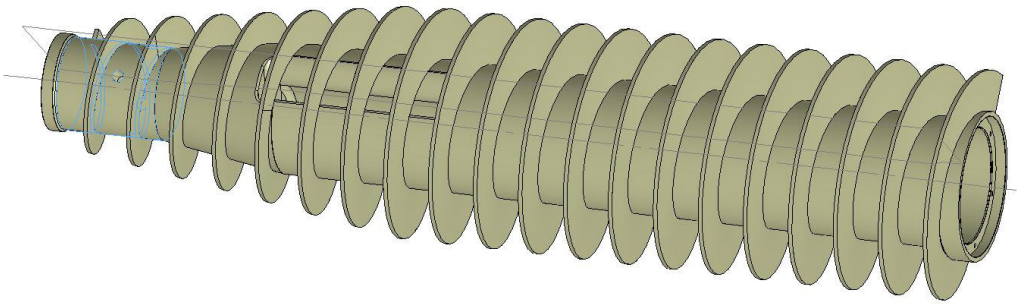

Figure 6.5 Scroll conveyor

The mass and inertia of the sections of the centrifuge are given in Table 6.1. These properties have been calculated using stainless steel as the material for the bowl, hubs, and scroll.

Table 6.1 Masses and inertias for the bowl, hubs, and scroll

Section	Mass (kg)	Inertia (kg.m^2)
Bowl and hubs	245.1	6.42
Bowl	183.8	5.60
Liquid and solid hubs	62.3	0.82
Scroll	251.3	2.07
Total	496.4	8.49

The energy required to accelerate the current rotating assembly to the working speed of 3250 rpm is shown in Table 6.2. Constant acceleration was assumed over the three minute run-up period. The calculation does not account for any other forms of power consumption during this period. The average power consumption is the additional rotational energy divided by the time taken to accelerate the assembly.

Table 6.2 Power required to accelerate the current rotating assembly to 3250 rpm

Section	Energy (kJ)	Power (kW)	Percent of total (%)
Bowl and hubs	371.6	2.06	75.5
Bowl	324.1	1.80	65.9
Liquid and solid hubs	47.6	0.26	9.6
Scroll	120.1	0.67	24.5
Total	491.7	2.73	100

Table 6.2 shows that the end hubs consume only a small amount to the rotational energy and this is due to their lower moment of inertia relative to the bowl. The bowl makes up the most significant portion of the inertia of the rotating assembly. While the scroll has a similar mass to the bowl its moment of inertia is significantly lower, therefore it contributes less.

Assuming that the bowl maintains the same geometry if the material is changed, the rotational kinetic energy for the new material is

$$E_{Knew} = \left(\frac{\rho_{new}}{\rho_{original}}\right) E_{Koriginal} \tag{6.2}$$

$$E_{Knew} = \left(\frac{\rho_{new}}{\rho_{original}}\right) \frac{1}{2} I_{original} \omega^2 \tag{6.3}$$

where

ρ_{new} density of new material (kg/m^3)

$I_{original}$ original moment of inertia of component/assembly (kg.m^2)

$\rho_{original}$ density of original material (kg/m^3).

The densities of various materials are given in Table 6.3 with their respective density ratios.

Table 6.3 Material densities

Material	Density (kg/m^3)	$\rho_{new}/\rho_{original}$
Mild steel	7850	0.981
316 stainless steel	8000	1
Aluminium – 2024-T6	2770	0.346
Titanium	4500	0.563
Nylon	1150	0.144
Polyethylene	900-950	0.116
Carbon fibre	2000	0.25

All of the materials listed above would reduce the power required to accelerate the bowl. Using a material such as aluminium would reduce the power required to accelerate the bowl by 65%. This saving would only be made while the bowl was being accelerated.

6.3 Conclusions

The power required to accelerate the bowl to the working speed is proportional to the mass of the assembly. The power is proportional to the angular velocity squared. When the centrifuge is run at a constant speed for long periods of time the power required to accelerate the rotating assembly is insignificant compared to the other losses. A lighter rotating assembly would reduce the loading on the main support bearings, this would slightly reduce the power consumed by the bearings. Other benefits of a lighter rotating assembly are reduced freight costs and improved ease of handling.

Chapter 7

Summary and Recommendations

7.1 Summary

There are four mechanisms that contribute to the power consumption in a decanter centrifuge, these are:

- Product transport $\dot{E}_P$
- Feed acceleration $\dot{E}_A$
- Power transmission $\dot{E}_T$
- Windage $\dot{E}_W$

The power consumed during product transport has two components, friction between the solids and the bowl and scroll, and the force required to lift the solids up the conical beach. Twice the amount of power required to lift the solids is recovered by the main drive motor, which is calculated using Equation 2.15. The product transport power for an infinitesimal slice of the product in the bowl is

$$\delta\dot{E}_P = \frac{\Delta r_{avx}(\sin\alpha + \mu_1\cos\alpha)\big((\sin\beta + \mu_3\cos\beta)\delta F_{cx} - \mu_2\delta F_{corx}\big)}{C} \tag{7.1}$$

where the partial centripetal force is

$$\partial F_{cx} = \frac{\rho_E}{\rho_S}\omega^2 r_{avx}\frac{2\pi\dot{m}_S}{\mathrm{G}\Delta}\partial x \tag{7.2}$$

and the partial Coriolis force is

$$\partial F_{corx} = -2\dot{m}_S\omega\tan\beta\,\partial x. \tag{7.3}$$

Feed acceleration power is comprised of two components, irreversible viscous losses during acceleration, and the loss of kinetic energy as the liquid and solids leave their respective discharge ports. The power consumed by feed acceleration is

$$\dot{E}_A = \left(\frac{1}{4}\omega^2(\dot{m}_S + \dot{m}_L + \dot{m}_{L2})(r_o^2 + r_{dL}^2)\right)_{Viscous} + \left(\frac{1}{2}\omega^2(\dot{m}_S r_{dS}^2 + \dot{m}_L r_{dL}^2) + \dot{m}_{L2} r_{dL2}^2\right)_{Kinetic}. \quad 7.4$$

Power transmission losses occur in the motors, belt drives, gearbox, bearings, and seals. These losses are typically a fixed proportion of the power being transmitted. The efficiency of each component varies with load. The power transmission losses were calculated using manufacturers data. The greatest transmission losses occur in the motors and the belt drives.

Windage is a function of speed and consists of the surface friction drag on the bowl and the pressure drag on components that protrude into the flow. Windage was calculated using empirical and computational models. The windage losses are small relative to the other components of power consumption.

7.2 Case Study

The power consumption was estimated for a GTech-Bellmor 1456 Centrifuge Decanter using the methods developed in Part I. Indicative values for the power consumption are given in Table 7.1. The transport power would normally be larger than the transmission losses, this would be true if a higher weight percentage of PVC was used.

Table 7.1 Estimated power consumption for a GTech-Bellmor 1456 Centrifuge Decanter processing 12 t/h of a 10%wt suspension of PVC and water

	Power (kW)
Product transport	3.56
Lifting recovery	-0.6
Feed acceleration	8.35
Transmission losses (@50%)	5.0
Windage	0.92
Total	17.40

The product transport consisted of 0.19 kW of lifting power and 3.37 kW of frictional losses. The acceleration power consisted of 4.81 kW of viscous losses and 3.54 kW of kinetic energy loss. The kinetic energy losses consist of 0.3 kW and 3.24 kW from the

discharging solids and liquid, respectively. The largest power transmission losses occur in the electric motors and belt drives. Other losses included those in the back-drive gearbox, bearings, and seals. The surface drag on the bowl and gearbox contributed 0.5 kW to the windage losses, and drag on the third phase ports and bolt heads contributed 0.45 kW.

7.3 Recommendations

Recommendations for improving a decanter centrifuge and their corresponding effects are presented in Table 7.2. Primary consideration should be given to the product output requirements when changing any parameters.

Table 7.2 Summary of recommendations and their corresponding effects

Recommendation	Effect
Reduce the coefficient of friction between the solids and the scroll faces	Reduced product transport power.
Reduce the coefficient of friction between the solids and the bowl wall in the axial direction	Reduced product transport power.
Increase the coefficient of friction between the solids and the bowl wall in the circumferential direction by the addition of axial ribs or corrugations	The circumferential coefficient of friction at the bowl wall must be greater than that between the solids and the scroll to stop the solids from rotating with the scroll. Increasing the circumferential coefficient of friction will promote axial transport of the solids.
Maximise the pool depth without reducing solids dryness	The product transport power would decrease due to the shortening of the conical beach. This would reduce the viscous losses during acceleration, and the kinetic energy lost by the discharging liquid phase. The pool depth should only be increased if the dryness of the discharging solids remains satisfactory.
Make the scroll blades perpendicular to the bowl wall	The scroll blades would no longer force the solids against that bowl wall and would therefore reduce the transport power.
Maximise the scroll pitch	The cake thickness and hence normal force on the bowl wall would reduce, resulting in a decrease in the product transport power. This should be carried out tentatively, as increasing the pitch increases the circumferential force on the solids, which can result in the solids rotating with the scroll.
Redirect the flow of the liquid as it is discharged	A portion of the kinetic energy lost by the discharging liquid phase would be recaptured, resulting in lower acceleration power.
Redesign the feed accelerator to maximize the acceleration efficiency	Maximising the acceleration efficiency would improve the performance of the machine by increasing the effective settling area of the cylindrical section. Other beneficial effects of a

	good accelerator are: increased throughput, increased solids recovery, higher centrate clarity, and reduced wear.
Ensure the power transmission components are correctly selected	The power transmission losses will be minimised given the components are correctly selected.
Reduce the mass of the rotating assembly	Reduced bearing loads, ease of handling during manufacturing and assembly, and reduced freight costs.
Recess the bolt heads and cover the third phase ports	Not only will this reduce the power consumption, it would potentially reduce the aero-acoustic sound generation.
Implement control of the bowl and differential speed, and pool depth	This would allow for optimisation of these variables, resulting improved product quality and/or minimisation of power consumption.
Minimise the bowl speed	Operating the machine at an excessively high speed is wasteful if the desired product quality can be achieved at a lower speed. The transport and acceleration power are proportional to the bowl speed squared. The windage is proportional to the bowl speed to the power of approximately three. A small decrease in the bowl speed can result in a large decrease in power consumption. This could also result in reduced wear on the bowl and scroll.

7.4 Conclusions

The power consumed within a decanter centrifuge has been comprehensively evaluated. A model for the product transport was created and a relationship for the feed acceleration power was derived. The transmission and windage losses were investigated. A list of recommendations for improving the performance of decanter centrifuges was presented. The findings from this work are useful to designers and operators of decanter centrifuges.

In the subsequent parts of the thesis two paths are taken to advance and improve the decanter centrifuge: a light-weight composite bowl is designed and manufactured, and the feed accelerator is investigated further.

A composite bowl provides several potential benefits, including:

- Weight reduction: lower bearing loads, reduced freight cost, and improved handling.
- Improved wear and friction characteristics.

- Removal of external protrusions resulting in reduced windage and aero-acoustic emissions.
- Manufacturing cost reduction.

Improved feed acceleration can result in increased product throughput, centrate clarity, or solids recovery. These benefits are achieved by reducing pool disturbance and increasing the tangential speed of the pool, which increases the effective settling area.

Part II

Wear Analysis of a Decanter Centrifuge and Development of a Composite Bowl

Part II begins with a chapter investigating the wear on several components from used decanter centrifuges. The second chapter contains the development and use of a wear testing apparatus that was designed to recreate the conditions within the centrifuge. The results from the wear testing are compared to results generated using a pin-on-disk wear test rig. The final chapter in this part focuses on the development of a new composite bowl for the GTech-Bellmor 1456 Centrifuge Decanter. The design process is presented, including design specifications, conceptual design, material testing, small-scale model preparation and testing, and full size design and manufacturing. The outcomes of this part are a better understanding of wear in a decanter centrifuge, wear testing results, a novel manufacturing method for a composite bowl, and a prototype full size composite bowl.

Chapter 8

Wear Analysis of a Decanter Centrifuge

8.1 Introduction

The environment within a decanter centrifuge is extremely harsh due to the abrasive nature of the product and the high centripetal force necessary for separation. The combination of high pressure and relative motion between the solids and the machine components is a formula for high wear. Leung [13] states that the wear is proportional to the product of the g-force and differential speed. Excessive wear can cause a decanter centrifuge to run inefficiently or require premature maintenance, leading to prolonged plant down-time and lower product throughput. Neither the high pressure nor relative motion can be removed; therefore methods must be employed to reduce wear. Methods of protecting against wear can be expensive so a balance must be made between anti-wear mechanisms and cost. Knowing the location and mechanisms of wear in a decanter centrifuge can assist in the design of more wear resistant features, which will consequently increase component life.

The GTech-Bellmor 1456 Centrifuge Decanter can operate with a bowl speed of up to 4000 rpm and acceleration levels reaching 3,200 times gravity. One method of increasing the durability of a decanter centrifuge, currently used by Bellmor Engineering Ltd., is to fit wear resistant tiles to the scroll blade tips and the exit ports. These tiles are costly and time consuming to install. The bowl can be completely lined with these tiles in machines that process highly abrasive materials. Another method commonly used to improve wear resistance is to apply hard-facing to the areas of the machine prone to high wear.

This chapter presents a study of the wear in several used decanter centrifuges. The components were from several machines that had been operating in a plant processing meat by-products. The wear on the inner surface of the bowl, scroll, feed accelerator, and discharge ports was analysed.

8.2 Worn Component Analysis

All components that are in contact with the product experience some form of wear; this analysis is limited to those areas that experience high wear, these include the inner surface of the bowl, scroll, feed accelerator, and discharge ports.

8.2.1 Inner bowl surface

There are three parts of the inner surface of the bowl that experience high wear; these are the conical beach, axial guide vanes, and feed zone.

The conical beach is worn by product transport. The normal force acting on the bowl wall increases as the solids are lifted out of the liquid pool due to a reduction in buoyancy. Figure 8.1 shows the wear in the conical section from a centrifuge used in a meat by-products processing plant; the surface has become polished on the dry beach and circumferential grooves have been cut into the bowl surface. The circumferential grooves suggest that the solids were rotating with the scroll or that solids have jammed between the scroll tip and bowl. If the solids are able to simply rotate with the scroll product transport will fail, causing separation to be severely hindered. Excessive wear can also change the profile of the bowl wall, increasing the gap between the scroll and the wall, allowing solids to move back down the conical section. On a few rare occasions the wear in the conical section was so severe that it cut through the wall, destroying the bowl; this was most likely the result of inadequate monitoring and maintenance.

Figure 8.1 Photo of worn conical section showing polishing of the conical section and circumferential grooves

Guide vanes or ribs are installed to promote axial movement of the solids. These vanes can experience significant wear in the conical section as shown in Figure 8.2. As they wear, the likelihood of the solids rotating with the scroll is increased, potentially stopping or severely reducing solids transport.

Figure 8.2 Worn axial rib within the conical section

Wear had occurred on the bowl wall adjacent to the feed accelerator; this implies that the incoming feed has disturbed the rotating pool and settled solids. The design of the feed accelerator could be reviewed to address this.

There was insignificant wear on the bowl at the liquid discharge end of the cylindrical section. The friction force is alleviated by buoyancy in the cylindrical section and the coefficient of friction is typically lower for fully saturated solids [9].

8.2.2 Scroll

The scroll experiences wear due to the relative motion between the scroll and the settled solids. Wear also occurs on the scroll adjacent to the feed accelerator. Figure 8.3 shows a worn scroll that was returned for refurbishment. Machines have reportedly been returned for servicing with as much as 20 mm of wear on the tips of the scroll; this would have severely reduced the performance of the machine. The product transport degrades as the clearance between the scroll and bowl increases. Wear resistant tiles are added to the tips of the scroll on some machines to reduce wear. These are expensive and time consuming to install; however, they have proven to reduce the wear.

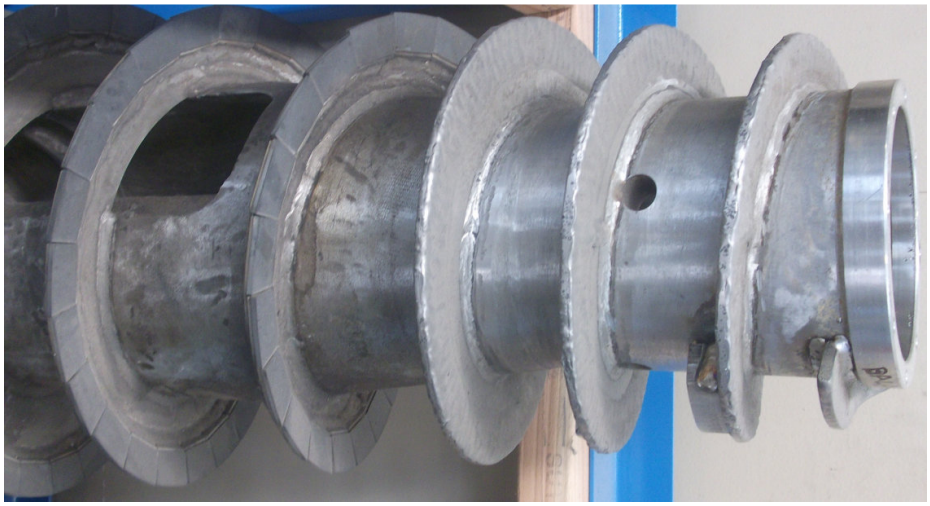

Figure 8.3 Worn scroll conveyor

8.2.3 Feed accelerator

As all feed passes through the accelerator there is a noteworthy amount of wear; this is shown in Figure 8.3. The current design does not have any concentrated feed streams that could cause localised wear. A concentrated incoming feed will eventually lead to erosion in that area. The incoming feed also wears the scroll as it passes over and around it to reach the rotating pool.

8.2.4 Discharge ports

The solids discharge ports are susceptible to high wear because the solids that are passed through them are at their driest. In some applications the ports are fitted with a ceramic bush to aid with wear resistance. The wear on the solids discharge ports is shown in Figure 8.4. In some instances the wear has transformed circular ports into ovals.

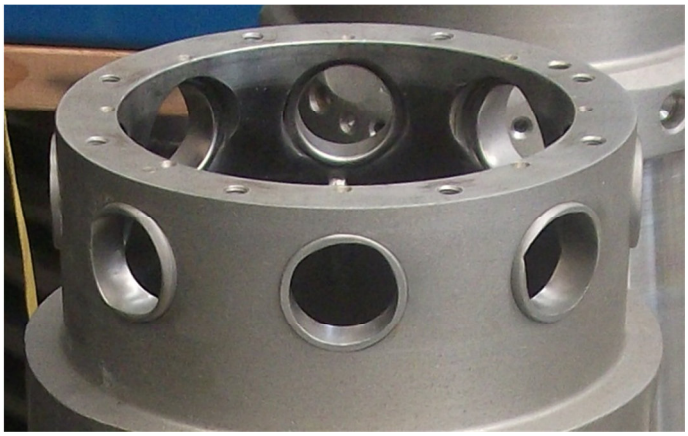

Figure 8.4 Worn solids discharge ports

8.3 Conclusions

Due to the harsh environment within the bowl significant wear was evident in several areas. The solids transport can fail when the wear reaches critical levels. The areas of high wear are the conical section, scroll, guide vanes, feed accelerator, and the solids discharge ports. Measures have already been taken to reduce wear by the addition of wear resistant tiles, which has proven to be successful but expensive to implement. Redesigning the feed accelerator to reduce disturbance to the pool by incoming feed could potentially reduce wear. Reducing the g-force or differential speed reduces wear [13]. Wear arises from flow impinging on a surface, dry solids moving over a surface, and flow concentrations. This knowledge can be used by designers to avoid developing machines that are prone to wear.

Chapter 9

Hydrodynamic Wear Testing

9.1 Introduction

This chapter deals with the development of a test apparatus for quantifying the wear characteristics of various materials. The apparatus allows wear testing in conditions similar to those present in a decanter centrifuge. In situ measurement of material wear is not practical and therefore a test apparatus that simulates the conditions in the centrifuge was required. If the bowl and scroll material were changed the new material must have equal or better performance than the current wear and friction properties of 316 stainless steel.

The objectives of this investigation were to:

- Design a testing apparatus that can quantitatively measure the wear rates and coefficients of friction for various materials in conditions similar to those inside the bowl of a decanter centrifuge
- Test several materials and compare the results to those measured with a pin-on-disk test rig

9.2 Test Apparatus

9.2.1 Specifications

The test rig design was to meet the following specifications:

- Measure the wear rate between two materials moving relative to each other
- Measure the coefficient of friction between two materials separated by various fluid films
- Operate unsupervised
- Continuously record data
- Allow samples to be inspected and changed easily

The conditions that were to be simulated within the GTech-Bellmor 1456 Centrifuge Decanter were determined. These variables were the interface pressure and the relative speed between the components and moving solids. The most crucial property to simulate

was the contact pressure between the fluid and the inner surface of the bowl. The hydrostatic pressure acting on the bowl wall is given by

$$P_r = \frac{\rho\omega^2}{2}(r_o^2 - r_i^2) \qquad 9.1$$

where

ρ density (kg/m^3)

ω bowl speed (rad/s)

r_o outer radius of fluid pool (m)

r_i inner radius of fluid pool (m).

The pressure acting on the bowl wall in the cylindrical section was calculated to be 1.4 MPa for an outer radius of 176.6 mm, inner radius of 98 mm, density of 1100 kg/m^3, and rotation speed of 3250 rpm. While this is the hydrostatic pressure, it is not necessarily the pressure on the bowl wall created by the solids due to buoyancy. However, the buoyancy effect is not present in the conical section where wear predominantly occurs. The axial scrolling speed can be varied between 2 and 52 mm/s in the GTech-Bellmor 1456 Centrifuge Decanter with a 70 mm scroll pitch.

A means of quantitatively measuring the wear rate and coefficient of friction between two materials separated by an abrasive fluid film was required. The test apparatus described in the following section was selected because the contact pressure between the materials could be easily regulated, and it was considered to sufficiently simulate the high pressure acting on the bowl wall.

9.2.2 Test apparatus

The final design was developed after several iterations of an initial concept. The test rig consisted of an electric motor driving a wheel at a constant speed; while a pneumatic actuator holds a block of material against the rotating wheel with a constant force. A film was produced between the block and the wheel by pumping process fluid at high pressure through the centre of the sample. To calculate the coefficient of friction, the speed and power of the motor driving the wheel were monitored. The wear rate was calculated by continuously measuring the change in length of the sample block. The individual components of the rig were manufactured by Bellmor Engineering Ltd. The rig was assembled and commissioned in the Automotive Lab in the Department of

Mechanical Engineering, University of Canterbury. The assembled test rig is shown in Figure 9.1, cross-sections are shown in Figure 9.2 and Figure 9.3.

Figure 9.1 Assembled wear test rig

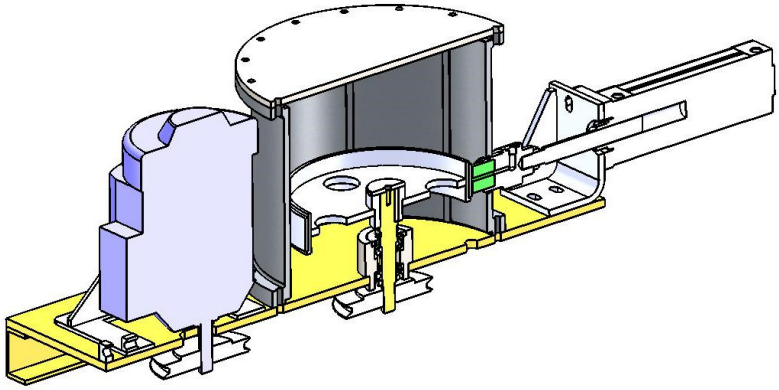

Figure 9.2 Wear test rig cross-section I

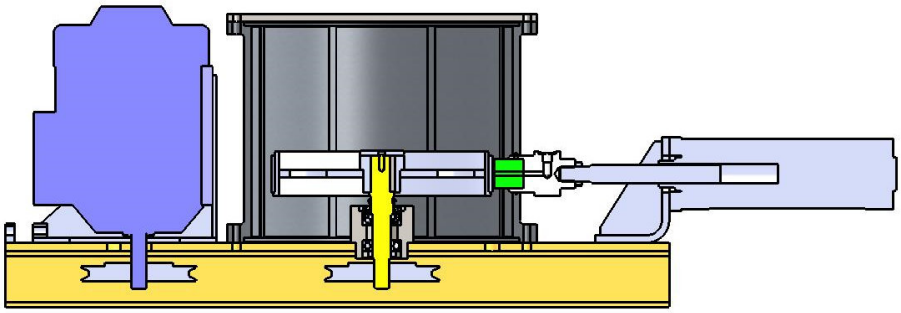

Figure 9.3 Wear test rig cross-section II

9.2.3 Componentry

The design required several bearings, seals, belts, pulleys, and various other components. These were selected from supplier catalogues and are listed in Table 9.1.

Table 9.1 Components used in the wear test rig

Belt drive	
Ratio	2:1
Hub diameter	125 mm – 250 mm
Centre distance	330 – 355 mm
Belt type	SPA V-belt
Belt thickness	10 mm
Belt efficiency	<98%
Bearings	
Upper bearing	SKF – Angular contact ball bearing 7205 BECBM 25x52x15 mm
Lower bearing	SKF – Deep grove ball bearing 6205 25x52x15 mm
Retaining nut	FAG KM5– Retaining nut M25 thread
Seals	
Radial shaft seal	SKF – CR 30X62X7 HMS5 RG
V – ring seal	SKF – CR 400305
O – ring	SKF - 50x3 mm

The pneumatic cylinder needed to apply a constant force of up to 1.75 kN on the sample, which is equal to a contact pressure of 1.4 MPa. A double-acting pneumatic cylinder with an 80 mm bore and 160 mm stroke was used, which could apply a force of up to 4 kN. The pressure was controlled using a digital pressure regulator.

The pump needed to provide sufficient flow Q and pressure to maintain a film between the sample and the wheel. Using a 40 mm diameter sample and assuming a film thickness of 0.25 mm is evenly spread across the diameter of the sample, the minimum required flow rate was

$$Q = Av = 0.04 \times 0.00025 \times 1.715 = 1.715 \times 10^{-5} \text{ m}^3/\text{s} \qquad 9.2$$

where

A interface area (m^2)

v relative velocity between sample and wheel (m/s).

The required pressure is the same as the contact pressure, plus any addition transport losses. All hydraulic components were purchased from Hyspecs. The hydraulic components included:

- Hyspecs heated oil tank (45 l)
- 5.5 kW Hengshui motor (B35 Mount)
- CAT390 Pump
- Suction line valve
- Bellhousing mount

A positive displacement piston pump with ceramic cylinder liners was used because of the abrasive nature of the process fluid. The reservoir included an electric element for temperature control of the process fluid. The selected pump could supply up to 45 litres per minute at 4 MPa.

The wheel drive motor needed to run at a constant speed and torque for extended periods. A 2.2 kW three-phase electric motor was available for use.

9.2.4 Control and data collection

Budinski [51] emphasised the necessity to record and document all test parameters when reporting wear and friction measurements. The variables that needed to be measured were:

- Drive motor speed (wheel speed)
- Drive motor power consumption
- Pneumatic cylinder pressure
- Cylinder displacement
- Fluid pressure
- Fluid temperature.

The control system for the rig was developed in LabView. The front panel is shown in Figure 9.4. The air pressure, cylinder direction, and fluid temperature were controlled from the front panel. The fluid pump and drive motor were control by two VSDs.

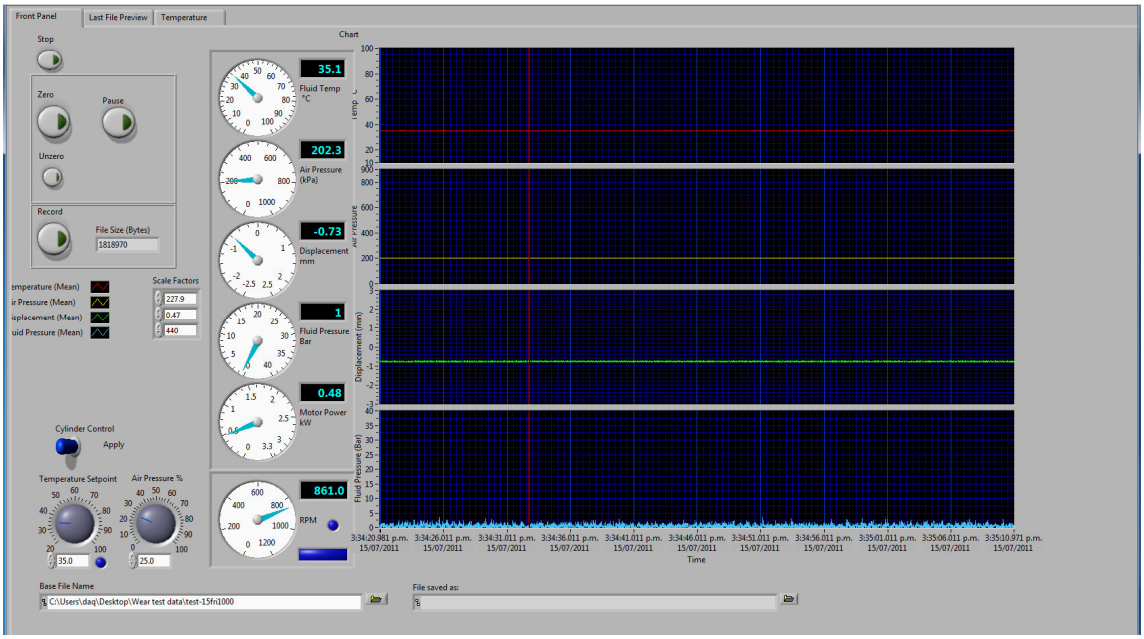

Figure 9.4 Front panel of LabView program

The measured variables and means of measurement are shown in Table 9.2. The pressure and displacement transducers are shown in Figure 9.5.

Table 9.2 Measured parameters and measurement devices

Sample displacement	LV displacement transducer
Fluid pressure	GEM pressure transducer
Air pressure	SMC E/P Regulator
Fluid temperature	J-Type thermocouple
Rotation speed	Laser counter
Motor speed	PDL motor driver

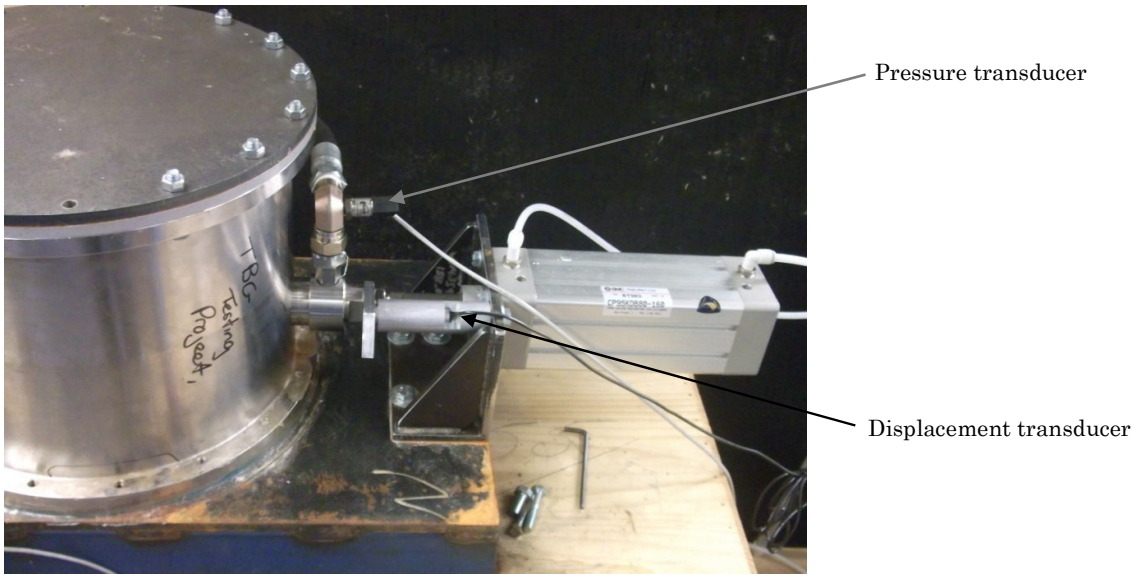

Figure 9.5 Photograph of the test rig showing the displacement and pressure transducers

9.2.5 Testing fluid

The abrasive fluid used for the experiment was a PVC-water mixture. The mixture was approximately 5% PVC by weight. An air line was fed into the reservoir that agitated the mixture to maintain the suspension of the PVC particles. The temperature of the tank was set to 35°C for all tests. A 390 CAT piston pump with a 5.5 kW motor was used to pump the abrasive solution. The pump was specially fitted with ceramic bores to minimise wear. The pump, motor, and reservoir are shown in Figure 9.6.

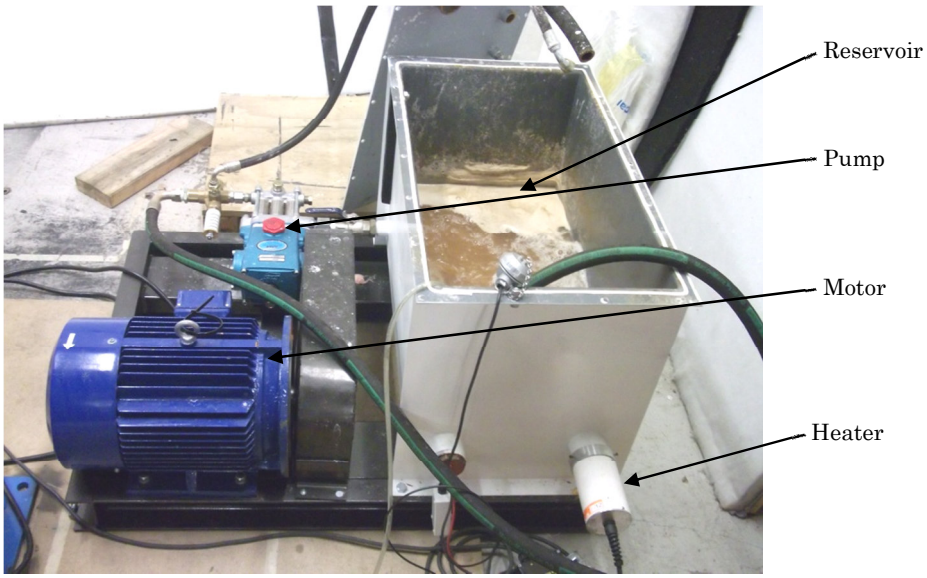

Figure 9.6 Pump, motor, and reservoir unit for wear test rig

9.2.6 Issues

To ensure repeatable and reliable results the wear rig needed to be run for extended periods of time without interruption. Several issues were encountered during commissioning that required remedial action. These issues were: current limiting of the drive motor, surface finishing and concentricity of the wheel, and bearing failure.

There was a significantly high current drawn by the drive motor as it was being run at a relatively low speed with a relatively higher torque. The motor driver had a built in function that would stop the motor after a set period of time if the current being drawn was too high. To alleviate this issue a new belt drive with a 2:1 reduction ratio was installed. This gave a greater torque range from the motor and reduced the current requirement.

The concentricity of the wheel had a large effect on the quality of the data as the displacement of the sample was being measured. The concentricity and surface finish of the wheel were initially too poor to allow for reliable displacement data. The surface of the wheel was machined to reduce the concentricity from 0.2 mm to 0.01 mm.

There were several bearing failures during testing. These were attributed to contamination, assembly errors, and excessive vibrations due to the wheel not initially being concentric. Once the concentricity of the wheel was corrected and the seals were fitted correctly, the bearings ran without failure.

9.2.7 Procedure

The testing procedure was the same for each material. The clean sample was placed in the sample holder and fixed in place with a locking screw. The sample was forced against the stationary wheel and released. At this point the displacement, fluid pressure, air pressure, motor power, and wheel rpm were all set to zero. The sample was retracted from the wheel. The pump and wheel were then started. The ‘no contact’ power consumption was recorded at this point. Once the speed and pressure had settled the sample was brought into contact with the wheel. The air pressure was increased to the operating pressure. Recording was started when the displacement settled. The test was left to run for several hours. When the sample was sufficiently worn recording was ceased and the sample retracted from the wheel. The sample was removed and cleaned before testing was repeated.

The wear rig was used to test the wear and friction properties of ultra-high molecular weight polyethylene (UHMWPE), acetal, and 316 stainless steel. The testing parameters are shown in Table 9.3.

Table 9.3 Wear test rig operating parameters

Interface pressure	1 MPa
Wheel speed	440 rpm
Fluid temperature	35°C
Fluid flow rate	2.6-3.3 l/min
Approximate film thickness	0.2 mm

9.3 Post-processing and data analysis

Once data had been collected for several samples of each material it needed to be post-processed to calculate the wear rate and coefficient of friction. The calculation procedure for the wear rate and coefficient of friction are presented in turn. An example of how the data was processed is presented.

The wear rate of the sample is the rate of change of displacement. This was monitored by the linear displacement transducer.

The coefficient of friction μ was calculated using the following procedure. The efficiency of the electric motor was not available and was not included in the calculation procedure, this will likely result in an over prediction of the coefficient of friction. The motor power $W_{NCstart}$ was recorded while the sample was not in contact with the wheel. The sample was brought into contact with wheel and the air pressure P_{Air} was recorded. The rotation speed of wheel N_{Wheel} and motor power W_C were recorded during the test when the sample was in contact with the wheel. The force applied by the cylinder was then calculated using

$$F_{Cylinder} = P_{Air}\frac{D_{Piston}^2}{4} \qquad 9.3$$

where

D_{Piston} diameter of pneumatic cylinder (m).

The torque applied to the wheel is equal to

$$T_{Wheel} = \mu F_{Cylinder} r_{Wheel} \quad 9.4$$

where

r_{wheel} radius of the wheel (m).

At the end of the test the sample was retracted from the rotating wheel and the motor power $W_{NCFinish}$ was recored. The two power measurements taken while the sample was not in contact with the wheel were averaged to give the no-contact power W_{NC}. The power consumed by friction W_F is the contact power minus the no-contact power. The coefficient of friction can then be calculated from

$$\mu = \frac{W_F}{F_{Cylinder} r_{Wheel} N_{Wheel}}. \quad 9.5$$

The raw data for run U-7-29-930 of UHMWPE is shown in Figure 9.7. The displacement, temperature, motor power, air pressure, and wheel speed are shown as a function of time.

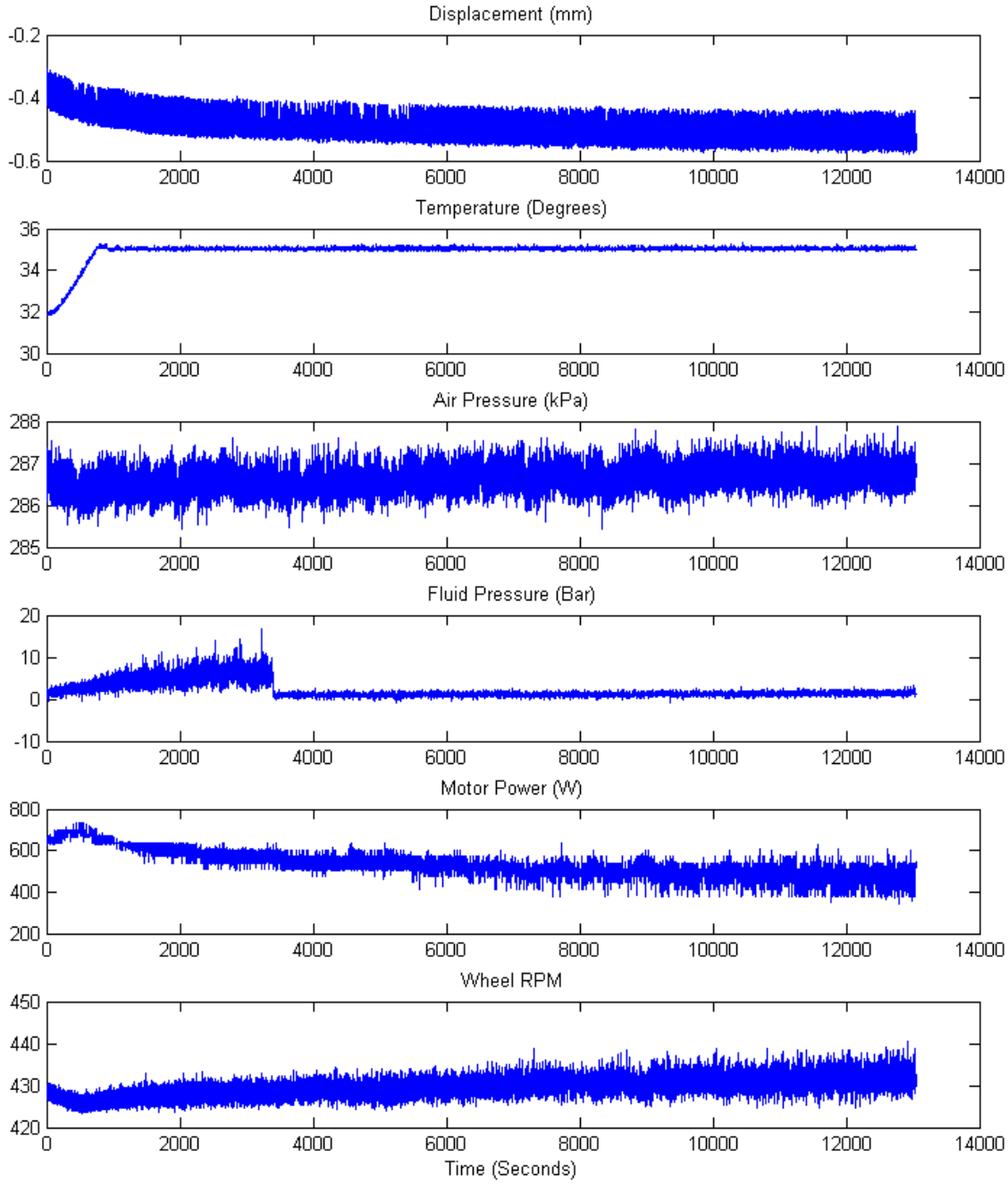

Figure 9.7 Raw wear testing data for test run U-7-29-930

The displacement of the sample block is unsteady due to either the lack of concentricity or the eccentricity of the wheel. The displacement was analysed using a moving average to account for the aforementioned unsteadiness. The moving average only covered enough steps to smooth the displacement without destroying the data. The moving average of the displacement data from run U-7-29-930 is displayed in Figure 9.8.

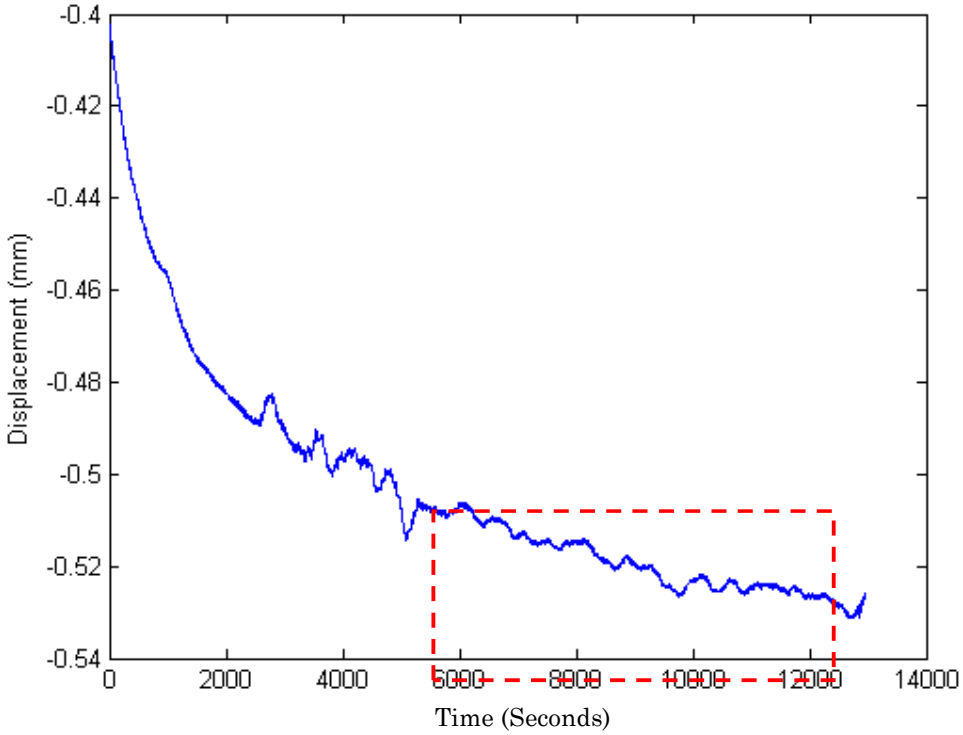

Figure 9.8 Averaged displacement for test run U-7-29-930

The wear rate is defined as the rate of change of the length of the sample. The units are meters per second. The wear rate was calculated by fitting a straight line to the smoothed section of the displacement data. The correlation coefficient was also calculated. A smoothed segment of the data from Figure 9.8 is shown in Figure 9.9. A linear line is fitted to the data; the gradient of the line is the wear rate, in this case it is 0.003 μm/s with a correlation coefficient of 0.93.

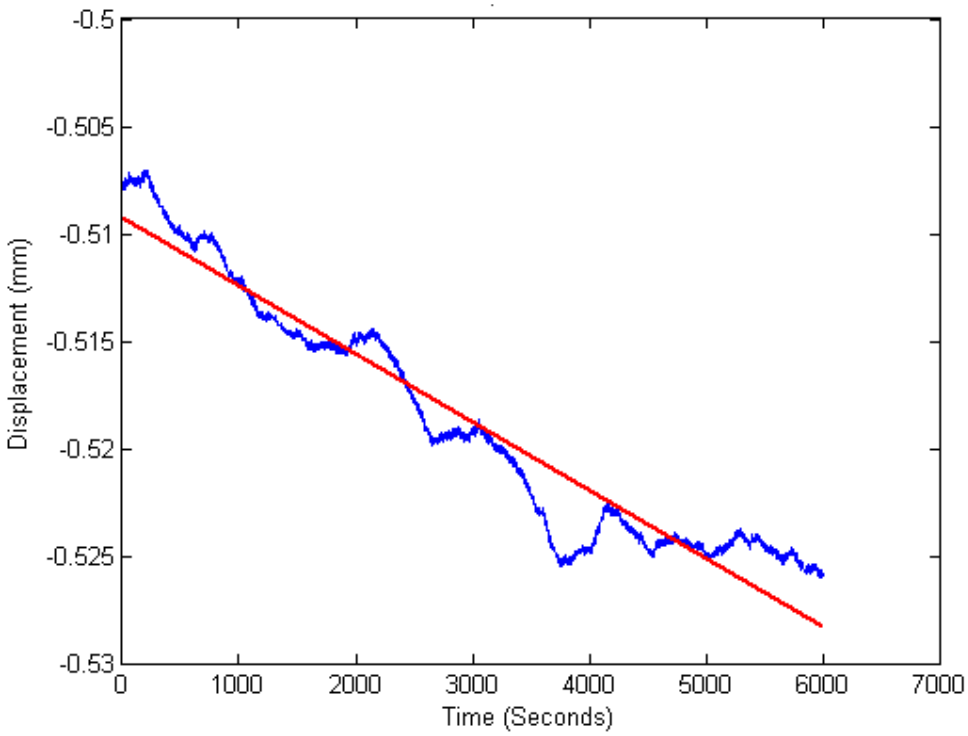

Figure 9.9 Partial averaged displacement data for test run U-7-29-930

9.4 Results and Discussion

The individual test results for UHMWPE, acetal, and 316 stainless steel are shown in Table 9.4, Table 9.5, and Table 9.6, respectively. The tables contain the test name, data recording range, wear rate, R^2 confidence value, and the coefficient of friction μ. The wear rate is given in micrometers per second.

Table 9.4 Test results for UHMWPE

Test name	Data range	Wear rate (μm/s)	R^2	μ
U-7-27-1415	1660-3000	0.028	0.968	0.257
U-7-27-1620	660-2100	0.023	0.963	0.262
U-7-28-935	2800-3400	0.023	0.985	0.196
U-7-28-935	3800-4400	0.019	0.982	0.186
U-7-28-1400	3500-6500	0.0058	0.925	0.163
U-7-28-1400	1000-6500	0.0102	0.944	0.178
U-7-29-930	3000-12900	0.0037	0.931	0.152
U-7-29-1300	800-3500	0.0024	0.973	0.122
U-8-2-930	500-1500	0.022	0.996	0.117
U-8-22-1810	1000-3100	0.041	0.912	0.134
U-8-1-1020	1000-12000	0.0066	0.934	0.078
U-7-6-1030	13200-15900	0.0125	0.987	0.188

Table 9.5 Test results for acetal

Test name	Data range	Wear rate (μm/s)	R^2	μ
A-8-26-1201	1150-1650	0.113	0.977	0.131
A-8-25-910	1800-4000	0.124	0.985	0.163
A-8-29-1540	1-1000	0.424	0.983	0.35
A-8-29-1720	50-460	0.189	0.947	0.358
A-8-30-1011	2400-2800	0.296	0.96	0.304

Due to high friction, a contact pressure of 1 MPa could not be obtained while testing stainless steel. Using a linear relationship between wear and force [13], the wear rate was extrapolated to 1 MPa.

Table 9.6 Test results for 316 stainless steel

Test name	Data range	Wear rate μm/s	R^2	Pressure kPa	Adjusted wear rate μm/s	μ
S-9-1-1020	100-280	0.155	0.992	459	0.338	0.504
S-9-1-1115	40-385	0.14	0.98	384	0.365	0.519
S-9-2-1430	100-400	0.105	0.868	460	0.228	0.445
S-9-2-1530	450-600	-	-	277		0.465

The average wear rates are shown in Table 9.7. A box and whisker plot of the wear rates is shown in Figure 9.10. UHMWPE wore almost 20 times slower than 316 stainless steel. The standard deviation for both UHMWPE and acetal are large, this may suggest that the wear measurements are on the limits of the capability of the test rig.

Table 9.7 Average wear rate and standard deviation

Material	UHMWPE	Acetal	316 Stainless Steel
Average wear rate (μm/s)	0.016	0.229	0.310
Standard deviation	0.011	0.131	0.072

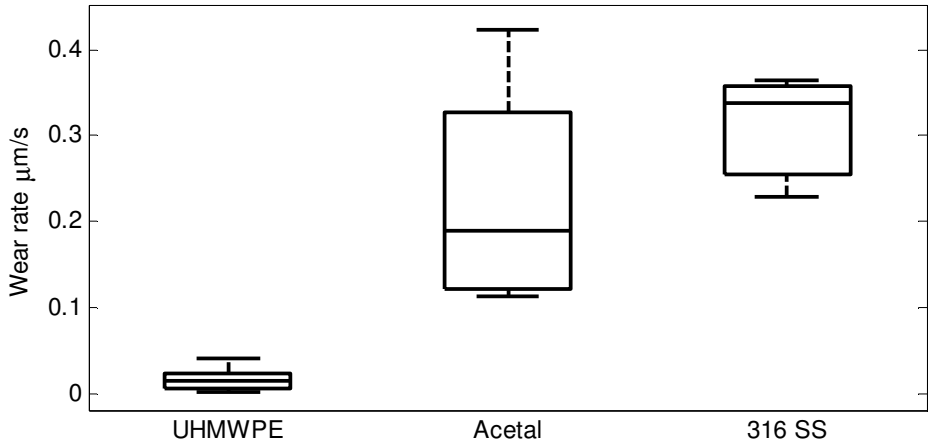

Figure 9.10 Wear rates of materials forced against a rotating stainless steel wheel and lubricated by an abrasive PVC water mixture

The average coefficients of friction are shown in Table 9.8. A box and whisker plot of the coefficients of friction is shown in Figure 9.11. The coefficient of friction of UHMWPE is almost one third of that of 316 stainless steel. The standard deviation for both UHMWPE and acetal is high, which indicates that the friction measurement may be on the limits of the capability of the test rig.

Table 9.8 Average coefficient of friction and standard deviation

Material	UHMWPE	Acetal	316 Stainless Steel
Coefficient of friction	0.169	0.261	0.483
Standard deviation	0.054	0.107	0.034

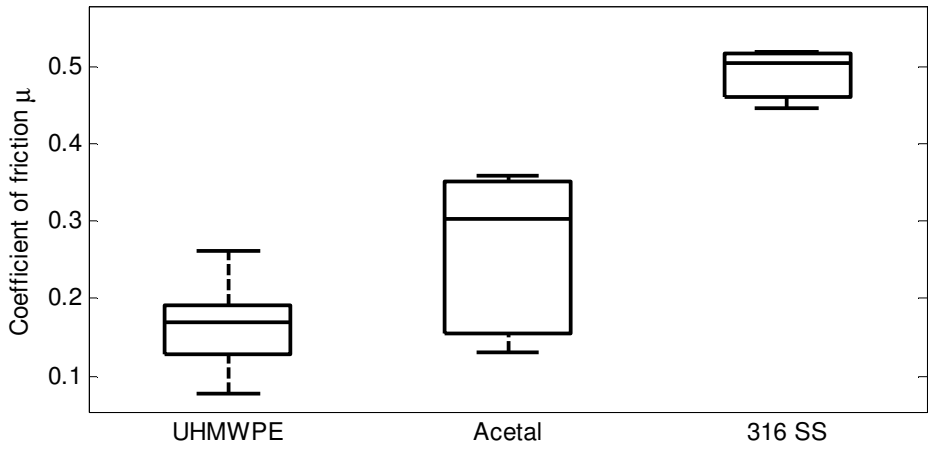

Figure 9.11 Coefficient of friction between sample material and a stainless steel wheel lubricated by an abrasive PVC-water mixture

9.4.1 Comparison to pin-on-disk

Pin-on-disk wear testing of the same materials was completed at the University of Canterbury by a visiting research assistant to compare the results against those of the hydrodynamic wear test rig [52]. An existing pin-on-disk wear rig was refurbished to meet ASTM G99-05. The test consisted of a cast-iron disk rotating at 240 rpm with a 5 mm diameter pin of the sample material pressed against the disk with a 50 N force. The sample was weighed, tested for two hours, and then weighed again. The mass loss was then converted to rate of change of volume so it could be compared to the hydrodynamic wear test results.

Only preliminary results were generated during the course of this work, therefore they are only a starting point for comparison. Figure 9.12 contains a box and whisker plot of the results, the relative wear rates can be clearly observed. The average wear rates are shown in Table 9.9.

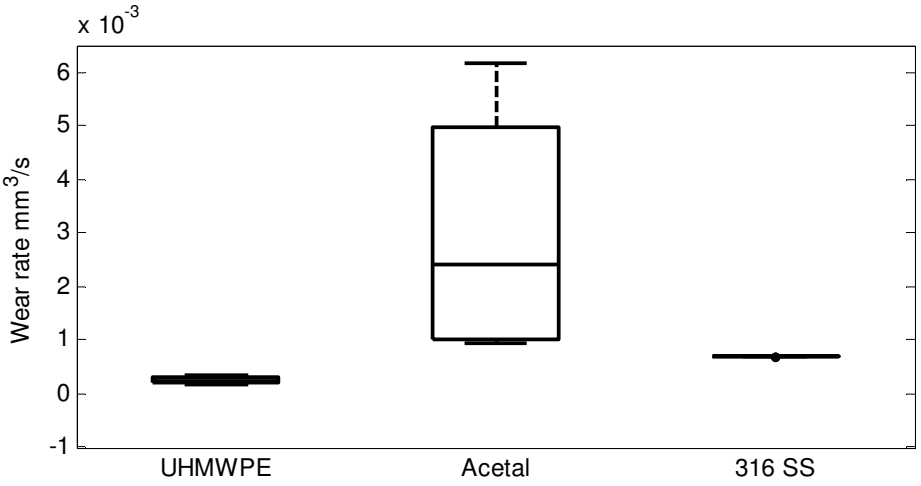

Figure 9.12 Wear rates for UHMWPE, acetal, and 316 stainless steel when tested to ASTM G99-05 in a pin-on-disk wear test rig

Table 9.9 Number of tests conducted and average wear rates for materials test using the pin-on-disk wear test rig

Material	Number of tests	Wear rate (mm^3/s)
UHMWPE	5	2.4×10^{-4}
Acetal	4	30×10^{-4}
316 stainless steel	1	6.8×10^{-4}

Little can be concluded from this experiment as only a limited amount of data was generated. There was agreement between the two testing methods that UHMWPE has a much lower wear rate. Little could be concluded about the wear rate of stainless steel as only one test was conducted. Future development of this test rig would potentially provide more reliable results. This would be preferable to the hydrodynamic wear test rig as it is simpler and easier to set up.

9.5 Conclusion

The results from the hydrodynamic wear testing showed that 316 stainless steel wears as much as 20 times faster than UHMWPE. Acetal wears faster than UHMWPE but there is little difference between acetal and 316 stainless steel. The coefficient of friction of 316 stainless steel was three times as high as UHMWPE and almost twice as high as acetal. The scatter of the wear rates and coefficients of friction were large, suggesting a considerable number of tests are required to confidently establish wear rates.

The comparison between the pin-on-disk and hydrodynamic wear tests confirmed that UHMWPE has better wear resistance than acetal. No other comparisons could be made between the tests due to the limited amount of data available. The pin-on-disk wear test, if developed further, would allow a quick and inexpensive comparison between materials.

Chapter 10

Development of a Composite Bowl for a Decanter Centrifuge

10.1 Introduction

The original design of a decanter centrifuge used either steel or stainless steel for the majority of components. Few developments have occurred over the past 40 years with regard to the use of different materials. Some of the other materials used in decanters include titanium, Hastelloy, nickel, and alloyed aluminium [13]. It was evident from the power consumption and wear analysis that there were several potential benefits to redesigning the bowl using different materials, including:

- Increased lifespan of components due to higher wear resistance
- Reduced power consumption and product destruction due to a lower coefficient of friction between the settled solids and the bowl wall
- Lower bearing loads, leading to extended life and lower power consumption
- Improved ease of handling during manufacturing and assembly of a lighter bowl
- Lower manufacturing costs
- Reduced freight cost due to lower weight
- Reduced noise emissions due to the removal of protrusions [14]
- Potential to increase operating speed due to higher specific strength materials

There are benefits to developing a new scroll, but this project was limited to the bowl due to time and financial constraints. Several concepts for modifying the scroll are presented, but no further development was conducted.

The design process of the new composite bowl for a GTech-Bellmor 1456 Centrifuge Decanter is presented in this chapter. The chapter includes a description of the current design, design specification, load calculations, concept generation, material selection, material testing, final design, and the manufacturing process.

10.2 Current Rotating Assembly Design

The current rotating assembly is shown in Figure 10.1 and Figure 10.2. The bowl and end hubs are made of cast 316 stainless steel and the scroll and centre hub are made of

304 stainless steel. The key dimensions and components of the rotating assembly are shown in Figure 10.3. The current rotating assembly weighs approximately 500 kg. The cost of the bowl alone, not including the end hubs, is approximately NZ$20,000. The cost of the bowl does not include any additional wear protection.

Figure 10.1 Current rotating assembly of a GTech-Bellmor 1456 Centrifuge Decanter

Figure 10.2 Current rotating assembly with partial cross-section showing the scroll

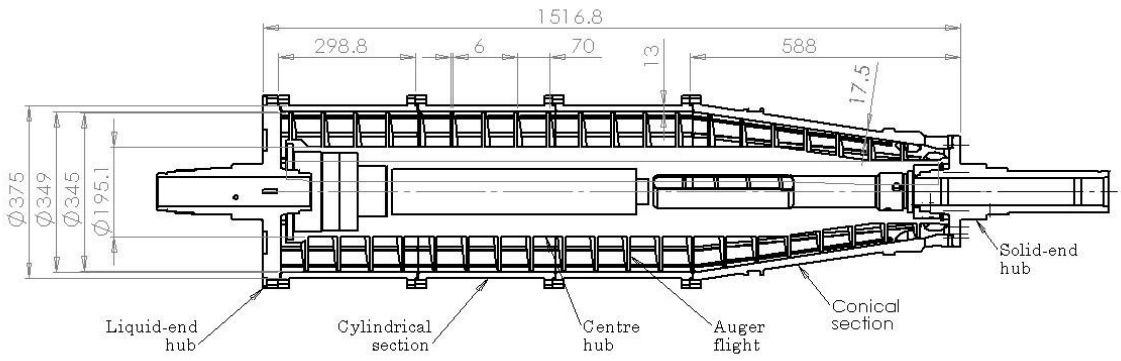

Figure 10.3 Cross-section of the rotating assembly with key dimensions (mm) and component labels

At present, all components, except the scroll flights, are sand cast and machined to size. The axial guide vanes on the inside of the bowl are manually welded on. The scroll flights are profile cut and pressed to the required shape. The flights are welded in place and the outside edge of the scroll is machined to be concentric with the centre hub. The assembly is then balanced and installed in the centrifuge. The material properties for 316 stainless steel were obtained from Ashby CES materials selection software and are shown in Table 10.1.

Table 10.1 Material properties for 316 stainless steel

Density	7870 – 8070 kg/m^3	Endurance limit	256 – 307 MPa
Young's modulus	190 – 205 GPa	Fracture toughness	112 – 278 MPa.m$^{1/2}$
Tensile strength	480 – 620 MPa	Hardness – Vickers	170 – 220 HV
Compressive strength	170 – 310 MPa	Modulus of rupture	170 – 310 MPa
Bulk modulus	134 – 152 GPa	Poisson's Ratio	0.265 – 0.275
Elongation	30 – 51 %	Shape factor	63
Elastic limit	170 – 310 MPa	Shear modulus	74 – 82 GPa

Bellmor Engineering Ltd. currently use several techniques to protect against wear depending on the product the centrifuge will be processing. For light applications, such as vegetable oil, the scroll flights are sometimes hard-faced as only some protection is required. For medium to high abrasive applications, such as meat rendering, the scroll flight tips are lined with tungsten carbide tiles and the inside of the bowl hard-faced. For extremely harsh applications, such as oil drilling mud or coal, all internal surfaces of the centrifuge are lined with tungsten carbide tiles. These methods are common and widely used in industrial centrifuges. The downside to using tungsten carbide tiles is they are expensive and time consuming to apply. One machine can require over one thousand tiles at NZ$35 per tile, each needing to be individually welding in place. The most commonly used materials by Bellmor Engineering Ltd. for hard-facing are tungsten, titanium, and chromium. The hard-facing aids significantly with reducing the initial wear but once the layer has worn off the product continues to wear into the stainless steel. If the hard-facing is not routinely reapplied then there is little advantage in using it.

There are several improvements that could be made to the current design:

- Find a cheaper method of wear protection, the difference arising from either: the initial cost of the materials, or in reducing maintenance costs

- Countersink all external bolt heads and other protrusions to reduce windage. This will reduce power consumption and the acoustic emissions
- Use a different material for the scroll and the inside of the bowl to reduce friction and hence wear and power consumption
- Optimise the scroll geometry for each process to maximise efficiency and product throughput

10.3 Design Specification

The primary focus of the overall project was to reduce the power consumption of the centrifuge. It was established in Chapter 2 that the friction generated during product transport accounts for a large portion of the total power consumption. This could be reduced by lowering the coefficient of friction between the machine components and the settled product. The circumferential coefficient of friction must be large enough to ensure product does not simply rotate with the scroll [10].

The wear of the bowl and scroll can be very high, in some applications the centrifuge may need to be refitted within six months. When the scroll flights and the inside surface of the bowl become too worn the centrifuge is no longer able to operate effectively. If the wear of the material is able to be decreased, the interval between overhauls can be increased, leading to less plant downtime and decreased plant maintenance cost. Foreign materials, such as pieces of steel or stones, can enter the centrifuge; therefore, the new material must be able to withstand these passing through.

The most common liquid processed by decanters is water. In most applications the water contains impurities that can make it acidic or basic. The temperature of the feed entering the centrifuge can range from 10 to 90°C, but due to localised friction within the centrifuge the temperature could exceed this. Any material used must be able to withstand temperatures up to 120°C and be able to operate in an acidic or basic environment.

The new assembly should be able to be assembled in the same amount of time taken to assemble the current design. Therefore it should have the same or fewer components. As centrifuges require regular cleaning while in service, the centrifuge should be able to be disassembled without the need for specialist tools or processes. It is important that the centrifuge can be repaired in the Bellmor Engineering Ltd. workshop. At present, the scroll and bowl can be completely rebuilt in-house. Worn scrolls and bowls can be built

up by welding, and broken tungsten carbide tiles can be individually replaced. The new design should allow for local parts to be replaced or rebuilt without the need to replace all components. It would be beneficial if the new bowl was interchangeable with the current design and therefore existing machines could be retrofitted with the new design.

The cost of the new assembly and predicted maintenance costs should be no more than they are presently. Theoretically, the maintenance and operating costs should reduce, this should absorb some or all of the extra initial capital cost. The current bowl costs approximately NZ$20,000, and the end hubs cost approximately NZ$3,000 each.

All of these design specifications were considered during the design stages. Consideration was also given to how the components would be manufactured.

10.4 Load Calculations

In this section the loads acting on the bowl are theoretically calculated. There are five main loads that give rise to appreciable stress within the bowl: hydrostatic hoop stress, hydrostatic axial stress, hoop stress from bowl mass, axial stress from solids transport, and shear stress from solids transport. There are other loads on the bowl, such as drive torque, but these are small relative to the five main loads and are not calculated here.

10.4.1 Hydrostatic hoop stress

The hoop stress in a pressure vessel is equal to the pressure acting on the wall multiplied by the radius r_o and divided by the wall thickness t. The hoop stress in the bowl as a function of the operating and design variables is

$$\sigma_{HH} = \frac{r_o \rho_S \omega^2 (r_o^2 - r_i^2)}{2t}. \qquad 10.1$$

where

ω bowl speed (rad/s)

ρ_S solids density (kg/m^3)

r_i radius of scroll hub (m).

The density of the solids and an inner radius equal to the hub radius were used as the worst case scenario.

10.4.2 Hydrostatic axial stress

The axial stress due to hydrostatic pressure P_r is not the same as for a pressure vessel because the pressure acts only on an annular ring. The load acting on the end face of the bowl is

$$F_A = \int_{r_i}^{r_o} P_r \, dr \tag{10.2}$$

$$F_A = \frac{\rho_S \omega^2}{2} \int_{r_i}^{r_o} (r^2 - r_i^2) \, dr \tag{10.3}$$

$$F_A = \frac{\rho_S \omega^2}{2} \left(\frac{r_o^3}{3} - r_i^2 r_o + \frac{2r_i^3}{3} \right). \tag{10.4}$$

The axial stress due to hydrostatic pressure is the axial load divided by the cross-sectional area of the bowl and is equal to

$$\sigma_{AH} = \frac{\rho_S \omega^2}{4\pi r_o t} \left(\frac{r_o^3}{3} - r_i^2 r_o + \frac{2r_i^3}{3} \right). \tag{10.5}$$

The solids density and centre hub radius for the inner radius were used as they are the worst case scenario.

10.4.3 Hoop stress due to bowl mass

The forces acting on a circumferential element of the bowl are shown in Figure 10.4. The diagram shows the internal hoop stress σ_{MH} that must counter the centripetal body force F_C.

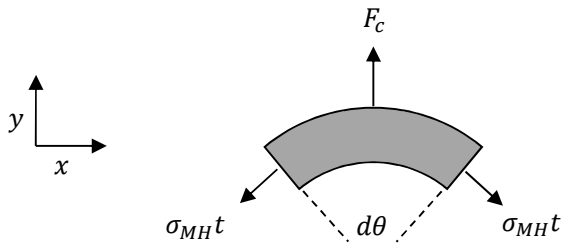

Figure 10.4 Free body diagram of an element of the bowl wall

Balancing the forces in the y-direction gives

$$F_c = 2\sigma_{MH} t \sin\frac{d\theta}{2} \tag{10.6}$$

where, for small angles

$$\sin\frac{d\theta}{2} \approx \frac{d\theta}{2}. \tag{10.7}$$

Substituting in the centripetal force and rearranging for the hoop stress gives

$$\sigma_{MH} = \rho_m \omega^2 (r^2 + rt) \tag{10.8}$$

where

ρ_m density of the bowl material (kg/m^3)

r average bowl radius (m).

10.4.4 Axial stress from solids transport

The force supplied by the scroll is limited by two conditions: maximum torque, and maximum power. The torque is limited by a clutch and a sensor, while the power is limited by what can be supplied by the motor. The axial force F_{Ax} can be calculated using the model created in Part I. Axial stress σ_{AT} due to product transport is therefore the maximum axial force divided by the cross-sectional area of the bowl.

$$\sigma_{AT} = \frac{F_{Ax}}{2\pi r_o t}. \tag{10.9}$$

10.4.5 Shear stress from solids transport

The torque provided by the scroll T_P is transferred to the bowl through the settled solids, this torque acts predominantly on the conical section but is maximum at the liquid end. The maximum torque is limited to 3.6 kNm in the GTech-Bellmor 1456 Centrifuge Decanter. The torque can be calculated using the product transport model presented in Part I. The shear stress τ_T due to product transport is

$$\tau_T = \frac{T_P}{2\pi r^2 t}. \tag{10.10}$$

10.5 Bowl Concepts

Several concepts were generated for the bowl; these are presented in this section. While the bowl and scroll are part of the same assembly, their designs are only dimensionally dependent.

10.5.1 Bowl material substitute

The material of the cylindrical and conical sections could be changed to reduce wear and friction. The new material should have superior wear and friction properties along with high corrosion resistance. This concept may not require any changes to the design of the bowl or manufacturing process. The new material could potentially be prohibitively more expensive than stainless steel.

10.5.2 Bowl insert

This concept involves inserting a liner material into the bowl, in a similar way that the wear resistant tiles line the bowl. The advantage of this is that the two layers would have a reduced number of functions. The outer layer would be required to provide strength, while the inner layer provides the appropriate wear and friction characteristics. In this concept there is a replaceable internal lining that can either be a solid removable piece or a coating on the inside of the bowl. This concept is shown in Figure 10.5 and Figure 10.6.

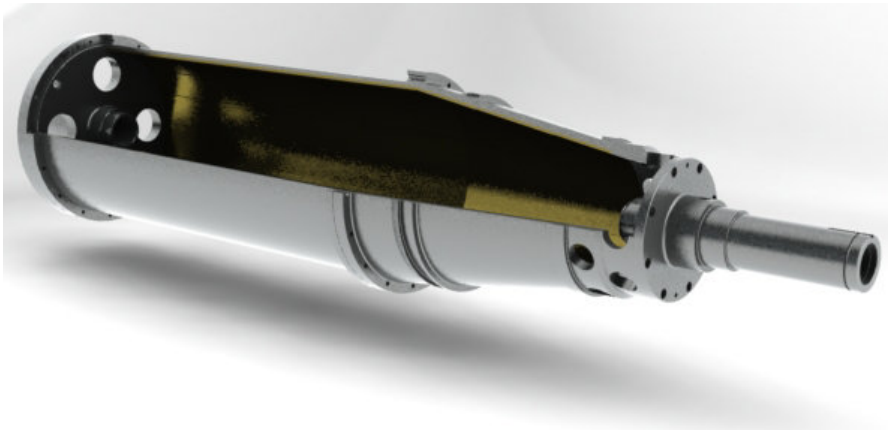

Figure 10.5 Bowl insert concept with stainless steel exterior and sacrificial wear resistant lining

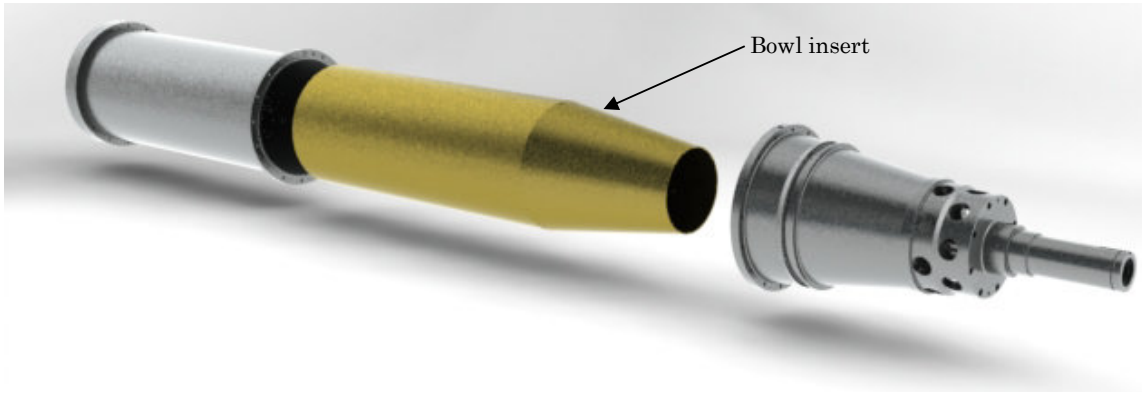

Figure 10.6 Exploded view of concept with internal lining

This concept allows for multiple material selections to account for the requirements of strength, wear, and friction. Use of an insert is likely to introduce challenges during manufacture and installation. The insert needs to be able to be repaired or replaced without damaging the bowl exterior. The material does not have to provide strength or stiffness, only wear resistance and a low coefficient of friction in the axial direction. A material that meets the full criteria for a bowl insert is nickel chromium alloy. It has the same environmental resistance as 316 stainless steel and higher wear resistance.

10.5.3 Dual layer bowl

A composite layer could be added to the exterior of the bowl to reduce weight and the number of bowl sections. As with the previous concept; the internal lining provides the wear and friction characteristics while the composite exterior provides strength, stiffness, and toughness. A partial cross-section view of a dual layered bowl is shown in Figure 10.7. A dual layered bowl would potentially be lighter than the current design due to the ability to use a composite layer. The bowl could be reduced to only one section, as opposed to the four that are presently used. The internal lining will not be easy to replace or refurbish, instead the whole bowl, excluding the hubs would need to be replaced. However, axial strips or corrugations could be included in the internal lining.

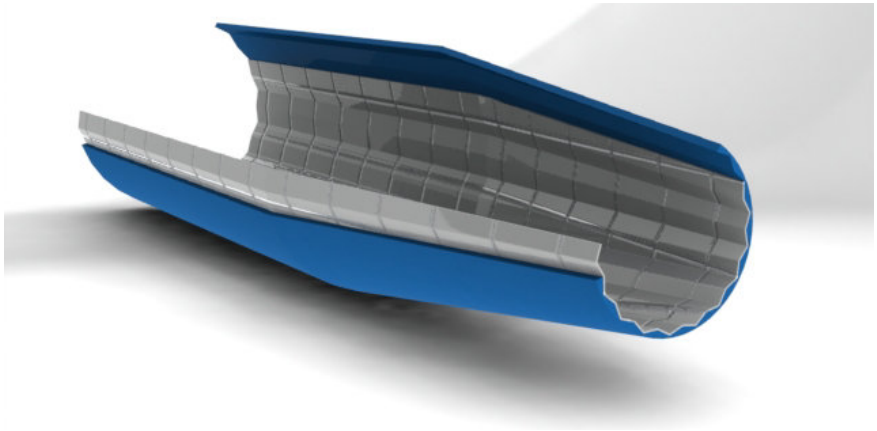

Figure 10.7 Composite bowl with internal lining for wear resistance and exterior layer to provide strength and stiffness

One of the more difficult aspects of the design of any composite component are the fixtures. A strong, reliable, and accurate design must be developed to attach the composite layer to the end hubs. The connection must not be a stress concentration and needs to be able to support the stress and torque present in the bowl. Two possible concepts are shown in Figure 10.8 and Figure 10.9. In the first concept the composite is turned into a radial flange and metal inserts are added for the bolts. In the second concept the composite layer is sandwiched between the hub and an outer layer, removing the need for metal inserts to be added to the composite layer. Consideration needs to be given to alignment, assembly, and sealing.

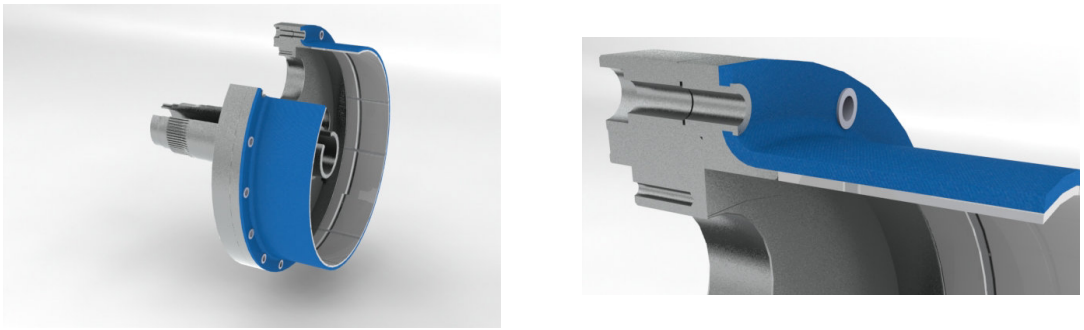

Figure 10.8 Connection concept between liquid end hub and dual layer composite bowl

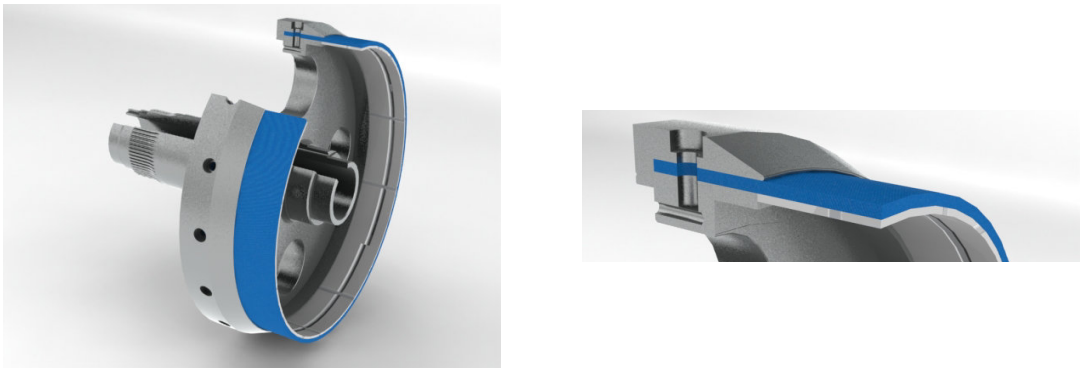

Figure 10.9 Second connection concept between liquid end hub and dual layer composite bowl

This second concept was selected for further development. The material selection is addressed in a later section.

10.5.4 Bowl profile

If the surface finish of the bowl is modified with axial strips, there will be a bi-directional coefficient of friction. A simple diagram of a saw-tooth surface having angle δ is shown in Figure 10.10. A free-body diagram of half a wavelength of the solids of mass m is shown in Figure 10.11.

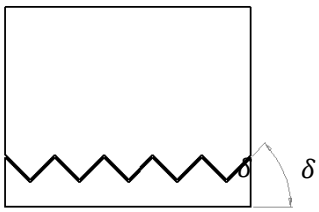

Figure 10.10 Example of a saw-tooth surface to increase the effective coefficient of friction in one direction

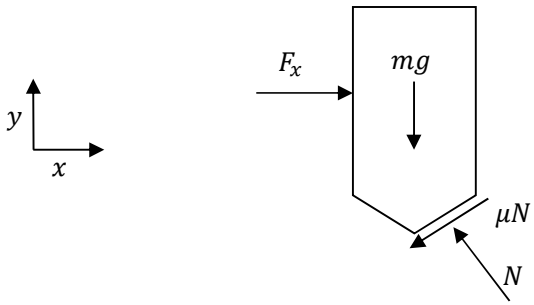

Figure 10.11 Free body diagram of body moving over a corrugated surface

Summing the forces in the x and y directions and solving for F_x gives

$$F_x = \frac{mg(\mu \cos\delta + \sin\delta)}{(\cos\delta - \mu\sin\delta)} \tag{10.11}$$

therefore, the effective coefficient of friction is

$$\mu_{eff} = \frac{F_x}{mg} = \frac{(\mu \cos\delta + \sin\delta)}{(\cos\delta - \mu\sin\delta)}. \tag{10.12}$$

The effective coefficient of friction reaches infinity when the denominator of Equation 10.12 is equal to zero, that is

$$\mu = \frac{1}{\tan\delta}. \tag{10.13}$$

Adding axial strips to the bowl wall increases the effective coefficient of friction in the circumferential direction, which is necessary to stop the settled solids from rotating with the scroll. This is assuming that the internal coefficient of friction of the bulk is relatively high.

10.6 Scroll Concepts

Several concepts for a new scroll were also produced, although a new scroll was not within the scope of the project.

10.6.1 Scroll material substitute

The material of the scroll could be changed to improve the wear and friction characteristics. The surface finish on the front face of the scroll could be improved, and hard facing or heat treatment could be used. This concept requires a simple material change, although it may only offer small improvements. Changes to the manufacturing process may also be needed.

10.6.2 Scroll face lining

In this concept a sacrificial layer is added to the front face of the scroll. The layer is either a coating or solid material, and can be mechanically fastened or welded in place. During maintenance the layer should be able to be removed and replaced. The concept is shown in Figure 10.12.

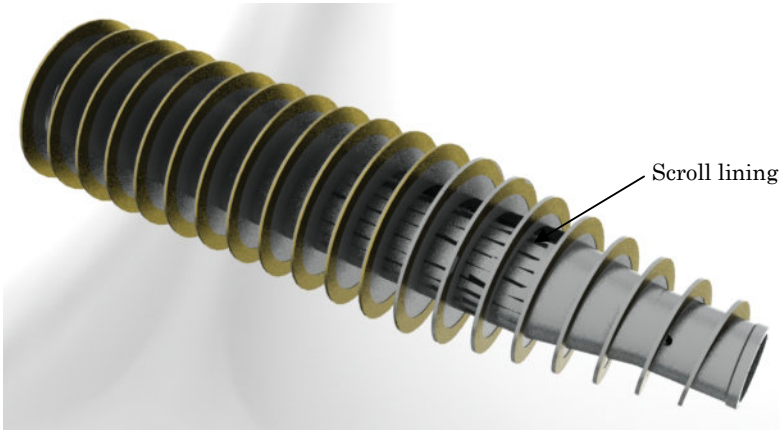

Figure 10.12 Scroll concept with a wear resistant lining added to the front face of the scroll

Adding a wear resistant layer is simple and requires minimal changes to the current design. However, there may be unforeseen issues while applying of the layer.

10.6.3 Detachable piecewise scroll

This concept involves replacing the scroll with detachable sections that are mechanically fixed in place. This allows for many options for the scroll blade material. Individual sections can easily be replaced. The cost of this design is potentially higher than the current design, as more machining and assembly would be required. This concept is shown in Figure 10.13.

Figure 10.13 Section of scroll concept with detachable scroll sections, including two pictorial views and one exploded view.

10.6.4 Rubber lipped scroll

In this concept a rigid rubber lip is added to the scroll edges, which would result in a very low coefficient of friction when wet. The loads on the scroll would need to be explored if this concept were to be developed further. A partial section of the scroll with a rubber lip is shown in Figure 10.14.

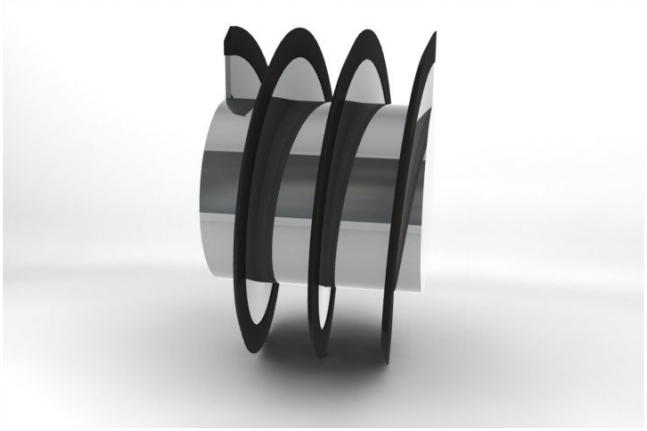

Figure 10.14 Rubber lipped scroll concept

10.7 Material Selection

For a dual layer bowl the construction materials are divided into two components: the internal liner, and the external layer. The considerations in the material selection are discussed here. Essential considerations for the external layer are:

- Provide structural integrity to the bowl
- Substrate for the bowl lining material
- Corrosion resistant
- Alkali and acidic resistant
- Ductile failure mode
- High fracture toughness

Materials with high specific strengths are desirable as the self-weight of the bowl generates a high internal stress. Composites have high specific strength, with carbon fibre reinforced polymer (CFRP) having one of the highest. They also have excellent specific stiffness. Assuming carbon fibre is used for the outer shell of the bowl, with a yield strength of 500 MPa and density 2500 kg/m^3, the required thickness is impractically thin at less than 1 mm. The thickness would be constrained by manufacturing, handling, and fastening requirements. A protective coating must be used where the product contacts the bowl because carbon fibre has poor wear resistance. Adding Kevlar to the laminate would increase the toughness and deter complete brittle failure.

The bowl liner must possess the following characteristics

- Low coefficient of friction in the axial direction
- Finite coefficient of friction in the circumferential direction
- High wear resistance
- Working temperature range of 10 to 120°C
- Corrosion resistance
- Alkali and acidic resistance

Two types of bowl liners could be used, a solid insert or a coating added to the external layer.

The coating could be applied directly to the bowl exterior. The coating would provide high wear resistance and a bi-directional coefficient of friction. It was determined using the Ashby software that alumina, silicon carbide, and nickel chromium alloy would be suitable materials; this does not consider the manufacturing implications. Silicon carbide and alumina could be applied as sacrificial coatings. Nickel chromium alloys have excellent properties, however, would cost significantly more than the materials employed in the original design.

Two potential materials were identified for the internal lining of the bowl. The first material was ARC 855-HTT, a particle reinforced matrix supplied by Chesterton's [54]. The supplier claims the material provides excellent wear resistance and decreases coefficient of friction. The product is applied as a two-part mixture, and can therefore be moulded into almost any geometry. The second material is a product from Pyrotek called O'-Sialon [55]. Pyrotek produces and sells O'-Sialon products primarily for handling molten metals in foundries. O'-Sialon is a combination of oxygen, silicon, alumina, and nitrogen. Silicon carbide particles reinforce a binding matrix. The silicon carbide particles give the material excellent wear and corrosion resistance. An O'-Sialon liner could be made and then wrapped with a composite layer.

10.8 Material Testing

Two material combinations were identified for future development and testing. The first uses an ARC 855-HTT liner with a carbon/Kevlar exterior. The second uses an O'-Sialon liner with a carbon/Kevlar exterior.

The stages of evaluating the ARC option were:

- Make ARC 855-HTT tensile test specimens and establish the Young's modulus and tensile strength
- Manufacture a flat composite panel of ARC 855-HTT and carbon/Kevlar to check the compatibility of the materials and confirm the Young's modulus, tensile strength, and hardness
- Manufacture a small pressure drum to check the proposed manufacturing method of a cylindrical component and establish whether the flange design can withstand the force requirement

The stages of testing the O'-Sialon option were:

- Conduct hardness testing on a small flat sample of O'-Sialon
- Manufacture a small cylinder of O'-Sialon wrapped with carbon/Kevlar and pressure test it

10.8.1 ARC 855-HTT strength and stiffness testing

The product ARC 855-HTT from Chesterton's was tested for strength and stiffness using a Hounsfield tensometer with a 10 kN load cell. The tensile samples were made by casting them in modelling gel, see Figure 10.15. The hardness, specified by Chesterton's as 85, was measured using a Durometer. The results are shown in Table 10.2.

Figure 10.15 ARC 855-HTT tensile test specimen

Table 10.2 Testing results of ARC 855-HTT

Sample	Young's modulus GPa	Tensile Strength MPa	Durometer Hardness Type D
1	7.2	27.8	80
2	5.5	25.6	82
3	2.9	32.5	79
4	4.7	27.0	85
Average	5.1	28.2	81.5

There was a lot of variability in the Young's modulus, which is likely to be due to measurement inaccuracies of the cross-sectional area or voids. However, it will be seen in the next section that the values are small relative to those of the carbon/Kevlar laminate, meaning that the exact value is unimportant. The hardness of the samples that were prepared was less than that specified on the product data sheet.

10.8.2 ARC flat panel

A flat panel was produced to test the tensile strength, toughness, and elastic modulus of the composite. Two panels, measuring 300 mm x 300 mm, were made at ASP Ltd. The panels had 3 mm of ARC 855-HTT and 3 mm of carbon/Kevlar. The fibre orientations are given in Table 10.3. There are more fibres on the 0° axis as the stress in the hoop direction is larger than in the axial direction. The ±45° layers are included for shear strength and they are required to support the bolts that are included in later models. The carbon plies were formed using uni-directional layers, while the Kevlar was applied as a bi-directional layer.

Table 10.3 Composite layup for test panels

Direction	Material	%	Number	Thickness (mm)
0° - 90°	450g CF	43.6	3	1.35
±45°	450g Kevlar	14.5	1	0.45
±45°	450g CF	29	2	0.9
0°	200g CF	12.9	2	0.4
	ARC 855-HTT			3

Six tensile specimens were water cut from the panel in each of the two principal directions, 0° and 90°. The force and extension of each sample were measured using a tensometer. The ultimate tensile strength and the Young's modulus of each sample are shown in Table 10.4. The values shown are the average values through the sample, including the ARC. The values in Table 10.2 show that the ARC has low strength and stiffness compared to the carbon/Kevlar laminate and therefore offers no additional strength and stiffness.

Table 10.4 Tensile strength and Young's modulus for the tensile test specimens cut from a flat panel of ARC 855-HTT-carbon/Kevlar composite

90°			0°		
Sample	UTS MPa	E GPa	Sample	UTS MPa	E GPa
1	246	25.9	10	252	26.8
2	268.6	28.2	11	260.7	27.7
3	257.5	26.8	12	262.7	27
4	256.3	24.8	13	281.5	27.5
5	241	26.7	14	274.3	28.1
Average	253.9	26.5		266.2	27.4
St. dev.	10.8	1.3		11.7	0.5

One of the failed specimens is shown in Figure 10.16. It can be seen that the ARC layer completely delaminated from the carbon. Failure most commonly occurred at the region around the reduction in area, with none of the specimens failing at the grips. It was common for the ARC material to completely delaminate from the fibres. Poor adhesion between the carbon and ARC was found; this was confirmed by the manufacturer, who noted that they should have bonded the epoxy to the ARC before it had cured.

Figure 10.16 Failed tensile test specimen showing delamination of the ARC layer

10.8.3 ARC pressure drum

A small cylinder of 150 mm internal diameter was manufactured using the proposed material combination of ARC and carbon/Kevlar. The method used was to coat a mandrel that had the required internal bowl profile with 3 mm of ARC. The mandrel and ARC were then wrapped with the laminate described in Table 10.5. Additional layers of 0°-90° carbon were added to the exterior of the bowl to allow for machining. The Kevlar layer was moved closer to the outer surface so it would act as an indicator when machining, if the layer was penetrated the strength of the laminate was compromised. The external diameter of the drum was then machined to the correct diameter and the radial bolt holes added before the ARC and laminate were removed from the mandrel as one part. A partial cross-section of the rib profile and flange is

shown in Figure 10.17. The ARC layer terminates before the end of the composite layer and is replaced by a stainless steel ring. The stainless steel rings act as a sealing surface for the stainless steel plugs. The end plugs are retained by twelve 8 mm radial bolts and sealed with a 3 mm o-ring. The 0° – 90° and ±45° plies were applied as bi-directional layers.

Table 10.5 Composite layup for pressure drums

Direction	Material	%	Number	Thickness (mm)
0° - 90°	200g CF	20	4	0.6
±45°	200g Kevlar	10	2	0.3
0° - 90°	200g CF	40	8	1.0
±45°	200g CF	20	4	0.6
0°	200g CF	10	2	0.3
	ARC 855			3

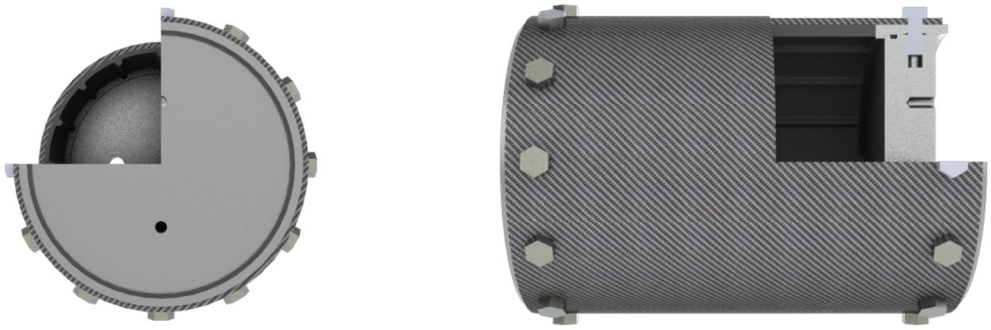

(a) (b)

Figure 10.17 CAD model of pressure drum with partial cross-section view of (a) ribs and (b) flange arrangement

The mandrel was gently heated before the ARC was applied. The mandrel was rotated while the ARC was being applied and during curing to eliminate slumping. A photograph of the mandrel coated in ARC is shown in Figure 10.18.

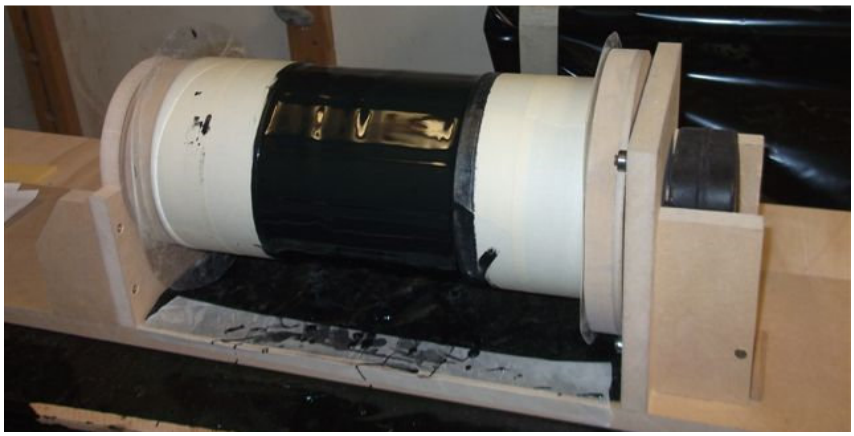

Figure 10.18 Mandrel coated with ARC 855-HTT

When the first drum was wrapped and vacuum bagged there was a large amount of wrinkling due to excess fibres. When the outside diameter was machined in a lathe, the Kevlar layers were revealed. The discontinuities in the fibres would have significantly reduced the strength. The inside surface of the drum was flawless and matched the mandrel. Photos of the outside and inside of the first ARC pressure drum are shown in Figure 10.19.

Figure 10.19 First pressure drum showing the Kevlar layer that was exposed during machining

A second drum was produced due to the unacceptable condition of the outside of the first ARC pressure drum. After the ARC was applied on the second drum it was machined to be precisely 3 mm thick; this has several advantages, including concentricity and surface finish. Concentricity is important in the final design so that it is well balanced. Machining the ARC enabled a roughened surface to be created, which is ideal for the subsequent laminate to adhere to and reduces the likelihood of delamination. When the laminate was applied to the second drum it was wrapped two or three layers at a time,

spot glued, and then vacuum bagged for several hours. This technique significantly reduced wrinkling. The drum could be machined without revealing any of the Kevlar. The finished drum with stainless steel end inserts is shown in Figure 10.20. The external diameter was 166.5 mm and the internal diameter of the composite was 156.1 mm.

Figure 10.20 Second pressure drum with no Kevlar exposed after external machining

The drum was pressure tested using water and failed at 5.14 MPa (745 psi) due to leakage between the stainless end insert and outer liner. The average hoop and axial stress was 82.3 MPa and 41.1 MPa, respectively. The calculated bearing stress on the bolts and laminate was 197.0 MPa.

Table 10.6 Average stress in ARC drum during pressure testing

Hoop stress	82.3 MPa
Axial stress	41.1 MPa
Bearing stress on bolt	197 MPa
Tearing stress from bolts	52.5 MPa
Shear stress in bolts	163 MPa

10.8.4 O'-Sialon liner

The initial testing of O'-Sialon showed that diamond scratched it, and tungsten carbide and carborundum, a type of silicon carbide, lightly marked the surface. The durometer hardness was approximately 95 but this is the minimum value as the surface was not perfectly flat.

A small O'-Sialon liner was produced for pressure testing. A solid mould of the internal shape of the liner was machined from steel. A flexible tube was placed over the mould

with approximately 30 mm of annular space. The annular space was filled with the O'-Sialon powder and sealed at both ends. The mould and tube were placed in a hydrostatic press, which was then pressurised to 170 MPa. At this point the part was rigid, although very weak. The part was removed from the mould and the external diameter was machined. The part was then fired at 1600°C. The liner that was produced is shown in Figure 10.21.

Figure 10.21 O'-Sialon liner

The inner surface of the liner was designed to contain 4 mm high ribs to demonstrate the capability of the process. Unfortunately, the ribs detached when the part was removed from the mould; this was attributed to the spring-back of the mould tightening on the ribs. The mould could have been modified to remove this interference. Due to the large pressure and thermal strains that are present during manufacturing the exact dimensions of the finished part are variable. This would need to be overcome if the liner were to be used in a centrifuge as these variations would lead to imbalance.

The O'-Sialon liner was wrapped with the laminate given in Table 10.5. The finished part is shown in Figure 10.22. The external diameter of the composite was 174.6 mm and the internal diameter was 163.0 mm. An o-ring was fitted between the stainless steel rings and the laminate instead of gluing them in place.

(a) (b)

Figure 10.22 O'-Sialon liner wrapped in carbon fibre and Kevlar

The drum was pressure tested using water and reached a maximum pressure of 7.12 MPa (1033 psi). The test was stopped at this pressure as it had demonstrated that the drum was capable of withstanding the required load. The calculated stresses in the bowl are given in Table 10.7.

Table 10.7 Average stress in O'-Sialon drum during pressure testing

Hoop stress	107 MPa
Axial stress	53.6 MPa
Bearing stress on bolt	267 MPa
Tearing stress from bolts	71.2 MPa
Shear stress in bolts	246 MPa

While the use of a one-piece O'-Sialon liner is promising because of the excellent wear resistance, the process was not pursued any further. The hydrostatic press that was used had an internal diameter of 400 mm, which was not large enough to produce a full size bowl for the GTech-Bellmor 1456 Centrifuge Decanter. A press was available in Melbourne, but the costs involved with this were high and therefore the O'-Sialon liner was not pursued beyond a pressure drum.

10.9 Final Design

A full-size bowl was designed with an ARC interior liner and a carbon/Kevlar exterior. A rendered model of the final design is shown in Figure 10.23. A partial cut-away revealing the different layers is shown in Figure 10.24. Existing end hubs were modified to accommodate the composite bowl. The solids discharge ports utilise 16 wear resistant

ceramic sleeves; the ports are machined and the sleeves are glued in place. The sleeves protrude above the exterior of the bowl to minimise contact between the solids and the bowl exterior. The thickness of the laminate is increased around the solids discharge ports to compensate for the removal of material and additional stress concentrations. 16 axial guide vanes were included to promote axial motion of the solids as they are transported along the bowl. The vanes stand 2.5 mm high and 8 mm wide. The total mass of the bowl and end hubs was calculated to be 103 kg. The laminate and lining weigh only 14 kg and 9 kg, respectively. The original bowl and end hubs weighed approximately 250 kg.

Figure 10.23 Rendered CAD model of the final design of the composite bowl including end hubs and solids discharge port liners

Figure 10.24 Rendered CAD model of the final design of the composite bowl with the layers revealed

Cross-sections of the liquid and solids end flanges are shown in Figure 10.25. The stainless steel end rings were removed as they were deemed too expensive to produce for such a large diameter and the pressure testing showed it was sufficient to seal on the

surface produced by the mould. The ARC layer was extended to the end of the laminate and the end hubs directly located and sealed on this surface. O-rings were fitted to the external diameter of the end hubs and seal against the ARC layer. The chamfers and stops were included on the mandrel, reducing the need for post-machining.

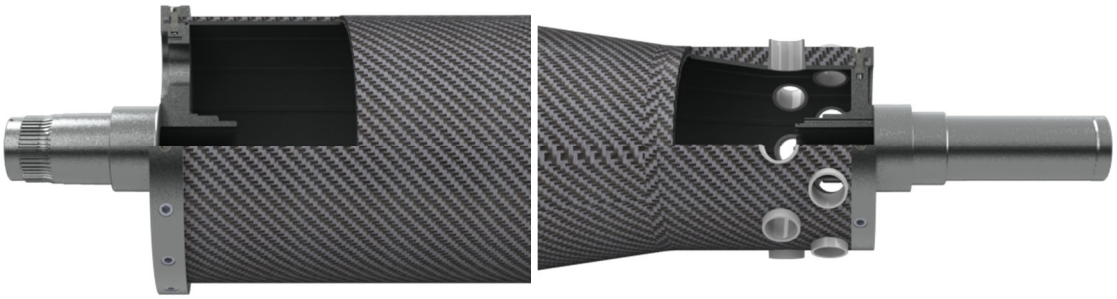

(a) (b)

Figure 10.25 Rendered CAD model of the flange assemblies for the (a) liquid end and (b) solids end

There are two sections of the bowl: the uniform layer and the thickened section around the solids discharge ports. The fibre orientations for the bowl are given in Table 10.8 and Table 10.9 for the uniform and thickened sections, respectively. The orientation of the plies was achieved using pre-impregnated uni-directional tape.

Table 10.8 Fibre orientations for the 6 mm section

Direction	Material	%	Number	Thickness (mm)
0° - 90°	200g CF	20	4	0.6
+-45°	200g Kevlar	10	2	0.3
+-45°	200g CF	10	2	0.3
0° - 90°	200g CF	20	4	0.6
+-45°	200g CF	10	2	0.3
90°	200g CF	10	2	0.3
0° - 90°	200g CF	20	4	0.6
	ARC 855HT-T			3

Table 10.9 Fibre orientations within the thickened region around solids discharge ports

Direction	Material	%	Number	Thickness (mm)
0° - 90°	200g CF	20		
0° - 90°	200g CF	20		
+-45°	200g CF	20		
0° - 90°	200g Kevlar	20		
+-45°	200g CF	20		
0° - 90°	200g CF	-	5	0.75
Different coloured indicator layer				
Layers running the full length of the bowl				

The individual stress components arising from hydrostatic pressure, self-weight, and product transport are given in Table 10.10. The most significant component is the hoop stress arising from hydrostatic pressure. The largest predicted stress is well below the measured tensile strength of a similar laminate shown to have a tensile strength of 266 MPa. These calculations only consider the stress in the composite layer, while the test tensile strength is for both the ARC and laminate.

Table 10.10 Stress components in composite bowl

Stress		Equation
σ_{HH}	9.6 MPa	10.1
σ_{AH}	54.0 MPa	10.5
σ_{MH}	7.7 MPa	10.8
σ_{AP}	17.2 MPa	10.9
τ_T	3.0 MPa	10.10

10.10 Manufacturing

A document containing detailed manufacturing instructions was prepared and supplied to all involved parties; this is provided in Appendix D. The manufacturing process for the prototype bowl was similar to that followed for the small pressure drums. The mandrel was coated with ARC and cured at approximately 50°C. The thickness of the ARC layer was slightly more than required. The ARC layer was machined to the required thickness of 3 mm. The mandrel and ARC layer were then wrapped with the laminate shown in Table 10.8 and Table 10.9. The bowl was wrapped, spot glued, and vacuum bagged in stages to reduce wrinkling and to produce a high fibre fraction. The fibres in the 90° and +-45° direction were initially applied as single continuous strands

of carbon and Kevlar. The axial layers were applied as sheets. Once all layers were added they were infused with epoxy resin. The resin was cured at 60°C to ensure that the bowl could be removed from the mould when it cooled. It was calculated that the mandrel increased in diameter by ~0.3 mm. Due to the wrapped fibres being too tightly packed the first attempt at infusion was unsuccessful. Only a ~1 mm layer on the outside was infused, resulting in an unusable part. The laminate was removed and reapplied using pre-impregnated tape. The bowl was balanced by removing material from the end rings. Several photos taken during the manufacturing process are included below.

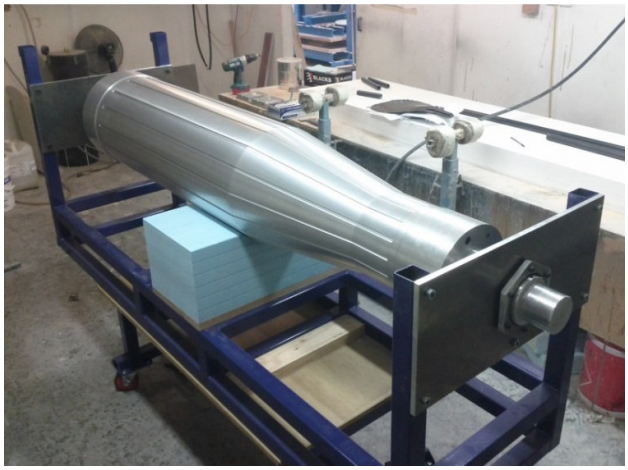

Figure 10.26 Mandrel support in frame constructed for manufacturing, the mandrel was driven by an electric motor (not shown here)

Figure 10.27 ARC coating being turned at Bellmor Engineering Ltd.

Figure 10.28 Machined ARC surface, showing machining lines and exposure of some porosity

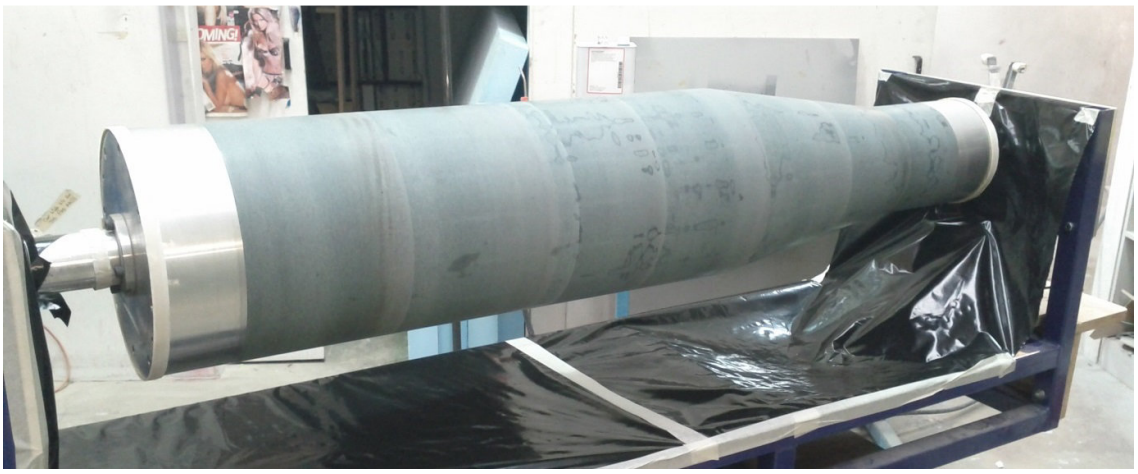

Figure 10.29 Mandrel with machined ARC layer

Figure 10.30 Carbon fibre being wrapped onto the mandrel, showing a close-up of the feed mechanism with three tows of carbon fibre

Figure 10.31 Carbon fibre being wrapped onto the mandrel

Figure 10.32 Carbon fibre bowl being infused with epoxy resin

Figure 10.33 Cured pre-impregnated bowl

10.11 Bowl Economics

The new bowl design will have benefits to both the manufacturer and customer. Increased wear resistance will result in a bowl that lasts longer and requires less frequent maintenance, and the decreased friction between the bowl and solids will result in reduced power consumption. The total manufacturing cost of the new bowl is expected to be lower than that of the existing bowl. There may be a loss of revenue due to the less frequent maintenance requirements. The novel bowl design is also expected to attract more customers as it is a point of difference over many competitor centrifuges.

The costs associated with the new bowl are described in Table 10.11. The cost of the bowl includes one-off costs, such as the mandrel and wrapping frame construction. These costs will not be incurred for future composite bowls made using the same mandrel and frame. The total cost for the mandrel was $19,170, including all material and machining. The cost is broken down as $13,667, $2,397, $1,236, and $1,870 for the middle ribbed section, liquid end, solids end, and two support shafts, respectively.

Table 10.11 Cost breakdown of the new composite bowl

	Cost
Mandrel material	$19,170
Frame construction and materials	$4,600
ARC 855-HTT	$1,725
Composite fabrication and materials	$7,600
Composite finish	$1,500
Machining	$2,500
Total cost	$35,370

The cost for the bowl alone is approximately $13,325, which is significantly cheaper than the cost of a stainless steel bowl ($20,000). Further improvements could be made to the manufacturing process to reduce cost and manufacturing time. Potential improvements include:

- Automation of the filament winding/wrapping
- Improve the application process for the ARC to remove the need for post-machining

The manufacturing time for the bowl would be expected to reduce once systems become established.

10.12 Conclusions

A new composite bowl was developed for a GTech-Bellmor 1456 Centrifuge Decanter. The new bowl promises several benefits over the existing design. The material combination and flange design were proven to work using tensile test specimens and small-scale pressure drums. A new manufacturing method was developed where an abrasion resistant layer is applied to a mandrel and the laminate is subsequently wrapped and infused above this layer. The composite bowl is then machined and

removed from the mandrel as one complete part. This manufacturing method allows for the production of accurate and repeatable composite components.

At the conclusion of the project the new composite bowl had been manufactured. Sufficient time was not available to conduct the tests necessary for full validation due to extensive delays during manufacturing. Full validation is required before the bowl can be deployed in a full-time processing situation.

Further development could be conducted on the O'-Sialon liner. This was not done as part of this project due to cost and time constraints.

Part III

Feed Accelerator Analysis

It was identified in Part I that the feed accelerator has a significant influence on the performance of a decanter centrifuge. Part III contains further analysis of the feed accelerator. There are four components to this part: theoretical, experimental, and computational analysis, and a parametric study.

Theoretical analysis of the feed accelerator in a decanter centrifuge was completed. Three mechanisms of flow acceleration were identified; these were viscous dissipation, impulse force, and mass flow induced velocity. The most commonly used designs were identified as the Conical, Disk, Drum, Esbjerg, and Plate accelerators. The Modified Disk accelerator was created based on the Disk accelerator and was also evaluated. An analytical analysis of the feed entering the accelerator was conducted and several performance metrics are presented.

An experimental method was developed to examine the decanter centrifuge feed accelerator designs. The method allowed for the measurement of acceleration efficiency and high-speed photography of the flow in the annular space between the accelerator and the rotating pool. It was not practical to conduct in situ measurements due to the accessibility of the feed zone in a decanter centrifuge; therefore a test rig was developed to simulate the feed conditions. The order of best to worst performing of the six tested designs was Modified Disk, Disk, Plate, Conical, Drum, and Esbjerg, having pool efficiencies of 91.7%, 85.5%, 77.2%, 77%, 75.8%, and 74.6%, respectively. The Modified Disk accelerator demonstrated the best efficiency; this was attributed to the over-speeding effect of the forward curving vanes and the larger discharge radius.

The six feed accelerators were modelled using ANSYS-CFX 14.5 and compared to the experimental results. There was excellent agreement between the flow in the annular space, observed using high-speed photography, and the paths predicted using the computational model. The predicted torque acting on the accelerator walls was found to have good correlation with the experimentally measured increase in pool speed.

A parametric study of the Drum and Disk feed accelerator designs was undertaken using the computational model. The parameters that were studied for the Drum

accelerator were the port diameter, number of ports, wall thickness, and stand-off tube height. The parameters that were studied for the Disk accelerator were the blade discharge angle, number of vanes, discharge radius, disk thickness, mass flow rate, and rotation speed.

Chapter 11

Theoretical Feed Accelerator Analysis

11.1 Introduction

It was shown in Part I that accelerating the feed uses a major portion of the total power consumed by a decanter centrifuge. Accelerating the feed to the rotational speed of the bowl, necessary for high separation rates, is performed by the feed accelerator. If the feed has not reached the solid body rotational speed of the bowl it is further accelerated within the liquid pool.

Analysis of the feed accelerator has so far been limited to overall considerations of the power consumption. The acceleration power is made up of two components, the rotational kinetic energy of the solids and liquids as they leave their respective discharge ports, and the viscous losses during acceleration [12]. The total power required by acceleration is

$$\dot{E}_A = \left(\frac{1}{4}\omega_b^2(\dot{m}_S + \dot{m}_L)(r_o^2 + r_{dL}^2)\right)_{Viscous} + \left(\frac{1}{2}\omega_b^2(\dot{m}_S r_{dS}^2 + \dot{m}_L r_{dL}^2)\right)_{Kinetic} \quad 11.1$$

where

ω_b bowl speed (rad/s)

$\dot{m}_L$ liquid mass flow rate (kg/s)

$\dot{m}_S$ solids mass flow rate (kg/s)

r_o inner radius of the bowl (m)

r_{dL} liquid discharge radius (m)

r_{dS} solids discharge radius (m).

While this equation gives the power consumption as a function of the operating variables, it offers no insight into the quality and efficiency of the feed acceleration.

It is important to note that irreversible viscous losses are inherent in all fluid flows that have regions undergoing shear. These regions include boundary layers near walls and free surfaces, and flows under viscous accelerations. Both of these are present in the accelerator of a centrifuge. Shear forces will also be present if the fluid is under-accelerated when it enters the rotating pool. The viscous losses do not increase the power consumption. When the control volume is drawn around the bowl the same power is required for acceleration regardless of the mechanism of acceleration. Viscous losses are important as their existence in the fluid pool is detrimental to the performance of the centrifuge. The three mechanisms of acceleration are discussed in Section 11.2.

The importance of the feed accelerator is often not appreciated. If the feed is not fully accelerated when it enters the rotating pool it is detrimental to the operation of the centrifuge. Detrimental effects of under-acceleration include re-suspension of settled solids, disturbance to the surface of the pool, poor solids recovery, poor centrate clarity, and high wear on the bowl and scroll adjacent to the feed ports [13, 18]. If the feed is under-accelerated the g-force will initially be lower, therefore a longer settling length is required to achieve the same separation rate. A more efficient accelerator will provide higher solids recovery and clearer centrate [18]. While the accelerator must increase the rotational speed of the feed, it must not significantly increase the radial velocity because this can lead to plunging of the incoming feed into the rotating pool. This can disturb previously settled solids and increase wear on the bowl in the region around the accelerator. The ideal feed accelerator would pre-accelerate the feed to the tangential speed of the rotating pool while minimising the radial velocity. The feed leaving the accelerator must be evenly distributed, both circumferentially and axially. If there is uneven distribution or localized jets, excessive wear can occur on both the scroll and bowl adjacent to the accelerator.

There is a limited amount of literature available that specifically focuses on the feed accelerator in decanter centrifuges.

The technology of accelerators has been investigated by Leung [5, 13, 15-19]. Experimental evaluation was completed to verify the performance of his Conical accelerator concept, also known as the XL-Plus accelerator. Several machines were fitted with the new accelerator design. All of the case studies showed improvements in solids recovery, centrate clarity, or throughput.

Tan et al [21] completed a computational analysis and optimisation of a Disk accelerator for a two-stage pusher centrifuge. They predicted an increase in the throughput. The design was installed in a full-size centrifuge and an increase in throughput was briefly observed. Conclusive results were not able to be generated due to mechanical failure of the design.

Fernandez [22] conducted a CFD analysis of the multiphase flow in a solid bowl centrifuge. The model did not include the specific accelerator geometry or the weir geometry. The incoming mixture was considered simply as a radial jet. It was observed that there is a high axial velocity in the liquid at the air interface. The pool also had a lower tangential velocity than the rigid body velocity, it was concluded that this was due to the under-acceleration of the incoming liquid jets from the accelerator; this is shown in Figure 11.1.

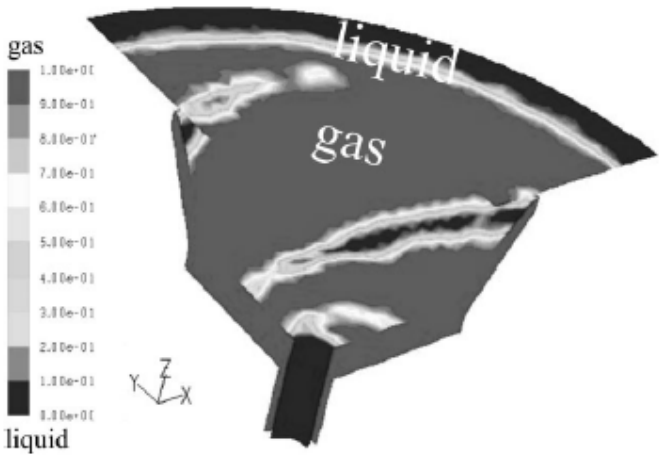

Figure 11.1 Phase distribution normal to the axis of rotation in the accelerator in a solid bowl centrifuge, copied from [22]

A centrifugal pump uses an encased impeller to create flow. The liquid enters the impeller from the middle and moves radially while gaining rotation. The liquid enters the outer casing of the pump where it is fed into downstream piping. The same techniques that are used to analyse centrifugal pumps can be used to model the feed accelerator. Zhang [56] analysed the flow field in a centrifugal pump to determine where energy was converted and lost. Zhang found that the efficiency of the pump was strongly related to the inlet blade angle and the middle section of the blades determined the energy conversion. The main component of loss within a centrifugal pump is viscous losses.

There is a clear opportunity to conduct further analysis of the feed accelerator, to not only find an optimal design, but to differentiate between designs that are commonly used by centrifuge manufacturers.

This chapter contains a description of the mechanisms of fluid acceleration relevant to centrifuges. Six accelerator designs are identified for further analysis. Key regions of the flow were identified, discussed, analysed analytically. This chapter precedes an experimental, computational, and parametric analysis of various feed accelerators.

11.2 Acceleration Mechanisms

There are three mechanisms by which rotation can be induced, these are viscous dissipation, impulse force, and mass flow induced velocity. A diagram of each mechanism is shown in Figure 11.2.

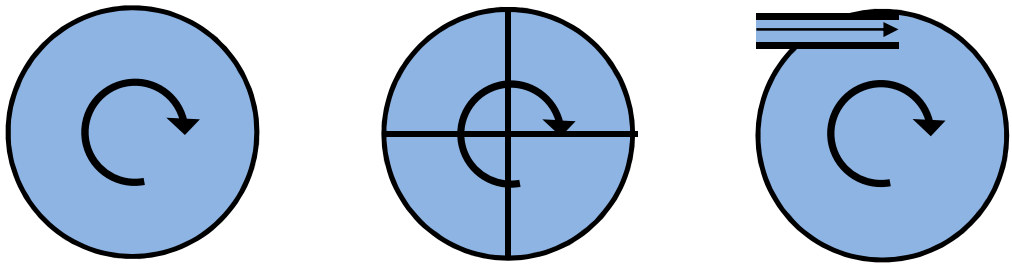

(a) (b) (c)

Figure 11.2 Diagrams showing the mechanisms of fluid acceleration (a) viscous dissipation (b) impulse force (c) mass flow induced velocity

Viscous dissipation occurs when rotation is induced by the boundary layer inside the accelerator. A simple example of viscous dissipation is inducing rotation of fluid in a circular container by spinning the container about the axis of the cylinder. This is typically a poor means of rotationally accelerating a fluid, especially in fluids with relatively low viscosity.

Applying an impulse force to rotationally accelerate a fluid occurs when a force is applied to the fluid by a solid body moving relative to a fluid. An example of an impulse force is rotating a circular container with radial paddles attached to the walls. The fluid adjacent to the paddles quickly reaches the solid-body rotation speed of the container.

Mass flow induced velocity occurs when the flow is forced to flow in the tangential direction, thereby increasing the tangential speed. An example of mass flow induced velocity is introducing water into a circular container so it causes rotation of the fluid.

It is intuitively known that viscous dissipation is a poor means of accelerating a liquid with low viscosity, and that imparting an impulse force is significantly better. Utilising the mass flow induced velocity is desirable to achieve additional acceleration.

11.3 Accelerator Designs

There are several feed accelerator designs that are commonly used in industrial centrifuges, but there is an absence of literature that presents the difference between these designs. Six designs were evaluated as part of this investigation; these were the Conical, Disk, Drum, Esbjerg, Plate, and Modified Disk accelerators. These designs are analysed experimentally and computationally in the two following chapters. The descriptions of the dimensions are for the model that was created for experimental and computational analysis. All accelerators rotate clockwise (as viewed on the page) and accept the stationary feed tube as shown in the figures.

11.3.1 Conical

The Conical accelerator with vanes was developed by Wallace Leung for the Bird Machine Company [13, 16, 17]. The design has a high level of complexity due to the vanes with consequent manufacturing implications. It was expected that the design would have good acceleration performance, and, given the correct design, would not significantly disturb the pool. Acceleration predominately occurs by an impulse force being applied by the vanes, some mass flow induced velocity will be captured by the forwards curving vanes.

The cone angle was 30° from the axis of rotation and the outer diameter was 115 mm. The cone was designed with eight, 8 mm high vanes that had a forward discharge angle of 45°. The vanes were set back from the edge of the cone by 5 mm to allow for the smoothening zone described by Leung.

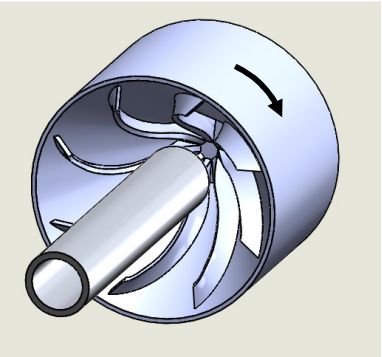

Figure 11.3 Conical accelerator

11.3.2 Disk

The Disk accelerator with vanes was also developed by Wallace Leung for the Bird Machine Company [13]. The design has a medium level of complexity due to the curved vanes and would therefore have some manufacturing complications. It was expected that the design would exhibit good acceleration performance, and, given the correct design, would not significantly disturb the pool. Acceleration predominately occurs by an impulse force being applied by the vanes, some mass flow induced velocity will be captured by the forward curving vanes.

There were six 20 mm high vanes. Each vane was 5 mm thick, starting as a radial vane in the centre and curving forwards to a discharge angle of 45° at a diameter of 115 mm. Unlike the conical accelerator, there was no method of flow smoothening.

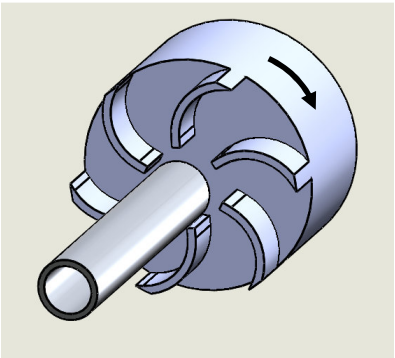

Figure 11.4 Disk accelerator

11.3.3 Drum

The Drum accelerator is the most common design in decanter centrifuges due to simplicity and ease of manufacturing. This type of accelerator offers no over-speeding effect and the use of discrete discharge ports would cause flow concentrations. A stand-

off tube is added to the accelerator discharge ports in some decanters to increase the radius. It is expected that the acceleration efficiency will be low as the accelerator relies on viscous dissipation from the inner wall, with a small amount of impulse force provided by the port faces.

There were four, equally spaced 20 mm diameter ports on the circumference of the 115 mm diameter cylinder. The wall thickness was 5 mm.

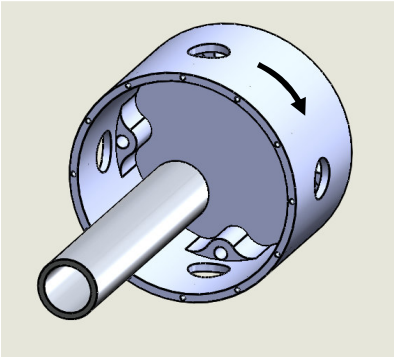

Figure 11.5 Drum accelerator

11.3.4 Esbjerg

The Esbjerg accelerator is a relatively simple design that can be easily incorporated into manufacturing by casting it into the solid conveyor hub. It was expected that the performance of this design would be poor as there is no over-speeding and wider discharge ports decrease the effective discharge radius. There will be viscous dissipation in the centre of the accelerator, with some impulse force provided by the accelerator faces. Some of the mass flow induced velocity will be lost as the profile of the accelerator causes the fluid to leave in a reverse direction.

The external diameter was 115 mm and the opening was 25 mm wide and 80 mm long.

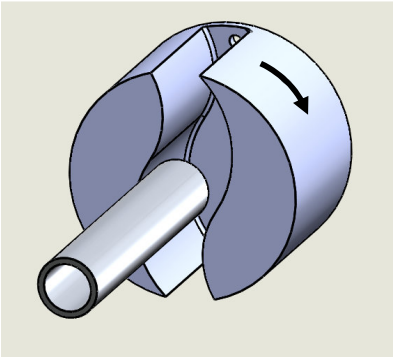

Figure 11.6 Esbjerg accelerator

11.3.5 Plate

The Plate accelerator has been adapted from the Drum accelerator. The port geometry was changed to slots and a plate was incorporated into the centre to reduce viscous acceleration and increase impulse acceleration. It was expected that this design would exhibit better performance than the Drum and Esbjerg accelerators, but would not match the Conical and Disk accelerators as it still offers no over-speeding. All of the acceleration provided by the Plate accelerator will be caused by impulse force due to the plate not allowing the fluid to rotate relative to accelerator. This configuration ensures the fluid will reach the solid body rotation speed of the accelerator but it offers no means of capturing the mass flow induced velocity.

The external diameter was 115 mm. The slots were 12.5 wide and 60 mm long. The wall thickness was 5 mm. A flow direction cone was included to aid with the redirection of flow from axial to radial.

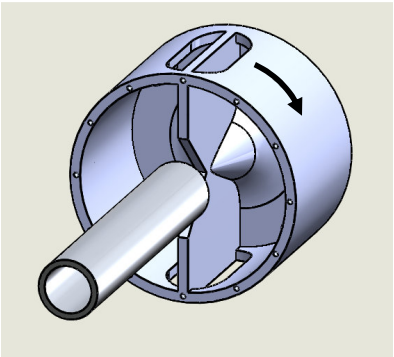

Figure 11.7 Plate accelerator

11.3.6 Modified Disk

The Modified Disk accelerator, shown in Figure 11.8, was created based on the test results of the previous five accelerators. The new design encompasses the features that were deemed effective. The Modified Disk accelerator is an adaptation of the Disk accelerator. Manufacturing of the Modified Disk accelerator will pose the same challenges as the Disk accelerator. It was expected that the Modified Disk accelerator would have the best performance of the tested designs as it attempts to capture the maximum amount of mass flow induced velocity.

The six vanes were curved so as to be tangential at the point of discharge. The discharge diameter was increased from 115 mm to 130 mm, and a cone was added to aid in the redirection of flow from axial to radial.

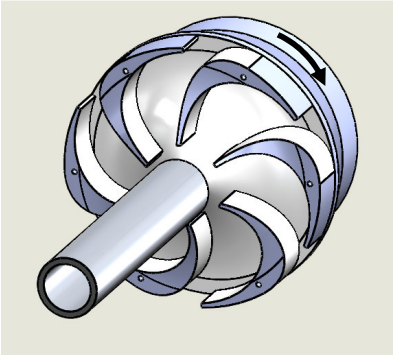

Figure 11.8 Modified Disk accelerator

11.4 Regions of Flow

There are five important regions of flow regarding the acceleration of the fluid: the feed tube, accelerator, annular space, disturbed pool, and undisturbed pool. The five regions are shown schematically in Figure 11.9. The critical flow characteristics within each region are highlighted and discussed in this section. The flow velocities, Reynolds numbers, and theoretical flow regime were determined where relevant.

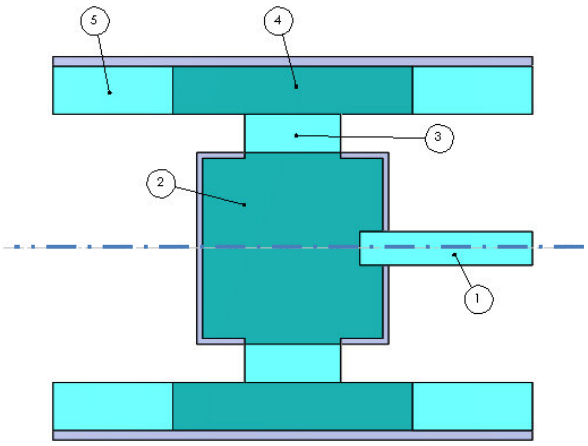

1. Feed tube
2. Accelerator
3. Annular space
4. Disturbed pool
5. Undisturbed pool

Figure 11.9 Regions in the feed acceleration process

11.4.1 Feed tube

The stationary feed tube brings the solids and liquid from outside the centrifuge to the feed accelerator. It is assumed that there is only axial flow in the tube and that swirl is negligible. The mean flow velocity in a pipe for a given mass flow rate is

$$v = \frac{\dot{m}}{\rho A} = \frac{4\dot{m}}{\rho \pi D_{FT}^2} \qquad 11.2$$

where

$\dot{m}$ mass flow rate (kg/s)

ρ density (kg/m^3)

A area normal to flow (m^2)

D_{FT} feed tube diameter (m).

The Reynolds number in a pipe is

$$Re = \frac{\rho v D_{FT}}{\mu} = \frac{4\dot{m}}{\mu \pi D_{FT}}. \qquad 11.3$$

where

μ dynamic viscosity (kg/m.s).

The flow is laminar for flows where the Reynolds number is less than 2200. The flow is turbulent for Reynolds numbers above 4000.

The GTech-Bellmor 1456 Centrifuge Decanter has a 35 mm diameter feed tube. The maximum flow rate is 12 tonnes per hour, which is equal to 3.3 kg/s. Considering the feed to be 25°C water, the Reynolds number is 136,000 and consequently fully turbulent flow probably exists. The average axial flow velocity is 3.5 m/s.

The experimental and computational analysis considers 0.5 kg/s of 25°C water passing through a 24 mm diameter feed tube. The Reynolds number in the feed tube for the experimental and computational analysis is 29,700, meaning fully developed turbulent flow exists. The average axial flow velocity is 1.1 m/s.

11.4.2 Accelerator

The accelerator must accept the axial flow from the feed tube and redirect it to radial and tangential flow. The flow within the accelerator is presented in Chapter 13.

11.4.3 Annular space

While the feed is not manipulated in the annular space it is a very important area for feed acceleration. The annular space is between the accelerator and the inner surface of the rotating fluid pool. A labelled diagram of the annular space is shown in Figure 11.10. The fluid leaves the accelerator at radius r_1 at an angle φ; it then enters the rotating fluid pool at radius r_2 at an angle ϑ from normal to the pool surface. Aerodynamic drag on the feed stream between the accelerator discharge ports and the liquid pool was deemed negligible as the relative velocity between the air and fluid stream is low.

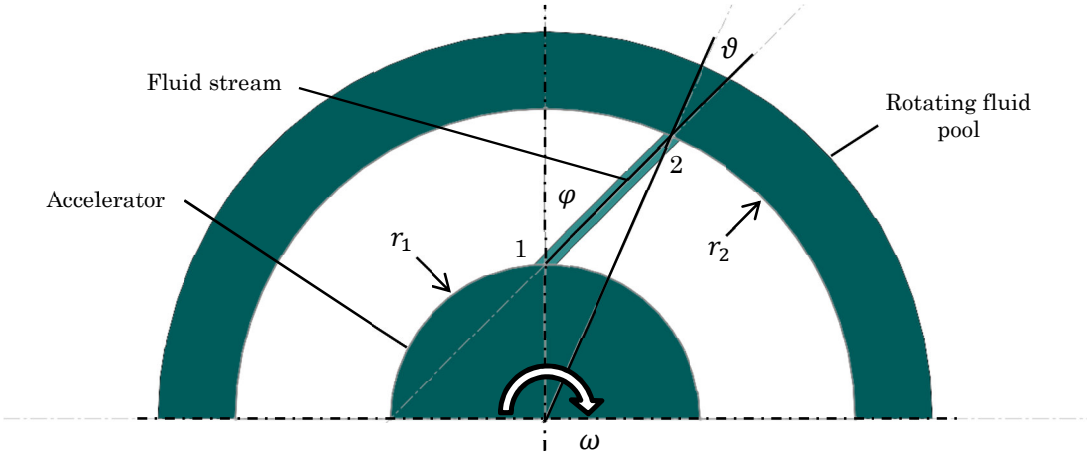

Figure 11.10 Diagram of annular space between the feed accelerator and rotating fluid pool

The velocity components at the accelerator exit are

$$u_{\theta 1} = u \sin \varphi \tag{11.4}$$

$$u_{r1} = u \cos \varphi \tag{11.5}$$

$$u = \sqrt{u_{r1}^2 + u_{\theta 1}^2} \tag{11.6}$$

where subscripts θ and r correspond to the tangential and radial components, respectively, and u is the magnitude of the absolute velocity of the fluid stream. The tangential velocity at the pool entry is

$$u_{\theta 2} = u \sin \vartheta. \tag{11.7}$$

The velocities that the feed has when it enters and leaves the annular space determine the acceleration efficiency. Leung [13] defined the accelerator efficiency as

$$\varepsilon_a = \frac{u_\theta}{\omega R}. \tag{11.8}$$

The radius R is defined as the discharge radius of the accelerator. The expression for the acceleration is simply the acquired tangential velocity of the flow divided by the solid body tangential speed of the bowl at a given radius. Another important performance metric is the pool efficiency, which is the ratio of the pool and bowl speeds

$$\varepsilon_p = \frac{\omega_p}{\omega_b}. \tag{11.9}$$

Leung also presented the expression for the g-force efficiency, which is the acceleration efficiency squared

$$\varepsilon_G = \left(\frac{u_\theta}{\omega R}\right)^2. \tag{11.10}$$

The g-force efficiency reveals the importance of acceleration on the attained g-force. If the fluid only has 50% of the solid body rotation speed of the bowl it will only have 25% of the required g-force. This can significantly reduce the equivalent settling area of the cylindrical section of the bowl.

The feed enters the annular space with the tangential and radial velocities $u_{\theta 1}$ and u_{r1}, respectively. When it leaves the annular space and enters the rotating pool it has the velocity components $u_{\theta 2}$ and u_{r2}. The ideal accelerator would ensure that the fluid has reached the solid body tangential speed at the pool entrance, which is equal to $u_{\theta 2} = \omega r_2$. The accelerator has a hub efficiency that is equal to

$$\varepsilon_H = \frac{u_{\theta 1}}{\omega r_1}, \tag{11.11}$$

which is equal to the acquired tangential velocity at point 1 divided by the solid body rotational speed at point 1, which is equal to the accelerator efficiency. The g-force efficiency at the point 2 (the pool surface) is

$$\varepsilon_G = \left(\frac{\varepsilon_H \omega r_1}{\omega r_2}\right)^2 = \left(\frac{\varepsilon_H r_1}{r_2}\right)^2. \tag{11.12}$$

With no over-speeding ($\varepsilon_H < 1$) the acceleration and g-force efficiency can never reach 100% due to r_1 being smaller than r_2. When ε_H is less than 1 the fluid has a lower tangential speed than the solid body tangential speed. When ε_H is greater than 1 the fluid has experienced over-speeding; this can only be achieved by utilising the mass flow induced velocity. This can be done by redirecting the fluid, giving it a tangential velocity component relative to the feed accelerator. The over-speeding effect is a function of volumetric flow rate and number, direction, and area of the feed streams. The additional tangential velocity is

$$u_{m\theta} = \frac{\dot{m}}{\rho A_F n} \sin \varphi \tag{11.13}$$

where

n number of fluid streams leaving the accelerator

A_F cross-sectional area of the fluid stream normal to the direction of flow (m^2).

The tangential velocity can be increased by increasing the mass flow rate or discharge angle φ, or decreasing the area of the fluid stream.

If the feed is over or under-accelerated it does not enter the pool adjacent to the feed port. It also enters the pool at a shallower angle than it left the feed port, this is apparent in Figure 11.10, where φ is always greater than ϑ. The accelerator and pool surface radii ratio is

$$q = \frac{r_1}{r_2}. \tag{11.14}$$

The actual angle that the feed enters the pool is

$$\vartheta = \sin^{-1}(q \sin(\varphi)) \tag{11.15}$$

The maximum angle that the feed can leave the accelerator is $\varphi = 90°$. The expression for ϑ simplifies to

$$\vartheta_{\varphi \to 90°} = \sin^{-1}(q). \tag{11.16}$$

This is the maximum angle that the feed can enter the rotating pool for a given radius ratio. The radius ratio of the GTech-Bellmor 1456 Centrifuge Decanter varies from 0.63 to 0.74. Figure 11.11 contains a plot of the accelerator discharge angle versus the pool entry angle. The plot reveals the maximum pool entry angle is less than 50°, even when the fluid leaves the accelerator at the optimum angle of 90°.

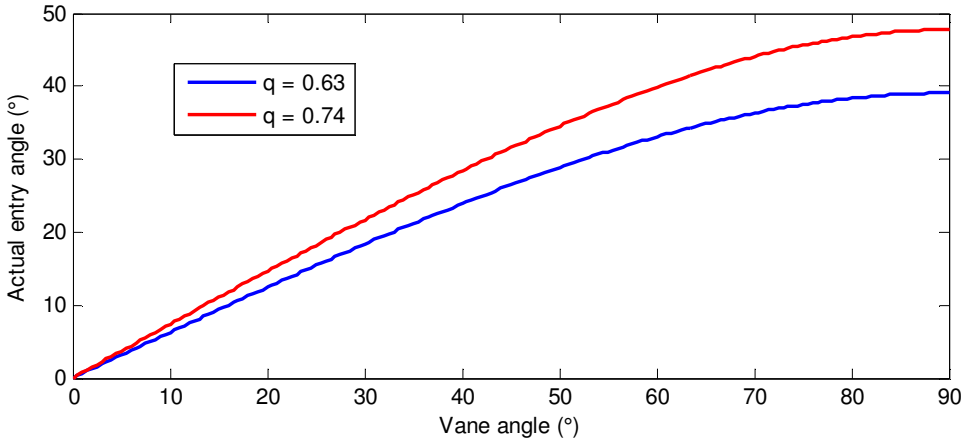

Figure 11.11 Accelerator discharge angle versus pool entry angle

Several conclusions can be drawn from the analysis of the annular space:

- With no over-speeding the acceleration efficiency is dominated by the radius ratio
- To achieve 100% efficiency the mass induced velocity through the accelerator ports must be high, this could potentially lead to the undesired pool penetration
- The over-speeding must compensate for the velocity difference between the accelerator outlet and the entry to the rotating liquid pool
- A simple method of increasing the efficiency of the accelerator is maximising the radius ratio

11.4.4 Disturbed pool

When the flow enters the pool it will inevitably cause some disturbance. Minimising the disturbed area is an important aspect of the accelerator design. The depth of penetration of the incoming feed stream is of the upmost importance. If the stream penetrates the pool too deeply it will disturb the settled solids. The rotating pool can be viewed as a stationary, quiescent layer of water. The pressure varies significantly throughout the shallow depth of water due to the centripetal acceleration. The effect of a translating jet of liquid plunging into a quiescent pool was studied by Gomez et al [57]. Gomez observed that after the jet has impacted the surface it creates two craters (one upstream and one downstream of the translating jet), it then quickly slows to a nearly constant speed and continues to propagate downwards. It is shown by Gomez that submerged jet velocity reduces to half of the initial jet velocity, this is also shown by Birkhoff & Zarantonello [58]. Bin [59] investigated the effect of a steady-state plunging jet, which causes air to be entrained in a bath. Further analysis of the effect of pool penetration is required.

11.4.5 Undisturbed pool

The fluid within the undisturbed pool will be rotating as a solid body at the same speed as the bowl. The only motion relative to the bowl will be in the mass flow of the liquid moving to the discharge ports and some disturbance by the rotating scroll. The flow regime in this region is of interest, as mixing of the settled solids and liquid is undesirable. Determining the Reynolds number in this region will indicate the flow regime. There are two ways of considering the flow in the settled pool, axial flow and helical flow. Axial flow ignores the path made by the scroll, while helical flow follows it.

Axial flow

The hydraulic diameter for axial flow is the wetted area

$$D_H = \frac{4A}{P} = \frac{2(r_o^2 - r_{dL}^2)}{r_o}. \quad 11.17$$

The flow velocity is

$$v = \frac{\dot{m}}{\rho A} = \frac{\dot{m}}{\rho\pi(r_o^2 - r_{dL}^2)}. \quad 11.18$$

The Reynolds number is

$$Re = \frac{\rho v D_H}{\mu} = \frac{2\dot{m}}{\mu\pi r_o}. \quad 11.19$$

The Reynolds number for the GTech-Bellmor 1456 Centrifuge Decanter processing 12 t/h of 25°C water is equal to 13,486. The average axial flow velocity is 0.085 m/s.

Helical flow

For fluid that follows the helical path created by the scroll the area of flow is

$$A = (r_o - r_{dL})G \quad 11.20$$

and the wetted perimeter is

$$P = 2(r_o - r_{dL}) + G. \quad 11.21$$

Therefore the hydraulic diameter is

$$D_H = \frac{4(r_o - r_{dL})G}{2(r_o - r_{dL}) + G}. \quad 11.22$$

The average flow velocity is

$$v = \frac{\dot{m}}{\rho A} = \frac{\dot{m}}{\rho(r_o - r_{dL})G}. \quad 11.23$$

The Reynolds number is

$$Re = \frac{\rho v D_H}{\mu} = \frac{2\dot{m}}{\mu(2(r_o - r_{dL}) + G)}. \quad 11.24$$

The majority of the flow occurs in a thin layer on the inner surface of the rotating liquid pool, this is due to the liquid discharging over weirs. The Reynolds number for the

GTech-Bellmor 1456 Centrifuge Decanter processing 12 t/h of 25°C water is equal to 49,880. The average flow velocity is 1.2 m/s. A Reynolds number of this magnitude suggests the flow is turbulent. The Reynolds number could be reduced by decreasing the liquid discharge radius or increasing the scroll pitch.

11.5 Performance Metrics

Hub efficiency	$\varepsilon_H = \frac{u_{\theta 1}}{\omega r_1}$	Indicates the effectiveness of the accelerator design at meeting the tangential speed at the exit of the accelerator
Accelerator efficiency	$\varepsilon_a = \frac{u_\theta}{\omega r_2}$	Gives the overall efficiency of accelerating the feed to the speed of the liquid pool
g-force efficiency	$\varepsilon_G = \left(\frac{u_\theta}{\omega r_2}\right)^2$	The g-force efficiency is the effectiveness of the accelerator at obtaining the required G-force
Radial entry speed	$u_{r2} = u \cos \varphi$	A measure of the radial speed that the feed stream enters the rotating pool
Pool efficiency	$\varepsilon_p = \frac{\omega_p}{\omega_b}$	Ratio of the pool speed and the bowl speed

11.6 Conclusions

The three mechanisms available for inducing a tangential velocity on the incoming feed are viscous dissipation, impulse force, and mass flow induced velocity. Intuitively, an impulse force is better than viscous dissipation, and the use of any mass flow induced velocity is desirable.

The accelerator designs that were identified for further analysis were the Conical, Disk, Drum, Esbjerg, Plate, and Modified Disk accelerators. It was expected that the Conical, Disk, and Modified Disk accelerators would be the best performing as they predominately use impulse force to accelerate the feed, and capitalise on the mass flow induced velocity.

Several performance metrics were derived during the analytical and geometrical analysis; these were the hub efficiency, accelerator efficiency, g-force efficiency, radial entry speed, and pool efficiency.

There are three methods available to improve the efficiency of the accelerator:

- Maximise the hub efficiency by careful design of the accelerator
- Discharge the fluid from the feed accelerator at a positive angle; this can be achieved by utilising the mass flow induced velocity

- Maximise the ratio of the accelerator discharge radius and the inner radius of the pool, either by increasing the pool depth or increasing the accelerator diameter

Chapter 12

Experimental Evaluation of the Feed Accelerator for a Decanter Centrifuge

12.1 Introduction

An experimental method was developed to quantitatively examine decanter centrifuge feed accelerator designs. The experiment allowed for the measurement of acceleration efficiency and high-speed photography of the flow in the annular space between the accelerator and the rotating pool. The designs considered were the Conical, Disk, Drum, Esbjerg, Plate, and Modified Disk accelerators as presented in Figure 11.3 to Figure 11.8. These designs were identified as being the most commonly used by industry and therefore the most appropriate to experimentally evaluate.

The test rig was developed to simulate the feed as it entered the centrifuge and is accelerated in the centre hub. The feed enters the centrifuge along the axis of rotation and must be moved radial to the rotating pool and attain the solid body rotation speed of the bowl. The experiment was designed to simulate the feed entering the centrifuge in this way and to allow for different accelerator designs to be tested. The experiment also allowed for insight into other aspects of the feed accelerator, such as vibration levels, and manufacturing implications of the different accelerator designs.

High speed photography allowed for a detailed insight into the subtly different flow patterns of the fluid in the annular space and in the disturbed pool. The images of the flow were also used to qualitatively validate the computational model.

This chapter includes a full description of the testing apparatus that was developed for this work, the testing procedure, results, and a discussion. The results are compared to the computational results in Chapter 13.

12.2 Testing Apparatus

A test rig was developed to recreate the flow entering the centrifuge. The rig needed to simulate an axial flow entering a rotating bowl on the axis of rotation. The helical scroll was not included in the test rig as it has no effect on the accelerator performance. The rotating bowl was supported at one end and water was fed in through a stationary feed

tube at the other. The accelerator was fixed to the rotating bowl. Free-wheeling paddles rotate with the pool and were used to deduce the rotational velocity of the pool. The bowl and rotation meter were enclosed in a sheet metal enclosure to capture the discharging water. One end could be opened to allow for high-speed photography. The specifications of the test rig are shown in Table 12.1. The ratio of the internal bowl diameter and the conveyor hub was 0.55, which is similar to the value used in full size decanter centrifuges. A schematic of the test rig is shown in Figure 12.1. A cross-section of the test rig is shown in Figure 12.2.

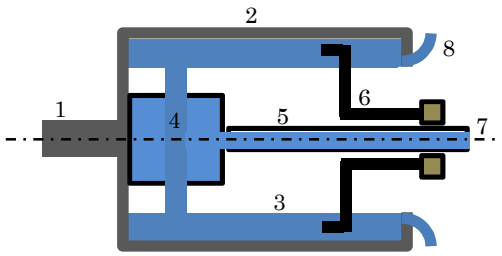

1. Drive shaft
2. Rotating bowl
3. Rotating liquid pool
4. Feed Accelerator
5. Stationary feed tube
6. Rotation meter
7. Water inlet
8. Water discharging over weir plate

Figure 12.1 Schematic of the feed accelerator test rig

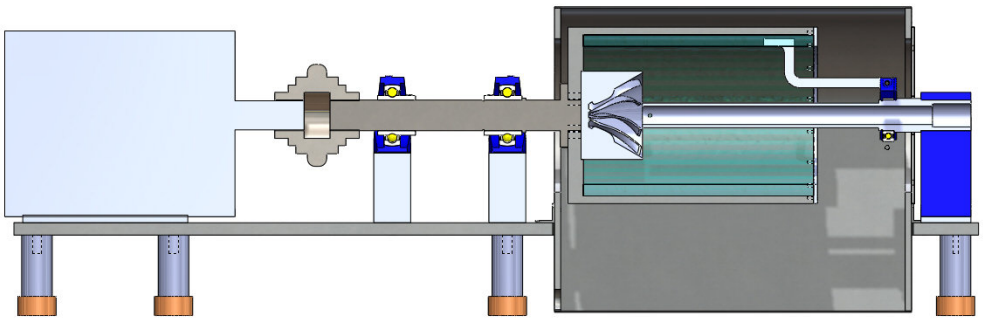

Figure 12.2 Cross-section of the feed accelerator test rig

Table 12.1 Feed accelerator test rig specifications

Motor power	7.5 kW
Bowl speed	1000 rpm
Maximum flow rate	40 l/min
Maximum g-force	117g
Pool ID	180 mm
Pool length	300 mm
Feed tube ID	24 mm
Bowl ID	210 mm

The test rig was manufactured by the technical staff in the Department of Mechanical Engineering at the University of Canterbury. Machining and fabrication of all the individual components took approximately 180 hours. The rig was assembled in the laboratory wing. A photograph of the fully assembled rig is shown in Figure 12.3.

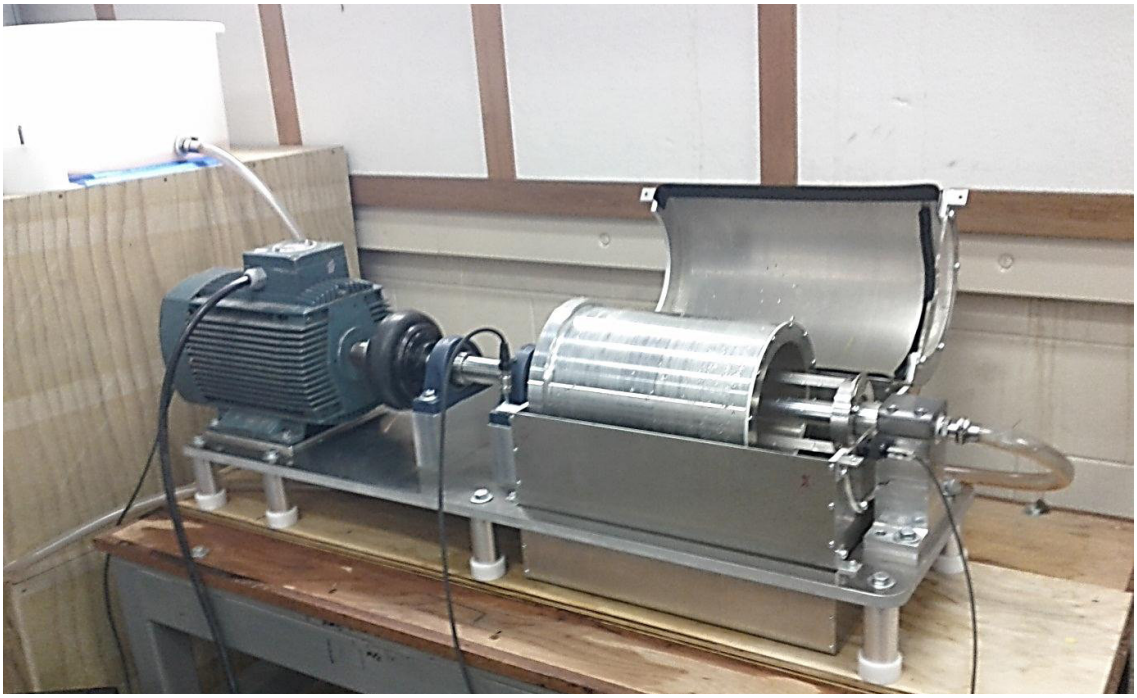

Figure 12.3 Assembled feed accelerator test rig

12.2.1 Bowl speed control

The bowl speed was controlled using a VSD. The speed was regulated with closed loop control between a shaft mounted encoder and the VSD. A signal was then fed to the data acquisition system and converted to rpm. It was found that the output was inconsistent and not sensitive to small speed variations. An optical tachometer was used to remedy this. The speed variation between the LabView output and the optical tachometer is shown in Figure 12.4. Due to the large discrepancy between the actual and measured bowl speed the tachometer output was used. The tachometer precision was 0.1 rpm below 1000 rpm and 0.5 rpm above 1000 rpm. At 1000 rpm this was only ±0.05%. The speed for the 1000 rpm test was measured to be 999.6 rpm; this value was used for the efficiency calculations.

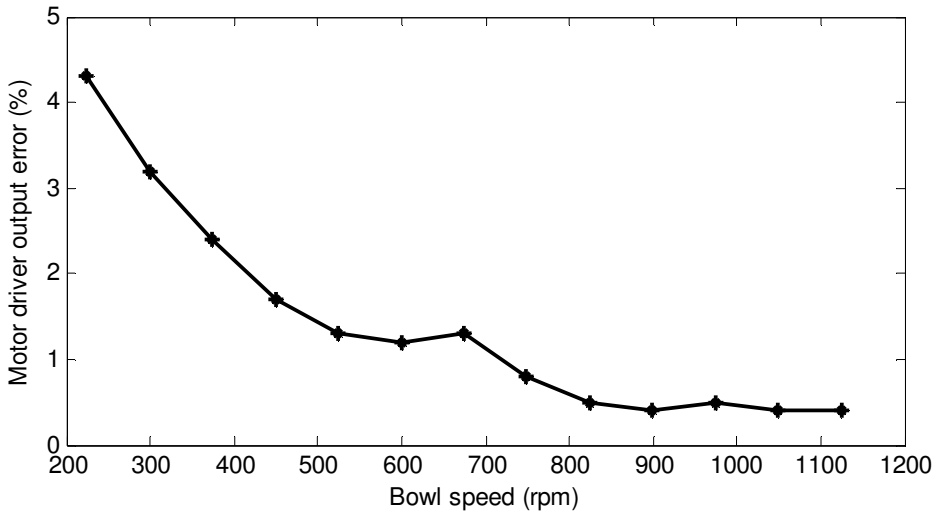

Figure 12.4 Percentage error of bowl speed output in LabView from the optical tachometer

12.2.2 Pool speed measurement

The pool speed was measured by the rotation meter, which consisted of two paddles mounted on a free-wheeling hub fixed to the feed tube. The paddles protruded 10 mm into the rotating pool. The speed was measured using a double-pass Hall Effect sensor. The rotation meter speed was validated using a handheld optical tachometer. A variation of approximately ±2 rpm was observed for the rotation meter speed. Slip between the rotation meter and the rotating pool occurred due to aerodynamic drag on the paddles and friction within the bearing. To determine the correct pool speed, the slip of the rotation meter s was measured. This was achieved by holding the bowl at a constant speed ω_b and recording the rotation meter speed ω_r once the steady-state for no water flow was achieved. The pool was filled to weir. This was based on the assumption that the pool eventually reached the solid body rotation speed of the bowl. The slip is expressed as

$$s = \left(1 - \frac{\omega_r}{\omega_b}\right). \qquad 12.1$$

The slip percentage for the rotation meter for 500 to 1100 rpm was measured for each accelerator design before and after each run. The slip varied between 5% and 10% of the bowl speed. The slip percentage for the rotation meter for 500 to 1100 rpm is shown in Figure 12.5. The differential speed between the bowl and rotation meter is shown in Figure 12.6. The slip was measured before and after each design was tested to ensure repeatability and accuracy. The slip is higher at lower running speeds. This is possibly

due to the bearing being more efficient at higher speeds and force exerted by the water on the paddles is greater at higher speeds.

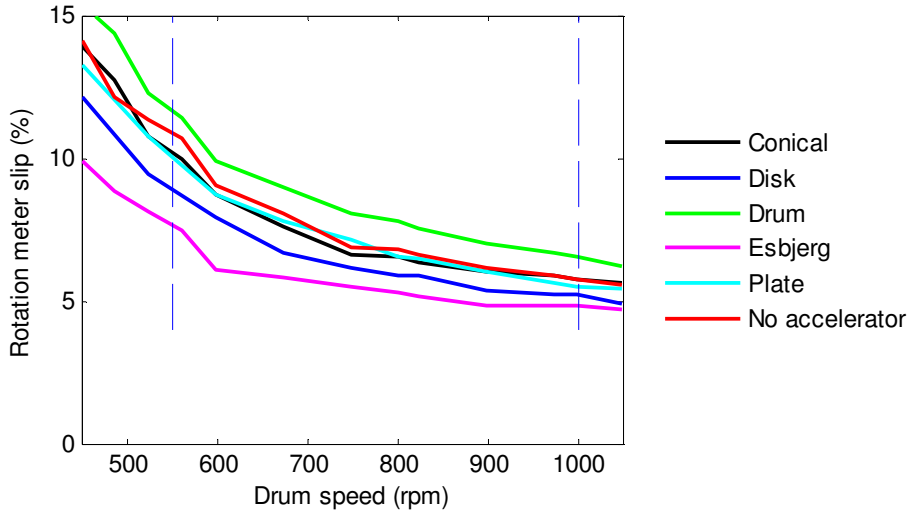

Figure 12.5 Rotation meter slip for bowl speeds from 500 to 1100 rpm, the vertical dashed lines enclose the measured speed range of all accelerator designs

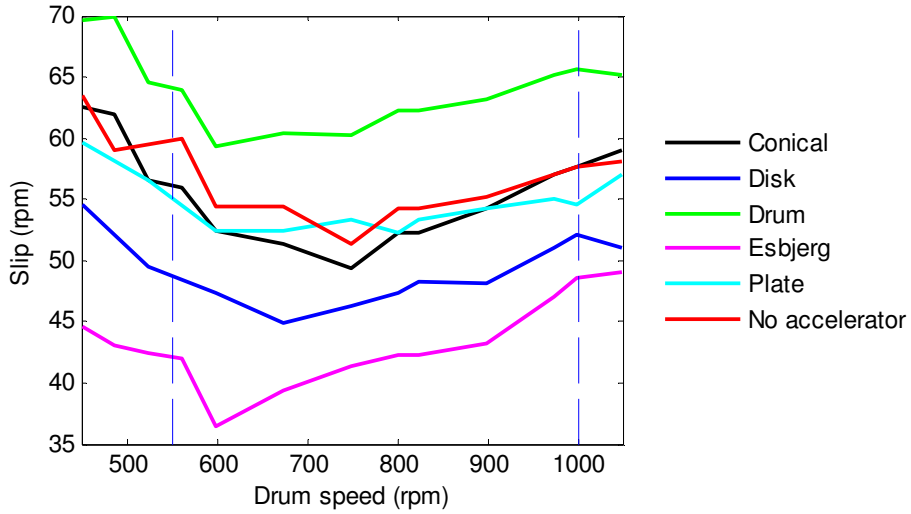

Figure 12.6 Rotation meter slip for bowl speeds from 500 to 1100 rpm, the vertical dashed lines enclose the measured speed range of all accelerator designs

12.2.3 Flow control

It was important to be able to accurately control the flow rate to obtain consistent results. A circuit was constructed with a positive displacement piston pump and a VSD to provide a constant flow rate. A header tank was included above the test rig to smooth

the pulses caused by the pump. The water level in this tank was able to fluctuate depending on the flow rate. A schematic of the flow circuit is shown in Figure 12.7.

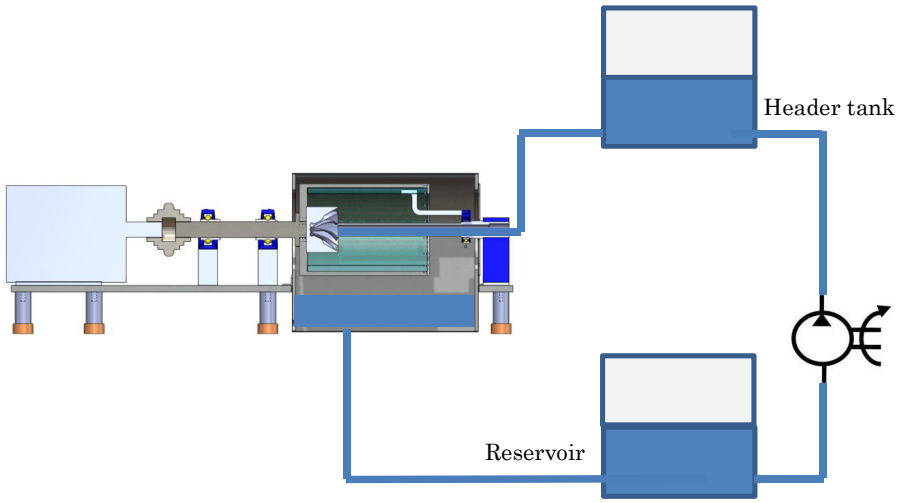

Figure 12.7 Flow control circuit for the feed accelerator test rig

The pump flow rate was measured as a function of the setting on the VSD. The time taken to fill a fixed volume of 10 litres was measured. The flow rate $\dot{V}$ in liters per minute as a function of the VSD setting C was

$$\dot{V} = 0.8142(C) - 0.6523. \qquad 12.2$$

12.2.4 Accelerometer

A single-axis accelerometer was mounted on the bearing housing closest to the bowl. The acceleration levels were recorded at each flow measurement for all accelerator designs. An FFT analysis was performed on five seconds of data from 0 to 100 Hz, this allowed for the peaks and overall amplitude to be examined for each accelerator. The increase in vibration level between the accelerator having no flow and 30 l/min was of interest. For the no flow vibration measurement, the bowl was filled with water and the flow was switched off. The measurement was taken once the pool speed reached steady state. This was intended to capture the vibration due to the imbalance of the bowl, shaft, and accelerator. The accelerometer was also used to balance the bowl and drive shaft.

12.2.5 Accelerator construction

All of the accelerator designs were made from ABS using a 3D printer. Printing the designs allowed for the analysis of complex geometries such as the Conical and Disk accelerators. The accelerators had a 1 to 1.2 mm skin and were filled with a honeycomb scaffold. Each model took approximately 12 hours to produce. Four accelerator models are shown in Figure 12.8.

Figure 12.8 Models prepared for testing using the 3D printer. From left: Conical, Disk, Esbjerg, and Plate accelerators

Each accelerator design, excluding the Conical accelerator, had a cover plate fitted over the end with a 40 mm diameter hole to accommodate the feed tube. The feed tube for the Conical accelerator was extended as far as possible towards the root of the vanes to ensure the effects of gravitational droop were negligible. The feed tube terminated at the inner surface of the cover plate for the other designs. An exploded view of the Disk accelerator with the cover plate is shown in Figure 12.9.

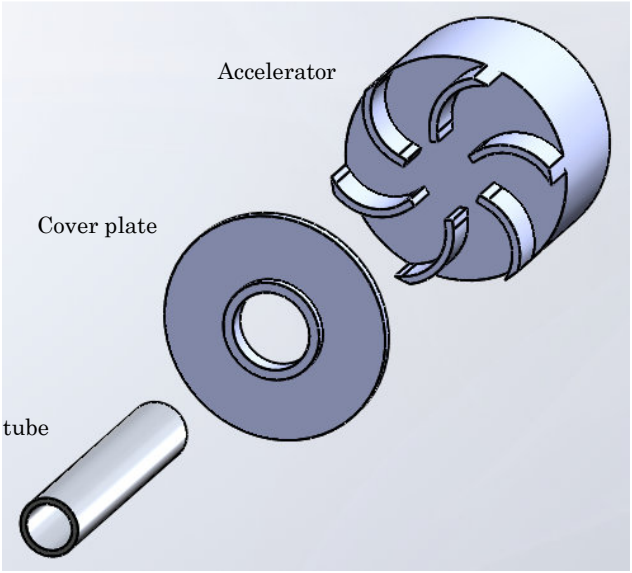

Figure 12.9 Exploded view of the Disk accelerator showing the end cover plate and feed tube

12.2.6 Testing procedure

The same test procedure was followed for each accelerator design. All designs were tested at least twice. The accelerator was fitted into the test rig and bolted in place. The water in the reservoir was heated to 25°C. The bowl was accelerated to the running speed and filled with water, the rotation meter slip was measured between 500 and 1000 rpm. The bowl speed was then set to 1000 rpm. The water pump was switched on and flow was passed through the rig. The flow rate was raised incrementally from 3.4 to 40 l/min. Once the steady-state was achieved at each flow setting, the rotation meter speed and acceleration levels were recorded. The rotation meter speed was adjusted to account for slip. At the conclusion of the test the slip was measured again.

A full test was completed with no accelerator fitted to give a control value for the accelerator performance The incoming feed poured out of the feed tube into the rotating bowl with no pre-acceleration. This was used to determine the amount of acceleration the rotating pool induced on the fluid. The amount each accelerator design increased the pool speed was then able to be determined.

12.2.7 High-speed photography

High-speed photography allowed for a detailed insight into the flow patterns within the test rig. A MotionPro X3 high-speed camera and a 1 kW stage light were employed to capture images of the flow passing through the annular space between the accelerator and rotating pool. A frame rate of 900 fps was used. The aperture time was decreased to

the minimum required level to ensure the images did not become blurred. The bowl speed and water flow rate were set to 1000 rpm and 30 l/min during filming, respectively.

The camera and light were positioned approximately 1 m from the end of the test rig. This distance was maintained as the splash guards had been removed and a small amount of water was being sprayed in the direction of the camera. The camera was fixed to a tripod to ensure repeatable images were obtained. The stage light was held by hand so small perturbations could be made to optimise the lighting. A diagram of the camera and light positions relative to the test rig are shown in Figure 12.10.

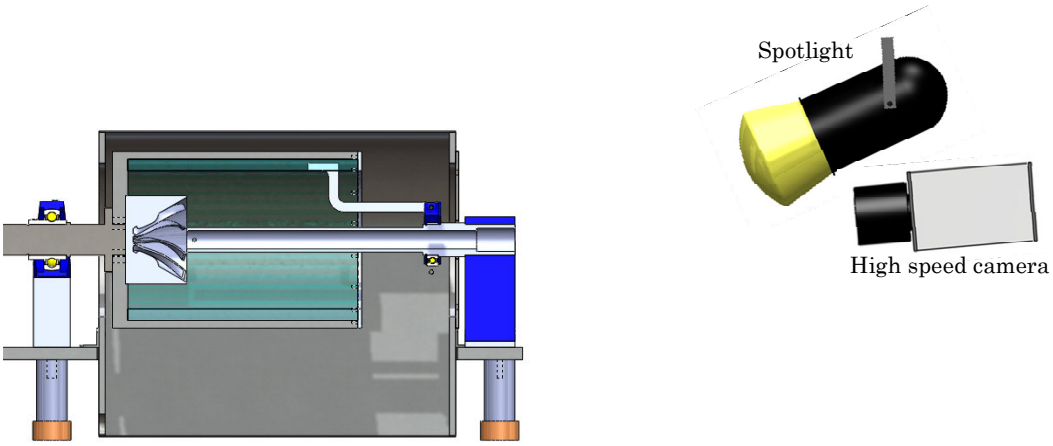

Figure 12.10 Location of light and high-speed camera relative to the test rig

Initial camera work was completed but the images were unclear due to poor lighting. The inability to shine the light directly on the accelerator was because nearby reflective surfaces caused wash-out. This was remedied by painting those reflective surfaces black. This significantly improved the quality of the images. A comparison is shown in Figure 12.11.

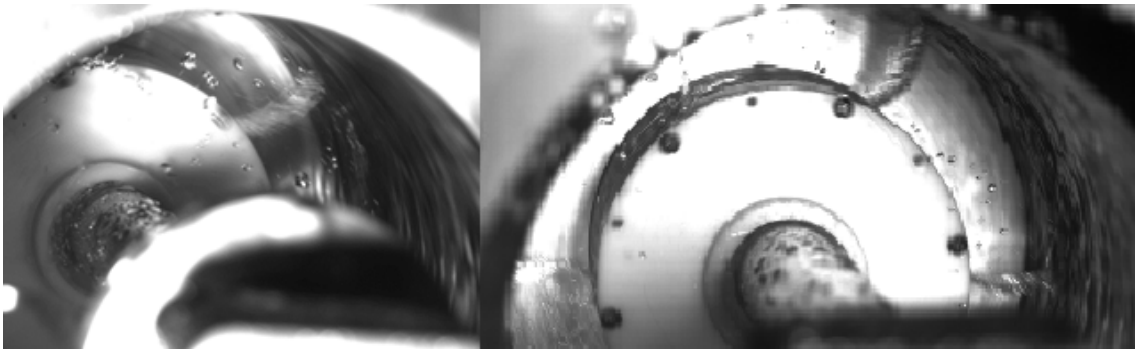

(a) (b)

Figure 12.11 The effect of painting the reflective surfaces black and increasing the light directed at the feed accelerator (a) unpainted (b) painted

The procedure for filming each accelerator was the same, involving focusing the image on the accelerator using the fine adjustment on the lens. The pump was then run until the required flow rate was achieved. The drive motor was turned on and the bowl and accelerator were accelerated to 1000 rpm. Once satisfactory lighting was achieved the images were recorded for approximately two seconds.

12.3 Results

The acceleration efficiency, both measured and corrected for slip, are given in Figure 12.12 (Conical), Figure 12.14 (Disk), Figure 12.16 (Drum), Figure 12.18 (Esbjerg), Figure 12.20 (Plate), and Figure 12.22 (Modified Disk), and for no accelerator in Figure 12.24. The corrected efficiencies for all designs are shown in Figure 12.28. The best images of the flow in the annular space are given in Figure 12.13 (Conical), Figure 12.15 (Disk), Figure 12.17 (Drum), Figure 12.19 (Esbjerg), Figure 12.21 (Plate), and Figure 12.23 (Modified Disk). The total vibration levels for each accelerator are shown in Figure 12.25. The FFT plots for the measured vibration are shown in Figure 12.26 and Figure 12.27.

12.3.1 Conical

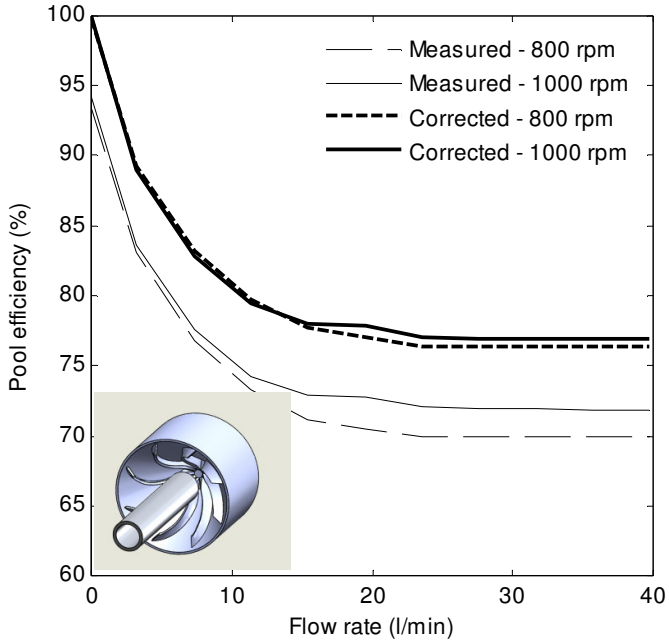

Figure 12.12 **Pool efficiency of the Conical accelerator, showing both measured and corrected values**

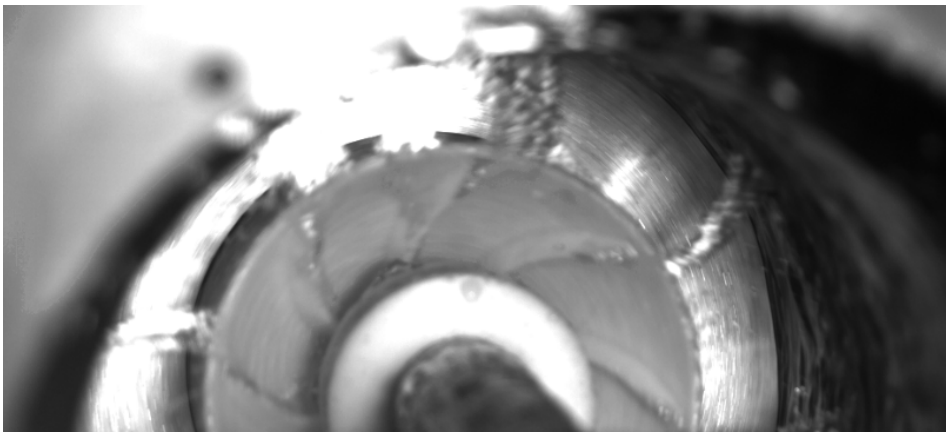

Figure 12.13 Photograph of the Conical accelerator operating at 1000 rpm and 30 l/min of water at 25°C

12.3.2 Disk

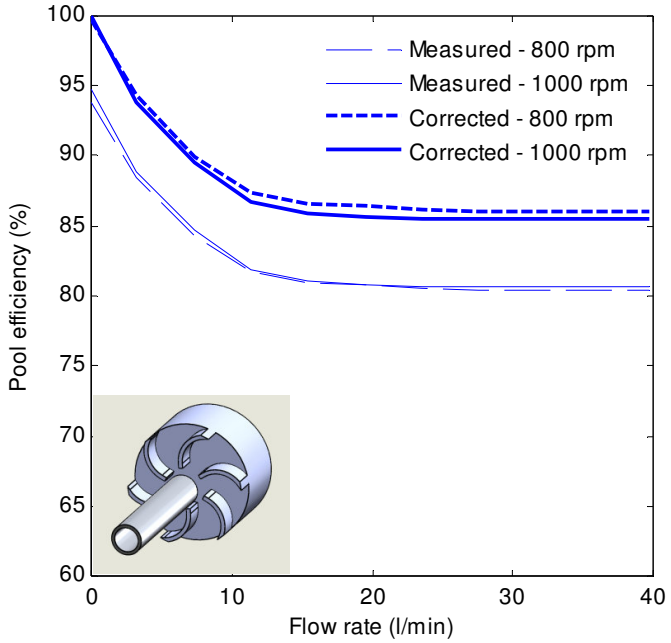

Figure 12.14 Pool **e**fficiency of the Disk accelerator, showing both measured and corrected values

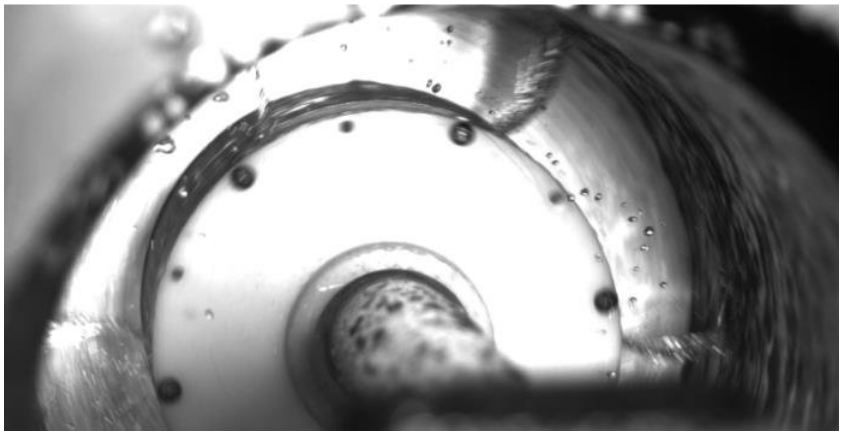

Figure 12.15 Photograph of the Disk accelerator operating at 1000 rpm and 30 l/min of water at 25°C

12.3.3 Drum

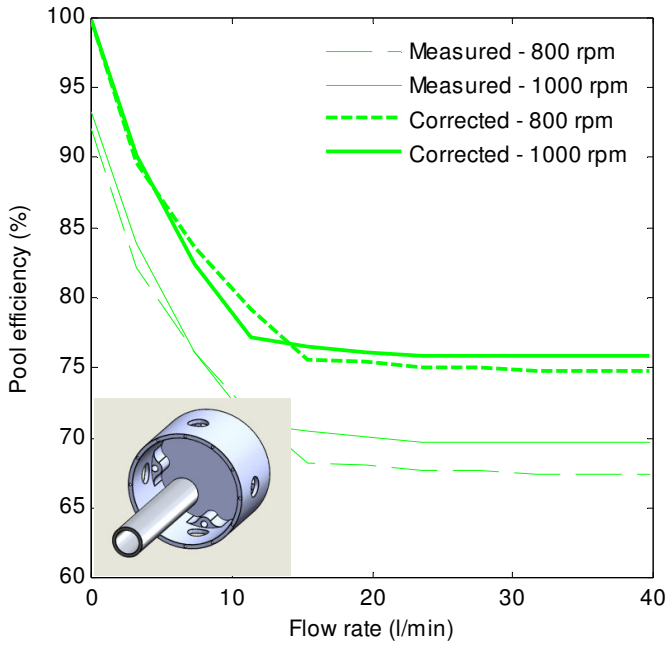

Figure 12.16 Pool efficiency of the Drum accelerator, showing both measured and corrected values

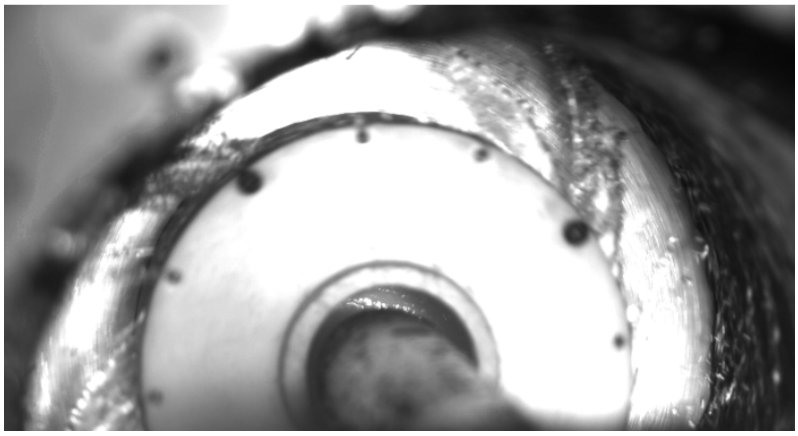

Figure 12.17 Photograph of the Drum accelerator operating at 1000 rpm and 30 l/min of water at 25°C

12.3.4 Esbjerg

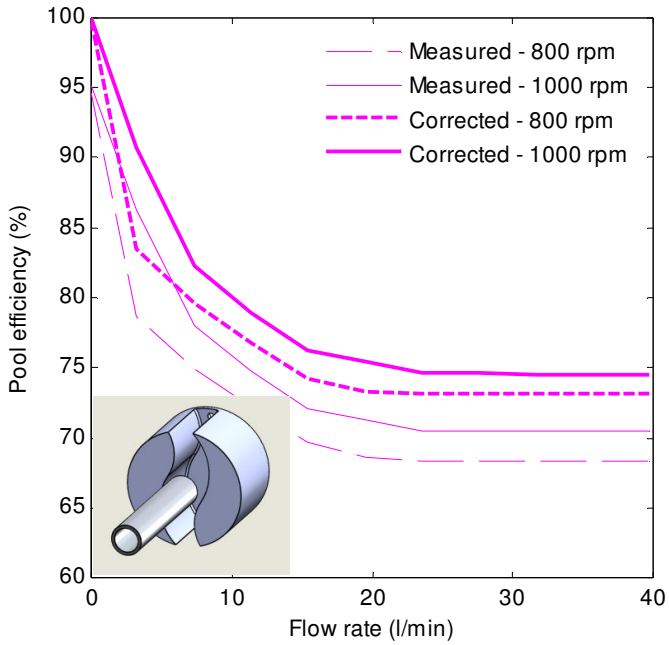

Figure 12.18 Pool efficiency of the Esbjerg accelerator, showing both measured and corrected values

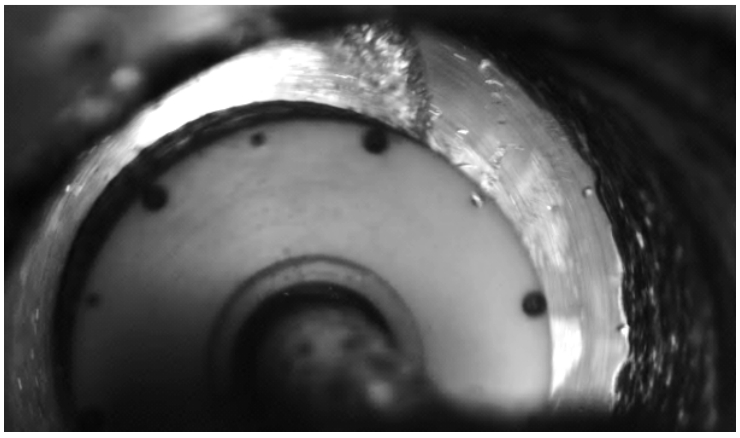

Figure 12.19 Photograph of the Esbjerg accelerator operating at 1000 rpm and 30 l/min of water at 25°C

12.3.5 Plate

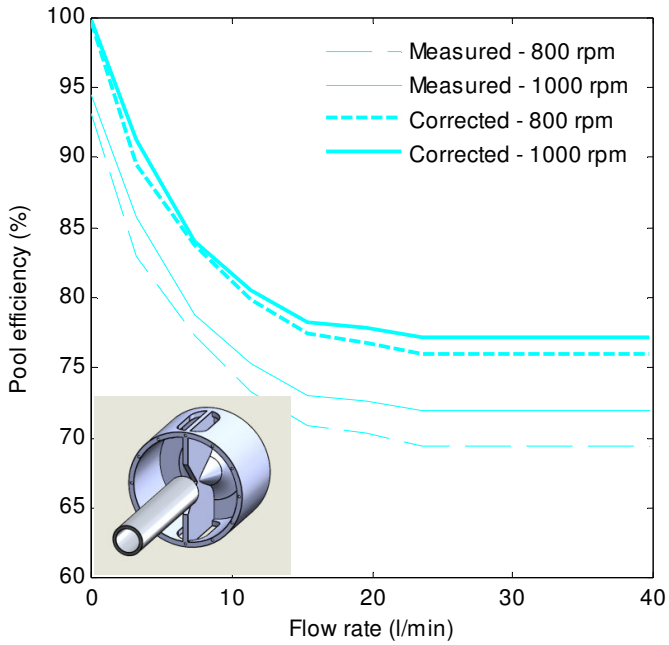

Figure 12.20 Pool efficiency of the Plate accelerator, showing both measured and corrected values

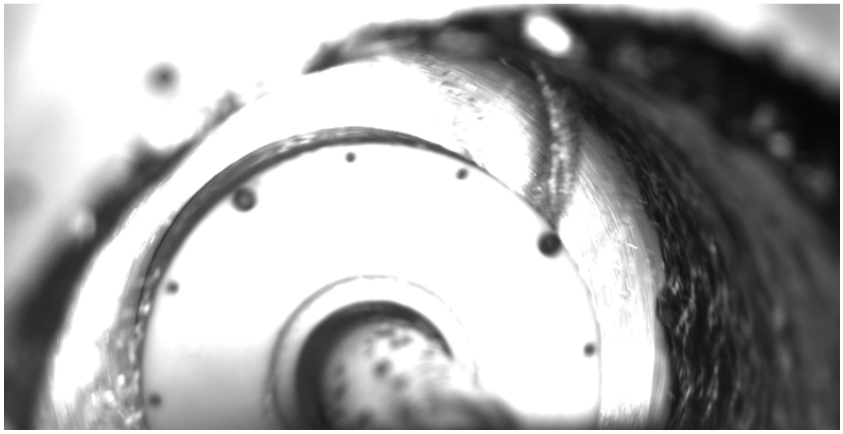

Figure 12.21 Photograph of the Plate accelerator operating at 1000 rpm and 30 l/min of water at 25°C

12.3.6 Modified Disk

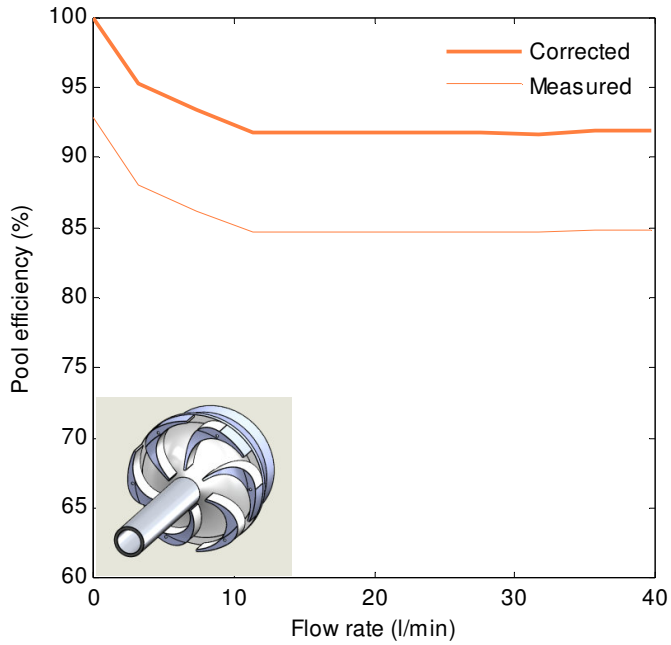

Figure 12.22 Pool **e**fficiency of the Modified Disk accelerator, showing both measured and corrected values

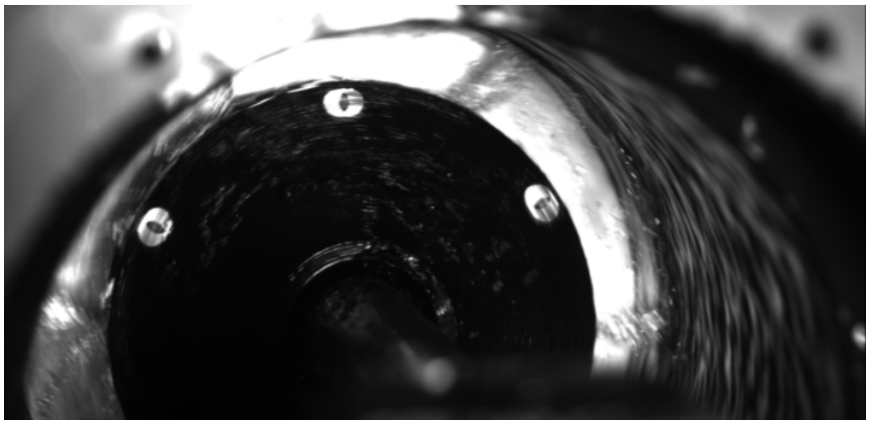

Figure 12.23 Photograph of the Modified Disk accelerator operating at 1000 rpm and 30 l/min of water at 25°C

12.3.7 No accelerator

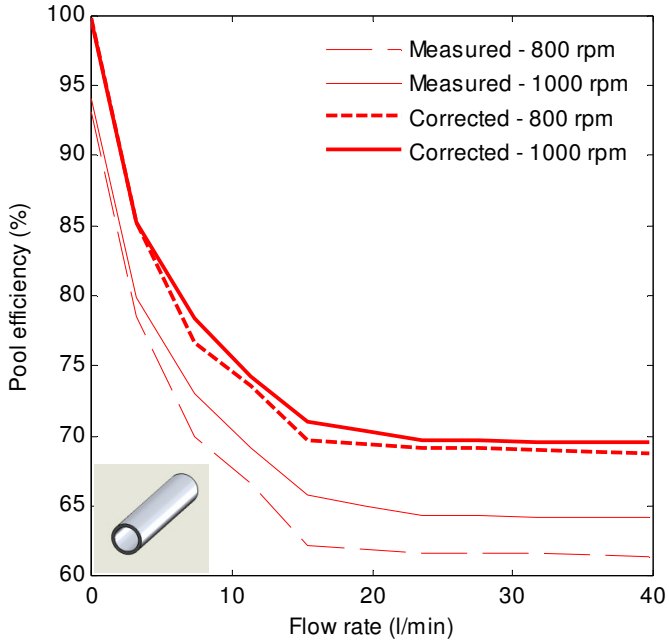

Figure 12.24 Pool efficiency with no accelerator fitted

12.3.8 Accelerometer results

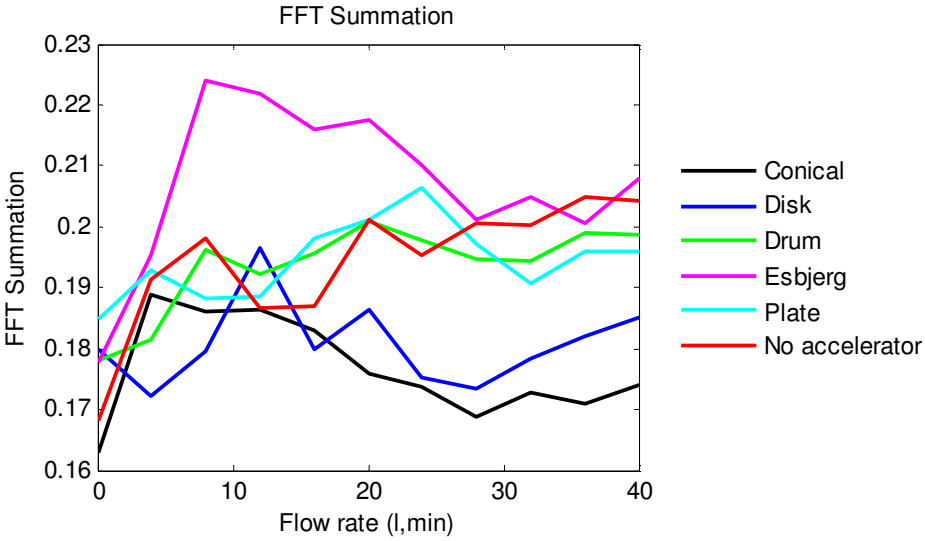

Figure 12.25 Total acceleration levels for all accelerator designs, excluding the Modified Disk accelerator

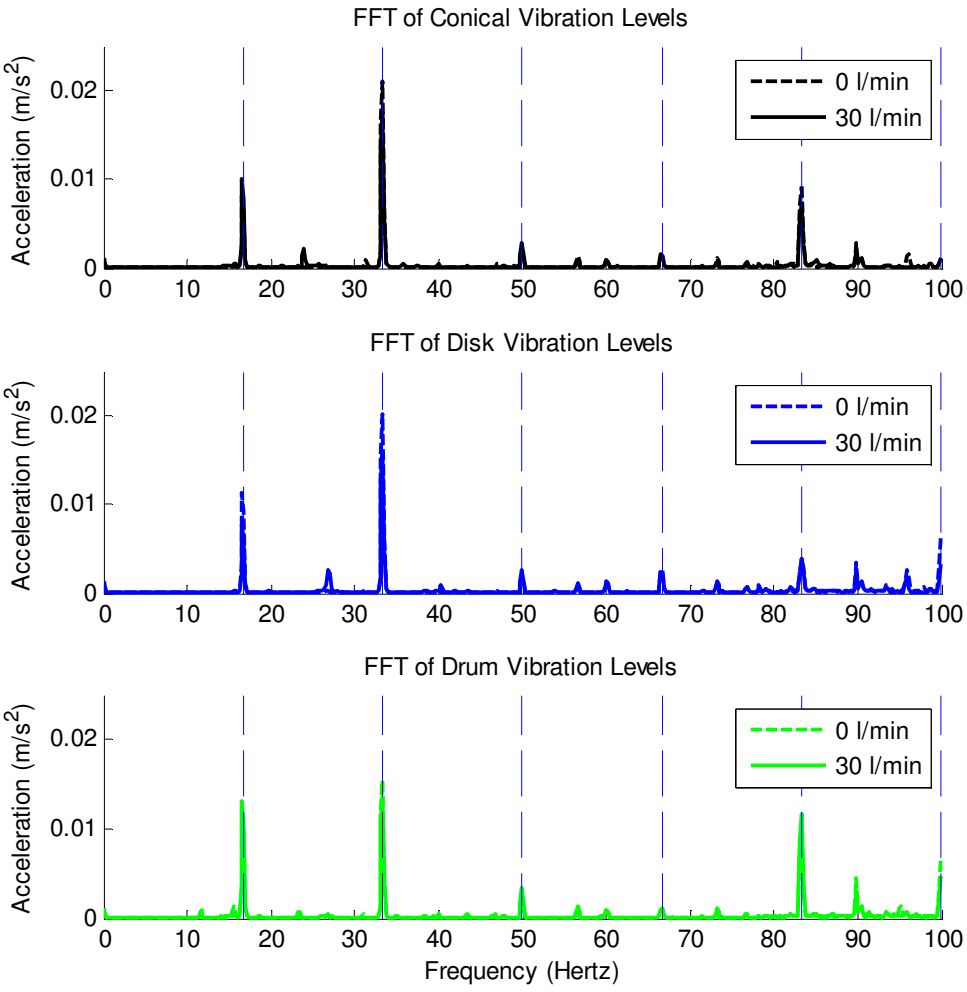

Figure 12.26 FFT plots for the Conical, Disk, and Drum accelerators for no flow and 30 l/min at 1000 rpm

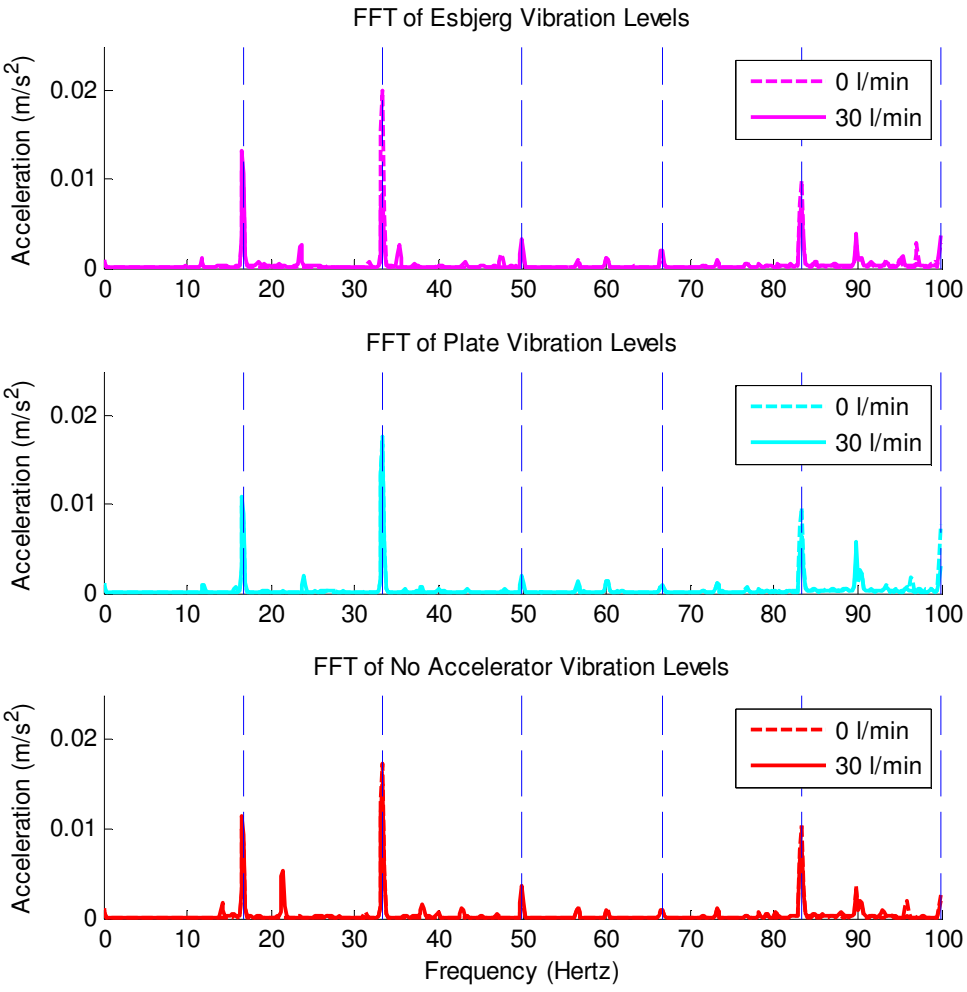

Figure 12.27 FFT plots for the Esbjerg and Plate accelerators, and no accelerator for no flow and 30 l/min at 1000 rpm

12.3.9 Results summary

Table 12.2 Accelerator efficiency at 30 l/min and 1000 rpm

Accelerator	Pool speed (rpm)	Pool speed increase (rpm)	Efficiency	Gain
Conical	769.5	74.0	77.0%	7.4%
Disk	855.0	159.5	85.5%	15.9%
Drum	757.6	62.1	75.8%	6.2%
Esbjerg	745.5	50.0	74.6%	5.0%
Plate	771.9	76.4	77.2%	7.6%
New Generation	917.0	221.5	91.7%	22.1%
No Accelerator	695.5	-	69.6%	-

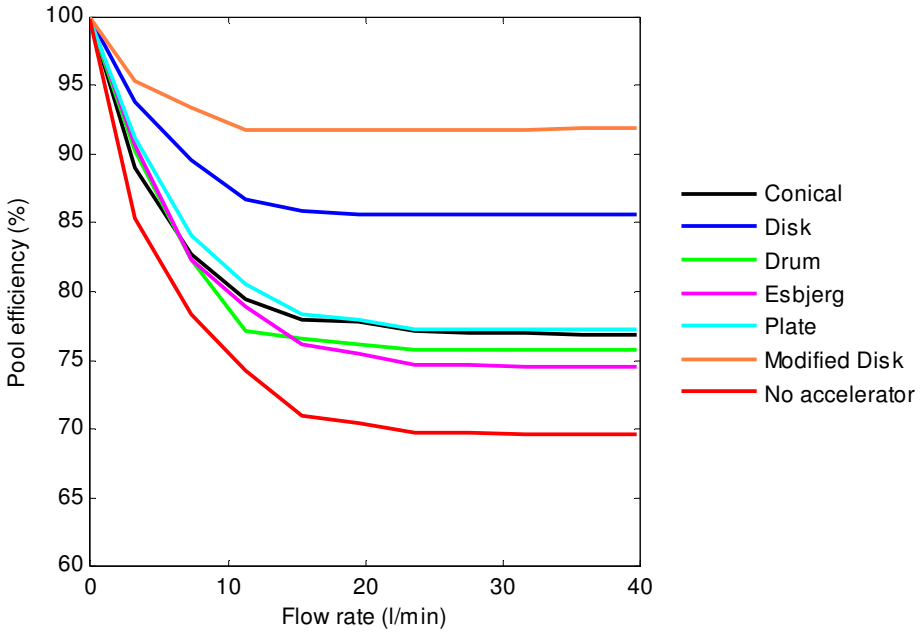

Figure 12.28 Corrected pool efficiency for all designs at 1000 rpm

12.4 Discussion

12.4.1 Acceleration efficiency

Of the six designs that were tested, the two disk type accelerator performed notably better than the others, accelerating the pool by up to an additional 145 rpm over the next best design. Similar efficiencies were observed for the Conical and Plate accelerators, and the Drum and Esbjerg accelerators. The acceleration efficiency was independent of speed; the results were similar for both 800 and 1000 rpm.

The Modified Disk accelerator performed better than the other designs due to the larger discharge radius and the greater discharge angle of the vanes. The ratio of the radius of the accelerator and inner surface of the pool is of significant importance. The smaller this ratio, the larger the radial jump the fluid must pass.

The acceleration efficiencies are higher at lower flow rates because of the longer residence time of the water in the bowl. It is during this time that the viscous forces act on the fluid, inducing rotation. Above 25 l/min the acceleration efficiencies began to tend to an asymptote, this is when the effect of the viscous acceleration by the bowl decreases and the acceleration is primarily provided by the feed accelerator.

Each design was tested at least twice to ensure the repeatability of results. Typically the measured speed only varied by a maximum of 2 rpm. This is only 0.2% at 1000 rpm.

12.4.2 High speed imaging

The flow in the Conical accelerator follows the guide vanes with only a small amount of spill-over near the centre. The effect of the smoothener is not apparent from these results, the flow still remains relatively concentrated and does not leave the accelerator in a smooth sheet as suggested in [18]. Further development of the Conical accelerator could be undertaken to improve the efficiency as it is theoretically capable of a similar efficiency as the Disk accelerator.

The Disk accelerator had more concentrated flow streams between the accelerator and the rotating pool. Over-speeding was achieved with the forward curving vanes; this is shown by the forward angle of the fluid stream in the annular space. Over-speeding is the reason that the Disk accelerator performed significantly better than the other designs. A parametric study of the design variables of the Disk accelerator would enable the design to be optimised to achieve the best possible performance. These variables include the vane discharge angle, number of vanes, discharge radius, and vane height.

The poor performance of the Drum accelerator is highlighted by the flow visualisation – the design does not offer a means of accelerating the fluid. The water leaves the accelerator at a shallow reverse angle. This was observed in the high speed photography. It would be beneficial to vary the parameters of the Drum accelerator, such as the port diameter, number of ports, and wall thickness, to improve the performance as it is the most commonly used and simple design.

The Esbjerg accelerator performed similarly to the Drum accelerator. The design did not offer any means of over-speeding the fluid, leading to a large reverse discharge angle. The accelerator appeared to be partially filled with water.

The Plate accelerator produced a semi-concentrated axial sheet of fluid between the accelerator and rotating pool. The plate forced the fluid in the accelerator to achieve the same tangential velocity as the accelerator. The design still offers no over-speeding and therefore limits the maximum possible efficiency. No water was observed to be leaving the trailing port, implying that it is unnecessary. The accelerator also has the potential to collect solids during operation that would be very difficult to remove.

Results for the Modified Disk accelerator clearly showed the fluid was leaving the accelerator at a forward angle. This over-speeding led to superior performance compared to the other designs that were evaluated.

12.4.3 Accelerometer

The acceleration levels were recorded at each flow measurement for all accelerator designs. The output was an FFT of the acceleration levels from 0 to 100 Hz. The run speed of 999.6 rpm (16.66 Hz) and multiples up to six are indicated on the FFT plots with vertical dashed lines in Figure 12.26 and Figure 12.27.

The overall vibration levels for each design are all relatively low, and little can be inferred from the results. The dominant cause of vibration is likely to be an imbalance existing within the test rig, albeit small. The imbalance is confirmed by the peaks on the FFT plots at one times the running speed. The peaks at other multiples of the run speed are probably a consequence of imbalance. Some of the peaks were dampened by the flow.

12.4.4 Limitations

No local velocity data could be extracted from inside the accelerator or in the annular space. This would have required significant development of the test rig, which was not feasible. It was deemed that measuring the pool speed was sufficient as this was of the most interest in the present study.

It was assumed that the incoming mixture acts like a liquid as it is a solid-liquid suspension.

If the fluid stream penetrates the liquid pool too far the settled solids will be re-suspended leading to unnecessary re-separation being required. The methods used for analysis do not offer a quantifiable means of comparing this for different accelerator designs. Further analysis could include a study into the quantification and effect of pool penetration.

Several modifications could be made to the testing apparatus to improve the quality of the high-speed photography, these are: dying the liquid to increase the contrast between the feed streams and photo background, further increasing the lighting, and painting the inside of the rotating bowl.

12.5 Conclusions

The order of best to worst performing for the tested designs is Modified Disk, Disk, Plate, Conical, Drum, and Esbjerg. There is insignificant difference between the Conical and Plate, and the Drum and Esbjerg accelerators.

The results are consistent with the conclusions from Chapter 11. Designs that rely on viscous dissipation to induce rotation performed poorly, these designs were the Drum and Esbjerg accelerators. The Conical, Disk, Plate, and Modified Disk accelerators impart an impulse force on the fluid, which lead to their superior performance over the Drum and Esbjerg accelerators. The Disk and Modified Disk accelerators performed even better than the Conical and Plate accelerators as they utilised the mass flow induced velocity; this is achieved with the forwards curving vanes.

Several conclusions regarding the design of the accelerator can be drawn from the test results:

- There is only a small difference between designs that have no features to utilise the mass flow induced velocity
- Adding a feature to the geometry to induce over-speeding, such as a forward curving vane, can significantly improve the efficiency of the design
- Increasing the discharge radius of the accelerator significantly improves its performance

Chapter 13

Computational Analysis of the Feed Accelerator for a Decanter Centrifuge

13.1 Introduction

ANSYS-CFX 14.5 was used to develop a three-dimensional model of the fluid flow through each of the previously introduced accelerator designs. Using a computational fluid dynamics (CFD) package, such as ANSYS-CFX, was well suited to the complex flow that occurs within the feed accelerator. The flow pattern, torque induced on the accelerator, and velocity distribution were calculated for each design. Using a computational model to predict the performance of a feed accelerator is useful as it replaces resource intensive testing.

It was not practical to conduct in situ measurements in a full size decanter due to the accessibility of the feed accelerator; therefore part of the test rig presented in Chapter 12 was modelled. The computational model considers only the internal volume of the accelerator and the annular space between the accelerator and the rotating fluid pool. The flow is fed axially into the rotating accelerator, and discharged into the rotating pool. The specifications of the feed accelerator are given in Table 13.1.

Table 13.1 Specifications of feed accelerator analysis

Fluid	25°C water
Mass flow rate	0.5 kg/s (30 l/min)
Rotation speed	1000 rpm
Internal diameter of pool	180 mm

The ANSYS CFX-Pre User's Guide [60], ANSYS CFX-Solver Modelling Guide [61] and ANSYS CFX-Solver Theory Guide [62] were used to determine the best strategies and methods for modelling.

This chapter contains a description of the computational model and a comparison with the experimental results. The chapter ends with a discussion of the results and conclusions about the analysis and feed accelerator design.

13.2 Computational Model

ANSYS CFX offers two models for multiphase flows: Eulerian-Eulerian model and the Lagrangian Particle Tracking Model. Eulerian models look at discrete locations within the flow, while Lagrangian models follow a particle throughout the flow. The Eulerian-Eulerian model was used in this analysis as it offers complete global information, is applicable to a wide range of volume fractions, and turbulence can be easily included.

The details and justification of settings used for the computational analysis are presented in this section. This includes a description of the geometry, mesh, model setup, turbulence model, boundary conditions, initial conditions, solver control, grid independence, and data post-processing.

13.2.1 Geometry

The domain included the internal space within the accelerator, and the annular space between the accelerator and the rotating fluid pool. Including the annular space allowed for comparison between the CFD results and the high-speed photography. The feed tube was not included in the model as it was assumed the pipe flow would have little influence on the results. The geometry for each accelerator was assumed to have periodic symmetry to decrease the solving time. This significantly reduced the number of elements in the mesh. The full geometry for the Disk accelerator is shown in Figure 13.1. The reduced geometries for all designs are shown in Figure 13.2.

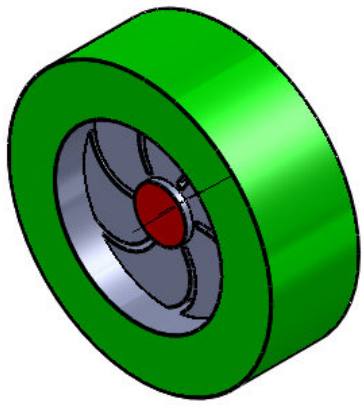

Figure 13.1 Fluid geometry for the Disk accelerator including the annular space between the accelerator and rotating fluid pool

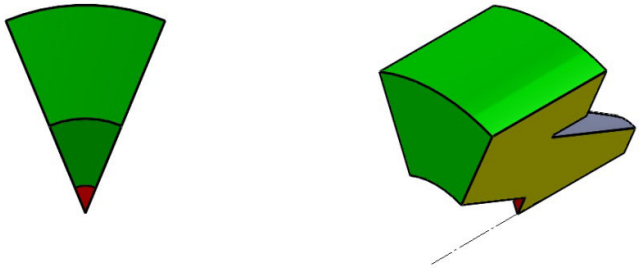

(a) Conical

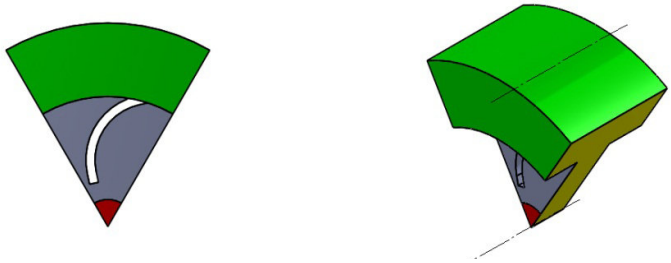

(b) Disk

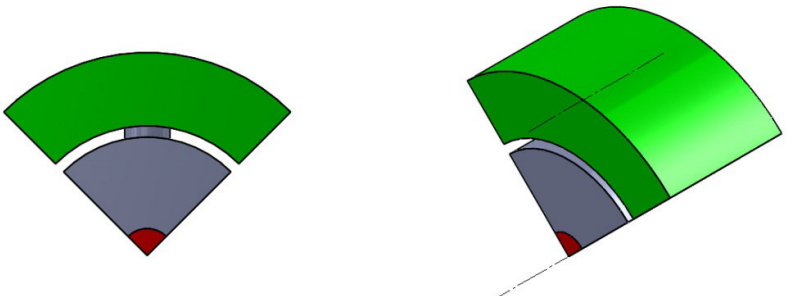

(c) Drum

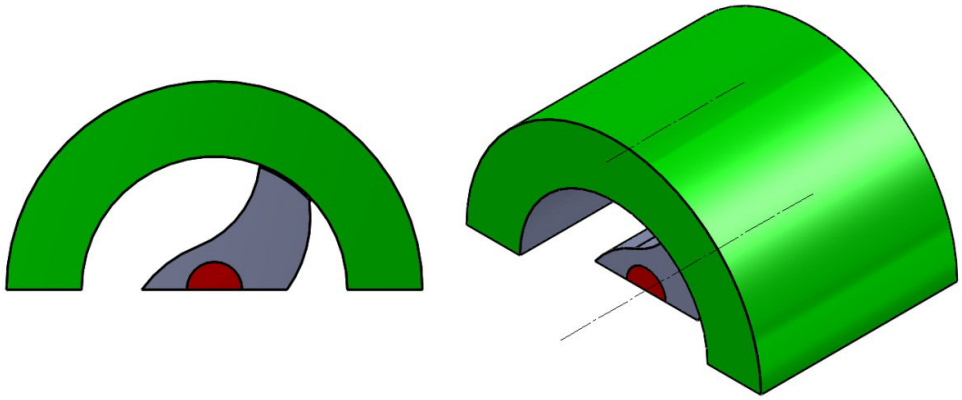

(d) Esbjerg

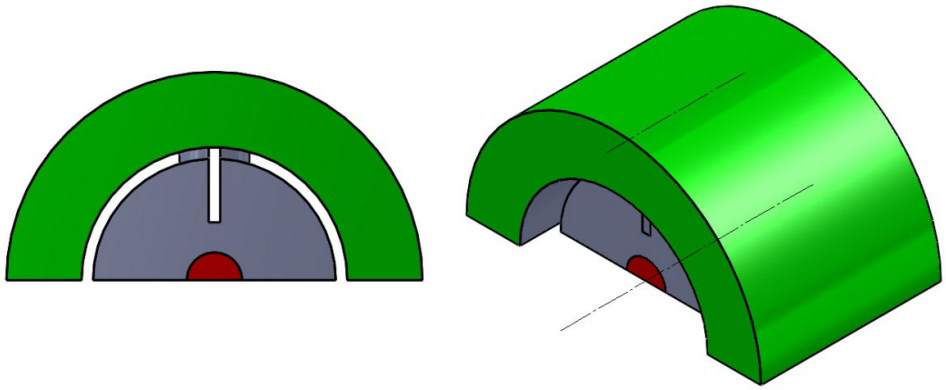

(e) Plate

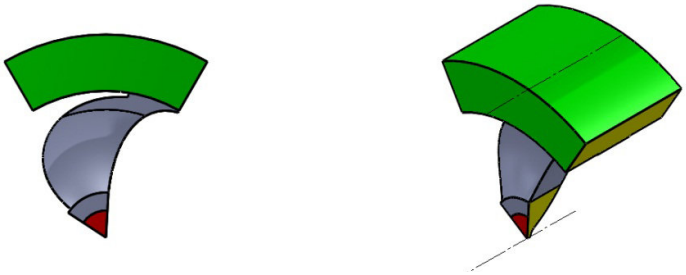

(f) Modified Disk

Inlet Outlet Wall Symmetry

Figure 13.2 Fluid domains for the feed accelerators showing locations of boundary conditions

13.2.2 Meshing

A mesh was created for each accelerator design. The mesh needed to be sufficiently fine to ensure all relevant flow effects were captured, while remaining computationally practical. The mesh influences whether a model will converge and the robustness of the simulation. A mesh that has been refined too much will cause the model to require significantly more processing capabilities.

A patch conforming tetrahedral mesh with boundary inflation was used. Inflation was added to all wall boundaries to ensure the boundary layer influence was correctly captured. At least 10 nodes are required within the boundary layer [63], 10 to 15 inflation layers with a first layer thickness of 0.2 to 0.3 mm were applied to all walls. The mesh statistics for each accelerator are given in Table 13.2. A cross-section view of each mesh for all accelerators is shown in Figure 13.3.

Table 13.2 Mesh statistics for each accelerator design

Conical	67,608	Esbjerg	165,411
Disk	58,790	Plate	204,204
Drum	156,310	Modified Disk	69,264

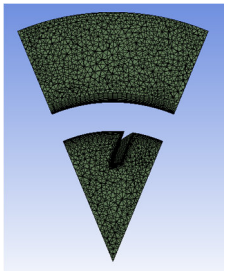

(a) Conical

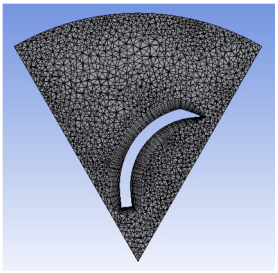

(b) Disk

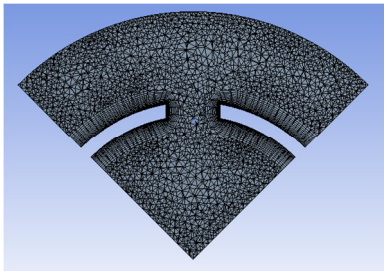

(c) Drum

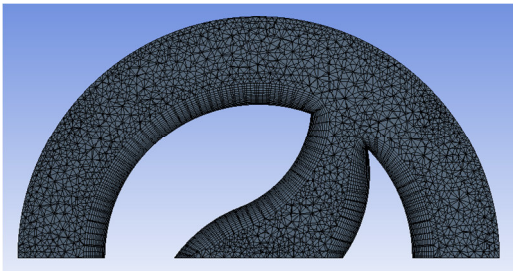

(d) Esbjerg

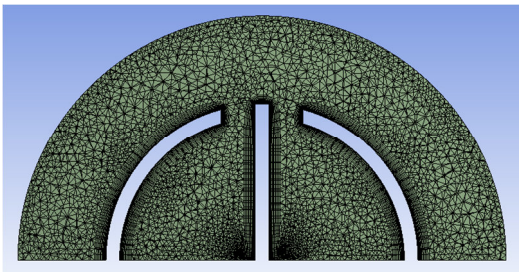

(e) Plate

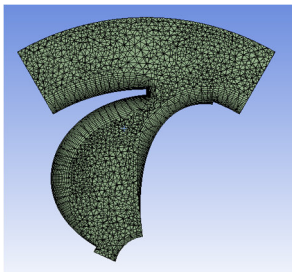

(f) Modified Disk

Figure 13.3 Cross-section of mesh for each accelerator design

13.2.3 Setup

A steady-state analysis was selected for this model. While there are some time dependent effects due to turbulence, the outputs of interest are steady-state. The multiphase Eulerian model was used in this analysis as it offers complete global information and turbulence can be included. A homogeneous model was chosen as the relative velocity between the water and air phases is small; also, this allowed for the solution to be reached faster as there are fewer equations to solve.

A rotating domain was used; which included the continuous phases of water and the air that is present within the accelerator and annular space. Both fluids were set to be at 25°C and were considered as continuous fluids. The interface between the water and air was set as a free surface with a surface tension coefficient of 0.073 N/m.

13.2.4 Turbulence models

The Reynolds number is the ratio of the inertial forces to the viscous forces, when this value becomes large it indicates turbulence. The high Reynolds numbers leading into, within, and exiting the accelerator suggest turbulent flow. While the standard Navier-Stokes equations can theoretically account for turbulence, an impractically fine mesh would be required to resolve the required components. Several models have been developed that predict the turbulence within a flow field, allowing for solutions to be achieved. The turbulence models available in CFX are the k-ε, shear stress transport (SST), BSL Reynolds Stress, and SSG-RSM.

The k-ε model was developed by Launder and Spalding [64]. They showed that the model accurately predicts free-shear-flow and it is computationally simple. The k and ε terms correspond to the turbulent kinetic energy and the dissipation rate, respectively. They are numerically robust and have the tendency to converge fast. The model insufficiently predicts the turbulence in flows with high vorticity as it cannot handle

flows with anisotropic turbulence. The k-ε model is recommended for use in continuous phases. It is currently considered the industry standard for simple flows and is suitable for many engineering situations due to its robustness and accuracy. It is not suitable for flows in rotating fluids and flows over curved surfaces.

The SST model created by Menter [65] offers improvements over the standard k-ε model in that the k-ω model is used in the near-wall regions and the k-ε model in the free stream. The use of SST model is recommended for high accuracy boundary layer simulations. Curvature correction can also be added to avoid swirl being dissipated too quickly. A more detailed description is available on page 61 of [62].

Reynolds Stress Model [66] solves the model for individual Reynolds stress components. While this is more accurate it requires significantly more processing power. Large Eddie Simulation (LES) model filters the eddy currents within the model into large and small categories, it then solves each individually. Shalaby et al [67] provide a more detailed discussion of the model. While this is more accurate in some cases it also requires significant processing power. The RSM and the LES turbulence models are more suitable for flows with high vorticity [67]. The RSM models include the effects of streamline curvature, sudden strain rate changes, and secondary flows, which may be inaccurately modelled by models using an eddy viscosity approximation. It is recommended to use the RSM for flows in rotating fluids. Of the available RSM options the Spexiale, Sarkar, and Gatski (SSG) model is considered to be the superior one. The RSM model has six additional transport equations that must be solved (over the k-e model), therefore it takes significantly longer to solve [68].

The SST turbulence model was used with curvature correction; this was chosen as it is suitable for modelling the turbulent boundary layers that are present in the feed accelerators [65].

13.2.5 Boundary conditions

Each accelerator has four types of boundary conditions: inlet, opening, wall, and symmetry. The inlet condition for each design was specified as a constant mass flow rate of 0.5 kg/s normal to the boundary, this was reduced depending on the degree of axial symmetry. The inlet was set to be stationary relative to the rotating domain. The turbulence at the inlet was set to a medium intensity of 5%. For fully developed flow in pipes the turbulence intensity I is

$$I = 0.16Re^{-\frac{1}{8}}. \quad 13.1$$

The Reynolds number for 0.5 kg/s of 25°C water flowing through a 24 mm diameter pipe is 29,770, resulting in a turbulence intensity of 4.4%. Openings were used as opposed to outlets because an outlet does not allow for fluid to enter the domain, therefore restricting the circulation of air. The fluid at the opening was set to be air, which allowed water to exit the domain but only air to enter. A no-slip condition was enforced at the walls of the accelerator. The wall boundary was set to rotate with the domain. Periodic symmetry was used at the symmetry faces.

13.2.6 Initialisation

Both fluids were set to have turbulence intensities of medium (5%). The volume fraction of air and water were set to 1 and 0, respectively. The air was set to initially rotate at 1000 rpm.

13.2.7 Solver control

An upwind advection scheme was used with a first order turbulence numeric. A convergence criterion of 1e-4 of the RMS values was used. The timescale was set to automatic and conservative.

13.2.8 Grid independence

To confirm the results were independent of the mesh the torque was recorded for several models with different meshes. The number of nodes was increased by globally refining the mesh. There was a 2.6% variation of the torque acting on the Disk accelerator when using 33,717 and 58,790 nodes. The Drum accelerator was modelled with 58,765 to 156,310 nodes, when more than 92,882 nodes were used the variation in torque was 5.9%. There was less than a 0.5% variation in the torque acting on the Plate accelerator when more than 121,816 nodes were used. The influence of the number of inflation layers was investigated. The Drum accelerator was meshed with 5, 8, 10, 15, and 25 inflation layers within the 5 mm boundary layer. When 10 or more layers were added the variation in torque was less than 3.8%. For 15 inflation layers on the walls of the drum accelerator using the first layer thicknesses of 0.5, 0.4, 0.35, 0.3, 0.25, and 0.2 mm there was less than 1% variation in the torque.

13.2.9 Data post processing

The results of interest from this analysis were the torque acting on the walls, the water distribution within the accelerator and in the annular space, and the velocity of the water entering the rotating fluid pool.

The volume fraction was displayed using volume rendering to obtain the water distribution. A constant colour was selected to show the location of the water. This sufficiently showed the water within the accelerator and in the annular space.

The torque on the walls was obtained using an inbuilt calculator. The torque induced on the walls by the water phase about the axis of rotation was the output. The torque was then used to calculate the average tangential velocity of the water leaving the accelerator and the hub efficiency

$$\varepsilon_h = \frac{u_{\theta 1}}{\omega r_1} = \frac{T/2}{\omega \dot{m} r_1^2} \tag{13.2}$$

where

T induced torque (Nm)

ω rotational velocity (rad/s)

$\dot{m}$ mass flow rate (kg/s)

r_1 discharge radius (m).

The cylindrical velocity components, v_r and v_θ, of the water leaving the accelerator were calculated by exporting the Cartesian velocity components, u and v , into MATLAB and converting them using

$$r = \sqrt{x^2 + y^2} \tag{13.3}$$

$$\theta = \tan^{-1}\frac{y}{x} \tag{13.4}$$

$$v_r = u\cos\theta + v\sin\theta \tag{13.5}$$

$$v_\theta = u\sin\theta - v\cos\theta. \tag{13.6}$$

The components were output as average tangential and radial velocities accompanied by histograms displaying the distributions. The distributions were used to determine the concentration and quality of the velocity components.

13.3 Results

The flow visualisations generated by CFD methods and high speed photography are presented in Figure 13.4. The shaded area in the images on the left hand side is water and shows the end-on view (no cross-section). The radial line segments show the symmetry planes. The predicted torque versus the measured increase in the rotation speed of the pool is plotted in Figure 13.5. The predicted velocity components and torque for all accelerators are shown in Table 13.3. The histograms for the tangential and radial velocity components of the fluid leaving the computational domain are shown in Figure 13.6.

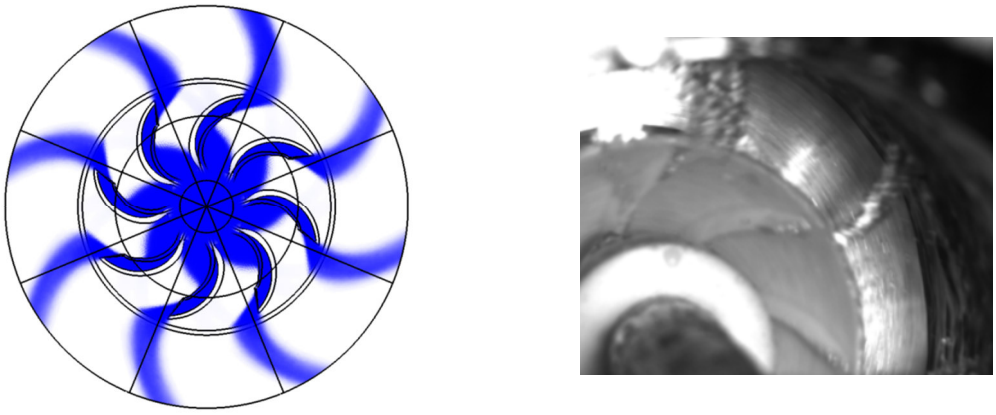

(a) Conical

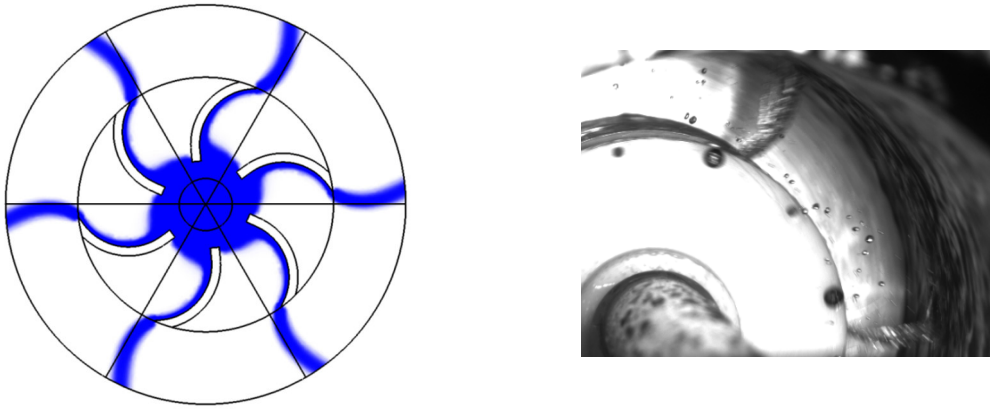

(b) Disk

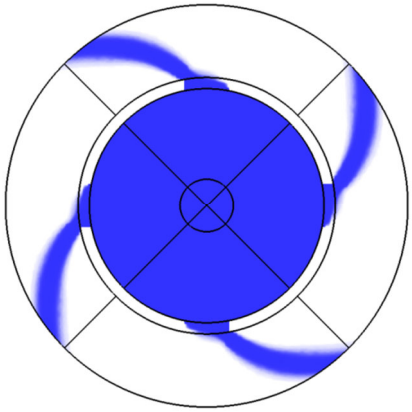

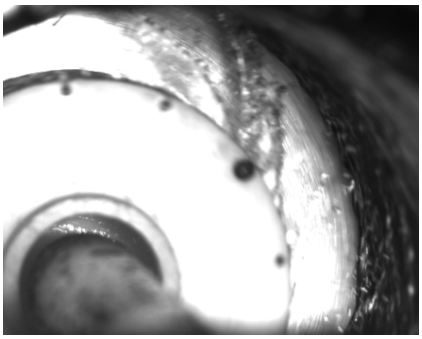

(c) Drum

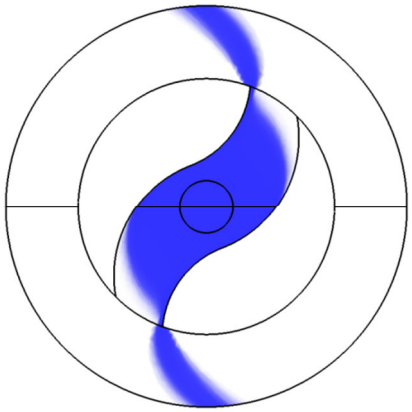

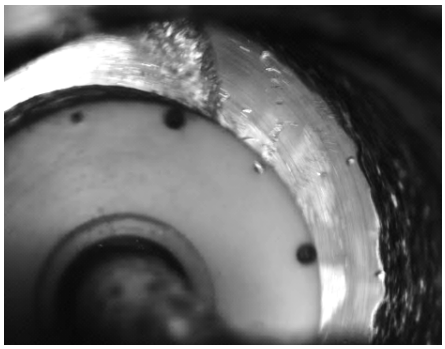

(d) Esbjerg

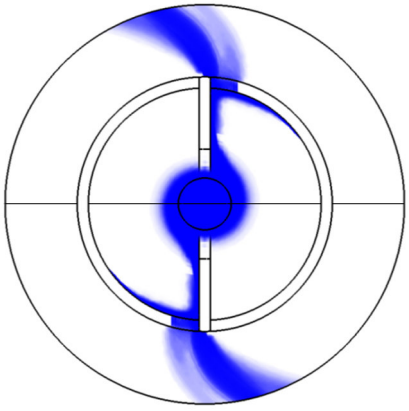

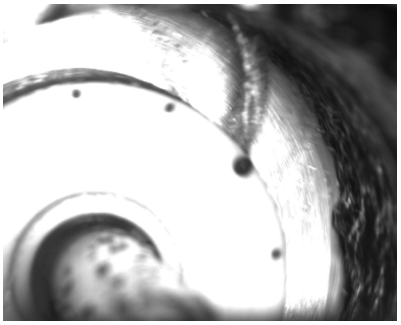

(e) Plate

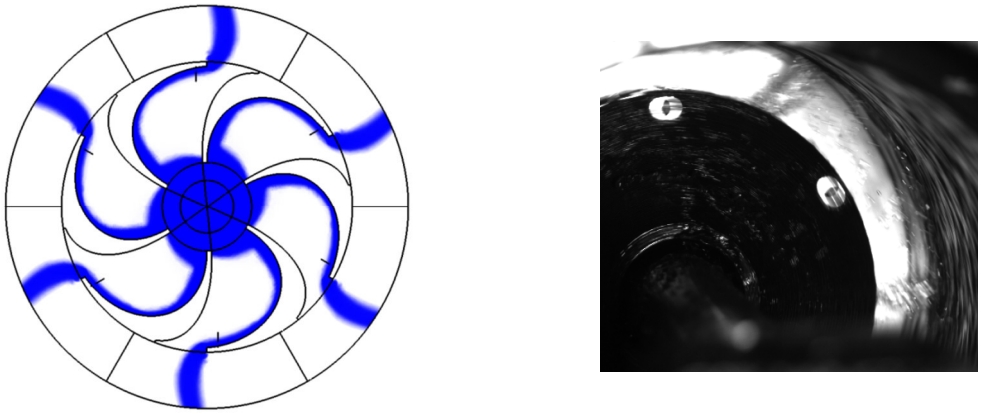

(f) Modified Disk

Figure 13.4 Flow within and around the feed accelerator, predicted using ANSYS CFX and captured using high-speed photography

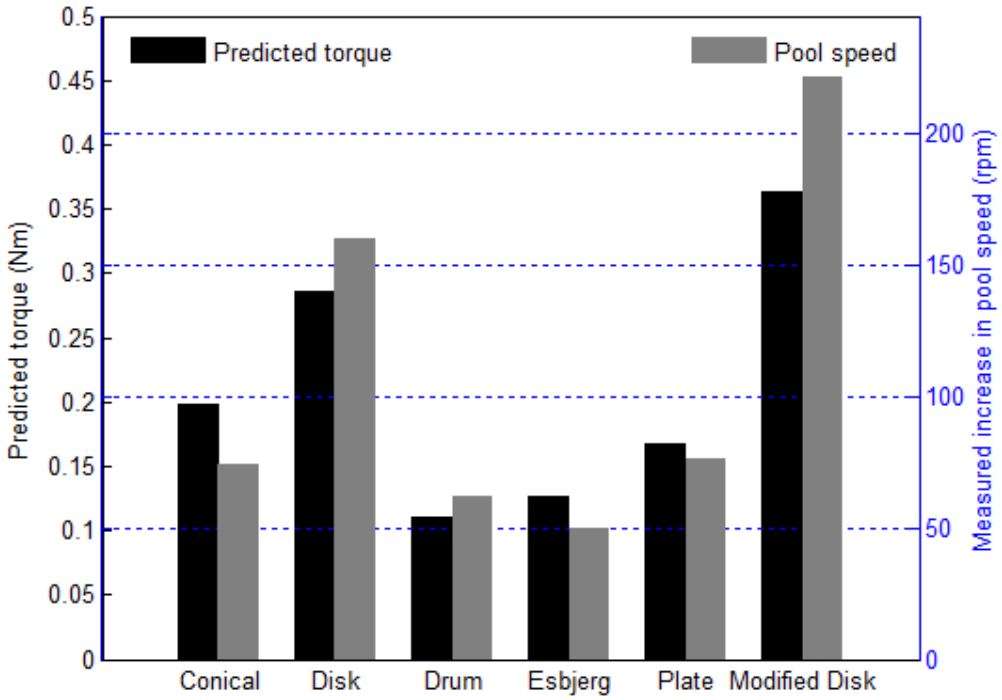

Figure 13.5 Comparison between the predicted torque acting on the walls of the accelerator and the measured increase in rotational speed of the liquid pool

Table 13.3 Results predicted using ANSYS CFX for each accelerator model

Accelerator	Average rpm at pool surface	Average tangential velocity (m/s)	Average radial velocity (m/s)	Torque (Nm)	Hub efficiency ε_h
Conical	422	3.98	5.73	0.198	0.572
Disk	624	5.88	7.56	0.286	0.826
Drum	310	2.92	4.01	0.110	0.318
Esbjerg	320	3.02	4.97	0.127	0.367
Plate	354	3.34	5.68	0.167	0.482
Modified Disk	747	7.04	7.09	0.364	0.823

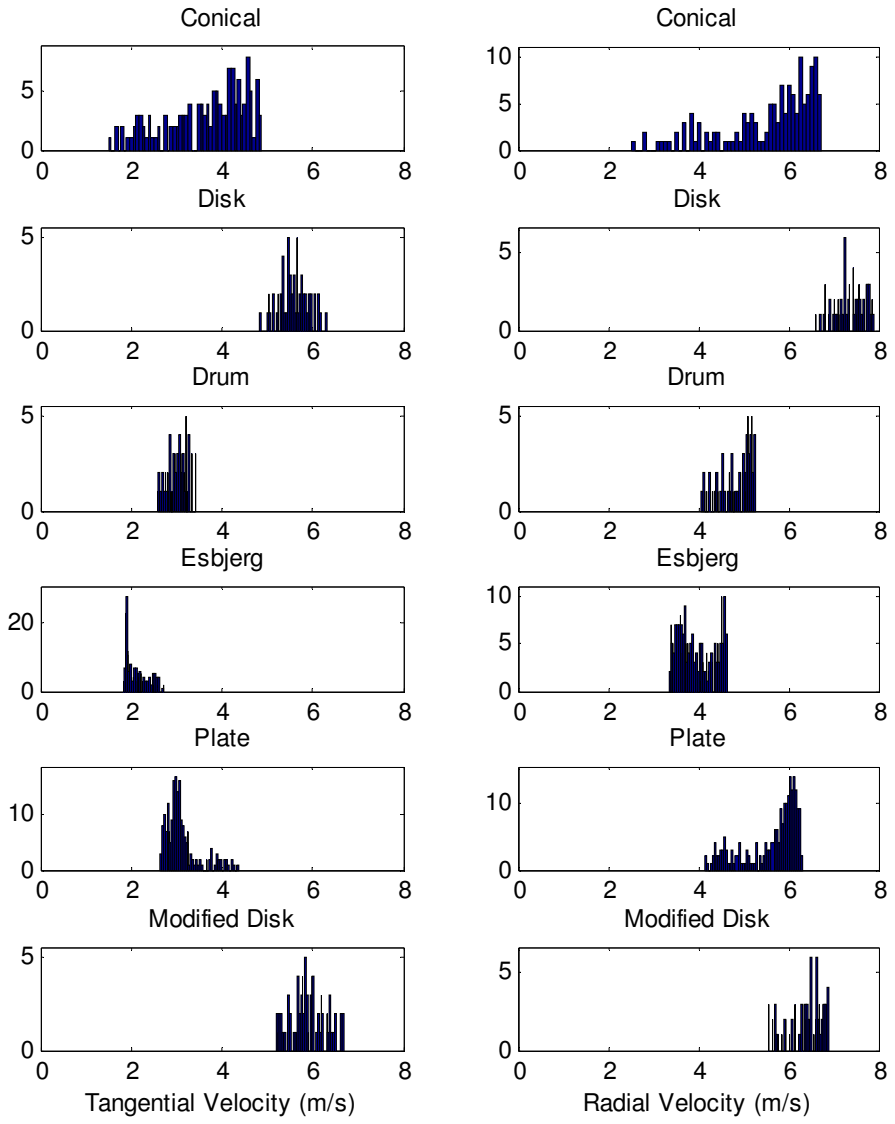

Figure 13.6 Distributions for tangential and radial velocity components of the fluid at the pool entrance

13.4 Discussion

13.4.1 Acceleration efficiency

The experimentally measured increase in the pool speed was compared to the predicted torque acting on the accelerator walls. Comparing these two values gave a good correlation between the measured and predicted results. The torque is proportional to the average tangential velocity of the fluid as it leaves the accelerator and is therefore a

good indicator of the performance. The torque acting on the accelerator walls could not be practically measured during experimentation. It was also not feasible to extend the fluid domain of the computational model to include the rotating fluid pool due to the significant increase in the processing time.

The computational and experimental results correlated well for the designs that were analysed. The computational model agreed with the experimental results that the two disk-type accelerators were superior at accelerating the fluid. The model predicted that the Conical would perform better than the Plate accelerator, although it was experimentally observed that these two designs performed similarly. The Drum and Esbjerg accelerator were the worst performing; this was observed both experimentally and predicted computationally.

13.4.2 Flow visualisation

The flow visualisation results allowed for qualitative validation of the computational model. The flows paths observed using high-speed photography showed excellent similarity with the predicted flow paths for all designs. The water only occupied a small portion of the volume inside the Conical, Disk, Plate, and Modified Disk accelerators; the majority of the flow in these accelerators occurred in a thin layer on the internal surfaces. The flow visualisations agreed well with the efficiency results for each design. The Disk and Modified Disk accelerators were the only designs that showed any over-speeding of the water as it left the accelerator; this gave rise to their high acceleration efficiencies when compared to the other designs. The concentration of the incoming feed could also be observed. The Drum and Esbjerg accelerators appeared to have relatively dispersed flow, while the Conical, Disk, Plate, and Modified Disk accelerators had somewhat concentrated flow streams. The depth of disturbance could not be observed.

Some anomalies occurred for several of the designs. The computational results for the Plate accelerators predicted a small amount of water would be discharged from the leading edge; this was not present in the experimental results. Smearing between the air and water phases was observed in some regions of the flow; this was primarily due to insufficient mesh refinement. The mesh was not refined further as the smearing primarily occurred in the annular space and would therefore have little effect on the predicted torque.

13.4.3 Velocity components

When the velocity components of the fluid leaving the domain were analysed they revealed the same results as the torque. The accelerator performance is proportional to the tangential velocity, which is proportional to the torque acting on the accelerator walls. This justifies the selection to use the torque as the value for comparison between the computational and experimental results. The average radial velocity is also of interest as it indicates the magnitude of penetration of the pool. The Disk, Plate, and Modified Disk accelerators all exhibited higher radial velocity components than the other designs. The effect of this was not explored any further during this study but should be investigated further.

13.4.4 Limitations

The computational and experimental analysis both used scale models relative to commercially available decanter centrifuges. It was assumed that the conclusions from the experimental and computational analysis could be extended to full-size centrifuges. When in service, the centrifuge will always be processing two or three phases, one solid and up to two liquid phases; this was not tested or modelled. It was assumed that the incoming mixture acted like a liquid as it is a solid-liquid suspension. There is potential to expand the computational model to include these particles, it should be cautioned that due to the wide range of applications for decanter centrifuges that there is not one single solid-liquid combination that is likely to be generally applicable.

13.5 Conclusions

The computational and experimental results agreed that the Disk and Modified Disk accelerators were superior at rotationally accelerating the incoming fluid. The agreement between the computational and experimental results allowed for further use of the computational model in a parametric study of the Drum and Disk accelerators. The effect of the radial velocity should be investigated further.

Chapter 14

Parametric Evaluation of the Drum and Disk Feed Accelerators

14.1 Introduction

None of the designs that were previously analysed were optimised prior to the analysis. The dimensions were selected arbitrarily and based on the proportions seen in industrial applications. A parametric study of the Drum and Disk accelerators was undertaken to gain an understanding of the effect of each parameter and to pursue an optimal design. While the Drum accelerator was demonstrated to have poor performance, it was selected for further analysis as it is the most commonly used accelerator and arguably the easiest to manufacture. The Disk and Modified Disk accelerators were shown to be the best performing of the six that were investigated.

It was shown in Chapter 13 that the torque acting on the accelerator walls predicted using the computational model was a good indicator of the relative performance of accelerator designs. This knowledge was applied in this work by varying parameters of the Drum and Disk accelerators and predicting the influence they have on the torque induced on the fluid being accelerated. A base case for all parameters was chosen for each accelerator, each parameter was then varied independently.

Using a software package, such as ANSYS-CFX 14.5, to conduct this analysis significantly reduced the number of experimental tests that were required. 28 runs were completed for the Drum accelerator, and 25 for the Disk accelerator. This would have required 43 different accelerators to be manufactured and tested.

The computational model was adapted for this analysis. The domain was reduced to only include the fluid within the accelerator and not the fluid in the annular space between the accelerator and the rotating pool; this was justified as only the torque acting on the accelerator walls was required. An rotating domain with periodic symmetry was used, the angle of the slice varied depending on the number of ports or vanes.

14.2 Drum Accelerator Analysis

The base design for the Drum accelerator was a 115 mm drum, 5 mm wall thickness, and four 20 mm diameter ports with no stand-off tube. A stand-off tube is an extension tube added to the accelerator ports. The Drum accelerator is displayed in Figure 14.1 with the dimensions of interest shown. The parameters for the Drum feed accelerator are given in Table 14.1, where the bolded numbers are the base case values.

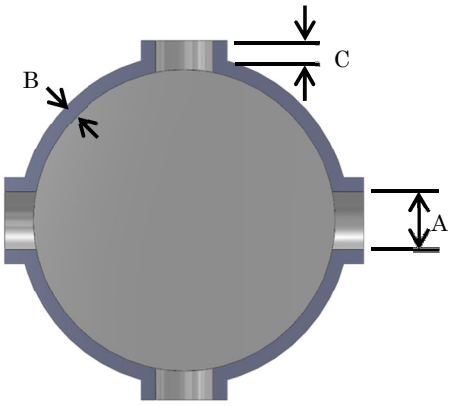

Figure 14.1 Drum accelerator dimensions, A – port diameter B – wall thickness C – stand-off tube height

Table 14.1 Parameters varied for the Drum accelerator

Port diameter	[5, 10, 15, **20**, 25, 30, 40, 50] mm
Number of ports	[2, **4**, 6, 8]
Wall thickness	[2, **5**, 10, 15, 20, 25] mm
Stand-off tube height	[**0**, 5, 10] mm

It was possible to deduce the amount of torque imparted on the fluid by the port faces and the inner surface of the drum. The port faces and inner surface correspond to impulse and viscosity induced torque, respectively. The results of the analysis are presented in Figure 14.2.

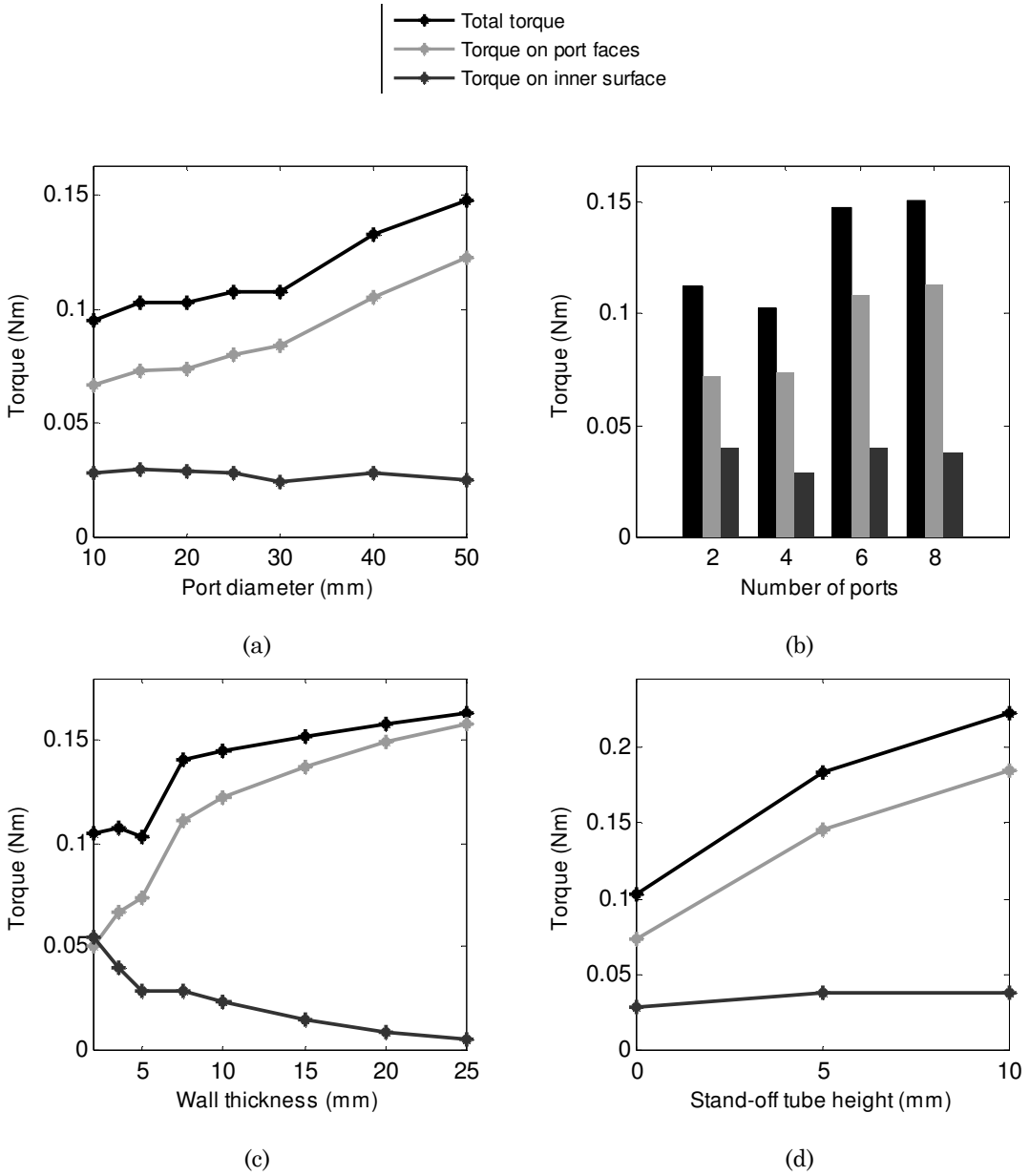

Figure 14.2 Effect of the Drum accelerator parameters on induced torque (a) port diameter (b) number of ports (c) wall thickness (d) stand-off tube height

The effect the port diameter has on the torque induced on the fluid is shown in Figure 14.2 (a). The majority of the torque, 80 to 85%, is applied by the port faces. As the port diameter is increased the viscous input remains relatively the same, while the torque from the port faces increases. The relative contributions from the port faces and inner surface indicates that the dominate component of torque arises from impulse forces.

Adding additional ports is an easy way of increasing the surface area of the port faces. From Figure 14.2 (b) it can be seen that it is desirable to have at least six ports as there

is a notable gain in the torque. The torque supplied by the inner surface remains at relatively the same magnitude. The observed increase arises from the increasing impulse force from the port faces.

The effect of varying the wall thickness is shown in Figure 14.2 (c). The wall thickness was increased inwards so the discharge radius was not changed. As the wall thickness was increased the viscous component of the torque decreased due to the smaller radius and surface area of the inner faces of the drum. As the thickness increased the surface area of the port faces increased, this led to a significant rise in the torque applied by the port faces.

A port stand-off tube is an easy way of increasing the discharge diameter and the apparent wall thickness. The effect of adding a 5 or 10 mm stand is shown in Figure 14.2 (d). A significant increase in the torque is observed with the addition of either stand, with the 10 mm stand increasing the torque the greatest.

14.3 Disk Accelerator Analysis

The base design for the Disk accelerator was 115 mm in diameter, with six, 20 mm high vanes, discharging at 45°. The Disk accelerator is shown in Figure 14.3 with the dimensions that were varied. All of the values of the parameters that were simulated are given in Table 14.2, where the bolded numbers are the base case values. The results of the analysis are presented in Figure 14.4.

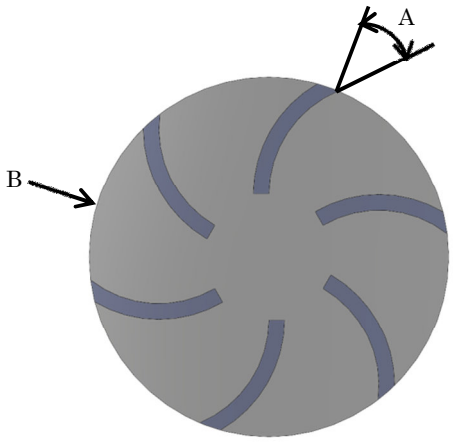

Figure 14.3 Disk accelerator dimensions, A – vane discharge angle B – discharge radius

Table 14.2 Parameters varied for the Disk accelerator

Vane discharge angle	[0°, 22.5°, **45°**, 67.5°, 90°]
Number of vanes	[2, 4, **6**, 8]
Discharge radius	[**57.5**, 62.5, 67.5, 72.5, 77.5]
Disk thickness	[5, 10, **20**, 30, 40] mm
Mass flow rate	[0.25, **0.5**, 1, 1.5, 2, 3]
Rotation speed	[500, **1000**, 1500, 2000, 2500] rpm

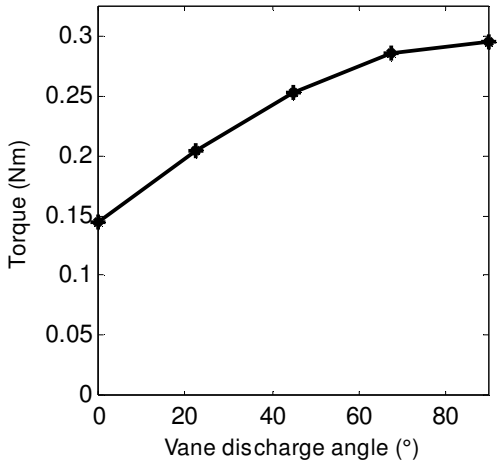

(a)

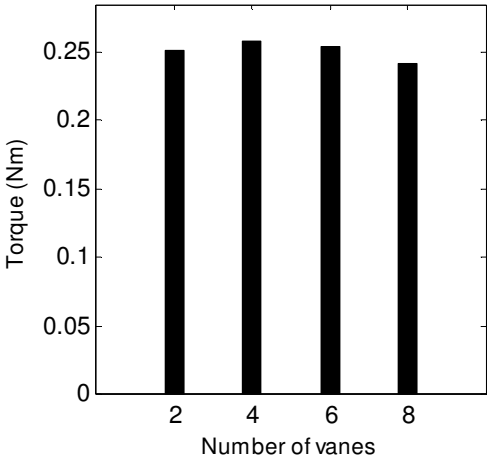

(b)

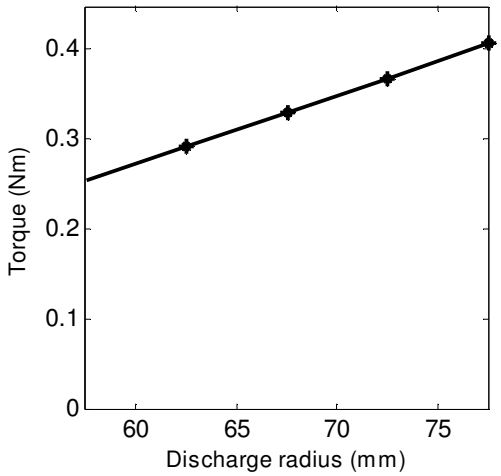

(c)

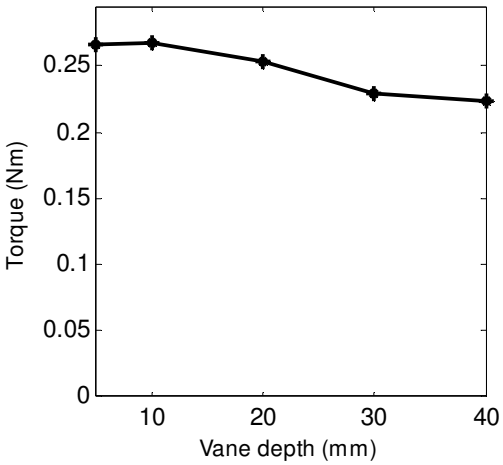

(d)

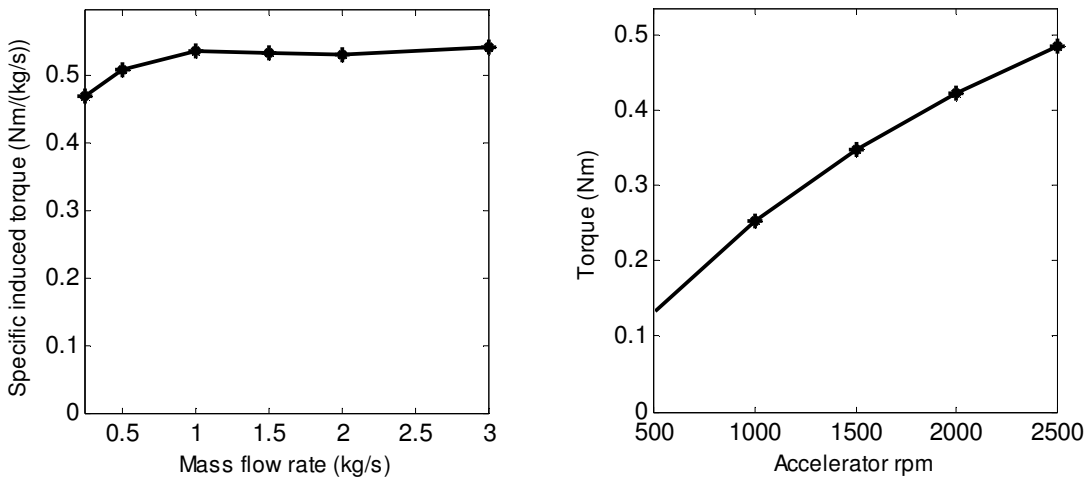

Figure 14.4 Effect of the Disk accelerator parameters on induced torque (a) vane discharge angle (b) number of vanes (c) discharge radius (d) disk thickness (e) mass flow rate (f) rotation speed

Optimising the vane discharge angle is an important part of the design of the Disk accelerator. The effect the vane angle had on torque is shown in Figure 14.4 (a). There is an almost linear relationship between the vane angle and torque up to 67.5°, the rate of gain decreases beyond this angle. The improvement with increased vane angle arises from the utilisation of the mass flow induced velocity to over-speed the fluid.

The number of vanes had little effect on the torque imparted on the water. This is shown in Figure 14.4 (b). When the number of vanes is increased the thickness of the water stream on each vane decreases, therefore decreasing the torque applied by each vane. As the thickness of the water passing over each vane decreases a larger portion of the flow moves into the boundary layer, increasing the viscous losses and decreasing the acceleration capability, although this only has a small effect over the range of the number of vanes analysed.

The discharge radius is linearly related to the torque imparted on the water; this is shown in Figure 14.4 (c). This arises from the increased tangential velocity at larger radii. Increasing the discharge radius is an easy and effective method of improving the performance.

Increasing the depth of the vanes is detrimental to the torque; this is shown in Figure 14.4 (d). Increasing the vane depth has a similar effect to adding extra vanes; the thickness of the flow is decreased. Again, this causes a greater portion of the flow to be in the boundary layer, therefore decreasing accelerator performance.

Figure 14.4 (e) shows the effect the mass flow rate has on the specific torque. The specific torque is the torque divided by the mass flow rate. The specific torque is approximately constant, except at lower flow rates where the efficiency decreases. There is a small increase in the torque due to mass flow at high rates; this is due to the mass flow induced velocity component and the decreased portion of the flow within the boundary layer travelling along the vanes.

The torque as a function of accelerator speed is shown in Figure 14.4 (f). The relationship is approximately linear, but starts to degrade at higher speeds. This could be due to higher turbulence and boundary layer effects.

14.4 Conclusions

The parametric study revealed the influence that each of the key design parameters of the Drum and Disk accelerators has on the torque imparted on the fluid. The port diameter, wall thickness, effect of a stand-off tube, and number of ports were examined for the Drum accelerator. It was found that increasing the port face area, by any means, improved the torque applied to the fluid by the Drum accelerator. This could be achieved by increasing the port diameter, adding additional ports, increasing the wall thickness, or adding a stand-off tube. The vane discharge angle, number of vanes, discharge radius, vane depth, mass flow rate, and speed were examined for the Disk accelerator. It was found that increasing the vane angle and increasing the thickness of the flow along each vane improved performance.

Several conclusions regarding the design of the accelerator can be drawn from this analysis:

- Adding a feature to the geometry of the feed accelerator to induce over-speeding, such as forward curving vanes, can significantly improve the acceleration efficiency of the design
- Increasing the discharge radius of the accelerator significantly improves the acceleration efficiency
- Viscous dissipation is a poor mechanism for accelerating the fluid and features should be included in the design that impart an impulse force on the fluid

The findings from this work can be used in the design and development for any application that requires fluid to undergo rotational acceleration.

Chapter 15

Conclusions and Future Work

15.1 Power Consumption Analysis

There are four components of power consumption in a decanter centrifuge: friction during product transport, viscous and kinetic losses during feed acceleration, power transmission inefficiencies, and windage on rotating components. Each of these components was analysed.

A mathematical model of the product transport within a decanter centrifuge was developed. The primary purpose of the model was to calculate the power and torque required to transport the solids along the bowl. The model can also be used to calculate the axial bearing loads, axial bowl stress, effect of design parameters, and the effect of operating variables. The model was compared to experimental data obtained from an existing publication; there was good agreement between the model and data.

A relationship for the power consumed during feed acceleration was derived from first principles. The model consists of two components, viscous losses during acceleration, and the loss of kinetic energy of the solids and liquids as they leave their respective discharge ports.

The power transmission losses are comprised of inefficiencies in the motors, belt drives, gearbox, bearings, and seals. The losses occurring within the motors and belts are the largest, consuming up to approximately 10% of the power they convert or transmit. The back-drive gearbox consumes a further portion of the power being supplied to the scroll. The bearings and seals consume a small but notable amount of power due to friction arising from relative motion of components.

The windage has two components, the surface drag on the bowl as it rotates in an annular space and the pressure drag on external protrusions on the bowl such as bolt heads, ports, and flanges.

The analysis delivered useful tools, including the product transport model, and the equation for the feed acceleration power, which can be used to predict the power

consumption of a decanter centrifuge. A list of recommendations for reducing the power consumption and improving the performance of a decanter centrifuge was also created.

15.2 Wear Analysis and Development of a Composite Bowl

The analysis of several worn centrifuges revealed that the majority of the wear occurs on the scroll tips and faces, and on the bowl wall in the conical section.

An attempt was made to design a test apparatus to recreate the wear conditions inside a centrifuge. A high pressure abrasive film was forced between materials moving relative to each other. Similar results were observed to those from a pin-on-disk wear test rig for acetel, UHMWPE, and 316 stainless steel. No further testing was conducted using this test rig.

The development of a composite bowl was the result of identifying advantages to changing the bowl material and manufacturing procedure. Reasons that were identified were:

- Weight reduction
    - Lower bearing loads
    - Reduced freight cost
    - Easier to handle than the current design
- Improved wear and friction characteristics
- Less expensive than the current design
- Reduced external protrusions and therefore less windage and aero-acoustic noise generation
- Reduced number of components
- Point of difference over competitor models
- Higher specific strength composite materials suggesting it may be possible to achieve higher speeds

The full design process was applied to the bowl and several concepts were generated for a new scroll. The design process included conceptual design, material selection, testing material samples, scale models, and the manufacturing of a full-size prototype bowl for a GTech-Bellmor 1456 Centrifuge Decanter. The novel manufacturing method developed during this project produces parts suitable for use in high-speed rotating machinery. The bowl was in the final stages of manufacturing at the conclusion of this project.

15.3 Analysis of the Feed Accelerator

The feed accelerator analysis consisted of three components: theoretical, experimental, and computational analysis.

The three mechanism of feed acceleration were identified as viscous dissipation, impulse force, and mass flow induced velocity. Six designs were identified for further analysis. Analysis of the geometry of the accelerator revealed that there are three fundamental ways of improving the acceleration efficiency of the feed accelerator:

- Maximise the hub efficiency by careful design of the accelerator
- Discharge the fluid from the feed accelerator at a positive angle; this can be achieved by utilising the mass flow induced velocity
- Maximise the ratio of the accelerator discharge radius and the inner radius of the pool, either by increasing the pool depth or increasing the accelerator diameter

An experimental method was developed to examine decanter centrifuge feed accelerator designs. The method allowed for the measurement of acceleration efficiency and high-speed photography of the flow between the accelerator and the rotating pool. The Modified Disk accelerator demonstrated the best efficiency; this was attributed to the over-speeding effect of the forward curving vanes and the larger discharge radius.

The feed accelerator was modelled using ANSYS-CFX 14.5 and compared to the experimental results. There was excellent agreement between the flow in the annular space observed using high-speed photography and the paths predicted using the computational model. The predicted torque acting on the accelerator walls was found to have good correlation with the experimentally measured increase in pool speed.

A parametric study of the Drum and Disk feed accelerator designs was undertaken using the computational model. The parameters that were studied for the Drum accelerator were the: port diameter, number of ports, wall thickness, and stand-off tube height. The parameters that were studied for the Disk accelerator were the: blade discharge angle, number of vanes, discharge radius, disk thickness, mass flow rate, and rotation speed. Increasing the surface area of the port faces of the Drum accelerator and ncreasing the discharge angle and discharge radius for the Disk accelerator gave the greatest improvement in performance.

15.4 Future Work

Several areas could be investigated further as a progression of this work, these include:

- Comprehensive field measurements of the power consumption within a decanter centrifuge to isolate the four components of power consumption
- Conduct additional verification of the product transport model
- Extend the wear testing program to include other candidate materials that could be used within decanter centrifuges and use the results to predict the in-service component life
- Develop a new scroll and centre hub from modern materials to reduce friction, wear, and cost
- Install the composite bowl in a centrifuge in parallel with an existing centrifuge in a processing plant to verify improvements
- Explore the effect of the radial velocity of the feed accelerator by either computational or experimental methods
- Implement a Disk accelerator into a decanter centrifuge and conduct field tests to verify improvements

Appendix A

Centrifuges

A.1 Separation

Materials are rarely extracted in a sufficiently pure form for subsequent use. Extracted material usually requires multiple processing steps before they become usable, separation is commonly one of these steps. Separation is defined as the act of items moving apart, it can refer to combinations of solids, liquids, and gases. Industrial separation is not only used in the production of products but in the recovery of valuable materials from waste streams. A detailed description of the separation process is presented by Leung [15]. The separation process aims to achieve at least one of the functions described in Table A.1 [13].

Table A.1 Different separation processes from [13]

Separation	Includes separating solid-liquid, liquid-liquid, or solid-liquid-liquid.
Clarification	Removal of residual solid particles from the liquid phase.
Classification	Separation of particles based on their size and density
Degritting	Removal of oversized or foreign particles
Thickening	Concentrating the feed slurry by removal of excess liquid
Dewatering	Removal of moisture from the settled cake
Washing	Removal of impurities from solids, achieved by washing solids after they have been separated from the liquid phase
Separation and repulping	Removing impurities by separation followed by reslurrying

One or more of the functions listed above can be achieved using a centrifuge. There are two distinct types of centrifuges: those based on sedimentation and those based on filtration.

A.2 Types of Centrifuges

There are two distinct types of centrifuges available today: these are filtration centrifuges and sedimentation centrifuges. Sedimentation uses the principle of buoyancy to distinguish between different phases. Over time, the heavier phases settle to the bottom leaving the lighter phases on top. A common example of this is the separation of

petroleum products in a distillation tower. The lighter fuels (such as liquefied petroleum gas) are extracted from the top, while the heavy asphalt settles to the bottom. Sedimentation is an essential stage in the production of many products. Filtration is most commonly used to separate solids from liquids. The mixture of solids and liquid is forced through a filtering medium that only the liquid can pass. The porosity of the medium determines the amount of solids extracted from the liquid. An example of a filter is a wine press; the grapes are pressed within a perforated basket that only the liquid can pass through. There are many applications where filtering centrifuges are used; the most common is the dewatering of granular materials [13].

A centrifuge operates in one of two possible modes, batch operation or continuous operation. During batch operation the centrifuge must be intermittently stopped to remove solids. During continuous operation the centrifuge continuously produces multiple streams of outputs (i.e. solids and liquid phases) without needing to stop. The types of centrifuges are shown in Table A.2. Norton [69] provides a more detailed description of batch and continuous centrifuges.

A general guide to centrifuge selection was produced by Hart [70].

Table A.2 Types of centrifuges

Centrifuges			
Sedimentation		Filtration	
Continuous	Batch	Continuous	Batch
Solid bowl Disc Tubular	Imperforate basket Tubular	Pusher Screen scroll Conical basket Vibratory Screen bowl	Vertical basket Peeler Inverting filter

The focus of this investigation is on a solid bowl decanter, which is a continuous, sedimentation centrifuge. Some parameters from each type of centrifuge shown in Table A.2 are outlined in Table A.3. These specifications are based on the information from Leung [13].

Table A.3 General centrifuge operating parameters [13]

Types	Particle size (μm)	Feed solids (%,w/w)	G-force	Capacity (ton/h)	Cake discharge method	Applications
Vertical	10-10,000	15	500-2,000	<6-10	Peel at low speeds of remove filter bag	Pharmaceutical and specialty minerals, need flexibility and low cake moisture with good wash
Peeler	20-10,000	15	1,000-2,000	<25	Peel at speed on non-breakable crystals	Products with extreme demand on residual moisture and wash requirement
Screen bowl	40-5,000	10	500-2,000	<30-150	Scroll conveyor	Chemicals, minerals, salts
Pusher, multistage	80-10,000	40	300-1,200	<90	Pushing	Chemicals, salts
Screen scroll	80-20,000	35	200-700	<100	Scroll conveyor	Minerals, chemicals, food, industrial
Screen vibratory	500-50,000	50	50-300	<250	Vibration	Coarse minerals
Disk	0.1-10	0.5-5	<15,000	<400	Manual/ dropping bottom/ continuous nozzles	Fine solids, good processing, chemicals
Solid bowl	0.8-5,000	0.2-75	<10,000	<100	Scroll conveyor	Chemicals, biological, minerals, waste food processing
Solid bowl batch	0.8-5,000	1	<2,000	<4	Bag	Biological waste, food processing

A.3 Solid Bowl Decanter Centrifuge

This study focused on a solid bowl decanter centrifuge. Solid bowl decanter centrifuges can handle a wide range of particle sizes and solids content so they can be used in many different applications. Due to their robustness and versatility, solid bowl decanter centrifuges are in widespread use for industrial separation. The key differences between decanter centrifuges and disk stack centrifuges are described by Belcher in [71]. Disk stack centrifuges are also used for separating mixtures of solids and liquids, but are typically reserved for applications with lower solids content.

Decanting centrifuges consist of two rotating components: the bowl and the scroll. The scroll rotates at a slightly different speed (differential speed) to the bowl. The key

components of a decanting centrifuge are described in Table A.4 and labelled in Figure A.1.

Table A.4 Descriptions of main components in a decanting centrifuge

Bowl	Both the cylindrical and conical sections that contain the scroll and product
Scroll	The scroll conveyor that moves the cake along the bowl, it is sometimes referred to as the auger
Conical	Solids are dried in the conical section, it is also known as the beach
Flight	One section of the scroll
Scroll pitch	Distance between two scroll flights
Hub accelerator	Rotationally accelerates the feed as it enters the bowl
Back-drive	Drive unit for the scroll conveyor. The gearbox is part of this unit
Main drive	Drive unit for bowl

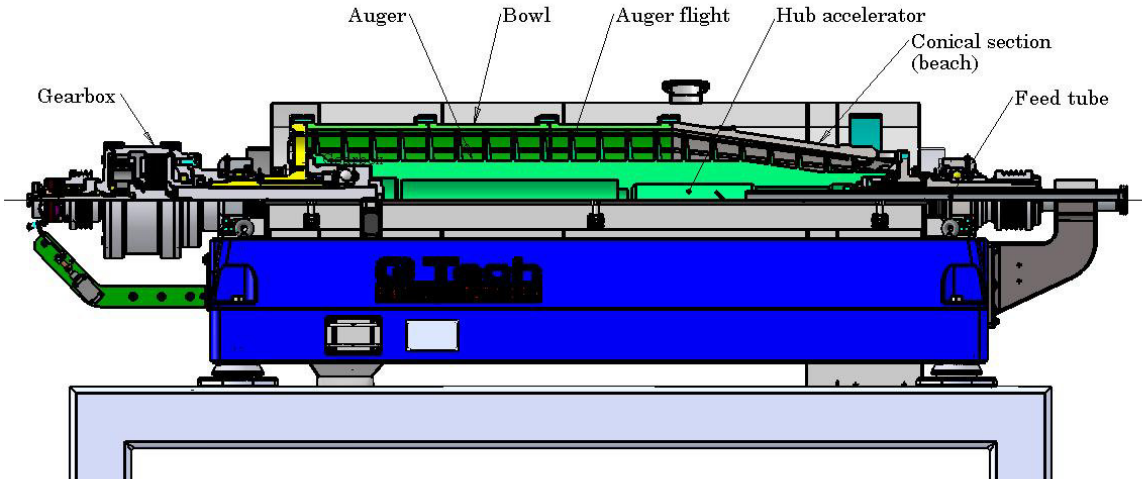

Figure A.1 Partial cross-section of a decanter centrifuge with component labels

The product is either gravity fed or pumped through the stationary feed tube into the hub accelerator. The product is partially accelerated before entering the bowl where it forms the pool. As the product moves along the helical path towards the liquid end it is subject to centripetal force, which moves the heavier solids to settle as cake against the bowl wall. The liquid is discharged through adjustable weirs. The cake is transported along the bowl and up the conical beach by the scroll conveyor, which is rotating at a different speed to the bowl. As the solids move up the conical beach they are lifted out of the liquid pool. A description of terms is given in Table A.5 and a labelled schematic is shown in Figure A.2.

Table A.5 Description of key terms to describe flow in a decanting centrifuge

Feed	The incoming product to be separated is known as the feed, it is sometimes referred to as the slurry or mixture
Solids	The solid phase of the product
Cake	When the solids settle against the bowl wall they form the cake
Light liquid	The third/lighter liquid phase in three-phase operation
Heavy liquid	The heavier liquid phase in either two or three-phase operation
Pool	The hollow cylinder of liquid formed in the bowl
Centrate	Liquid discharged from the centrifuge

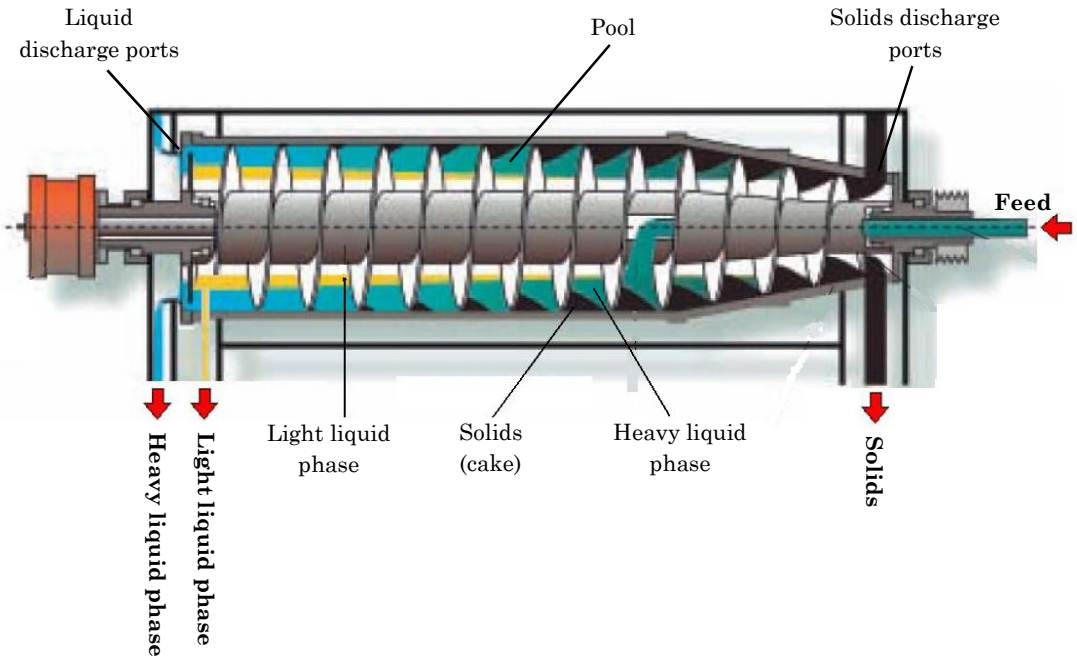

Figure A.2 Flow paths in a three-phase decanting centrifuge

Appendix B

Gearbox Test Rig

B.1 Introduction

In order to verify the predicted performance of the gearbox a test rig was designed. The rig was designed to fulfil two requirements: 1) determine the efficiency of the gearbox and 2) test the gearbox under full operating load prior to installation. This appendix contains the conceptual design process for the gearbox test rig.

B.2 Current Rig

A simple rig is currently used to rotate the gearboxes after they have been assembled (see Figure B.1). The gearbox is not placed under load and consequently the gearbox will not reach its working stress and temperature. Potential issues within the gearbox may not be detected prior to installation.

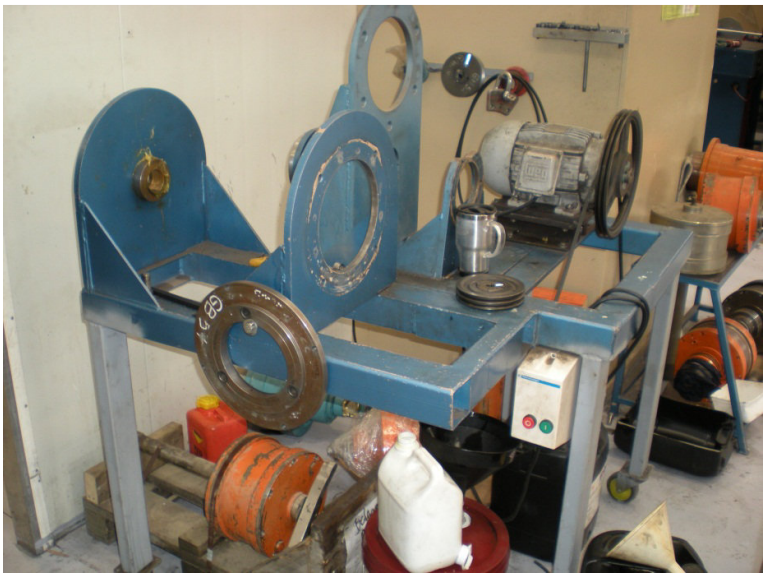

Figure B.1 Present gearbox test rig

B.3 Requirements

The first step of the design process was to evaluate the power, torque and speed requirements of the rig. The rig must be able to replicate the duty cycle of the gearbox.

The parameters for the input and output shafts are shown in Table B.1. The maximum torque rating of the GB-57 gearbox is 3.6 kNm.

Table B.1 Input and output parameters for the GB-57 gearbox

Parameter	Input	Output
Power (kW)	15	<15
Speed (rpm)	3,420	45
Torque (Nm)	41.9	3,183

B.4 Layout

Before detailed concepts were created the layout of the rig was addressed. This involved selecting components that could operate within the parameters in Table B.1. Various possible layouts were identified and are described below.

B.4.1 Layout One

This layout involves driving a single gearbox with a 15 kW electric motor via a belt drive (see Figure B.2). Resistance is applied to the output of the gearbox by wrapping a rope around a drum; one end of the rope is anchored whilst the other carries weights that can be adjusted to vary the loading. The drum has water continuously running through it to remove heat generated by the rope sliding against the drum. The torque and speed are measured by the transducers on both the input and output of the gearbox.

The torque on the output shaft is very high. Consequently the rope drum would need to have a large diameter to provide enough resistance torque. The transducers for this duty are expensive and difficult to source. This concept allows the current gearbox test rig to be modified and used as a base.

The clutch is not included in this layout; this could cause potential issues if the gearbox is overloaded. Although the clutch does not consume power under normal operation it should be included when testing the gearbox under load.

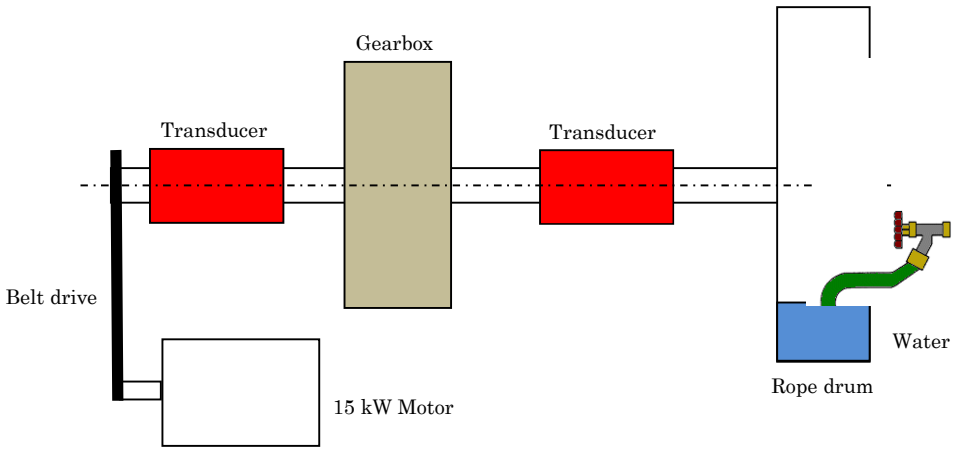

Figure B.2 Layout One schematic

B.4.2 Layout Two

This layout involves driving two gearboxes with a 15 kW motor via a belt drive (see Figure B.3). By running the second gearbox in reverse the speed is increased and the torque is decreased. Resistance is applied to the output of the second gearbox by wrapping a rope around a drum. The drum has water continuously running through it to remove heat generated by the rope sliding against the drum. The torque and speed are measured by the transducers on both the input and output of the whole system. The advantage of this layout over Layout One is the output torque is significantly reduced to less than 100 Nm.

The efficiency of the gearbox is not necessarily the same when the gearbox is run in reverse. This would need to be accounted for in the efficiency calculation. The torque on the output shaft could be measured using strain gauge telemetry measurement equipment to establish the efficiency of the second gearbox in reverse.

Use of a rope drum is undesirable as it is not an ideal method of applying a resistance torque in a test rig that is intended for future use in a production environment. It is also wasteful of water unless a recirculation circuit is used.

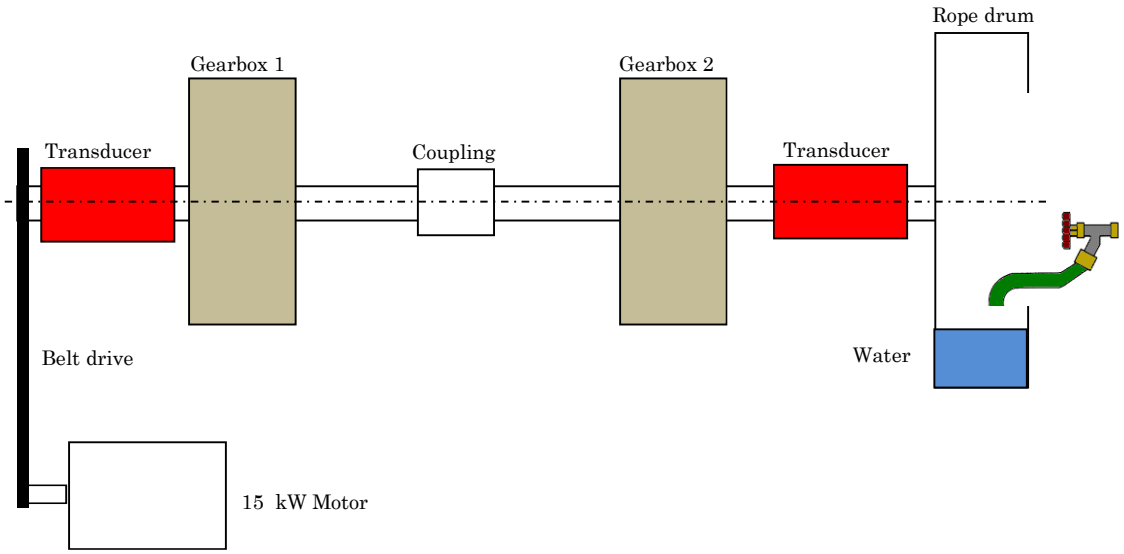

Figure B.3 Layout Two schematic

B.4.3 Selected Layout

The chosen layout is shown in Figure B.4. The path of power transmission is shown by the connecting line. The first motor drives the input of the first gearbox; the output drives the output of a second gearbox in reverse, the input of the second gearbox is connected to a second electric motor that acts as a generator by dissipating power in a resistor bank. The power could also be fed back into the input for the first motor if desired; this would reduce the energy consumption of the rig. This configuration was selected as the torque was considered too high for a practical rope drum and the system is easier to employ in a production environment. Transducers would be placed on the low torque inputs of each gearbox to measure the torque decrease of the gearboxes. The torque on the output shafts would need to be measured to calculate the efficiency of a single gearbox.

When the transducers are removed the power consumed by the drive motor and absorbed by the generator can be used to roughly estimate the efficiency of the gearboxes. To do this, the efficiency of the motors must be known. If the output from the generator is fed back into the motor the system efficiency can reach 65-89% [72].

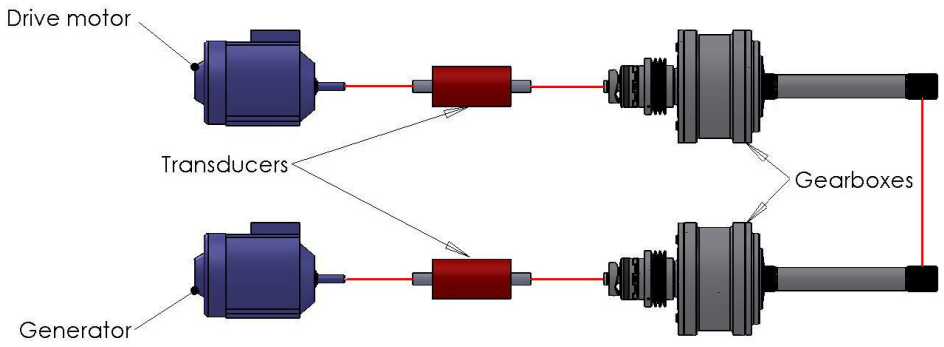

Figure B.4 Selected layout schematic

B.5 Transducers

The transducers must provide the power (or torque) at the point of measurement. They can either directly output the power or the torque and speed. Several transducers were available; they are *EEL 2400 Series Torque Transducers*. The CA model is rated to 135 Nm and 6000 rpm making them suitable for use in the rig. The transducers do not need to be permanently installed as they are only required to measure the efficiency of the gearboxes.

As the efficiency of the gearbox will be significantly different while running in reverse the torque and speed of the output shaft will need to be measured. The torque on these shafts exceeds 3 kNm; this introduces significant issues in sourcing an acceptable transducer. The solution is to use telemetry equipment to measure the torque. The speed can be measured using a tachometer or a laser counter.

B.6 Gearbox Models

While the GB-57 gearbox is the primary focus of this investigation, the rig must be able to accommodate the range of gearboxes produced by Bellmor Engineering Ltd. There are four gearboxes that must be able to fit in the rig, see Figure B.5. The widest gearbox is the GB-168 (Ø 340 mm), the longest is the GB-53 (length 1092 mm). Every gearbox has a different mounting flange and this needs to be accounted for in the rig design.

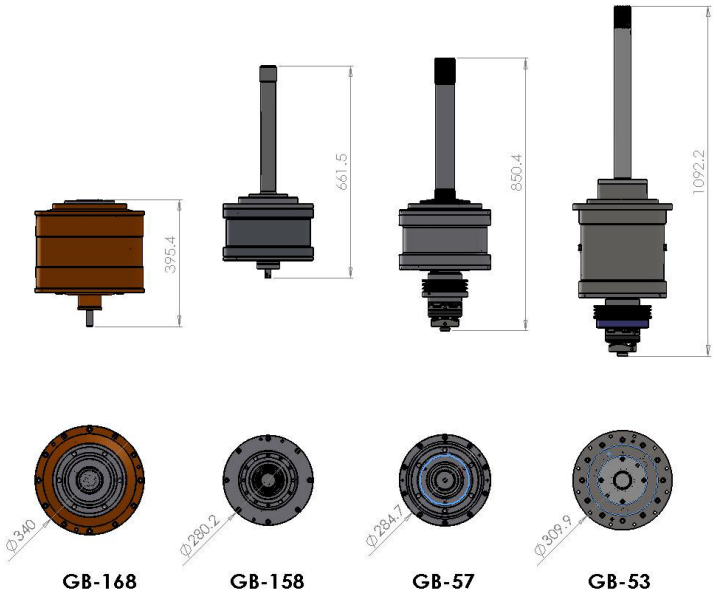

Figure B.5 Gearbox models required to fit in the test rig

B.7 Concepts

Concepts were identified and developed before a satisfactory arrangement was arrived at.

B.7.1 Concept One – In-Line

Concept One (see Figure B.6 and Figure B.7) is a simple layout where all elements in the rig are along a single axis. This is easy to construct but it occupies a lot a space as it is 3.77 metres long. The gearboxes are mounted on removable plates so different gearboxes can be tested by having a set of mounting plates for each type of gearbox. The clutch arrangements must be removed in this concept, which does not alter the efficiency but it is desirable to test the full gearbox assembly (including the clutch) prior to installation.

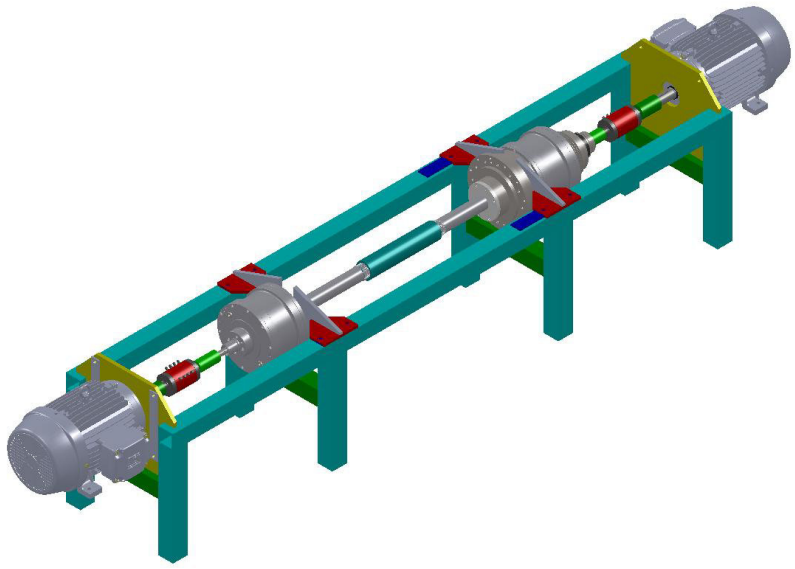

Figure B.6 Concept One pictorial view

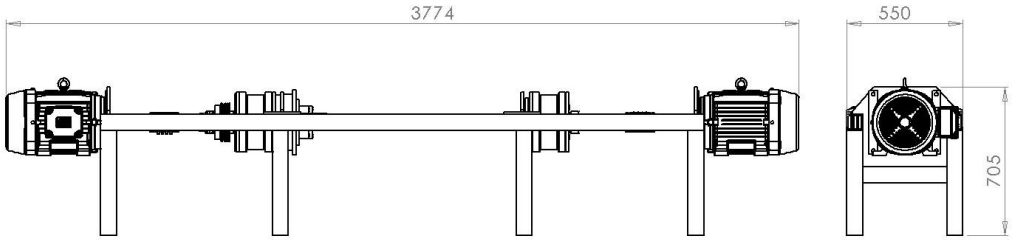

Figure B.7 Concept One dimensions (mm)

B.7.2 Concept Two - Folded

Concept Two (see Figure B.8 and Figure B.9) is similar to Concept One, but it is much shorter because a consequence of using a chain drive between the output shafts. A chain drive was selected as a belt drive would be impractical to use with such high torque. The length has been reduced but the plan area is the same and the clutch arrangement is still missing. The efficiency calculation will need to account for the use of a chain drive.

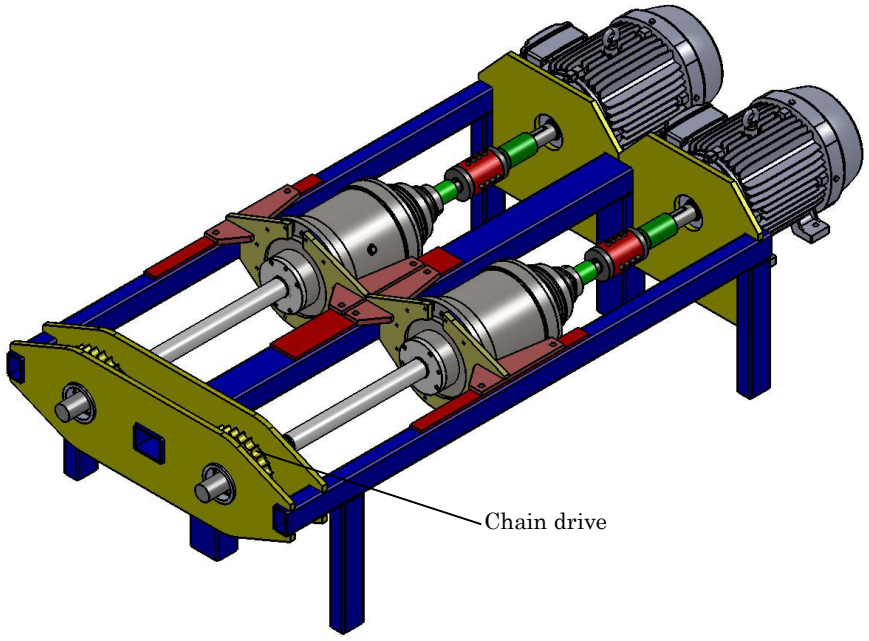

Figure B.8 Concept Two pictorial view

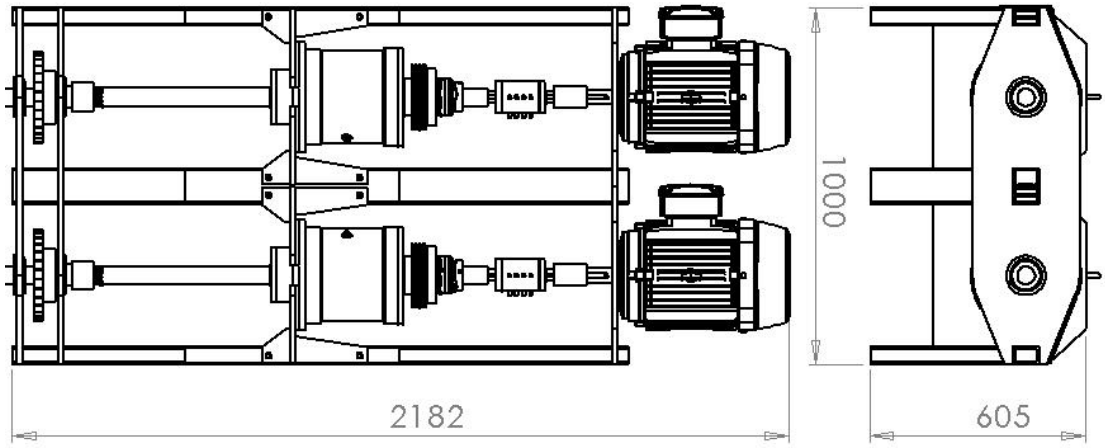

Figure B.9 Concept Two dimensions (mm)

B.7.1 Concept Three - Stacked

Concept Three (see Figure B.10 and Figure B.11) is the final design. This concept reduces the plan area by stacking the motors and gearboxes vertically. This also allows for the clutch assemblies to be included. The belt and chain drives will need to be accounted for in the efficiency calculation. The heat generated within the gearboxes will need to be removed so an oil pump has been included in this design. The lower gearbox is intended to remain as part of the rig and the upper gearbox is the one being tested.

The mounting assembly for the gearboxes can be changed depending on the type of gearbox being tested.

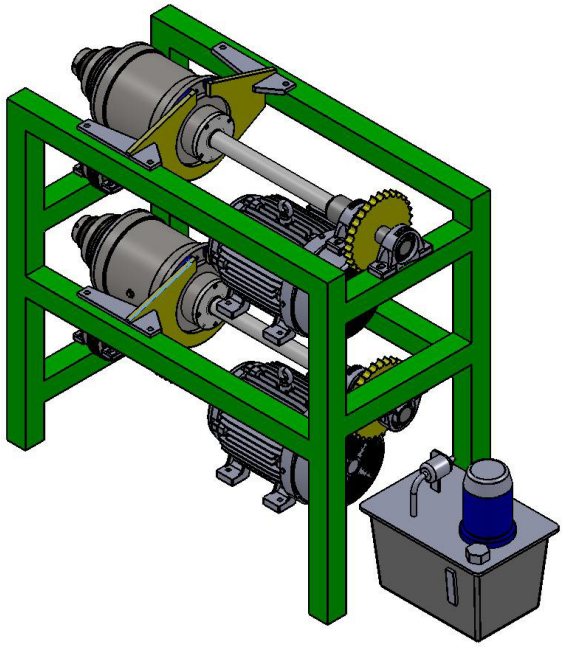

Figure B.10 Concept Three pictorial view

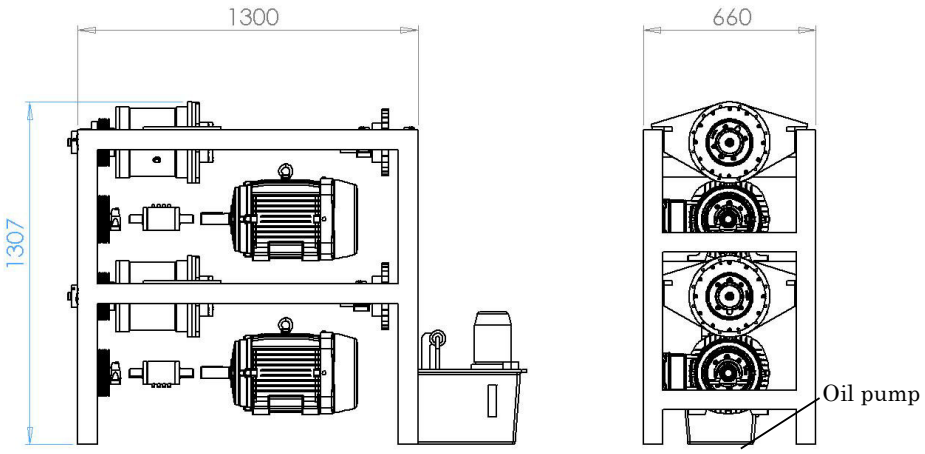

Figure B.11 Concept Three dimensions (mm)

B.8 Design Review

Concept Three is the final evolution of the gearbox test rig. It has a relatively small floor plan area and meets the requirements for testing the gearboxes under load in a production environment. This concept will provide a means of accurately measuring the efficiency of a gearbox under full load.

To enhance the accuracy of the rig the torque and speed of the gearbox output shafts could be measured using telemetry measuring equipment. Therefore the chain drive efficiency can be measured, rather than estimated. The belt drives will also consume power, therefore this must be accounted for in the efficiency calculation.

As the outside of the gearbox is not rotating the convection coefficient is severely reduced and hence the temperature of the gearbox increases. The maximum temperature was estimated by numerical modeling at approximately 100°C. An oil pump and heat exchanger were added to the design to reduce this temperature.

The rig has evolved into a relatively complex design. The belts and chain drive will require tensioning mechanisms to insure they operate at their rated tension. It also requires a permanent gearbox to reduce the torque before the generator.

Appendix C

Wear Test Results

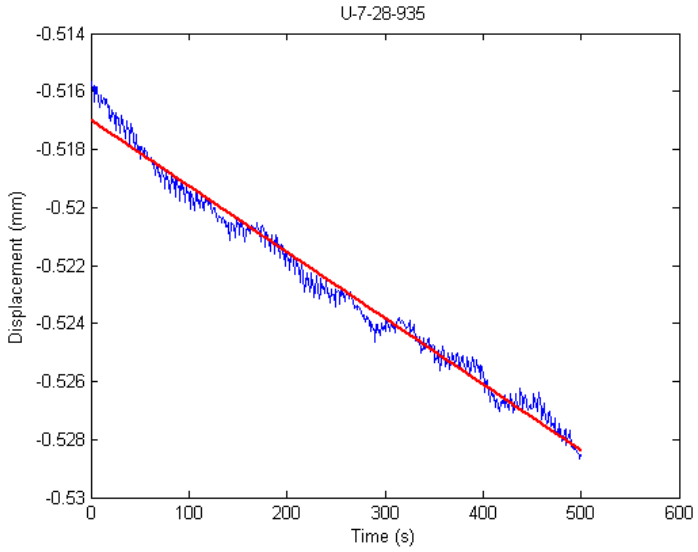

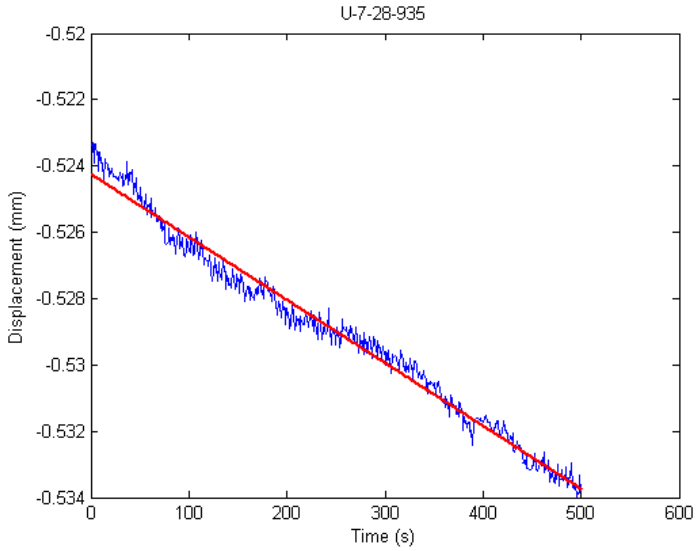

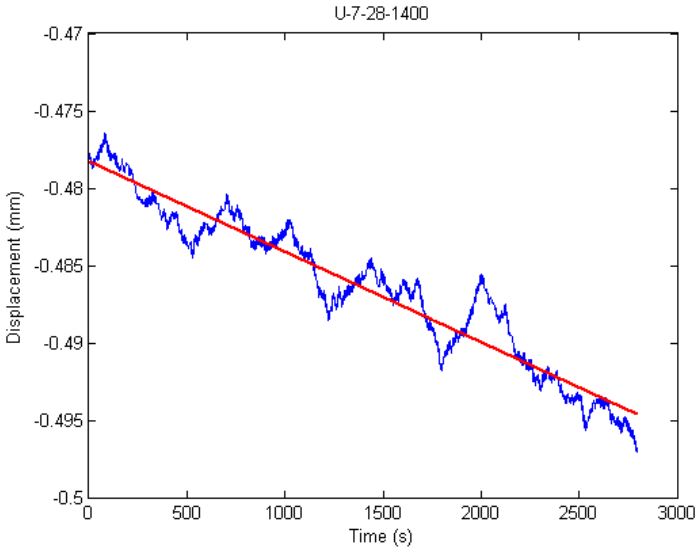
U-7-28-1400
Displacement (mm)
Time (s)
-0.47
-0.475
-0.48
-0.485
-0.49
-0.495
-0.5
0
500
1000
1500
2000
2500
3000

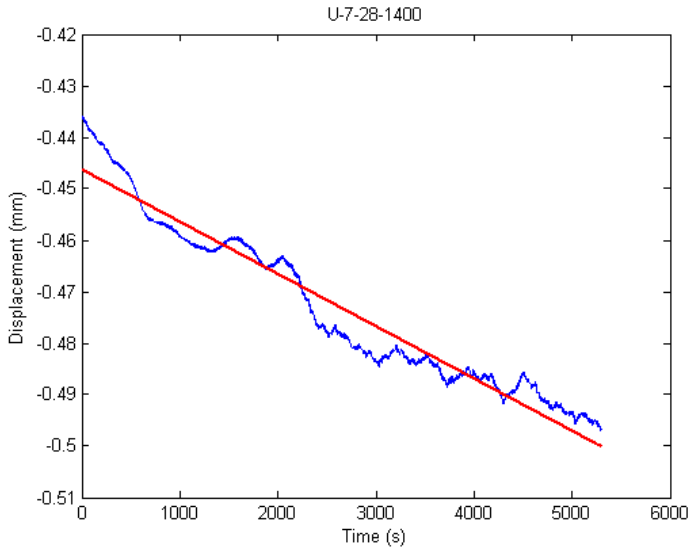
U-7-28-1400
Displacement (mm)
Time (s)
-0.42
-0.43
-0.44
-0.45
-0.46
-0.47
-0.48
-0.49
-0.5
-0.51
0
1000
2000
3000
4000
5000
6000

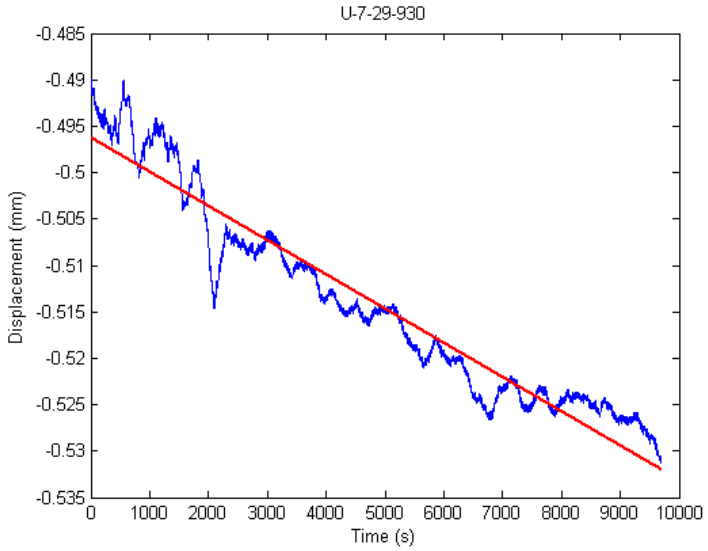
U-7-29-930
Displacement (mm)
Time (s)
-0.485
-0.49
-0.495
-0.5
-0.505
-0.51
-0.515
-0.52
-0.525
-0.53
-0.535
0
1000
2000
3000
4000
5000
6000
7000
8000
9000
10000

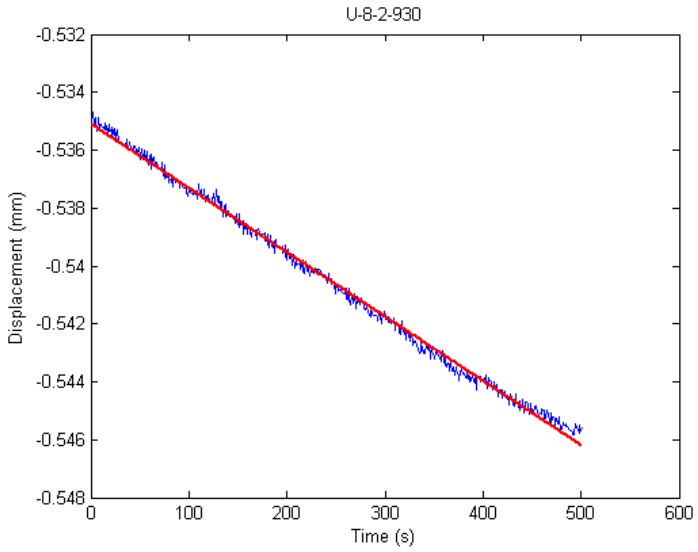
U-8-2-930
Displacement (mm)
Time (s)
-0.532
-0.534
-0.536
-0.538
-0.54
-0.542
-0.544
-0.546
-0.548
0
100
200
300
400
500
600

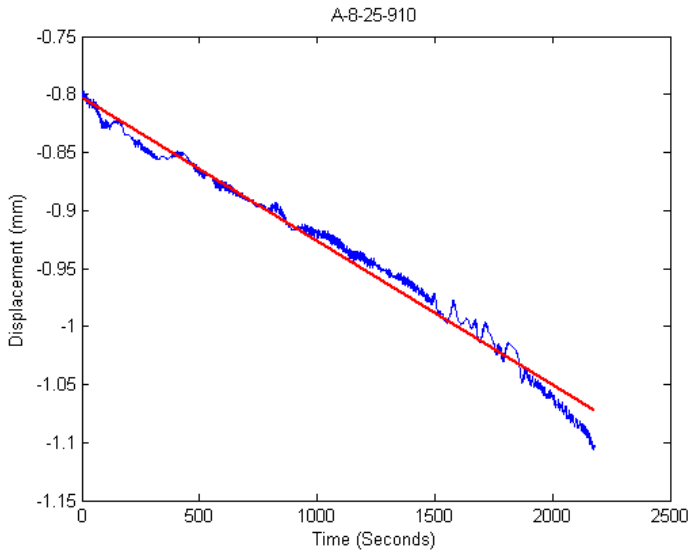
A-8-25-910
Displacement (mm)
Time (Seconds)
-0.75
-0.8
-0.85
-0.9
-0.95
-1
-1.05
-1.1
-1.15
0
500
1000
1500
2000
2500

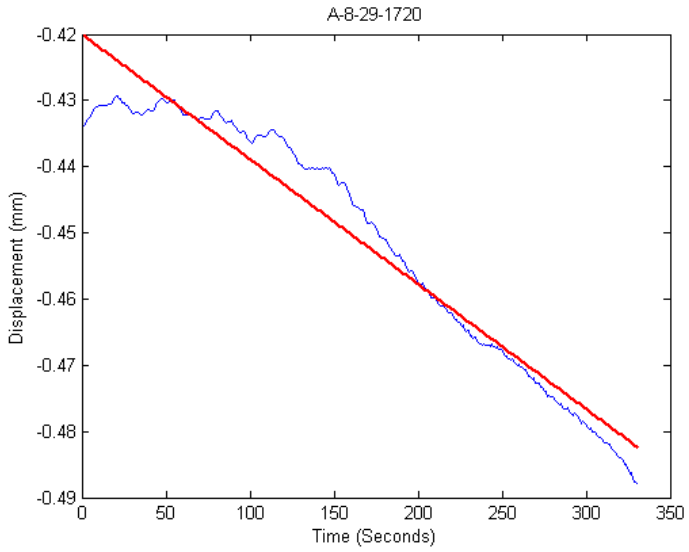
A-8-29-1720
Displacement (mm)
Time (Seconds)
-0.42
-0.43
-0.44
-0.45
-0.46
-0.47
-0.48
-0.49
0
50
100
150
200
250
300
350

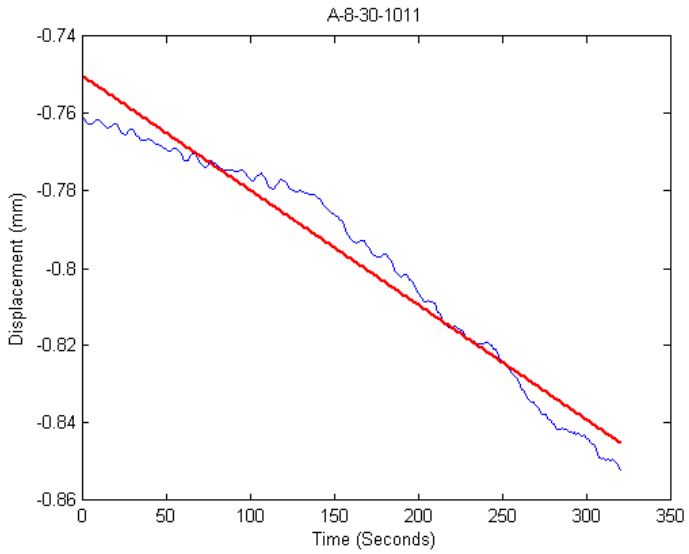
A-8-30-1011
-0.74
-0.76
-0.78
-0.8
-0.82
-0.84
-0.86
Displacement (mm)
0
50
100
150
200
250
300
350
Time (Seconds)

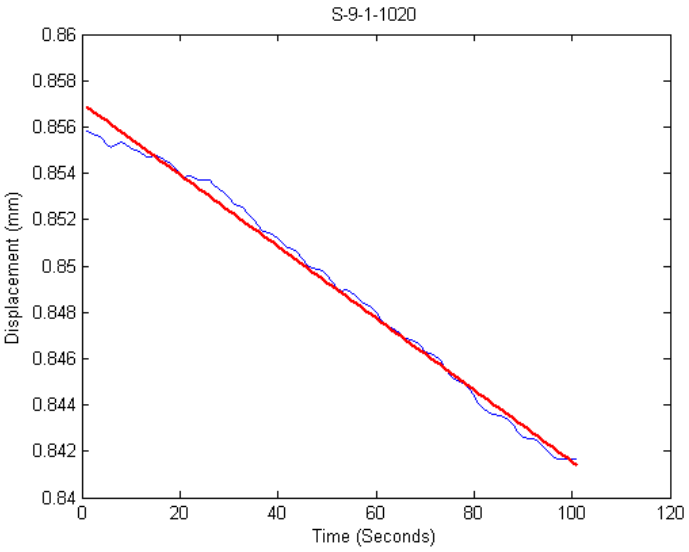
S-9-1-1020
0.86
0.858
0.856
0.854
0.852
0.85
0.848
0.846
0.844
0.842
0.84
Displacement (mm)
0
20
40
60
80
100
120
Time (Seconds)

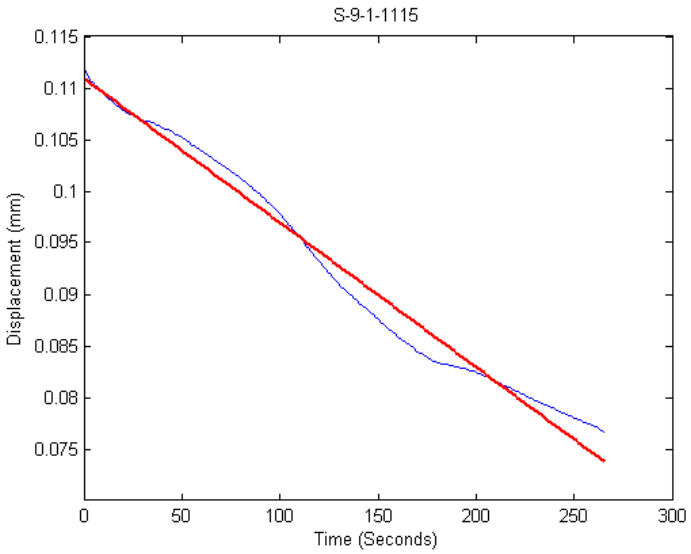
S-9-1-1115
Displacement (mm)
Time (Seconds)
0.115
0.11
0.105
0.1
0.095
0.09
0.085
0.08
0.075
0
50
100
150
200
250
300

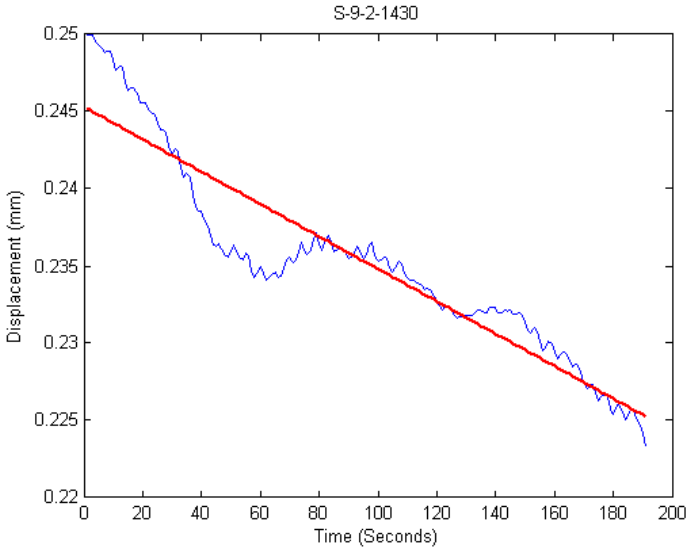
S-9-2-1430
Displacement (mm)
Time (Seconds)
0.25
0.245
0.24
0.235
0.23
0.225
0.22
0
20
40
60
80
100
120
140
160
180
200

Appendix D

GTech-Bellmor 1456 Decanter Centrifuge Composite Bowl Manufacturing Instructions

Prepared by George Bell

For:

- Bellmor Engineering Ltd.
- ASP Ltd.

This document contains the manufacturing instructions for the composite decanter bowl.

Important notes:

Never rest the bowl horizontally while it is on the mandrel, this will crush the composite and render the bowl unusable.

D.1 Mandrel Manufacturing

The mandrel is to be machined from solid 6061 aluminium alloy. The maximum outside diameter of the mandrel is 359.2 mm. It is important that a good surface finish is achieved on the mandrel as it determines the exact interior finish of the bowl. Upon completion of mandrel it should be assembled and delivered to ASP Ltd.

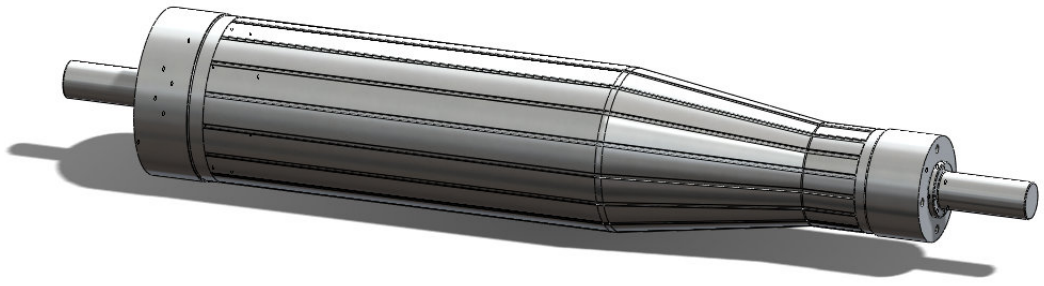

Figure D.1 Fully assembled mandrel

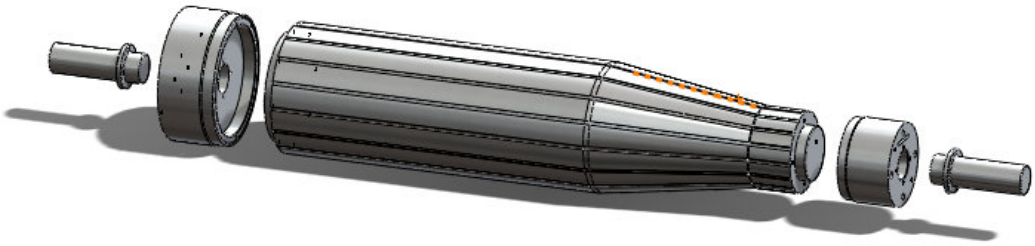

Figure D.2 Exploded view of the fully assembled mandrel, all parts are bolted together with M10 cap screws

D.2 ARC Application

The mould should be disassembled, cleaned, and coated with mould release before the ARC is applied. The final amount (cured) of ARC 855-HTT required is 5.1 litres. The mixing and application instructions are supplied with the ARC.

Figure D.3 The ARC is applied in a layer approximately, but no less than, 3 mm thick in the region shown

D.3 ARC Turning

Once the ARC has cured the mould should be transported back to Bellmor Engineering Ltd. for machining. The ARC is to be turned to be 3 mm (+-0.1) above the surface of the mandrel, not including the depth of the ribs. While the ARC coating has an epoxy matrix it is very hard wearing on cutting tools due to the ceramic fillers. For the smaller prototype a CBN (cubic boron nitride) cutting tip was successfully used. The ideal, post-machining, surface finish is slightly roughened. A roughened surface will aid with the adhesion between the ARC and subsequently applied composite layers.

D.4 Fibre Layup

The mandrel with the machined ARC layer is to be returned to ASP Ltd for application of the composite layers. The fibres are to be laid up and infused in two stages: the continuous 6 mm layer that covers the entire bowl, and the thickened region around the solids discharge ports. Depending on the number of layers, the cloth should be wrapped and vacuum bagged in stages to minimise wrinkling. **If excessive wrinkling occurs do not infuse the composite.** The fibre orientations for the 6 mm thick section are given in Table D.1. 0° is along the rotational axis of the bowl.

Table D.1 Fibre orientations for the 6 mm section

Direction	Material	%	Number	Thickness (mm)
0° - 90°	200g CF	20	4	0.6
+-45°	200g Kevlar	10	2	0.3
+-45°	200g CF	10	2	0.3
0° - 90°	200g CF	20	4	0.6
+-45°	200g CF	10	2	0.3
90°	200g CF	10	2	0.3
0° - 90°	200g CF	20	4	0.6
	ARC 855HT-T			3

A different colour cloth should be added above the final layer on the exterior of the bowl. This is to be used as an indicator during machining No more material should be removed if the layer is exposed. Five extra layers of 200g 0°-90° cloth should be added above the coloured layer. This is to allow for material removal during machining. If the post-infusion layer around the solids discharge ports is not suitable for applying the next layer the surface is to be machined.

The thicker section around the solids discharge ports should be comprised of the orientations described in Table D.2.

.

Table D.2 Fibre orientations within the thickened region around solids discharge ports

Direction	Material	%	Number	Thickness (mm)
0° - 90°	200g CF	20		
0° - 90°	200g CF	20		
+-45°	200g CF	20		
0° - 90°	200g Kevlar	20		
+-45°	200g CF	20		
0° - 90°	200g CF	-	5	0.75
Different coloured indicator layer				
Layers running the full length of the bowl				

Additional layers of 0°-90° should be added to the exterior surface to allow for material removal during machining.

Figure D.4 Composite bowl with both layers applied

D.5 Exterior CFRP Turning

- **Never rest the bowl on its side while on the mandrel**
- **Do not machine discharge ports at this stage**
- **Cutting fluid must be used to ensure the structural integrity of the epoxy is not compromised by heat damage**
- **Inform ASP of any surface cleaning, as mould release will need to be reapplied**

The bowl should be returned to Bellmor Engineering Ltd for machining of the composite exterior. The exterior surface of the bowl is to be turned to that shown in Figure D.1. The radial holes are to be added at this stage, the drill should only penetrate the mandrel the minimum distance required. It is essential that the radial holes align with

the ribs. This ensures that the indentations from drilling through align when the mandrel is used again. The ends of the mandrel have a slot machined into them to allow for a reference plane. The liquid end mandrel section can be removed to allow for machining of internal chamfers. If the part is loose on the mandrel do not continue machining.

Figure D.5 Exterior surface machining of the bowl

D.6 Exterior Finishing Layer

The bowl should be returned to ASP Ltd so the final finishing layer of carbon can be applied. To give the bowl a smooth finish and to seal the carbon from any impurities a finishing layer is to be added. Once the layer has been added the bowl can be removed from the mould. The layer is to cover the exposed parts of the bowl; this starts 40 mm from the liquid end (left) and up to the edge of the step at the solids end (right).

Figure D.6 The exterior surface of the bowl is to have a smooth layer added after machining, this should cover the exposed surface of the carbon

D.7 End Hubs

A standard set of end hub castings can be altered for this design. The axial holes and flange has been removed and replaced with radial holes. The critical outside diameter is determined by the dimensions of the finished composite bowl. These components should be finished after the bowl has been completed.

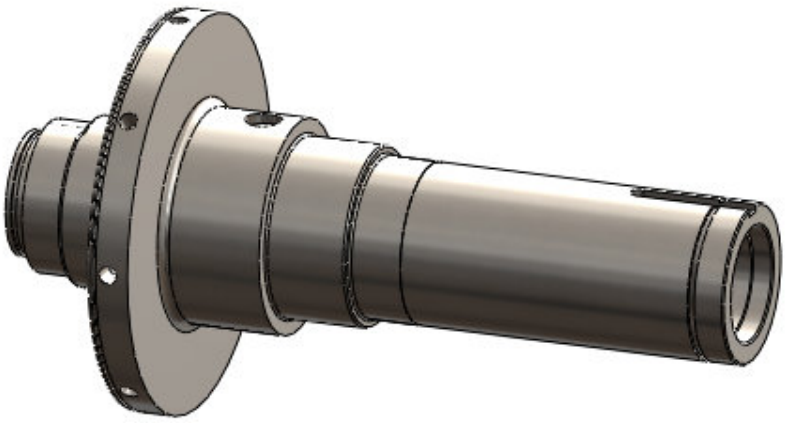

Figure D.7 Solids end hub – machined to a smaller diameter with radial holes and an o-ring groove

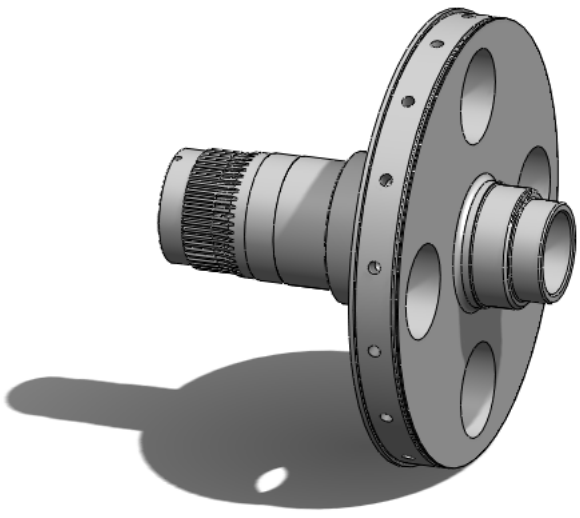

Figure D.8 Liquid end hub – machined to a smaller diameter with radial holes and an o-ring groove

Figure D.9 Solids end over ring – machined from 316 stainless steel

Figure D.10 Liquid end over ring – machined from 316 stainless steel

D.8 Solids Discharge Port Machining

Once the exterior finishing layer has been applied, the bowl should be returned to Bellmor Engineering Ltd so the solids discharge ports can be machined. The bowl can be supported on the end hubs or mandrel ends during machining.

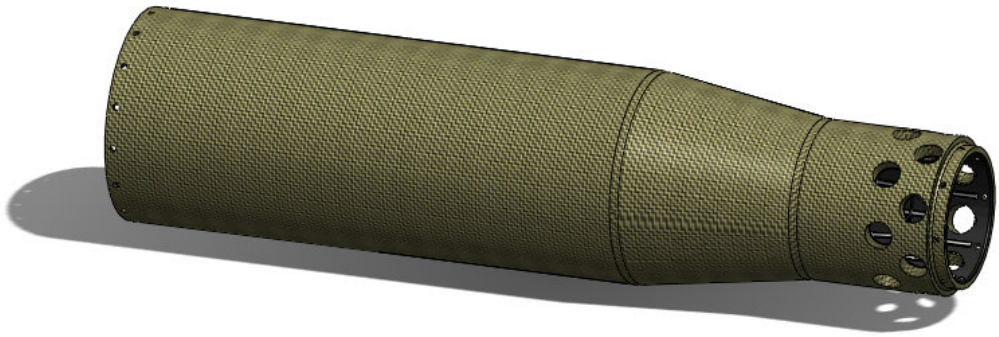

Figure D.11 Discharge port machining

D.9 Attaching Discharge Port Liners

The 16 ceramic port liners should be glued in place with a compatible adhesive. The internal face of the liner should sit flush with the ribs inside the bowl.

Figure D.12 Completed bowl assembly with end hubs

D.10 Balancing

Once the bowl is fully assembled it should be balanced. Material can be removed from the end over rings to account for any imbalance. Balancing should be done with the bowl and hubs only, the scroll only, and then the full rotating assembly should be trim balanced.

References

1. Sutherland, K., Filtration and separation technology: What's new with centrifuges? *Filtration and Separation*, **2009**, 46 (3), 30-32.
2. *Alfa Laval - ALDEC G3*. [cited 2013 Jan 15]; Available from: www.alfalaval.com/solution-finder/products/aldec-g3.
3. *Decanters from GEA Westfalia Separator*. [cited 2013 Jan 15]; Available from: www.westfalia-separator.com/products/decanters.html.
4. ANDRITZ. *ANDRITZ - Solid bowl decanter centrifuge*. [cited 2013 Jan 15]; Available from: www.andritz.com.
5. Leung, W.W.F., Shapiro, A.H. Feed Accelerator System Including Accelerating Vane Apparatus. Patent: 5380266, May 28, 1996.
6. Pasol, L., Dousset, C., Huyghe, J.-M., Krammer, G., New centrifuge pond level control system handles variable feeds. *Filtration & Separation*, 47 (5), 18-21.
7. Leung, W.F., Shapiro, A.H., Dewatering of fine-particle slurries using a compound-beach decanter with cake-flow control. *Minerals and Metallurgical Processing*, **2002**, 19 (1), 1-8.
8. Minaker, V.E., Prospects For Future Developments in Screw-Conveyor Sedimentation Centrifuges (Decanters): A Discussion. *Chemical and Petroleum Engineering*, **1995**, 31 (3), 8-13.
9. Reif, F., Stahl, W. *Friction Coefficient of Moist Bulk Solids in a Centrifugal Field*, Proceedings of Procession of the Fifth International Symposium on Multiphase Transport & Particulate Phenomena, Miami, Florida, 1988.
10. Reif, F., Stahl, W., Transportation of moist solids in decanter centrifuges. *Chemical Engineering Progress*, **1989**, 85 57-67.
11. Leung, W.W.F., Torque requirement for high-solids centrifugal sludge dewatering. *Filtration & Separation*, **1998**, 35 (9), 883-887.
12. Fainerman, I.A., Paramonov, I.A., Calculation of the power of centrifuge drives required for the acceleration of suspensions. *Chemical and Petroleum Engineering*, **1985**, 21 (4), 184-186.
13. Leung, W.W.F., *Industrial Centrifugation Technology*. McGraw-Hill, New York, 1998.
14. Randle, P., Noise and Vibration Control for a Decanter Centrifuge. Master of Engineering Thesis, Department of Mechanical Engineering, University of Canterbury, Christchurch, New Zealand, 2011.
15. Leung, W.W.-F., *Centrifugal Separations in Biotechnology*. Elsevier, Oxford, 2007.
16. Leung, W.W.F., Shapiro, A.H. Feed Accelerator System Including Accelerator Cone. Patent: 5380266, Jan 10, 1995.
17. Leung, W.W.F., Shapiro, A.H., Improved design of conical accelerators for decanter and pusher centrifuges. *Filtration and Separation*, **1996**, 33 (8), 735-738.
18. Leung, W.W.F., Shapiro, A.H., Improved design of conical accelerators for decanter and pusher centrifuges. *Filtration & Separation*, **1996**, 33 (8), 735-738.
19. Leung, W.W.F., Shapiro, A.H., Yarnell, R., Improvements in the classification of fine-particle slurries using decanter centrifuges. *Filtration & Separation*, **1999**, 36 (9), 32-37.
20. Lavanchy, A.C. Centrifuge Apparatus. Patent: 70,946, 1981.

21. Tan, W., Qiao, L., Sha, E., Tao, Y., Liu, L., Optimal design of the accelerator disk in a two-stage piston pusher centrifuge using numerical simulation. *Industrial and Engineering Chemistry Research*, **2012**, 51 (12), 4632-4642.
22. Fernandez, X.R., Nirschl, H., Multiphase CFD simulation of a solid bowl centrifuge. *Chemical Engineering and Technology*, **2009**, 32 (5), 719-725.
23. Reif, F., Stahl, W., Transportation of moist solids in decanter centrifuges. *Chemical Engineering Progress*, **1989**, 85 (11), 57-67.
24. Peeters, B., Weis, S., Relationship between pool depth and internal washing on the beach of a solid bowl decanter centrifuge. *Filtration & Separation*, **2004**, 41 (6), 36-40.
25. Day, N., Centrifuge focus: Evaluation, testing and optimisation. *Filtration & Separation*, **2005**, 42 (6), 22-24.
26. King, R.H., Fine-tunable centrifuge conserves energy. *Design News (Boston)*, **1994**, 49 (20), 67-68.
27. Records, A., Sutherland, K., *Decanter Centrifuge Handbook*. 1st edition. Elsevier, 2001.
28. Stahl, W.H., *INDUSTRIE-ZENTRIFUGEN*. DrM Press, Switzerland, 2004.
29. Reif, F., Stahl, W., Langeloh, T., Optimising decanter centrifuges. *Filtration & Separation*, 27 (6), 408-410.
30. Corner-Walker, N., Records, F.A., The dry solids decanter centrifuge: Conveyor torque and differential. *Filtration & Separation*, **2000**, 37 (8), 18-23.
31. Abel, P.G., Zur Kapillarkohasion Feuchter Haufwerke. *Publications of the Institute for Soils and Rock Mechanics*, **1969**, 43
32. Goesele, W., Scale-up of Helical Conveyor Type Decanter Centrifuge. *German Chemical Engineering*, **1980**, 3 (6), 353-359.
33. WEG. *WEG Motor Catalogue*. [cited 2011 Jan 25]; Available from: www.catalogo.weg.com.br.
34. Erickson, W.D., *Belt selection and application for engineers*. M. Dekker, New York, 1987.
35. Francis, R., Pushing Belt Drive Efficiency - The Goodyear Tire and Rubber Company, 1998**.**
36. Rapp, P., *Engineers Black Book*. 2nd edition. Pat Rapp Industries, Perth, 2002.
37. Roymech. *V-Belts*. [cited 2011 Feb 8]; Available from: www.roymech.co.uk/Useful_Tables/Drive/Vee_belts.html.
38. Broadbent, Centrifuge Upgrade Significantly Increases Chemical Throughput. *Filtration & Separation*, **2003**, 40 (5), 15.
39. Stokes, A., *Gear Handbook: Design and Calculations*. Butterworth-Heinemann, Oxford-Boston, 1992.
40. Dudley, D.W., Townsend, D.P., *Dudley's Gear Handbook*. 2nd edition. McGraw Hill, New York, 1991.
41. *Mobil SHC 600 Series*. 2001 [cited 2011 Feb 7]; Available from: http://www.mobil.com/USA-English/Lubes/PDS/GLXXENINDMOMobil_SHC_600.aspx.
42. Geropp, D., Turbulent heat transfer from rotating cylinder - Der turbulente waermeuebergang am rotierenden zylinder. **1969**, 38 (4-5), 195-203.
43. Gschwendtner, M.A., The Eckert number phenomenon: Experimental investigations on the heat transfer from a moving wall in the case of a rotating cylinder. *Heat and Mass Transfer/Waerme- und Stoffuebertragung*, **2004**, 40 (6-7), 551-559.
44. SKF. *Friction*. [cited 2011 Jan 25]; Available from: http://www.skf.com/portal/skf/home/products?maincatalogue=1&lang=en&newlink=1_0_35.

45. Plath, S., Meyer, S., Wollesen, V.M., Friction torque of a rotary shaft lip type seal - A comparison between test results and finite element simulation. *Mechanika*, **2005**, (4), 55-59.
46. Bilgen, E., Functional dependence of torque coefficient of coaxial cylinders on gap width and Reynolds numbers. *Transactions of the ASME. Series I, Journal of Fluids Engineering*, **1973**, 95 (1), 122-126.
47. Çengel, Y.A., Turner, R.H., *Fundamentals of thermal-fluid sciences*. 2nd edition. McGraw-Hill Companies, Boston, 2005.
48. Wendt, F., Turbulente Stromungen Zwishen zwei rotierendes konaxialen zylindern. *Ingenieur-Archiiv*, **1933**, 9 (4), 577.
49. Wild, P.M., Djilali, N., Vickers, G.W., Experimental and computational assessment of windage losses in rotating machinery. *Journal of Fluids Engineering, Transactions of the ASME*, **1996**, 118 (1), 116-122.
50. Bies, D.A., Hansen, C.H., *Engineering Noise Control - Theory and Practice*. Taylor & Francis Group, Adelaide, 2003.
51. Budinski, K.G., *Guide to Friction, Wear, and Erosion Testing*. ASTM International, Mayfield, 2007.
52. Bertin, M., *Wearing Tests for a Decanter Centrifuge*, 2013, Department of Mechanical Engineering, University of Canterbury, Christchurch, New Zealand.
53. *Standard test Method for Wear testing with a Pin-on-Disk Apparatus*, ASTM G99-05.
54. Chesterton. [cited 2012 Aug 1]; Available from: www.chesterton.com.
55. Pyrotek. [cited 2012 Aug 1]; Available from: www.pyrotek.info.
56. Zhang, X., Wang, Y., Xu, X., Wang, H., Energy conversion characteristic within impeller of low specific speed centrifugal pump. *Nongye Jixie Xuebao/Transactions of the Chinese Society of Agricultural Machinery*, **2011**, 42 (7), 75-81.
57. Gomez-Ledesma, R., Kiger, K.T., Duncan, J.H., The impact of a translating plunging jet on a pool of the same liquid. *Journal of Fluid Mechanics*, **2011**, 680 (1), 5-30.
58. Birkhoff, G., Zarantonello, E.H., Jets, Wakes, and Cavities. *Academic Press*, **1957**,
59. Bin, A.K., Gas entrainment by plunging liquid jets. *Chemical Engineering Science*, **1993**, 48 (21), 3585-3630.
60. *ANSYS CFX-Pre User's Guide*. SAS IP. Inc., 2010.
61. *ANSYS CFX-Solver Modeling Guide*. SAS IP. Inc., 2010.
62. *ANSYS CFX-Solver Theory Guide*. SAS IP. Inc., 2010.
63. *LEAP Support Team: Inflation Layer Meshing in ANSYS*. 2012 [cited 2013 Feb 14]; Available from: http://www.computationalfluiddynamics.com.au/tips-tricks-inflation-layer-meshing-in-ansys/.
64. Launder, B.E., Spalding, D.B., Numeric Computation of Turbulent Flows. *Computer Methods in Applied Mechanics and Engineering*, **1974**, 3 (2), 269-289.
65. Menter, F.R., Two-equation eddy-viscosity turbulence models for engineering applications. *AIAA journal*, **1994**, 32 (8), 1598-1605.
66. Launder, B.E., Reece, G.J., Rodi, W., Progress in the development of a Reynolds-stress turbulence closure. *Journal of Fluid Mechanics*, **1975**, 68 (3), 537-66.
67. Shalaby, H., Pachler, K., Wozniak, K., Wozniak, G., Comparative study of the continuous phase flow in a cyclone separator using different turbulence models. *International Journal for Numerical Methods in Fluids*, **2005**, 48 (11), 1175-97.
68. Singh, H., Fletcher, D.F., Nijdam, J.J., An assessment of different turbulence models for predicting flow in a baffled tank stirred with a Rushton turbine. *Chemical Engineering Science*, **2011**, 66 (23), 5976-5988.

69. Norton, V., Wilkie, W., Clarifying centrifuge operation and selection. *Chemical Engineering Progress*, **2004**, 100 (8), 34-9.
70. Hart, R.R., General considerations to aid centrifuge selection. *Industrial Chemist*, **1962**, 38 (448), 270-278.
71. Belcher, T., Decanter and disc-stack centrifuge systems. *Filtration & Separation*, **1991**, 28 (6), 387-388.
72. Whitaker, J.C., *AC power systems handbook*. 3rd edition. CRC Press/Taylor & Francis, Boca Raton, FL, 2007.